

MEMOIRS
OF THE
FACULTY OF ENGINEERING
OSAKA CITY UNIVERSITY

MEMOIRS OF THE FACULTY OF ENGINEERING OSAKA CITY UNIVERSITY

VOL. 54

DECEMBER 2013

PUBLISHED BY THE
GRADUATE SCHOOL OF ENGINEERING
OSAKA CITY UNIVERSITY

VOL. 54. 2013

MEMOIRS OF THE FACULTY OF ENGINEERING
OSAKA CITY UNIVERSITY

VOL. 54

DECEMBER 2013

CONTENTS

Regular Articles 1

Mechanical and Physical Engineering

Applied Mathematics

**Note on Backward Uniqueness for Heat Equations with Coefficients Non-Lipschitz
Continuous in Time**

Shigeo TARAMA 1

Physical Electronics and Informatics

Applied Physics and Electronics

**Complete Extraction of Statistics Values in Cellular Automata using Special Purpose Parallel
Computers Constructed in FPGA**

Makoto HOSODA and Yoshiaki NAITOH 13

Electric and Information Engineering

A Mobile Measurement System for Sound Source Level of Wild Dolphin Whistles

*Tadamichi MORISAKA, Mai SAKAI, Kazunobu KOGI, Tomio SHINKE, THI THI ZIN, and
Hiromitsu HAMA* 25

Urban Engineering

Civil Engineering

Classification of based on the Collapse Mechanism for a Corroded Damaged Steel Girder End <i>Makoto USUKURA and Takashi YAMAGUCHI</i>	31
---	----

An Analysis on Influencing Factors on Difficulty of Shopping Accessibility by Considering Individual Attributes and Area Characteristics <i>Noboru ISE and Yasuo HINO</i>	37
---	----

An Empirical Study of Verbal Map Guidelines for Visually-impaired people to Enhance Daily Mobility <i>Mei TAKAHASHI and Takashi UCHIDA</i>	47
--	----

Urban Engineering

Consolidation of Predicted Disaster Information and Expectation of Coincident Disaster <i>Shouta MORI and Takaaki SHIGEMATSU</i>	57
--	----

Abstracts of Papers Published in Other Journals	67
---	----

Mechanical and Physical Engineering

<i>Mechanical Engineering</i>	69
<i>Intelligent Materials Engineering</i>	78
<i>Machine Workshop</i>	87

Physical Electronics and Informatics

<i>Applied Physics and Electronics</i>	88
<i>Electric and Information Engineering</i>	97

Applied Chemistry and Bioengineering

<i>Applied Chemistry</i>	101
<i>Bioengineering</i>	112

Urban Engineering

<i>Architecture and Building Engineering</i>	119
<i>Civil Engineering</i>	122
<i>Environmental Urban Engineering</i>	137

Note on Backward Uniqueness for Heat Equations with Coefficients Non-Lipschitz Continuous in Time

Shigeo TARAMA*

(Received September 30, 2013)

Synopsis

Modifying the weight function given by Del Santo and Prizzi, we draw Carleman estimates, which show the uniqueness of solutions to the backward Cauchy problem for some class of heat equations with coefficients non-Lipschitz continuous in time.

KEYWORDS: Heat equation, Backward Cauchy problem, Uniqueness

1. Introduction

We consider a heat operator in the time backward form,

$$Lu = \partial_t + \sum_{j,k=1}^d \partial_{x_j}(a_{jk}(x, t)\partial_{x_j}u) \quad (1.1)$$

with real, bounded and continuous coefficients $a_{jk}(x, t)$ on $\mathbb{R}^d \times [0, T]$, for some $T > 0$, satisfying $a_{jk}(x, t) = a_{kj}(x, t)$ ($j, k = 1, 2, \dots, d$) and

$$\sum_{j,k=1}^d a_{jk}(x, t)\xi_j\xi_k \geq D_0|\xi|^2 \quad (1.2)$$

for any $\xi \in \mathbb{R}^d$ with some positive D_0 .

We consider the the Cauchy problem with Cauchy data on the plane $t = 0$. Concerning the uniqueness of solutions to the Cauchy problem, there are many works since the work of Mizohata ⁶⁾. See for example Vessella's survey ⁸⁾ and that of Del Santo and Jäh ³⁾ and the papers cited therein.

Del Santo and Prizzi ^{1) 2)} consider an operator whose coefficients $a_{jk}(x, t)$ ($j, k = 1, 2, \dots, d$) are $C_b^0(\mathbb{R}^d)$ -valued μ continuous function on $[0, T]$. Here $C_b^0(\mathbb{R}^d)$ is a space of bounded and continuous functions on \mathbb{R}^d . That is, there exists a constant $M \geq 0$ such that we have

$$\sup_{x \in \mathbb{R}^d} |a_{jk}(x, t+s) - a_{jk}(x, t)| \leq M\mu(s) \quad (1.3)$$

for any t, s satisfying $s \in (0, 1]$ and $t \in [0, T-s]$. Here the modulus of continuity $\mu(s)$ is assumed to be a continuous, concave and strictly increasing function on $[0, 1]$ that satisfies $\mu(0) = 0$ and

$$\lim_{\varepsilon \searrow 0} \int_{\varepsilon}^1 \frac{1}{\mu(s)} ds = \infty. \quad (1.4)$$

On the regularity of a_{jk} with respect to x , Del Santo and Prizzi ²⁾ assume that $a_{jk}(x, t)$ are Lipschitz continuous in x uniformly with respect to t , that is, with some $L \geq 0$,

$$\sum_{j,k=1}^d |a_{jk}(x, t) - a_{jk}(y, t)| \leq L|x - y| \quad (1.5)$$

for any $x, y \in \mathbb{R}^d$ and any $t \in [0, T]$.

Under these conditions Del Santo and Prizzi ²⁾ show the uniqueness of solutions to the Cauchy problem.

In this paper, we show that the assertion of Del Santo and Prizzi ²⁾ is still valid even if the coefficients $a_{jk}(x, t)$ ($1 \leq j, k \leq d$), belonging to $C^b([0, T] \times \mathbb{R}^d)$, satisfy

$$\int_0^T \sup_{s \in (0, \min\{1, T-t\}] } \sup_{x \in \mathbb{R}^d} |a_{jk}(x, t+s) - a_{jk}(x, t)|/\mu(s) dt < \infty. \quad (1.6)$$

*Professor, Laboratory of Applied Mathematics

More precisely, we show the following theorem.

Theorem 1.1. *Assume that the coefficients $a_{jk}(x, t)$ ($j, k = 1, 2, \dots, d$) of the operator (1.1) are real, continuous, bounded and symmetric and satisfy (1.2), (1.5) and (1.6).*

Let $u(x, t) \in L^2([0, T], H^1(\mathbb{R}_x^d)) \cap C^0([0, T], L^2(\mathbb{R}_x^d))$ satisfy $Lu \in L^2([0, T], L^2(\mathbb{R}_x^d))$,

$$\|Lu(\cdot, t)\| \leq C\|u(\cdot, t)\|_1 \quad \text{almost all } t \in [0, T],$$

and $u(x, 0) = 0$. Then we have $u(x, t) = 0$ on $\mathbb{R}^d \times [0, T]$.

Here the spaces L^2 and H^1 and their norms $\|\cdot\|$ and $\|\cdot\|_1$ are standard ones whose definitions are given below. For a Banach space X , we denote by $L^2([0, T], X)$ and $C^0([0, T], X)$ the space of X -valued square integrable functions and the space of X -valued continuous functions respectively.

Remark 1. We note that $Lu \in L^2([0, T], L^2(\mathbb{R}_x^d))$ and $u(x, t) \in L^2([0, T], H^1(\mathbb{R}_x^d))$ imply $\partial_t u(x, t) \in L^2([0, T], H^{-1}(\mathbb{R}_x^d))$. While $\partial_t u(x, t)$ being in $L^2([0, T], H^{-1}(\mathbb{R}_x^d))$ and $u(x, t)$ in $L^2([0, T], H^1(\mathbb{R}_x^d))$ imply $u(x, t) \in C^0([0, T], L^2(\mathbb{R}_x^d))$ (see for example Theorem 1. §1.1 Ch. XVIII in Dautray and Lions ⁴). Then the assumption $u(x, t) \in C^0([0, T], L^2(\mathbb{R}_x^d))$ follows from the other assumptions.

In the next section we recall the properties of the Hardy-Littlewood decomposition and the properties of the modulus of continuity and related functions for the preliminaries. We draw the Carleman estimate in the section 3. Finally we give the proof of Theorem 1.1 in the section 4. We consider examples of functions satisfying (1.6) in the Appendix.

We denote the space of square integrable functions on \mathbb{R}^d by $L^2(\mathbb{R}^d)$. The inner product in $L^2(\mathbb{R}^d)$ is given by

$$(u, v) = \int_{\mathbb{R}^d} u(x) \overline{v(x)} dx$$

and the norm by $\|v(\cdot)\| = \sqrt{\int_{\mathbb{R}^d} |v(x)|^2 dx}$.

The space $H^1(\mathbb{R}^d)$ consists of $u(x) \in L^2(\mathbb{R}^d)$ whose derivatives $\partial_{x_j} u(x)$ ($j = 1, 2, \dots, d$) belong also to $L^2(\mathbb{R}^d)$. The norm $\|\cdot\|_1$ of $H^1(\mathbb{R}^d)$ is given by $\|u(\cdot)\|_1 = \sqrt{\|u(\cdot)\|^2 + \sum_{j=1}^d \|\partial_{x_j} u(\cdot)\|^2}$. We set $\|\nabla u\|^2 = \sum_{j=1}^d \|\partial_{x_j} u\|^2$.

Let $C^\infty(\Omega)$ be the space of infinitely differentiable functions on Ω , $W^{1,\infty}(\mathbb{R}^d)$ the space of bounded and Lipschitz continuous functions on \mathbb{R}^d with the norm

$$\|u(\cdot)\|_{W^{1,\infty}} = \|u(\cdot)\|_{L^\infty} + \sum_{j=1}^d \|\partial_{x_j} u(\cdot)\|_{L^\infty}.$$

Here we denote by $\|u(\cdot)\|_{L^\infty}$ the essential supremum of $|u(x)|$ on \mathbb{R}^d .

We denote by $\hat{v}(\xi)$ the Fourier transform of $v(x)$ given by

$$\int_{\mathbb{R}^d} e^{-ix\xi} v(x) dx,$$

while the inverse Fourier transform of $w(\xi)$ is defined by

$$\frac{1}{(2\pi)^d} \int_{\mathbb{R}^d} e^{ix\xi} w(\xi) d\xi.$$

In the following, we use C or C with some suffix in order to denote positive constants that may be different line by line.

2. Preliminaries

2.1. The Littlewood-Paley decomposition

We recall some properties of the Littlewood-Paley decomposition and the related results referring to Metivier ⁵. See also the paper of Del Santo and Prizzi ².

Let $\phi_0(\xi) \in C^\infty(\mathbb{R}^d)$ satisfy $0 \leq \phi_0(\xi) \leq 1$, $\phi_0(\xi) = 1$ for $|\xi| \leq 11/10$ and $\phi_0(\xi) = 0$ for $|\xi| \geq 19/10$. We define $\phi_n(\xi)$ with $n = 1, 2, 3, \dots$ by

$$\phi_n(\xi) = \phi_0\left(\frac{\xi}{2^n}\right) - \phi_0\left(\frac{\xi}{2^{n-1}}\right).$$

For a function $\phi(\xi)$, we denote the Fourier multiplier with $\phi(\xi)$ by ϕ ; that is ϕv is the inverse Fourier transform of $\phi(\xi)\hat{v}(\xi)$. We remark that the support of $\phi_n u$ is contained in $\{\xi; 2^{n-1} \leq |\xi| \leq 2^{n+1}\}$ when $n > 0$ and that

$$C^{-1}\|u\|^2 \leq \sum_{n=0}^{\infty} \|\phi_n u\|^2 \leq C\|u\|^2. \quad (2.1)$$

In the next section, we use the following lemma whose proof can be found in the author's paper⁷⁾ for example. But for convenience we give the proof.

Lemma 2.1. *For $a(x) \in W^{1,\infty}(\mathbb{R}^d)$, we have*

$$\sum_{n=0}^{\infty} \|\phi_n a u - a \phi_n u\|_1^2 \leq C(\|a\|_{W^{1,\infty}} \|u\|)^2. \quad (2.2)$$

Proof. We define the paraproduct $T_a u$ by $\sum_{l=0}^{\infty} a_{l-3} \phi_l u$. Here a_l is the inverse Fourier transform of $\phi_0(2^{-l}\xi)\hat{a}(\xi)$. It is well known that we have

$$\|a u - T_a u\|_1 \leq C\|a\|_{W^{1,\infty}} \|u\|.$$

See for example Theorem 5.2.8 of Metivier⁵⁾. This estimate and (2.1) imply

$$\begin{aligned} \sum_{n=0}^{\infty} \|(a \phi_n u - T_a \phi_n u)\|_1^2 &\leq C(\|a\|_{W^{1,\infty}} \|u\|)^2, \\ \sum_{n=0}^{\infty} \|\phi_n (a u - T_a u)\|_1^2 &\leq C(\|a\|_{W^{1,\infty}} \|u\|)^2. \end{aligned}$$

Then we have only to show

$$\sum_{n=0}^{\infty} \|\phi_n T_a u - T_a \phi_n u\|_1^2 \leq C(\|a\|_{W^{1,\infty}} \|u\|)^2.$$

In the following, we assume that l and n are non-negative integers. Note that the spectrum of $a_{l-3} \phi_l u$, that is, the support of the Fourier transform of $a_{l-3} \phi_l u$ is contained in $2^{l-1} < |\xi| < 2^{l+1}$ if $l \geq 1$, while the spectrum of $a_{-3} \phi_0 u$ is contained in $|\xi| < 2$. Then we see

$$\phi_n a_{l-3} \phi_l u = 0 \quad |l - n| \geq 3.$$

We remark also that $\phi_l(\xi)\phi_n(\xi) = 0$ if $|l - n| > 1$. Then $\phi_n T_a u - T_a \phi_n u$ is equal to

$$\sum_{l:|l-n|\leq 2} \phi_n a_{l-3} \phi_l u - a_{l-3} \phi_l \phi_n u,$$

which, using the symbol of commutator, is equal to

$$\sum_{l:|l-n|\leq 2} [\phi_n, a_{l-3}] \phi_l u.$$

Since $a_l(x) = \int_{\mathbb{R}^d} a(y) 2^{ld} P(2^l(x-y)) dy$ where $P(x)$ is the inverse Fourier transform of $\phi_0(\xi)$, then we have $|a_l(x) - a_l(y)| \leq C\|a\|_{W^{1,\infty}} |x - y|$. Note that $[\phi_n, a_{l-3}] \phi_l u$ is equal to

$$2^{nd} \int_{\mathbb{R}^d} Q(2^n(x-y))(a_l(y) - a_l(x)) \phi_l u(y) dy$$

where $Q(x) = P(x) - 2^{-d}P(x/2)$ if $n \geq 1$ and $Q(x) = P(x)$ if $n = 0$. Then

$$|[\phi_n, a_{l-3}] \phi_l u(x)| \leq C\|a\|_{W^{1,\infty}} 2^{-n} 2^{nd} \int_{\mathbb{R}^d} P_1(2^n(x-y)) |\phi_l u(y)| dy$$

where $P_1(x) = |P(x)||x|$. Since $P_1(x)$ is integrable, we have

$$\|[\phi_n, a_{l-3}]\phi_l u\| \leq C\|a\|_{W^{1,\infty}} 2^{-n}\|\phi_l u\|.$$

If $|l - n| \leq 2$, the spectrum of $[\phi_n, a_{l-3}]\phi_l u$ is contained in $|\xi| \leq 2^{n+2}$, then

$$\|[\phi_n, a_{l-3}]\phi_l u\|_1 \leq (2^{n+4} + 1)\|[\phi_n, a_{l-3}]\phi_l u\|.$$

Hence we obtain

$$\left\| \sum_{l:|l-n|\leq 2} [\phi_n, a_{l-3}]\phi_l u \right\|_1 \leq \sum_{l:|l-n|\leq 2} C\|a\|_{W^{1,\infty}} \|\phi_l u\|.$$

Since $\phi_n T_a u - T_a \phi_n u = \sum_{l:|l-n|\leq 2} [\phi_n, a_{l-3}]\phi_l u$, we have

$$\|\phi_n T_a u - T_a \phi_n u\|_1 \leq \sum_{l:|l-n|\leq 2} C\|a\|_{W^{1,\infty}} \|\phi_l u\|,$$

from which we obtain (2.2). □

2.2. The modulus of continuity

Following Del Santo and Prizzi¹⁾, we recall the properties of a function $\mu(s)$ on $[0, 1]$ which is continuous, concave, strictly increasing and satisfies $\mu(0) = 0$ and (1.4).

Note that the concavity and $\mu(0) = 0$ implies that $\mu(s)/s$ is decreasing and $\mu(s)/s \geq \mu(1)$ on $(0, 1]$. Hence $\mu(s)/s^2$ is also decreasing.

Next we recall the properties of the function introduced in the paper cited above¹⁾ with the different notation. Let $x(s)$ be a solution of the equation $\frac{dx}{ds} = -\mu(x)$ satisfying $x(1) = 1$. We see that $x(s)$ is given by

$$\int_{x(s)}^1 \frac{1}{\mu(x)} dx = s - 1.$$

Then $x(s)$ is decreasing. The assumption (1.4) implies that $x(s)$ is defined on $[1, \infty)$ and that $x(s) \rightarrow 0$ as $s \rightarrow \infty$. Then $x(s)$ is a one to one map from $[1, \infty)$ onto $(0, 1]$. Now we set $\Phi(s) = 1/x(s)$. Then $\Phi(s)$ is a strictly increasing function defined on $[1, \infty)$. We see that

$$\Phi'(s) = \Phi^2(s)\mu(1/\Phi(s)) \quad (s \geq 1).$$

From the properties of $\mu(s)$, we see that $\Phi(s)$, $\Phi(s)\mu(1/\Phi(s))$ and $\Phi^2(s)\mu(1/\Phi(s))$ are increasing and that $\lim_{s \rightarrow \infty} \Phi(s) = \infty$ and $\lim_{s \rightarrow \infty} \Phi^2(s)\mu(1/\Phi(s)) = \infty$. Then $\Phi(s)$ is convex on $[1, \infty)$. Since $\Phi'(1) > 0$, we see

$$\Phi(s) \geq Cs \quad (s \geq 1) \tag{2.3}$$

with some positive constant C . We remark that

$$\Phi^2(s)\mu(1/\Phi(s)) \geq \Phi(s)\mu(1) \quad (s \geq 1) \tag{2.4}$$

3. Carleman estimate

Let $\tau_0 \in (0, \min\{1, T\})$ and set $T_0 = T - \tau_0$. We define a function $w(t)$ on $[0, T_0]$ by

$$w(t) = 1 + \sum_{j,k=1}^d \sup_{0 < s \leq \tau_0} \|a_{jk}(\cdot, t+s) - a_{jk}(\cdot, t)\|_{\infty} / \mu(s). \tag{3.1}$$

The assumption (1.6) implies that $w(t)$ is integrable on $[0, T_0]$.

Using the function $\Phi(s)$ defined in the section 2.2, we define $\psi_{\gamma}(t)$ and $\psi_{1,\gamma}(t)$ with $\gamma \geq 1$ by

$$\begin{aligned} \psi_{\gamma}(t) &= \Phi\left(\gamma\left(1 + \int_t^{T_0} w(s) ds\right)\right) \\ \psi_{1,\gamma}(t) &= \int_t^{T_0} \psi_{\gamma}(\tau) d\tau. \end{aligned}$$

We remark that $\psi_{\gamma}(t)$ is decreasing and $\psi_{\gamma}(t) \geq \Phi(\gamma)$ on $[0, T_0]$.

In this section we show the following Carleman estimate.

Proposition 3.1. *There exists a positive γ_0 such that*

$$\int_0^{T_0} e^{2\psi_{1,\gamma}(t)} (\|u(\cdot, t)\|^2 + \|\nabla u(\cdot, t)\|^2) dt \leq \frac{C}{\gamma} \int_0^{T_0} e^{2\psi_{1,\gamma}(t)} \|Lu(\cdot, t)\|^2 dt \quad (3.2)$$

for any $\gamma \geq \gamma_0$ and any $u(x, t) \in L^2(\mathbb{R}^d \times [0, T_0])$ satisfying $\partial_{x_j} u(x, t) \in L^2(\mathbb{R}^d \times [0, T_0])$ ($j = 1, 2, \dots, d$), $Lu \in L^2(\mathbb{R}^d \times [0, T_0])$, $u(x, 0) = 0$ and $u(x, T_0) = 0$. Here the constant C is independent of γ and $u(x, t)$.

We define the operator L_γ by $L_\gamma = e^{\psi_{1,\gamma}(t)} L e^{-\psi_{1,\gamma}(t)}$; that is,

$$L_\gamma u = \partial_t u + \gamma e^{\psi_\gamma(t)} u + \sum_{j,k=1}^d \partial_{x_j} (a_{jk}(x, t) \partial_{x_k} u).$$

Then, by replacing u by $e^{\psi_{1,\gamma}(t)} u$, (3.2) is equivalent to

$$\int_0^{T_0} (\|u(\cdot, t)\|^2 + \|\nabla u(\cdot, t)\|^2) dt \leq \frac{C}{\gamma} \int_0^{T_0} \|L_\gamma u(\cdot, t)\|^2 dt. \quad (3.3)$$

We remark that from (2.2) it follows that

$$\sum_{n=0}^{\infty} \|\phi_n \partial_{x_j} (a_{jk} \partial_k u) - \partial_{x_j} (a_{jk} \partial_k \phi_n u)\|^2 \leq C \|\partial_{x_k} u\|^2,$$

from which we obtain

$$\sum_{n=0}^{\infty} \|\phi_n L_\gamma u - L_\gamma \phi_n u\|^2 \leq C \|u\|_1^2.$$

Then, by (2.1) we get

$$\sum_{n=0}^{\infty} \|L_\gamma \phi_n u\|^2 \leq C (\|L_\gamma u\|^2 + \|u\|_1^2). \quad (3.4)$$

Therefore we consider the estimate of $\|L_\gamma \phi_n u\|$.

We show the following lemma.

Lemma 3.2. *There exists a positive γ_0 such that we have the following estimates. When $\gamma \geq \gamma_0$, we have*

$$C \int_0^{T_0} \|L_\gamma \phi_n u\|^2 dt \geq \gamma \int_0^{T_0} (\|\nabla \phi_n u\|^2 + \|\phi_n u\|^2) dt \quad (3.5)$$

for any $u(x, t)$ satisfying the assumptions of Proposition 3.1.

Proof. We denote $\phi_n u$ by u_n .

First we remark that

$$-\Re(L_\gamma u_n, u_n) = \sum_{j,k=1}^d (a_{jk}(x, t) \partial_{x_k} u_n, \partial_{x_j} u_n) - \psi_\gamma(t) \|u_n\|^2 - \frac{1}{2} \frac{d}{dt} \|u_n\|^2.$$

Note that (1.2) implies

$$\sum_{j,k=1}^d (a_{jk}(x, t) \partial_{x_k} v, \partial_{x_j} v) \geq D_0 \|\nabla v\|^2. \quad (3.6)$$

Then, if $n \geq 1$, we have

$$-\Re(L_\gamma u_n, u_n) \geq (D_0 2^{2n-2} - \psi_\gamma(t)) \|u_n\|^2 - \frac{1}{2} \frac{d}{dt} \|u_n\|^2. \quad (3.7)$$

For we have $\|\nabla u_n\|^2 \geq 2^{2(n-1)} \|u_n\|^2$ if $n \geq 1$.

By Schwarz's inequality and Young's inequality, we see the left hand side of (3.7) is dominated by

$$\frac{1}{2} \left(\frac{2}{D_0 2^{2n-2}} \|L_\gamma u_n\|^2 + \frac{D_0 2^{2n-2}}{2} \|u_n\|^2 \right).$$

Then, assuming $n \geq 1$, if there exists $t_n \in (0, T_0)$ satisfying $D_0 2^{2n-2}/4 = \psi_\gamma(t_n)$, we obtain the following: for $u(x, t)$ vanishing at $t = T_0$,

$$\frac{1}{D_0 2^{2n-2}} \int_{t_n}^{T_0} \|L_\gamma u_n\|^2 dt \geq D_0 2^{2n-2}/2 \int_{t_n}^{T_0} \|u_n\|^2 dt + \frac{1}{2} \|u_n\|^2|_{t=t_n}. \quad (3.8)$$

Here we used the fact that $\psi_\gamma(t)$ is decreasing, which implies that $D_0 2^{2n-2} - \psi_\gamma(t) \geq D_0 2^{2n-2} \times \frac{3}{4}$ on $[t_n, T_0]$.

Note that $\psi_\gamma(t) \geq \psi_\gamma(T_0) = \Phi(\gamma)$ on $[t_n, T_0]$. Then we obtain from (3.8)

$$C_1 \int_{t_n}^{T_0} \|L_\gamma u_n\|^2 dt \geq C_2 \Phi(\gamma) 2^{2n} \int_{t_n}^{T_0} \|u_n\|^2 dt + 2^{2n} \|u_n\|^2|_{t=t_n}. \quad (3.9)$$

The argument above implies that

$$C_1 \int_0^{T_0} \|L_\gamma u_n\|^2 dt \geq C_2 \Phi(\gamma) 2^{2n} \int_0^{T_0} \|u_n\|^2 dt, \quad (3.10)$$

if $n \geq 1$ and $D_0 2^{2n-2}/4 \geq \psi_\gamma(t)$ on $[0, T_0]$.

Assume still $n \geq 1$ and that there exists $t_n \in (0, T_0)$ satisfying $D_0 2^{2n-2}/4 = \psi_\gamma(t_n)$. Consider now the estimate on $[0, t_n]$.

Note that $\|L_\gamma u_n\|^2$ is equal to

$$\begin{aligned} \|\partial_t u_n\|^2 + 2\Re(\partial_t u_n, \psi_\gamma(t) u_n) + 2 \sum_{j,k=1}^d \Re(\partial_t u_n, \partial_{x_j} a_{jk}(x, t) \partial_{x_k} u_n) \\ + \|\psi_\gamma(t) u_n + \sum_{j,k=1}^d \partial_{x_j} a_{jk}(x, t) \partial_{x_k} u_n\|^2. \end{aligned} \quad (3.11)$$

Since $\psi'_\gamma(t) = -\psi_\gamma^2(t) \mu(\frac{1}{\psi_\gamma(t)}) \gamma w(t)$ and $\psi_\gamma(t) > 0$, by integration by parts, we see that

$$\int_0^{t_n} 2\Re(\partial_t u_n, \psi_\gamma(t) u_n) dt \geq \int_0^{t_n} \psi_\gamma^2(t) \mu(\frac{1}{\psi_\gamma(t)}) \gamma w(t) (u_n, u_n) dt \quad (3.12)$$

for u_n satisfying $u_n(x, 0) = 0$. Hence

$$\begin{aligned} \int_0^{t_n} (\|\partial_t u_n\|^2 + 2\Re(\partial_t u_n, \psi_\gamma(t) u_n)) dt \\ \geq \int_0^{t_n} (\|\partial_t u_n\|^2 + (\psi_\gamma^2(t) \mu(\frac{1}{\psi_\gamma(t)}) \gamma w(t)) \|u_n\|^2) dt. \end{aligned} \quad (3.13)$$

While Schwarz's inequality implies that

$$|(\partial_t u_n, \partial_{x_j} a_{jk}(x, t) \partial_{x_k} u_n)| = |(\partial_{x_j} \partial_t u_n, a_{jk}(x, t) \partial_{x_k} u_n)| \leq C 2^{2n} \|\partial_t u_n\| \|u_n\|. \quad (3.14)$$

Here we used the fact that the Fourier transform of u_n and $\partial_t u_n$ vanish for $|\xi| \geq 2^{n+2}$, which follows from $u_n = \phi_n u$. We remark that, since $w(t) \geq 1$ and $t^2 \mu(1/t) \geq \mu(1)$ on $[1, \infty)$ (see Section 2.2), we have

$$\psi_\gamma^2(t) \mu(\frac{1}{\psi_\gamma(t)}) \gamma w(t) \geq \gamma \mu(1).$$

Then, by (3.11), (3.13) and (3.14) we see that, for any positive integer N_0 , there exists a $\gamma_0 > 1$ so that we have

$$\int_0^{t_n} \|L_\gamma u_n\|^2 dt \geq C \gamma \int_0^{t_n} \|u_n\|^2 dt \quad (3.15)$$

for any u vanishing at $t = 0$, any positive integer n satisfying $n \leq N_0$ and any $\gamma \geq \gamma_0$. We remark that the estimate above (3.15) is still valid even if t_n is replaced by T_0 . Furthermore, the estimate above (3.15) with $n = 0$ and $t_0 = T_0$ is valid.

For the estimate for large n , we consider the regularization of a_{jk} . We set $\varepsilon = 2^{-4} D_0$ and we pick a positive integer N_0 so that $2^{-2N_0}/\varepsilon \leq \tau_0$. Then we assume $n > N_0$, which implies that $2^{-2n}/\varepsilon \leq \tau_0$.

Let $\chi(s) \in C^\infty(\mathbb{R})$ satisfy $\chi(s) \geq 0$ on \mathbb{R} , $\chi(s) = 0$ on $(-\infty, 0] \cup [1, \infty)$ and $\int_{-\infty}^{\infty} \chi(s) ds = 1$. Set $D_1 = \sup_{s \in \mathbb{R}} (|\chi(s)| + |\chi'(s)|)$. We define the regularization of a_{jk} , $a_{jk}^n(x, t)$, by

$$a_{jk}^n(x, t) = 2^{2n} \varepsilon \int_{-\infty}^{\infty} \chi(2^{2n} \varepsilon (s - t)) a_{jk}(x, s) ds.$$

We see that

$$a_{jk}^n(x, t) = \int_{-\infty}^{\infty} \chi(s) a_{jk}(x, t + 2^{-2n} s / \varepsilon) ds$$

from which and from $\int_{-\infty}^{\infty} \chi(s) ds = 1$ we see

$$a_{jk}^n(x, t) - a_{jk}(x, t) = \int_{-\infty}^{\infty} \chi(s) (a_{jk}(x, t + 2^{-2n} s / \varepsilon) - a_{jk}(x, t)) ds,$$

while from $\partial_t a^n(x, t) = -2^{2n} \varepsilon \int_{-\infty}^{\infty} \chi'(s) a_{jk}(x, t + 2^{-2n} s / \varepsilon) ds$ and from $\int_{-\infty}^{\infty} \chi'(s) ds = 0$, it follows that

$$\partial_t a_{jk}^n(x, t) = -2^{2n} \varepsilon \int_{-\infty}^{\infty} \chi'(s) (a_{jk}(x, t + 2^{-2n} s / \varepsilon) - a_{jk}(x, t)) ds.$$

Then, by the definition of $w(t)$, we see

$$\begin{aligned} |a_{jk}^n(x, t) - a_{jk}(x, t)| &\leq D_1 \mu(2^{-2n} / \varepsilon) w(t), \\ |\partial_t a_{jk}^n(x, t)| &\leq D_1 2^{2n} \mu(2^{-2n} / \varepsilon) w(t). \end{aligned} \tag{3.16}$$

Indeed the definition of $w(t)$ implies

$$|a_{jk}(x, t + 2^{-2n} s / \varepsilon) - a_{jk}(x, t)| \leq \mu(2^{-2n} s / \varepsilon) w(t).$$

Since $\mu(s)$ is increasing, we obtain (3.16). Furthermore we note that

$$|a_{jk}^n(x, t)| \leq \sup_{t \in [0, T]} \|a_{jk}(\cdot, t)\|_{L^\infty}$$

implies

$$|a_{jk}^n(x, t) - a_{jk}(x, t)| \leq 2 \sup_{t \in [0, T]} \|a_{jk}(\cdot, t)\|_{L^\infty}.$$

Then we have

$$|a_{jk}^n(x, t) - a_{jk}(x, t)| \leq C \left(\mu(2^{-2n} / \varepsilon) w(t) \right)^{1/2},$$

from which, similarly to the estimate of (3.14), we see that $|(\partial_t \partial_{x_j} u_n, (a_{jk}(x, t) - a_{jk}^n(x, t)) \partial_{x_k} u_n)|$ is dominated by

$$C 2^{2n} \left(\mu(2^{-2n} / \varepsilon) w(t) \right)^{1/2} \|\partial_t u_n\| \|u_n\|.$$

Hence we obtain

$$\begin{aligned} &\sum_{j,k=1}^d |(\partial_t \partial_{x_j} u_n, (a_{jk}(x, t) - a_{jk}^n(x, t)) \partial_{x_k} u_n)| \\ &\leq \frac{1}{2} \|\partial_t u_n\|^2 + C 2^{4n} \mu(2^{-2n} / \varepsilon) w(t) \|u_n\|^2. \end{aligned} \tag{3.17}$$

Since

$$-2\Re \sum_{j,k=1}^d (\partial_t \partial_{x_j} u_n, a_{jk}^n(x, t) \partial_{x_k} u_n)$$

is equal to

$$-\partial_t \sum_{j,k=1}^d (\partial_{x_j} u_n, a_{jk}^n(x, t) \partial_{x_k} u_n) + \sum_{j,k=1}^d (\partial_{x_j} u_n, \partial_t a_{jk}^n(x, t) \partial_{x_k} u_n),$$

we see that

$$\begin{aligned}
& \int_0^{t_n} \left(-2\Re \sum_{j,k=1}^d (\partial_t \partial_{x_j} u_n, a_{jk}^n(x, t) \partial_{x_k} u_n) \right) dt \\
&= - \sum_{j,k=1}^d (\partial_{x_j} u_n, a_{jk}^n(x, t) \partial_{x_k} u_n) \Big|_{t=t_n} + \sum_{j,k=1}^d \int_0^{t_n} (\partial_{x_j} u_n, \partial_t a_{jk}^n(x, t) \partial_{x_k} u_n) dt.
\end{aligned} \tag{3.18}$$

While we obtain from (3.16)

$$|(\partial_{x_j} u_n, \partial_t a_{jk}^n(x, t) \partial_{x_k} u_n)| \leq C 2^{4n} \mu(2^{-2n}/\varepsilon) w(t) \|u_n\|^2.$$

Therefore we see that $\int_0^{t_n} \left(-2\Re \sum_{j,k=1}^d (\partial_t \partial_{x_j} u_n, a_{jk}^n(x, t) \partial_{x_k} u_n) \right) dt$ is not less than

$$- \sum_{j,k=1}^d (\partial_{x_j} u_n, a_{jk}^n(x, t) \partial_{x_k} u_n) \Big|_{t=t_n} - C \int_0^{t_n} 2^{4n} \mu(2^{-2n}/\varepsilon) w(t) \|u_n\|^2 dt,$$

which is not less than

$$-C_0 2^{2n} \|u_n\|^2 \Big|_{t=t_n} - C \int_0^{t_n} 2^{4n} \mu(2^{-2n}/\varepsilon) w(t) \|u_n\|^2 dt.$$

Hence

$$\begin{aligned}
& \int_0^{t_n} \left(-2\Re \sum_{j,k=1}^d (\partial_t \partial_{x_j} u_n, a_{jk}^n(x, t) \partial_{x_k} u_n) \right) dt \\
& \geq -C_0 2^{2n} \|u_n\|^2 \Big|_{t=t_n} - C \int_0^{t_n} 2^{4n} \mu(2^{-2n}/\varepsilon) w(t) \|u_n\|^2 dt,
\end{aligned}$$

from which and from (3.11), (3.13) and (3.17) we obtain

$$\begin{aligned}
\int_0^{t_n} \|L_\gamma u_n\|^2 dt & \geq \frac{1}{2} \int_0^{t_n} \|\partial_t u_n\|^2 dt - C_0 2^{2n} \|u_n\|^2 \Big|_{t=t_n} \\
& + \int_0^{t_n} (\psi_\gamma^2(t) \mu(\frac{1}{\psi_\gamma(t)}) \gamma - C 2^{4n} \mu(2^{-2n}/\varepsilon) w(t) \|u_n\|^2) dt.
\end{aligned} \tag{3.19}$$

Since

$$\psi_\gamma^2(t) \mu(\frac{1}{\psi_\gamma(t)}) \geq \psi_\gamma^2(t_n) \mu(\frac{1}{\psi_\gamma(t_n)})$$

on $[0, t_n]$ and $\psi_\gamma(t_n) = 2^{-4} D_0 2^{2n} = 2^{2n} \varepsilon$, we see

$$\psi_\gamma^2(t) \mu(\frac{1}{\psi_\gamma(t)}) \geq 2^{4n} \varepsilon^2 \mu(2^{-2n}/\varepsilon)$$

on $[0, t_n]$. Then there exists a $\gamma_1 \geq 1$ such that we have

$$\begin{aligned}
\int_0^{t_n} \|L_\gamma u_n\|^2 dt & \geq \frac{1}{2} \int_0^{t_n} \|\partial_t u_n\|^2 dt - C_0 2^{2n} \|u_n\|^2 \Big|_{t=t_n} \\
& + C \int_0^{t_n} \psi_\gamma^2(t) \mu(\frac{1}{\psi_\gamma(t)}) \gamma w(t) \|u_n\|^2 dt.
\end{aligned} \tag{3.20}$$

for any $u(x, t)$ satisfying $u(x, 0) = 0$ and any $\gamma \geq \gamma_1$. Since $\psi_\gamma^2(t) \mu(\frac{1}{\psi_\gamma(t)}) \geq \psi_\gamma^2(t_n) \mu(\frac{1}{\psi_\gamma(t_n)})$ on $[0, t_n]$ and $\psi_\gamma(t_n) \mu(\frac{1}{\psi_\gamma(t_n)}) \geq \mu(1)$ (see Section 2.2), we have $\psi_\gamma^2(t) \mu(\frac{1}{\psi_\gamma(t)}) \geq \psi_\gamma(t_n) \mu(1)$. Then since $\psi_\gamma(t_n) = 2^{2n} \varepsilon$ and $w(t) \geq 1$, we have

$$\begin{aligned}
\int_0^{t_n} \|L_\gamma u_n\|^2 dt & \geq \frac{1}{2} \int_0^{t_n} \|\partial_t u_n\|^2 dt - C_0 2^{2n} \|u_n\|^2 \Big|_{t=t_n} \\
& + C 2^{2n} \gamma \int_0^{t_n} \|u_n\|^2 dt.
\end{aligned} \tag{3.21}$$

for any $u(x, t)$ satisfying $u(x, 0) = 0$ and any $\gamma \geq \gamma_1$.

Therefore from (3.9), (3.15) and (3.21), it follows that, if $n \geq 1$

$$\int_0^{T_0} \|L_\gamma u_n\|^2 dt \geq C\gamma 2^{2n} \int_0^{T_0} \|u_n\|^2 dt \quad (3.22)$$

for any $u(x, t)$ satisfying $u(x, 0) = 0$ and $u(x, T_0) = 0$ and any $\gamma \geq \max\{\gamma_0, \gamma_1\}$. Here we used the inequality $\psi_\gamma(t) \geq C\gamma$ which is valid for $t \in [0, T_0]$ and $\gamma \geq 1$. Indeed this inequality is verified by $\psi_\gamma(t) \geq \Phi(\gamma)$ and (2.3).

When we have

$$\psi_\gamma(t) \geq D_0 2^{2n-2}/4 \quad \text{on } [0, T_0], \quad (3.23)$$

we see the estimate (3.21) is valid with $t_n = T_0$. Then in the case where (3.23) is valid, we have

$$\int_0^{T_0} \|L_\gamma u_n\|^2 dt \geq C\gamma 2^{2n} \int_0^{T_0} \|u_n\|^2 dt \quad (3.24)$$

for any $u(x, t)$ satisfying $u(x, 0) = 0$ and $u(x, T_0) = 0$ and any $\gamma \geq \gamma_1$.

Finally, consider the estimate for u_0 . The remark after (3.15) asserts that the following estimate is valid.

$$\int_0^{T_0} \|L_\gamma u_0\|^2 dt \geq C\gamma \int_0^{T_0} \|u_0\|^2 dt \quad (3.25)$$

for any $u(x, t)$ satisfying $u(x, 0) = 0$ and $u(x, T_0) = 0$ and any $\gamma \geq \gamma_1$.

Noting $\|\nabla u_n\|^2 + \|u_n\|^2 \leq (2^{2n+2} + 1)\|u_n\|^2$, we see that (3.5) is valid from (3.10), (3.22), (3.24) and (3.25). The proof of Lemma 3.2 is complete. \square

Now we complete the proof of Proposition 3.1. We choose γ_0 so that the assertion of Lemma 3.2 is valid. Then from (3.5) and (2.1) We obtain

$$C \sum_{n=0}^{\infty} \int_0^{T_0} \|L_\gamma \phi_n u\|^2 dt \geq \gamma \int_0^{T_0} (\|\nabla u\|^2 + \|u\|^2) dt.$$

Noting (3.4), we have

$$C \int_0^{T_0} (\|L_\gamma u\|^2 + \|u\|_1^2) dt \geq \gamma \int_0^{T_0} (\|\nabla u\|^2 + \|u\|^2) dt$$

Then, by choosing γ_0 so large, we obtain the desired estimate (3.3). The proof of Proposition 3.1 is complete.

4. Proof of Theorem 1.1

First, we show the following proposition.

Proposition 4.1. *Suppose that the assumptions of Theorem 1.1 is satisfied. Then for any $\tau_0 \in (0, \min\{1, T/2\})$, we have $u(x, t) = 0$ for $t \in [0, T - 2\tau_0]$.*

Proof. Set $f = Lu$. Then we see from the assumptions of Theorem 1.1, that $f \in L^2([0, T], L^2(\mathbb{R}^d))$ and $\|f(\cdot, t)\|^2 \leq C_0(\|\nabla u(\cdot, t)\|^2 + \|u(\cdot, t)\|^2)$ for almost all $t \in [0, T]$.

Now we set $T_0 = T - \tau_0$ and $T_1 = T - 2\tau_0$. Let the non-negative function $\chi_0(t) \in C^\infty(\mathbb{R})$ satisfy

$$\chi_0(t) = \begin{cases} 1 & t < 3/4 \\ 0 & t > 7/8. \end{cases}$$

Set $v(x, t) = \chi_0((t - T_1)/\tau_0)u(x, t)$. Then we see that

$$v(x, t) = \begin{cases} u(x, t) & t \in [0, T_1 + 3\tau_0/4] \\ 0 & t \geq T_1 + 7\tau_0/8. \end{cases} \quad (4.1)$$

Then we see that $v(x, 0) = 0$, $v(x, T_0) = 0$ and that

$$Lv = \chi_0((t - T_1)/\tau_0)f + \frac{\chi_0'((t - T_1)/\tau_0)}{\tau_0}u.$$

Then from (3.2) we obtain

$$\begin{aligned} & \int_0^{T_0} (\|\nabla v\|^2 + \|v\|^2) e^{2\psi_{1,\gamma}(t)} dt \\ & \leq \frac{2C}{\gamma} \int_0^{T_0} (\|\chi_0((t-T_1)/\tau_0)f\|^2 + (\frac{\chi_0'((t-T_1)/\tau_0)}{\tau_0})^2 \|u\|^2) e^{2\psi_{1,\gamma}(t)} dt. \end{aligned}$$

Since

$$\|\chi_0((t-T_1)/\tau_0)f\|^2 \leq C_0(\|\nabla v\|^2 + \|v\|^2),$$

by taking large γ_0 , we have

$$\int_0^{T_0} (\|\nabla v\|^2 + \|v\|^2) e^{2\psi_{1,\gamma}(t)} dt \leq \frac{C}{\gamma} \int_0^{T_0} (\frac{\chi_0'((t-T_1)/\tau_0)}{\tau_0})^2 \|u\|^2 e^{2\psi_{1,\gamma}(t)} dt \quad (4.2)$$

for any $\gamma \geq \gamma_0$. Since $\chi_0'((t-T_1)/\tau_0) = 0$ for $t \leq T_1 + 3\tau_0/4$ and $\psi_{1,\gamma}(t)$ is decreasing, we note that the right hand side of (4.2) can be dominated by

$$\frac{C}{\gamma} e^{2\psi_{1,\gamma}(T_1+3\tau_0/4)}.$$

On the other hand, the left hand side is larger than

$$\int_0^{T_1} (\|\nabla u\|^2 + \|u\|^2) e^{2\psi_{1,\gamma}(t)} dt$$

Since $\psi_{\gamma,1}(t) \geq \psi_{\gamma,1}(T_1)$ on $[0, T_1]$, we see that

$$e^{2\psi_{\gamma,1}(T_1)} \int_0^{T_1} (\|\nabla u\|^2 + \|u\|^2) dt \leq \int_0^{T_0} (\|\nabla v\|^2 + \|v\|^2) e^{2\psi_{1,\gamma}(t)} dt.$$

Hence

$$\int_0^{T_1} (\|\nabla u\|^2 + \|u\|^2) dt \leq \frac{C}{\gamma} e^{2(\psi_{1,\gamma}(T_1+3\tau_0/4) - \psi_{\gamma,1}(T_1))}.$$

Since $\psi_{1,\gamma}(T_1 + 3\tau_0/4) - \psi_{\gamma,1}(T_1) < 0$, the right hand side converges to zero as γ tends to infinity. Then we see that $\int_0^{T_1} \|u\|^2 dt = 0$, which implies $u(x, t) = 0$ on $[0, T - 2\tau_0]$. \square

Under the assumption of Theorem 1.1, Proposition 4.1 asserts that $u(x, t) = 0$ on $[0, T - 2\tau_0]$ for any $\tau_0 \in (0, \min\{1, T/2\})$. Then we have $u(x, t) = 0$ on $[0, S]$ for any $S \in (0, T)$ and thus $u(x, t) \in C^0([0, T], L^2(\mathbb{R}_x^d))$ implies $u(x, t) = 0$ on $[0, T]$. The proof of Theorem 1.1 is complete.

5. Appendix

We study functions that satisfy the condition (1.6). In this section, we assume that the modulus of continuity $\mu(s)$ is defined by $\mu(s) = s(1 - \log s)$. This is a typical example satisfying all the required properties. We define a bounded and continuous function $g(t)$ by

$$g(t) = \begin{cases} 0 & t \geq e^{-1} \\ (\log t)^{-1} \sin(\pi \log t) & e^{-1} > t > 0 \\ 0 & t \leq 0. \end{cases} \quad (5.1)$$

Then we see that

$$\lim_{0 < s \leq 1} \frac{|g(t+s) - g(t)|}{\mu(s)} \leq Cw(t) \quad (5.2)$$

where $w(t) = \min\{1, \frac{1}{|t|(\log|t|)^2}\}$. We remark that $w(t)$ is integrable on any finite interval in \mathbb{R} .

We remark also that, for $t_n = e^{-(1/2-2n)}$ and $s_n = t_n(e^{1/2} - 1)$ with a positive integer n , we see $g(t_n) = -(\log t_n)^{-1}$ and $g(t_n + s_n) = 0$ if n is large. Then, noting that $s_n < t_n$ implies $\mu(s_n) < \mu(t_n)$,

$$\frac{|g(t_n + s_n) - g(t_n)|}{\mu(s_n)} \geq C \frac{1}{(\log t_n)^2 t_n}.$$

We show that (5.2) is valid. First remark $g(t)$ has a uniformly bounded derivative on $[e^{-2}/2, e^{-1}]$. $g(t)$ is Lipschitz continuous on $[e^{-2}/2, \infty)$. Since $\mu(s) \geq Cs$. We see that (5.2) is valid for $t \geq e^{-2}/2$. For the case where $0 < t < e^{-2}/2$, if $s + t \leq e^{-1}$, we have

$$|g(t+s) - g(t)| \leq |(\log(t+s))^{-1} - (\log t)^{-1}| + |\log t|^{-1} \min\{2, |\log(t+s) - \log t|\}. \quad (5.3)$$

Here we used $|\sin x - \sin y| \leq \min\{2, |x - y|\}$ which follows from $|\sin x - \sin y| \leq |x - y|$ and $|\sin x - \sin y| \leq 2$.

Since $(\log t)^{-1}$ is decreasing and convex on $(0, e^{-2})$, we have

$$|(\log(t+s))^{-1} - (\log t)^{-1}| \leq \frac{s}{t(\log t)^2}$$

if $0 < t < t+s \leq e^{-2}$. Then, $\mu(s) \geq Cs$ shows

$$\frac{|(\log(t+s))^{-1} - (\log t)^{-1}|}{\mu(s)} \leq \frac{C}{t(\log t)^2}.$$

When $s+t \geq e^{-2}$ and $0 < t < e^{-2}/2$, we get $s > e^{-2}/2$ which implies $\mu(s) \geq C$. Hence, by the boundedness of $g(t)$ we see

$$\frac{|g(t+s) - g(t)|}{\mu(s)} \leq C$$

if $s+t \geq e^{-2}$ and $0 < t < e^{-2}/2$. Now consider the estimate of

$$\frac{|\log t|^{-1} \min\{2, |\log(t+s) - \log t|\}}{\mu(s)}.$$

Since $|\log(t+s) - \log t| \leq \frac{s}{t}$ for $t, s > 0$, we have

$$\frac{|\log(t+s) - \log t|}{\mu(s)} \leq \frac{1}{t|1 - \log s|},$$

which implies

$$\frac{|\log(t+s) - \log t|}{\mu(s)} \leq \frac{1}{t|\log t|},$$

when $0 < s \leq t < 1$. While, in the case where $1 \geq s > t$ and $e^{-2} > t > 0$, we have $\mu(s) > \mu(t) > t|\log t|/2$, which shows $\frac{2}{\mu(s)} \leq \frac{4}{t|\log t|}$. Then we have

$$\frac{|\log t|^{-1} \min\{2, |\log(t+s) - \log t|\}}{\mu(s)} \leq \frac{4}{t(\log t)^2}.$$

Then we have

$$\frac{|g(t+s) - g(t)|}{\mu(s)} \leq C \max\{1, \frac{1}{t|\log t|^2}\}$$

when $s \in (0, 1]$ and $t \in (0, e^{-2}/2)$. Consider the case where $t \leq 0$. Let $t = -\tau$ with $\tau \geq 0$. Since $g(t)$ vanishes outside of $(0, e^{-1})$, we may assume $e^{-1} > t+s = s-\tau > 0$. Then $s > \tau$. In such a case, we have

$$\frac{|g(t+s) - g(t)|}{\mu(s)} = \frac{|g(t+s)|}{\mu(s)} \leq \frac{|(\log(t+s))^{-1}|}{\mu(s)}.$$

Since $\log(t+s) = \log(s-\tau) < \log s < 0$ if $0 < s < 1$, we have

$$\frac{|(\log(t+s))^{-1}|}{\mu(s)} \leq \frac{1}{s(\log s)^2}.$$

Since $\frac{1}{s(\log s)^2}$ is decreasing on $(0, e^{-2})$, we have

$$\frac{|g(t+s) - g(t)|}{\mu(s)} \leq \frac{1}{\tau(\log \tau)^2} = \frac{1}{|t|(\log |t|)^2}.$$

Finally if $e^{-2} \leq s \leq 1$, we have $\mu(s) \geq C$, which shows

$$\frac{|g(t+s) - g(t)|}{\mu(s)} \leq C.$$

Therefore the estimate (5.2) is verified.

Similarly we have, for any $k \in (0, 1]$,

$$\lim_{0 < s \leq 1} \frac{|g((t+s)/k) - g(t/k)|}{\mu(s)} \leq Cw(t/k)/k \quad (5.4)$$

where $w(t) = \min\{1, \frac{1}{|t|(\log|t|)^2}\}$. Here the constant C is independent of k . Using $g(t)$ we construct a function $h(t)$ by

$$h(t) = \sum_{n=1}^{\infty} t_n k_n g((t - t_n)/k_n)$$

where $t_n = e^{-n}$ and $k_n = e^{1-n}$. We note $g((t - t_l)/k_l)g((t - t_n)/k_n) = 0$ if $l \neq n$.

We see from (5.4) that

$$\int_0^1 \lim_{0 < s \leq 1} \frac{|h((t+s)) - h(t)|}{\mu(s)} dt < \infty.$$

Using functions $g(t)$ or $h(t)$, we can construct functions $a_{j,k}(x, t)$ which are not μ continuous but verify (1.6) with $\mu(s) = s(1 - \log s)$.

REFERENCES

- 1) D. Del Santo and M. Prizzi, *Backward uniqueness for parabolic operators whose coefficients are non-Lipschitz continuous in time*, J. Math. Pures Appl., 84(2005) 471–491.
- 2) D. Del Santo and M. Prizzi, *A new result on backward uniqueness for parabolic operators*, arXiv:1112.2472
- 3) D. Del Santo and C. P. Jäh, *Non-uniqueness and uniqueness in the Cauchy problem of elliptic and backward-parabolic equations*, 27–52, in Progress in Partial Differential Equations - Asymptotic Profiles, Regularity and Well-Posedness, ed. by M. Reissig and M. Ruzhansky, Springer-Verlag, Berlin, 2013.
- 4) R. Dautray and J.L. Lions, *Mathematical Analysis and Numerical Methods for Science and Technology Volume 5 Evolution Problems 1*, Springer-Verlag, Berlin, 2000
- 5) G. Metivier, *Para-differential calculus and applications to the Cauchy problem for nonlinear systems*, Centro di Ricerca Matematica "Ennio De Giorgi" (CRM) Series 5, Edizioni della Normale, Pisa, 2008
- 6) S. Mizohata, *Le Problème de Cauchy pour le Passé pour Quelques Équations Paraboliques*, Proc. Japan Acad., 34(1958) 693–696.
- 7) S. Tarama, *Backward uniqueness for heat equations with coefficients of bounded variation in time*, Electron. J. Diff. Equ., 2013(2013)No. 189, 1–14.
- 8) S. Vessella, *Unique Continuation Properties and Quantitative Estimates of Unique Continuation for Parabolic Equations*, 421–500. Handbook of Differential Equations Evolutionary Equations, Volume 5, ed. by C.M. Dafermos and M. Pokorný, Elsevier B.V., Amsterdam, 2009

Complete Extraction of Statistics Values in Cellular Automata using Special Purpose Parallel Computers Constructed in FPGA

Makoto HOSODA and Yoshiki NAITOH

(Received October 14, 2013)

Synopsis

We have developed a special purpose parallel computer constructed in a Field Programmable Gate Array (FPGA), which extracts statistics values in cellular automata called Conway's Game of Life. We calculated the cellular automaton under two types of boundary conditions: limited and cyclic boundary conditions. The unit cell size was 8 by 8, and we performed complete calculation toward 6-by-6 all initial patterns, whose huge operation exceeds 10^{16} . Therefore, we designed and implemented parallel hardware into an FPGA and reduced the total calculation time to a few tens of hours. From our calculation, the complete statistics values of the automata were extracted. Our result indicates that the symmetry of the initial pattern strongly affects the cycle length of the final converged periodic patterns. This conclusion is complete, since we calculated the whole dynamics for all initial patterns unlike the Monte-Carlo method that only searches for a subset of all by random trials. This technique might be useful to study the dynamics of physical systems that resemble the cellular automata, for example, the Ising model.

KEYWORDS: Cellular automaton, Parallel hardware, Extraction of statistics values, FPGA

1. Introduction

In the analysis of complex physical systems where all cells interact with their neighbors, e.g. the Ising model,¹⁾ the extraction of statistics values has been calculated by the Monte-Carlo method.²⁾ This method uses random trials to reduce the calculation time. However, since all of the initial conditions are not calculated, and the search area is only a subset of all of them, dynamics that happen in rare cases might be lost, and therefore, a complete conclusion is not obtained.

To obtain a complete conclusion, we must calculate the dynamics of the whole initial conditions. However, the time cost is huge. In this report, we present a special purpose parallel computer that extracts the statistics values for a dissipative system. Although the system corresponds to many physical systems, some cellular automata in informatics have a similar logic.²⁾ From this viewpoint, as a calculation example, we choose a system called Conway's Game of Life³⁾ whose clear and easily calculated algorithm has been attracted much interest in informatics and physics.²⁻⁴⁾ However, to the best of our knowledge, complete solutions from the viewpoint of statistics remain un-reported

2. Experimental

Figure 1 shows an example that explains the life game's algorithm. The central cell's birth, life, and death are determined by the number of living cells at eight adjacent neighborhoods. When the central cell is alive and the number of living cells is two or three, the central cell remains alive. When it is empty and the number is three, the central cell is born. When the number is one or greater than three, the central cell dies due to excessive population density. Therefore, this is a dissipative system, whose features are different from the Ising model where the number of particles is conserved.

To realize fast parallel operation, we used an FPGA board (Terasic, DE2-115) on which we mounted a mid-scale FPGA (Altera, EP4CE155: 155k logic cells, 3888k-bit SRAM). The calculated statistics values are stored in an SRAM in the FPGA and sent to a PC for analysis. The operation clock is 50 MHz. However, the parallel operation modules, which were designed and embedded in the FPGA, reduce the operation time to 100ns or less on average per convergence period for one initial pattern. Since the predicted number of operations is greater than 10^{16} , i.e., 10peta = ten quadrillion, this operation time raises the total operation time from several to a few tens of hours under our designed parallel hardware; the amount of time is experimentally acceptable. If conventional PC clusters were used, the time might be increased to a few years.

In addition, the price of the DE2-115 is much less than that of the PC clusters.

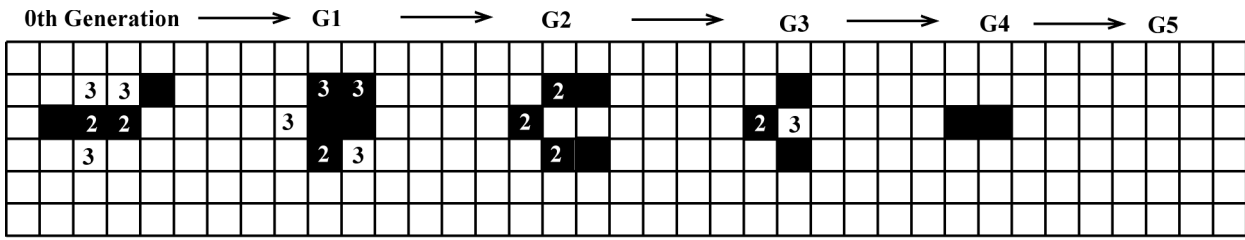


Fig. 1 Game of life algorithm. G-number is Generation number. Number in cell denotes living cells in eight neighborhoods. Only numbers 2 and 3 are displayed, where new birth or lives occur in the next generation. Cells without numbers have a number greater than 3 or less than 2, and will die or remain empty at the next generation.

Figure 2(a) shows a birth/life/death decision module, which can calculate the next generation pattern for a 9-cell area (central and eight neighborhoods) in one clock period (20ns). $6 \times 6 = 36$ modules for a limited boundary condition or $8 \times 8 = 64$ modules for a cyclic boundary condition are implemented as one operation module (OP-module) to cover the whole operation area of the unit cell, which is designed by the notation of the for/end parallel hardware generation in the Verilog-HDL.⁵⁾ To extract the statistics values, we implemented the extraction module (EX-module) shown in Fig. 2(b) with the OP-module. After this, one set of the OP- and EX-modules is called an OE-module. One OE-module compares the current pattern data with the previous patterns at every clock cycle (20 ns). Figure 3 shows a schematic block diagram of the total FPGA design except for the PC interface. When the same pattern is extracted by the EX-module, the matched-signal output, the generation number, and the cycle number of the finally converged cyclic pattern are output from the OE-module. Since multiple OE-modules generate requests, they are arbitrated by the arbiter module. Then the FIFO module buffers the selected request. Since the paralleled multiple OE-modules asynchronously output the request signals, the FIFO is necessary. The FIFO data are written onto the fast SRAM in the FPGA. The generation and cycle numbers are supplied as the SRAM address, where the SRAM data are incremented by 1, to generate a histogram for the statistics values of the dynamics. The paralleled OE-modules start from different initial pattern (36-bits) for parallelism. For example, module-0 starts from 0x00000000 and ends at 0x1fffffff, module-1 starts from 0x20000000 and ends at 0x3fffffff, etc.

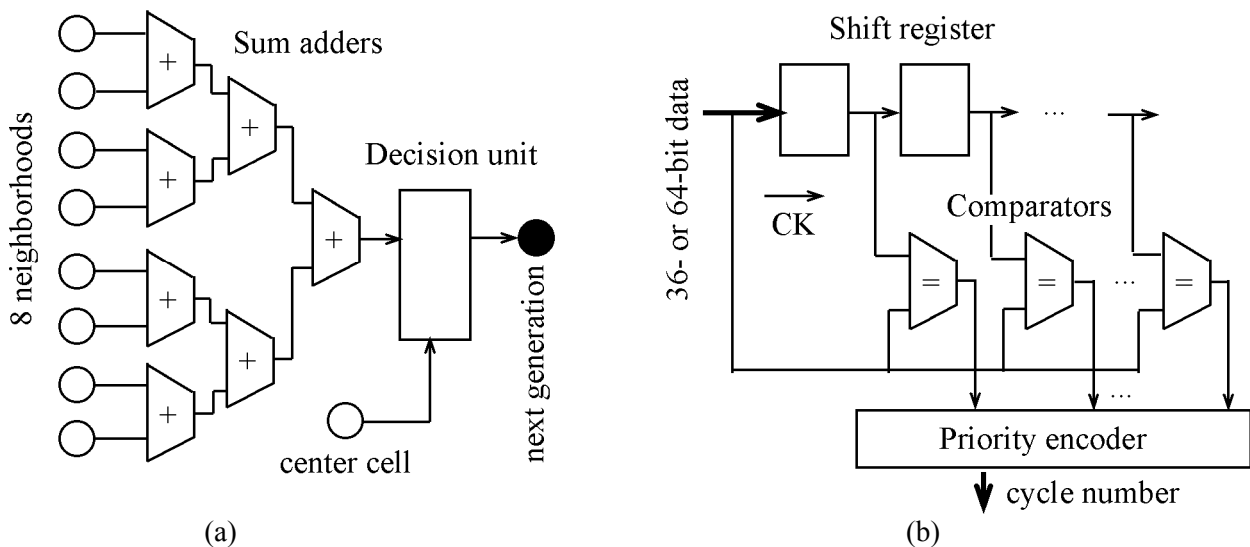


Fig. 2(a) Next generation decision unit. Fig. 2(b) Loop cycle number extraction unit. Maximum of 512 stages are installed.

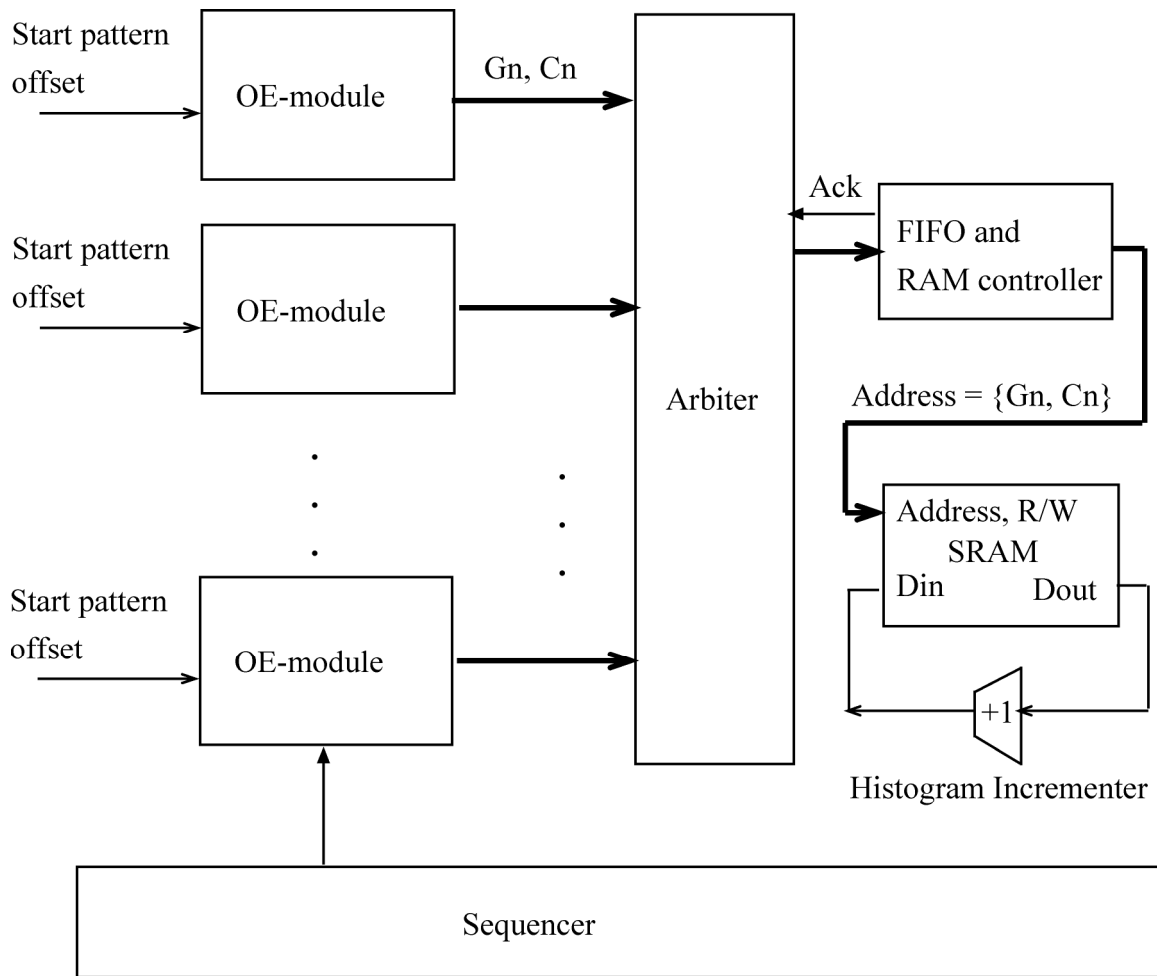


Fig. 3 Schematic diagram of total operation unit.

The design of the above modules and the number of parallel modules are slightly different for the cyclic-boundary condition, since the covered area and the corresponding gate resources to the FPGA are different. We omit the details due to space limitations. For the cyclic-boundary condition, since less than half of the parallel modules could be implemented, the calculation time was about 16-fold. In this situation, we used two DE2-115 boards to reduce the calculation time, where each board started from different start pattern numbers.

3. Statistics values

The statistics values to be extracted are the generation numbers (G_n) up to the fall into the final cyclic oscillation pattern and the cycle numbers (C_n), i.e., the oscillation period. As shown in Fig.1, the 0-th generation pattern (initial pattern) falls into the final pattern (all cells die) after five generations; after this, the pattern does not vary, and the stationary state is a fixed point in the dynamics. In this case, $G_n = 5$ and $C_n = 1$. The $C_n = 1$ case also appears when the last pattern is not all-death but becomes a fixed pattern that does not vary with time. An example of the other dynamics is shown in Fig. 4. The initial pattern enters an oscillating mode at generation 1, and then $G_1 \sim G_3$ patterns are repeated. In this case, $G_n = 3$ and $C_n = 2$, since the entry into the loop is first detected at generation 3 (G_3). Loop count $C_n = 2$ means that the oscillation period spans two generations.

We extracted the statistics values by collecting histograms for all G_n and C_n numbers. For example, regarding $G_n = 5$ and $C_n = 3$, if the appearance of this pattern was 1000 when searching for the total

dynamics starting from all the initial patterns, the histogram values at $G_n = 5$ and $C_n = 3$ become 1000.

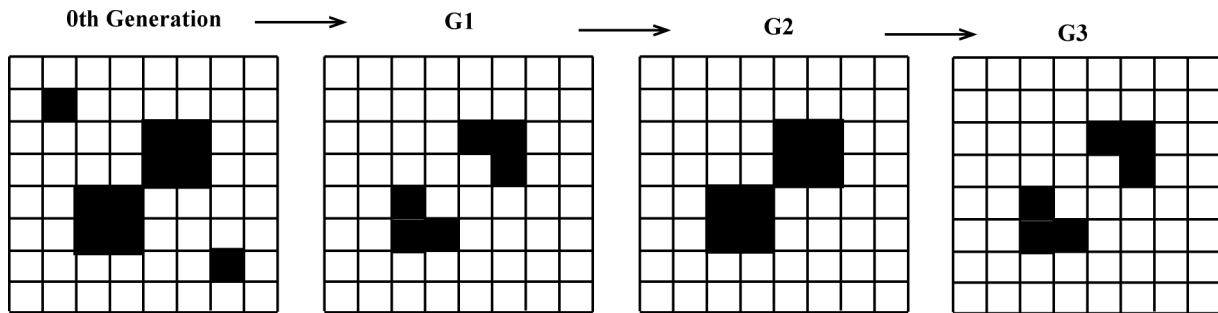


Fig. 4 An oscillating pattern.

We applied two types of boundary conditions. Note that the initial pattern, 6×6 , reflects the limitation of the calculation time. Even at 6×6 data, the number of variations is $2^{36} = 64$ giga. The more that the bits increase, the more the calculation time exponentially explodes. For the 6×6 initial pattern, an 8×8 area is sufficient. Figure 5 shows the boundary conditions. In the limited boundary condition, a time varying pattern cannot escape from the unit cell area. The gray area in Fig. 5(a) is always maintained at zero (no living cells). Therefore, patterns cannot override the 6×6 space or escape from this area.

Unlike the limited boundary condition, the cyclic boundary condition in Fig. 5(b) allows migration to the adjacent unit cells. However, the moved cells are reflected into the central unit cell. As shown in Fig. 5(b), when circle cell A moves to the right upper unit cell, we assume that it has moved to the lowest left cell in the central unit cell. Other movements B and C are reflected, as shown in Fig. 5(b). Migrations to the lower and left unit cells are not displayed, but their reflection into the central unit cell are vice versa.

This cyclic-boundary condition is frequently used in physics especially for solid-state physics, since the unit cell is identical and periodically continued in crystals. When this condition is applied to the analysis of the game of life, patterns moving a longer distance than a unit cell can be treated. Due to an increase in the operation units, the cyclic-boundary condition requires greater hardware resources and calculation time than those of the limited boundary condition.

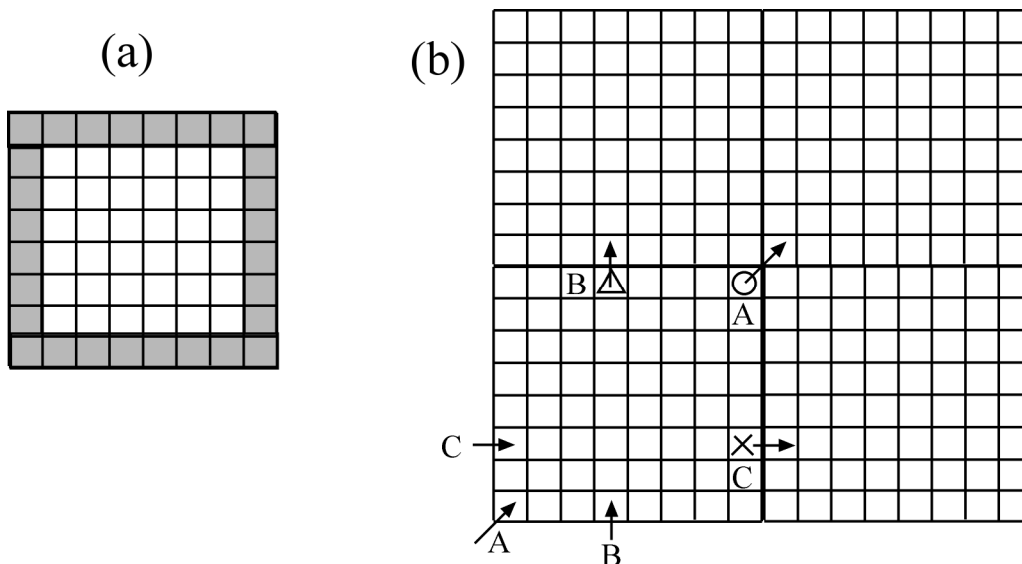


Fig. 5 Limited boundary condition (a), and cyclic boundary condition (b).

4. Implementation

The following are our implementation results on the Altera EP4CE155 FPGA. For the limited boundary condition, 16 OE-modules are paralleled, and the logic elements = 76 k (66%) and SRAM = 597 k bit (15%). The number of operations = multiplication of the number of initial patterns (= 64 G), operations per generation (= approx. 3000), and average G_n (= 40) = approx. 10^{16} . The 3000-operations is evaluated as translated assembler instruction processing if we use a conventional CPU for one OE-module. The calculation time by FPGA was 1 h 10 min. The average processing time of approx. 100ns for convergence from each initial pattern was realized. For the cyclic boundary condition, two FPGA boards are used in parallel, and the results per board are logic elements = 101 k (89%), SRAM = 2.4 M bit (59%), the number of operations = 8×10^{16} , and calculation time was 8 h 30 min. per board. Two OE-modules are paralleled on a board.

We also used another fast parallel hardware design to extract an initial pattern to converge G_n and C_n . After receiving the G_n and C_n parameters from a PC, the FPGA hardware extracts 10,000 initial patterns that satisfy the G_n and C_n conditions. The pattern data are 36-bit and are stored in the SRAM in the FPGA. This function is useful to find rare patterns that show small histogram counts. The hardware resource is almost the same as above. However, when the histogram count exceeds several millions, processing time is reduced. Due to space limitations, we omit the detail.

5. Results and Discussion (limited boundary condition)

Figure 6 shows the statistics values under the limited boundary condition. The vertical axis represents the appearance counts that correspond to G_n and C_n . From this figure, we conclude that the maximum G_n is 82, and the patterns with the largest appearance counts are those of $C_n = 1$. Since the patterns having $C_n = 1$ are all-death or non-time-varying fixed patterns, most of the all initial patterns fall into these states. The final state of $C_n > 1$ is a time-varying oscillating cyclic pattern. From our complete calculation, we conclude that the maximum C_n is 4 and no pattern has $C_n > 4$.

All curves peak at a G_n that slightly exceeds each C_n , and they show a monotonic decrease as a whole. This tendency resembles the statistics curves that are frequently derived from statistics mechanics. The curves have dips, meaning that some final patterns appear slightly less often. This phenomenon probably comes from the pattern symmetry that will be described from the next paragraph.

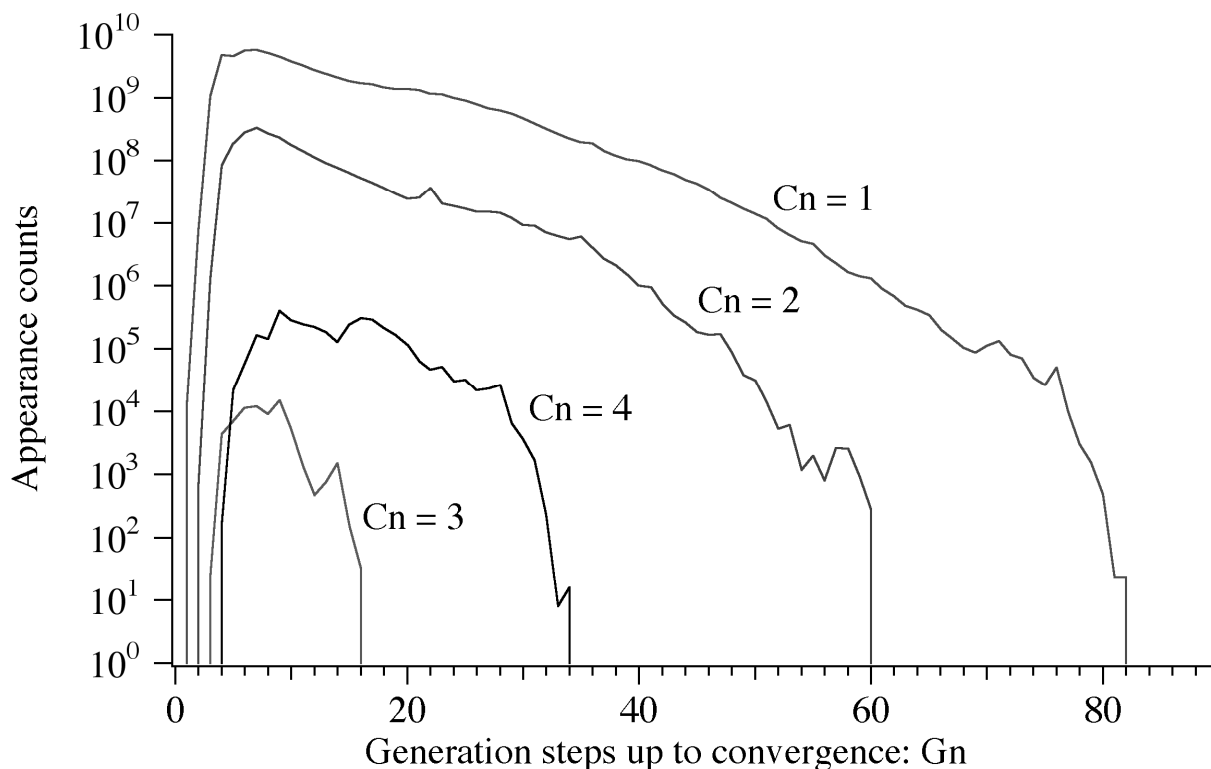


Fig. 6 Statistics values under limited boundary condition.

Although only few initial patterns have just 1-symmetry, these patterns tend to fall rapidly into $C_n = 1$ due to the game of life's algorithm. These symmetries greatly affect the statistics of the game of life. We analyzed the symmetry of the initial patterns for the $C_n = 3$ case. Regarding the $C_n = 1, 2,$ and 4 cases, since the number of initial patterns is huge, we cannot analyze the symmetry of the whole initial patterns. However, since occurrences of $C_n = 3$ are scarce, we extracted the initial patterns and analyzed their symmetry by a hardware implementation on FPGA, as denoted previously in Sec. 4. After the pattern extraction, the data were sent to a PC, and their symmetry was analyzed with a C program.

Figure 9 shows the result.

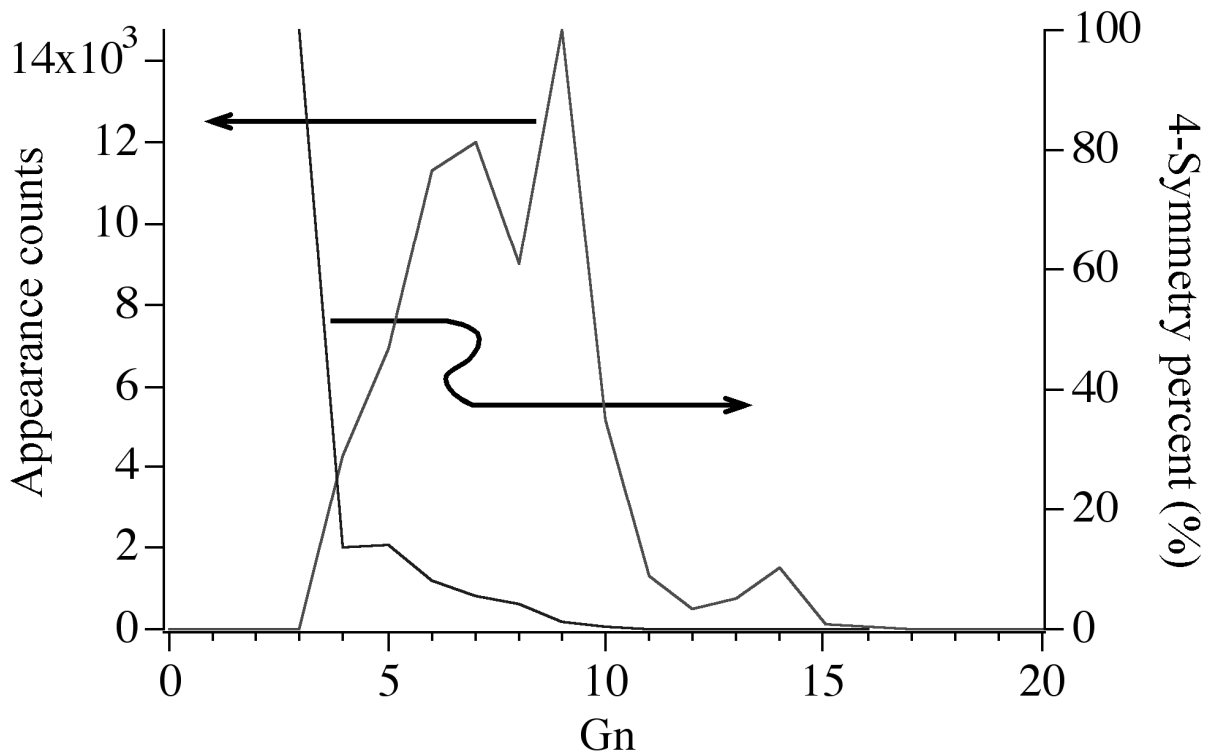


Fig. 9 Symmetry of initial pattern for $C_n = 3$.

Only six patterns for the initial patterns have $C_n = 3$ and $G_n = 3$. Since the number is very small, in the above graph, value 6 seems to be contacting the zero line. Surprisingly, all the patterns have 4-symmetry (4-symmetry percent = 100%). As the G_n increases, the 4-symmetry percentage decreases. However, sufficient numbers of initial states start from the 4-symmetry pattern. This finding suggests that the symmetry of the initial state strongly affects the statistics of the dynamics for cellular automata. Also in physical systems, a similar influence of asymmetry on the final state has frequently been observed. Regarding the cases other than $C_n = 3$, we only extracted $G_n = 4$ and $C_n = 4$ case. In this case, the 8-symmetry is 100%. This suggests that even-symmetry initial states might have tendency to generate an even C_n .

Some final states for $C_n = 1$ to 4 are shown in Fig. 10. All the final patterns for $C_n = 3$ are shown in Fig. 11. Surprisingly, there are only six final states. This is a perfect conclusion, since we completely researched the whole initial patterns. In the $C_n = 3$ final states, mirror symmetry to a 45 degree line exists. In contrast, the $C_n = 1$ and $C_n = 4$ final states do not (see Fig. 10). For $C_n = 2$, we could not search all patterns due to their huge number.

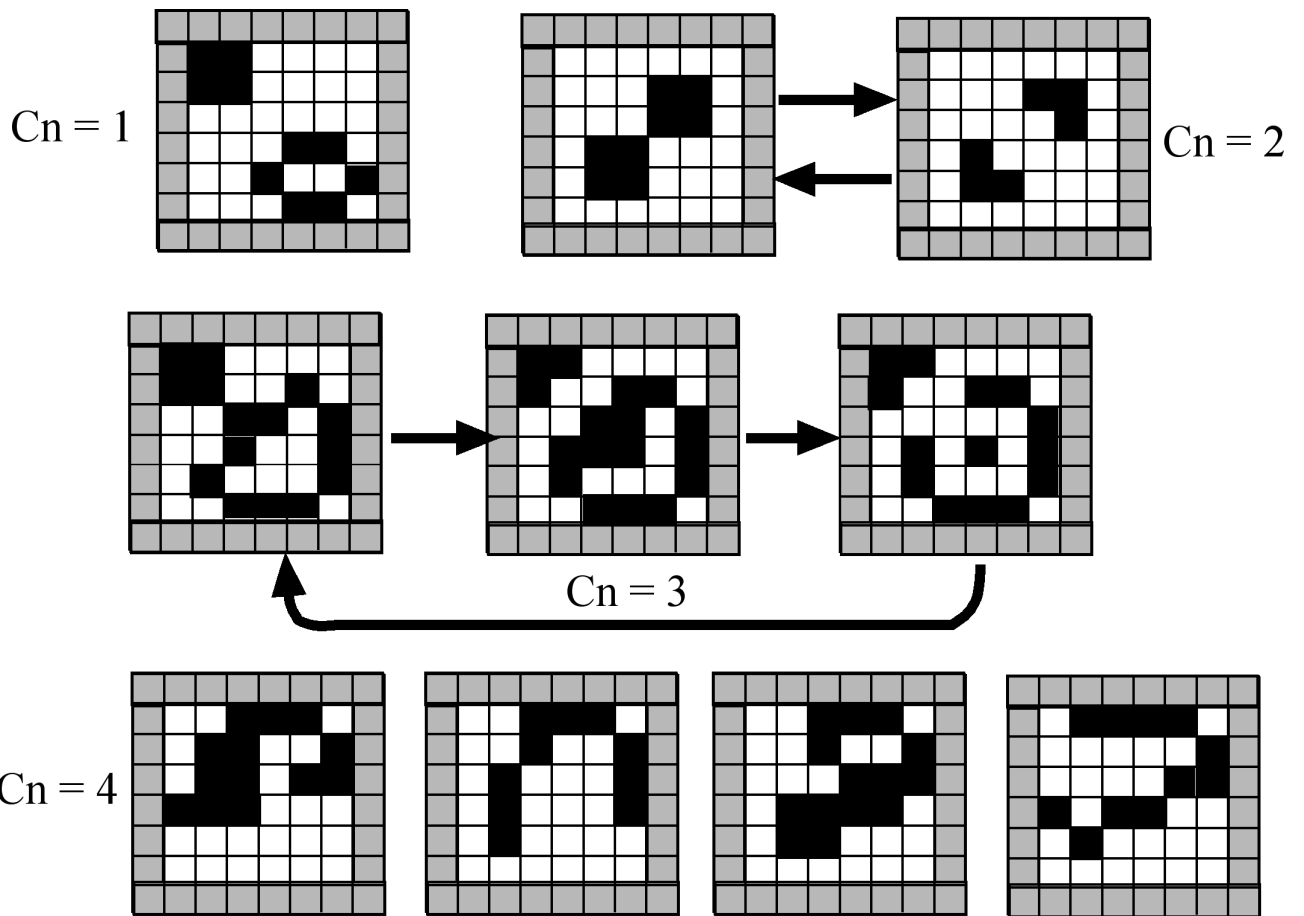


Fig. 10 Example of final pattern for various C_n 's.

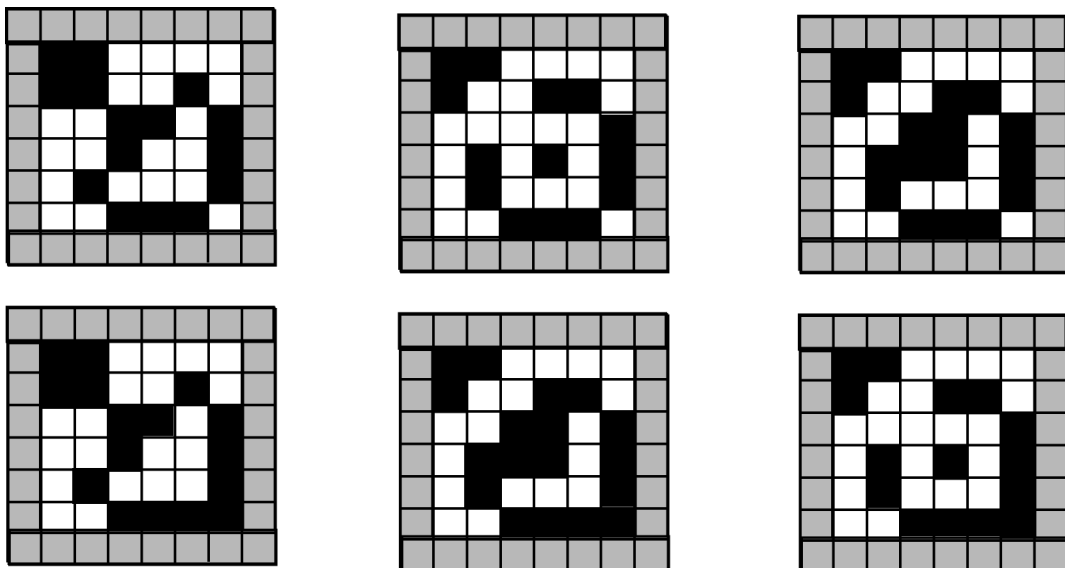


Fig. 11 Whole final patterns with $C_n = 3$.

6. Results and Discussion: cyclic boundary condition

Figure 12 shows the total appearance counts for each C_n . Remarkably, there are no appearances for many C_n 's. Although the graph does not show data values under 100, no counts are under 100. Appearances at odd C_n numbers 5 and 7 are zero. This seems to come from a mismatch of the final patterns to $8 \times 8 \times 8 \times 8 = 64 \times 64$ calculation cells. In the cyclic boundary condition, an 8×8 unit cell was conjugated with adjacent 8×8 unit cells, and is finally configured to an 8×8 macro unit cell. Since the least movement of the cyclic reflection into a unit cell is one, if a one-cell movement to the X-coordinate occurs after the 8-cell movement to the Y-coordinate, we can return to the same X-coordinate position after 8-unit cell movements in the Y-direction. Therefore, the total unit cell number increases to 8×8 , meaning that the micro cell number is $(8 \times 8) \times 8 \times 8$. This 64×64 micro cell introduces a larger number of C_n 's than the limited boundary condition. For this reason, $C_n = 64$ exists (see Fig. 12).

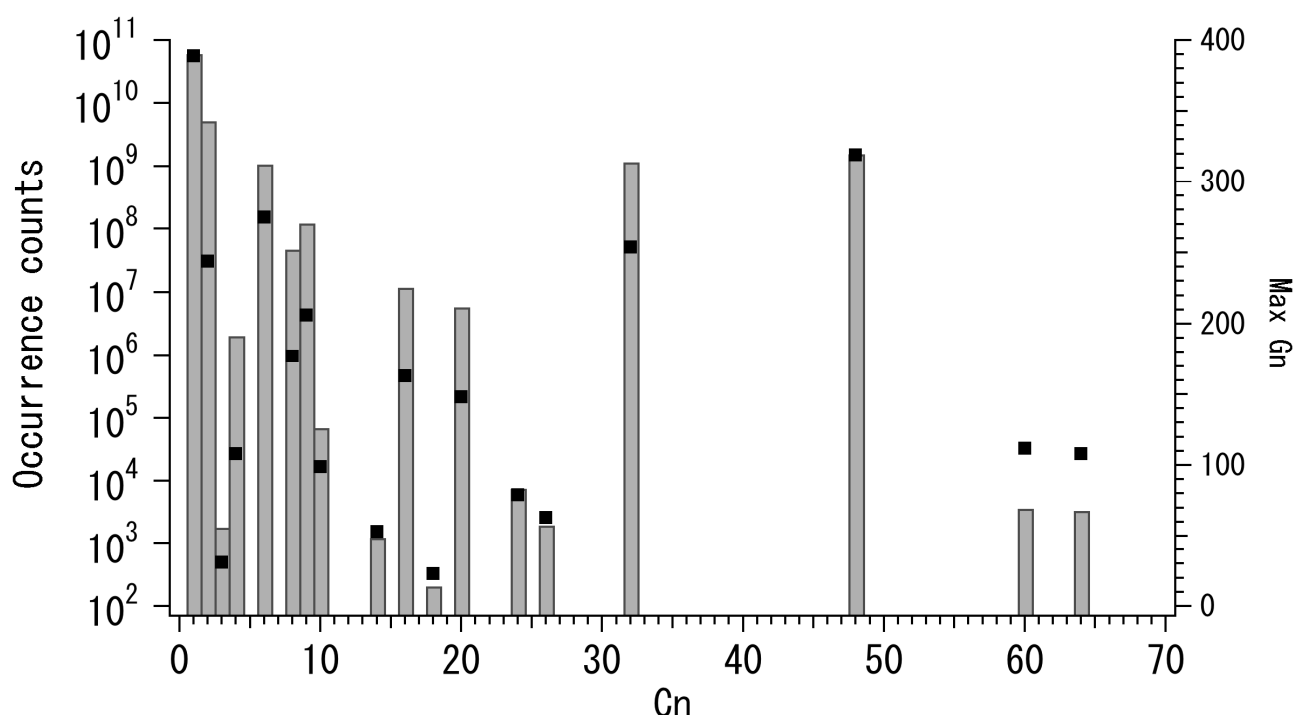


Fig. 12 Total appearance counts versus C_n (bar graphs: left axis) and maximum G_n for each C_n (filled squares: right axis)

However, occurrence counts for some even-number C_n s are zero. This is mysterious. For example, $C_n = 12$ and 40 are eliminated. The numbers are $12 = 8 \times 1.5$ and $40 = 8 \times 5$. These constructions are multiplications of 8 by fractional or odd numbers. Therefore, mismatch to the boundary condition to one macro cell (8×8 unit cells = 64×64 fundamental cells) might arise for these C_n numbers. Different from the above C_n s, a C_n conformed from 8 by even numbers exists, e.g. 16, 32, and 48. These results reveal that symmetry consideration for dynamics is important. Although the existence of $C_n = 8$ is 8 by 1 (= odd number), this occurrence is allowed, since the transition pattern is limited in a unit cell (8×8 fundamental cells) and does not move toward the other unit cells. Patterns having a C_n greater than 8 move over multiple unit cells. Therefore, the existence probably originates from symmetry matching. Surprisingly, $C_n = 9$ exists. This is because the pattern moves within 64×64 cells and shifts one X-direction per unit cell, and returns to the same pattern after the movement of the 64×64 macro cell.

The curves of the appearance counts versus G_n for some C_n s are shown in Fig. 13. A similar tendency is seen to those under the limited boundary condition, that is, a monotonic decrease. The maximum G_n also tends to be proportional to the peak appearance counts for each C_n curve. This tendency is also seen in Fig. 12. In contrast to the limited boundary condition, the maximum G_n increased to 389 for $C_n = 1$ because of

movement of the patterns to multiple unit cells.

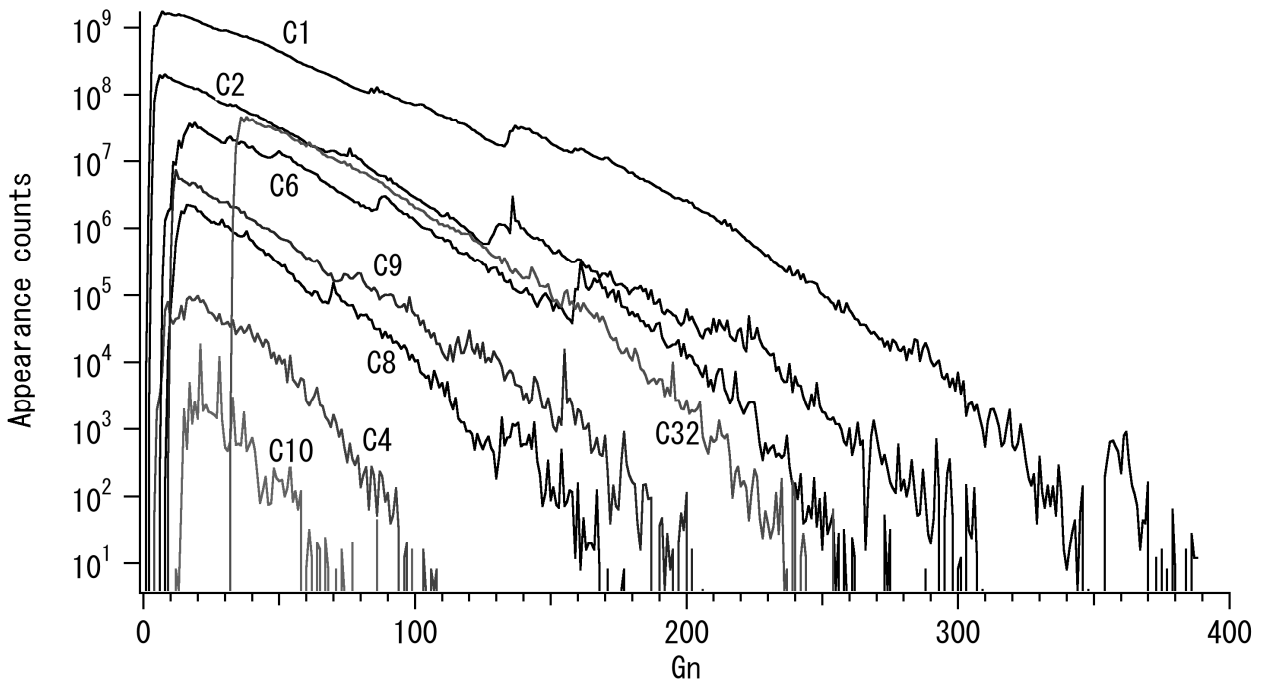


Fig. 13 Statistics curves for some C_n values under cyclic boundary condition. C_1 means $C_n = 1$, C_2 means $C_n = 2$, and so forth.

In contrast to the monotonic decrease shown in Fig. 13, some statistics curves with low occurrence counts have different features. Figure 14 shows the statistics curves for $C_n = 14$ and 26.

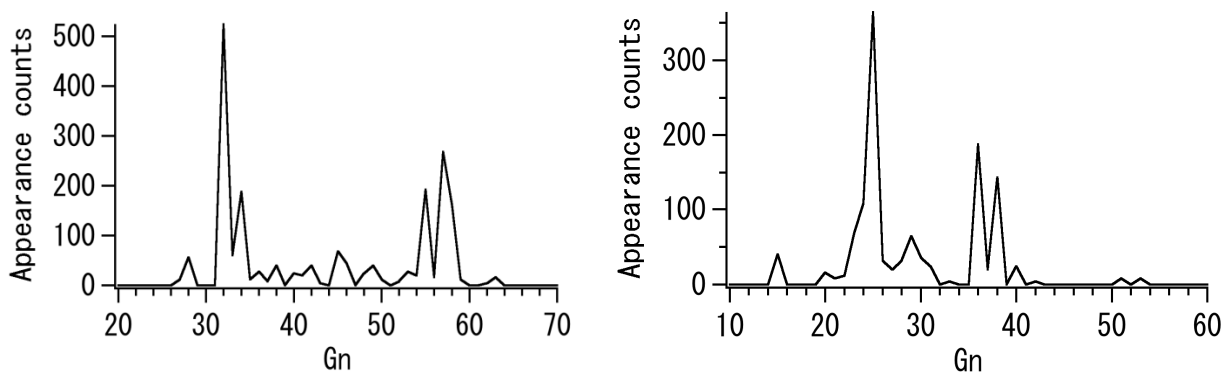


Fig. 14 Statistics curve for $C_n = 14$ (left curve) and $C_n = 26$ (right curve)

In these curves, the tendency is not monotonic, and separate peaks are found. This is thought to originate from the multiple groups in the transition type. One group quickly converges into the final state, but the other does not. This result suggests multiple and very different transition types in the small occurrence C_n patterns.

Finally, we present some rare patterns extracted under the cyclic boundary condition (Fig. 15). Since the number 3 is not a conjugate of 64 and is less than 8, the transition of the $C_n = 3$ final pattern is limited in a unit cell and does not migrate to the 64×64 macro cell.

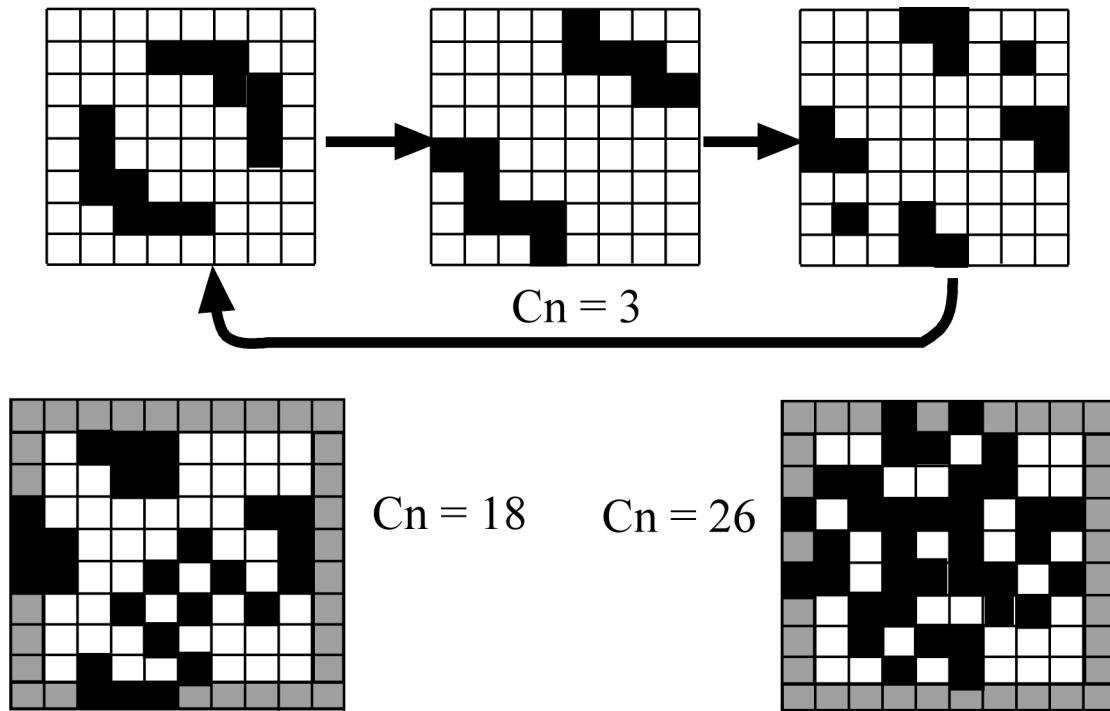


Fig. 15 Rare patterns under cyclic-boundary condition. Gray area in $C_n = 18$ and 26 figures is connection area to adjacent unit cells.

7. Conclusions

We implemented a complete calculation for a 6 by 6 initial pattern cellular automaton called Conway's Game of Life on an FPGA and extracted the statistics values. Over 10^{16} operations were calculated by special paralleled hardware within an acceptable time, e.g. several hours. From our calculated results, we conclude that the symmetry of the initial pattern strongly affects the appearance counts of the final state. This conclusion is perfect, since all of the dynamics have been completely calculated.

8. References

- 1) T. M. Liggett, *Interacting Particle Systems*, Springer (2005).
- 2) H. Gould, J. Tobochnik, and W. Christian, *An Introduction to Computer Simulation Methods, Applications to Physical Systems*, Addison Wesley (2006).
- 3) W. Poundstone, *The Recursive Universe: Cosmic Complexity and the Limits of Scientific Knowledge*, Dover Publications (1985).
- 4) M. Schroeder, *Fractals, Chaos, Power Laws*, W. H. Freeman and Company, New York (1991).
- 5) M. D. Ciletti, *Advanced Digital Design with the Verilog HDL*, Prentice Hall (2010).

A Mobile Measurement System for Sound Source Level of Wild Dolphin Whistles

Tadamichi MORISAKA*, Mai SAKAI**, Kazunobu KOGI***, Tomio SHINKE****,
THI THI ZIN***** and Hiromitsu HAMA*****

(Received October 16, 2013)

Synopsis

This paper reports the feasibility to use a newly-developed mobile measurement system for sound source level of wild dolphin whistles. This system consists of four hydrophones, amplifiers, one 4-channel recorder, and video. One person can handle this system throughout the survey. We successfully took the whistles from free-ranging wild dolphins and calculated the sound source level of the whistles. In future, the system should be smaller and accuracy and precision of the sound source location measured should be higher.

KEYWORDS: dolphin, whistle, sound source level, measurement, hydrophone array

1. Introduction

Dolphins, or small toothed-whales, are communicating with each other by various sounds. A pure-tone like whistle is one of such sounds (Fig. 1). Dolphins use whistles to maintain group cohesion ^{1,2)}, for mother-calf interactions ³⁾, to broadband caller's identification and location ⁴⁾, and for greeting call ⁵⁾. Whistles are thus important for dolphins to maintain their social lives.

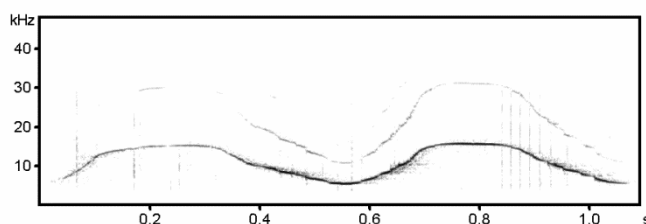


Fig.1 Example of dolphin whistle.

However, human activities around coastal area, such as over-shipping, dolphin-watching, or construction, are now increasing, and resulting artificial background noise increase ⁶⁾. If the background noise in the dolphin habitat increase, the dolphin sounds would be masked by the noise, and the communication range, or active space of the whistles becomes dramatically decreased. It will bring mother-calf separation and group separation, resulting increase of mortality.

We need to measure sound source level of the whistles to know how noise influence on the active space of the whistles. To know sound source level from a free-ranging dolphin, the distance between sound source (the vocalizing animal) and the hydrophone and the sound attenuation of the sound from vocalizing animal to the hydrophone should be measured. Since it is difficult to measure the distance between a free-ranging dolphin and the hydrophone directly in a field, researchers usually use hydrophone array system. There are several studies that measures sound source level of dolphin whistles using a hydrophone array ^{2,7)}. Bottlenose dolphins in Moray Firth, Scotland, produce whistles with mean source level of 158 ± 1 dB re $1 \mu\text{Pa}$ at 1 m^2 , and those in Koombana Bay, Western Australia produced whistles with mean source level of 147 ± 6 dB re $1 \mu\text{Pa}$ at 1 m^7 . Those studies used

* Lecturer, Tokai University Institute of Innovative Science and Technology

** RPD of Japan Society for the Promotion of Science, Wildlife Research Center of Kyoto University

*** Mikura Island Tourist Information Center

**** Director, AquaSound Inc.

***** Research Associate, Information and Communication Engineering, Dept. of Physical Electronics and Informatics

***** Incubator, R&D Center of 3G Search Engine, Osaka City University

widely separated hydrophone arrays and did not identify which animal produce that sound. Several previous systems can identify dolphin identity by simultaneous sound and video recording system^{8,9)}. But those systems seem to be expensive and large which is not good for field use.

Here we develop mobile system to measure sound source level of wild dolphin whistles and test the feasibility to use this in a field condition.

2. Material and Method

Our system can be divided into two parts, underwater video system and sound recording system (Fig. 2). Underwater video system consists of two commercial products (Underwater housing: RVH-CX700VSD, NTF corp., Japan; Video: HDR-CX590V, Sony, Japan). Sound recording system consists of two commercial product (4-channel sound recorder: R-44, Roland, Japan; 4 hydrophones: AQH-020, Aquasound Inc., Japan), and handmade products (Amplifiers and underwater housing: Aquasound Inc., Japan). Hydrophones had - 193 dB re 1 V / 1 μ Pa sensitivity and the flat frequency response (\pm 3dB) between 100 Hz to 20 kHz. The distance between 4 hydrophones are all 13 cm. Amplifiers were fixed 12 dB gain. First version of this system (without underwater video system) had 13.3 kg in air and -2.7 kg under water. New version of the system had 7.3 kg in air and -0.1 kg under water, so the mobility was improved dramatically. One author (TM) was able to handle this system throughout the study period only by himself.

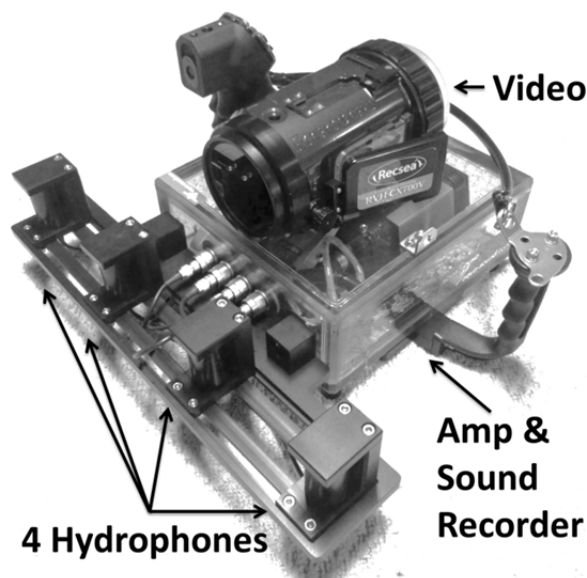


Fig.2 System for measuring sound source level of dolphin whistles.

Underwater video system and sound recording system do not connected directly, so we need to synchronize video image and sounds recorded by hydrophone array. Underwater video system also records sounds, so we can synchronize video and sounds using recorded dolphin sounds. We identified who was the caller of the sounds from the image using ID catalogues provided by Mikura Island Tourist Information. The sounds recorded by 4 hydrophones were first analyzed using Avisoft-SASLab Pro Ver. 5 (Avisoft Bioacoustics, Germany). We selected sounds with good S/N ratio and adopt appropriate band-pass filters to reduce noise. After that, Time-delay-of-arrival (TDOA) measurement function in Avisoft-SASLab Pro was used to measure time difference of arrival between 4 hydrophones (Fig. 3). Received levels of the whistles were also measured using Avisoft-SASLab Pro. To know absolute value of the sound pressure level, a calibration signal (sine wave, 8 kHz) was recorded before each recording using Minirator MR1 (NTI, Liechtenstein).

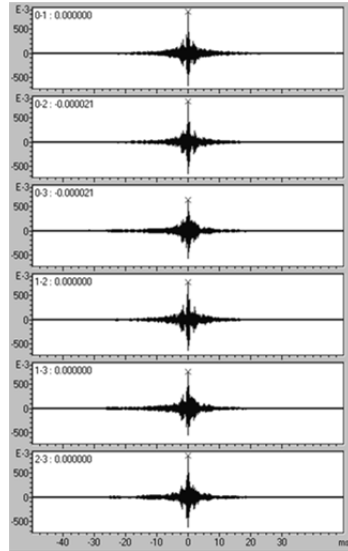


Fig.3 An example of time difference of arrival between 4 hydrophones using Avisoft-SASLab Pro. X-axis: Cross-correlation function; Y-axis: Time difference of arrival.

To back-calculate the sound source level from the sound received level we need to know the sound transmission loss between the system and the dolphin whistle. Sound transmission loss can be calculated by the distance between hydrophones and a dolphin whistle and sound speed at the location using Pythagorean theorem^{10,11}. Sound speed can be calculated from water temperature and salinity using Francois & Garrison (1982) equation¹². For each hydrophone pairs produced 6 hyperbolas. In ideal condition, all hyperbolas intersect on one point. In our recordings, hyperbolas usually did not intersect on one point (Fig. 4), but several adjacent points. We selected the feasible points from the video image, and averaged the points. Then we calculated the sound transmission loss using Francois & Garrison (1982) which needed the distance between the dolphin and the hydrophone, water temperature, salt concentration and pH¹². We built custom-written program for calculating the 2-dimensional relative place and distance to the system from TDOA data using IGOR Pro ver. 6 (Wavemetrics, USA).

Field studies were all conducted the shallower water off Mikura Island, Tokyo, Japan. Indo-Pacific bottlenose dolphins (*Tursiops aduncus*) inhabit throughout the year. Almost all dolphins, around 120 dolphins, are identified by the Mikura Island Tourist Information Center using video-image identification technique¹³.

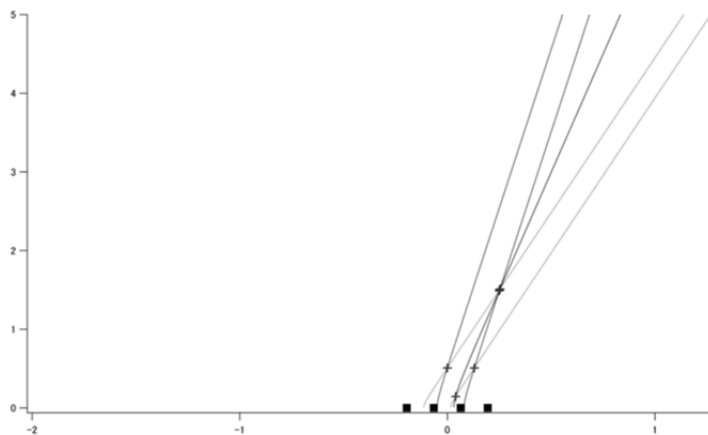


Fig.4 Possible sound source location calculated from time difference of arrival by 4 hydrophones. Square: Hydrophone location; Line: Hyperbolas calculated by hydrophone pairs; Cross: Possible sound source location

3. Results

Field recordings were made 14th Sept. 2012 for 1st system and 2nd July 2013 for 2nd system. Sound speed of the environment was calculated to 1539 m/s using measurements of the water temperature (27°C), salinity (34 ppt) and pH (8.2) from the Francois & Garrison (1982) equation.

We identified several sounds from two individuals (27 whistles from #008 adult male (Kobuhei) and 2 whistles from #314 adult female (Oonami-Konami)) using 1st system, and from three (6 whistles from #609 juvenile female, 2 from unidentified calf #32, 2 from #600 subadult female (Shasen)) using 2nd system.

The distance between the dolphin and the hydrophone was 1.6 m in average (0.7 – 3.1 m) resulting 4.6 dB of sound transmission loss in average. Sound source level of the dolphin whistles was 130 ± 8 dB re 1 μ Pa for 1st system, and 165 ± 4 dB re 1 μ Pa for 2nd system.



Fig.5 1st system and a dolphin in Mikura Island.

4. Conclusion

We successfully recorded dolphin sounds and calculated the sound source level from each identified individual. However, the sound source level of the 1st recordings seemed too low considering those in other published data^{2,7)}. We need to check that this difference was the 1st recording system problem or the individual difference of sound source level of the whistles. We must test the accuracy and precision of acoustic localizations of the system in near future.

For field use, the systems were still large even the smaller 2nd system. We still need to make it smaller to take good data because dolphins move fast and quick.

Sound source level of the whistles presents the active space of the dolphin whistles. It needs not only for conserving dolphins from artificial ocean noise such as boat noise, but also for pursue the function of the whistles. If dolphins adjust their sound source level of the whistles in different conditions, it means that they have the distance where their “voice” should be and not be transferred. Our system will contribute such important topics of dolphins.

Acknowledgment. This work is supported by KAKENHI 23310166 Grant-in-Aid for Scientific Research (B). We are grateful to Yoshinori Hirose and Shingo Hirose for permission to board their boats without a fee. We also thank MIDO (Mikura dolphin team for dolphin identification), Toru Hishii, Mitsuko Hirose, Akihiko Hirose, Masamichi Kuroda, Isoko Kokatsu, Keiko Hirose, members of the Mikura Island Tourist Information Center, boat captain of the Mikura Island, and people living in Mikura Island for their support for conducting this study.

5. References

- 1) V. M. Janik, P. J. B. Slater, Context-specific use suggests that bottlenose dolphin signature whistles are cohesion calls. *Animal Behaviour* 56: 829-838 (1998).
- 2) V. M. Janik, Source levels and the estimated active space of bottlenose dolphin (*Tursiops truncatus*) whistles in the Moray Firth, Scotland. *Journal of Comparative Physiology a-Sensory Neural and Behavioral Physiology* 186: 673-680 (2000).
- 3) L. S. Sayigh, P. L. Tyack, R. S. Wells, M. D. Scott, Signature whistles of free-ranging bottlenose dolphins *Tursiops truncatus* - Stability and mother-offspring comparisons. *Behavioral Ecology and Sociobiology* 26: 247-260 (1990).
- 4) V. M. Janik, L. S. Sayigh, R. S. Wells, Signature whistle shape conveys identity information to bottlenose dolphins. *Proceedings of the National Academy of Sciences of the United States of America* 103: 8293-8297 (2006).
- 5) N. J. Quick, V. M. Janik, Bottlenose dolphins exchange signature whistles when meeting at sea. *Proc Biol Sci* 279: 2539-2545 (2012).
- 6) G. V. Frisk, Noiseconomics: the relationship between ambient noise levels in the sea and global economic trends. *Sci Rep* 2: 437 (2012).

- 7) F. H. Jensen, K. Beedholm, M. Wahlberg, L. Bejder, P. T. Madsen, Estimated communication range and energetic cost of bottlenose dolphin whistles in a tropical habitat. *J Acoust Soc Am* 131: 582-592 (2012).
- 8) K. R. Ball, J. R. Buck, A beamforming video recorder for integrated observations of dolphin behavior and vocalizations. *J Acoust Soc Am* 117: 1005-1008 (2005).
- 9) W. W. Au, D. L. Herzing, Echolocation signals of wild Atlantic spotted dolphin (*Stenella frontalis*). *J Acoust Soc Am* 113: 598-604 (2003).
- 10) P. T. Madsen, M. Wahlberg, Recording and quantification of ultrasonic echolocation clicks from free-ranging toothed whales. *Deep Sea Research Part I: Oceanographic Research Papers* 54: 1421-1444 (2007).
- 11) W. M. X. Zimmer *Passive Acoustic Monitoring of Cetaceans*: Cambridge University Press (2011).
- 12) R. E. Francois, G. R. Garrison, Sound absorption based on ocean measurements. Part II: Boric acid contribution and equation for total absorption. *The Journal of the Acoustical Society of America* 72: 1879-1890 (1982).
- 13) K. Kogi, T. Hishii, A. Imamura, T. Iwatani, K. M. Dudzinski, Demographic parameters of Indo-Pacific bottlenose dolphins (*Tursiops aduncus*) around Mikura Island, Japan. *Marine Mammal Science* 20: 510-526 (2004).

Classification of based on the Collapse Mechanism for a Corroded Damaged Steel Girder End

Makoto USUKURA*, and Takashi YAMAGUCHI**

(Received October 10 2013)

Synopsis

In this study, FE analysis for the girder ends with corrosion has been carried out in order to understand the collapse process and to evaluate its ultimate strength. At first, the strength of the girder end with various corroded damages is evaluated based on the current design standards, “Specifications for Highway Bridges in Japan”. Secondly, these collapse mechanism are analyzed from the analytical results, such as shapes of the deformation mode, stress distribution, and load-deflection relationships and so on. Finally, we had summarized a flow diagram of a failure process.

KEYWORDS: Corrosion of girder ends, Collapse mechanism

1. Introduction

In recent years, it has been well known that some of steel bridges are deteriorated by corrosion at the girder ends as shown in Fig. 1.



Fig.1 Examples of corroded girder ends

These are caused by stagnant water and sediment deposition due to water leakage, such as salt-laden from the expansion joint and airless environment. Various studies have been undertaken for how to evaluate decrease of the ultimate strength and how to repair corrosion damage of the girder end. At the present time, it has been almost cleared the collapse mechanism, but the evaluation method is not established considering the mechanism for load carrying capacity at the girder end with corrosion. In order to solve these technical issues, parametric analysis using FEM has been executed. It has been also discussed tendency of load carrying capacity decrease caused by corrosion damage at the bottom of stiffeners or the web plate adjacent the support.

* Student, Doctor Course of Dept. of Civil Engineering Osaka City University

** Professor ,Dept. of Civil Engineering Osaka City University

2. FEM MODEL

2.1. MODEL

In this study, the FEM program ABAQUS has been used. As shown in Fig. 2, the subject is a simple plate girder bridge end for national trunk roads which is shown in the standard design drawings of the 1994 version. As shown in Fig. 3, forced vertical displacement is applied at the mid-span of the model where is between the intermediate and the end sway bracing in order to realize the actual loading condition of the girder end as much as possible. The model consists of a web panel, an upper and a bottom flange plate, vertical stiffeners, horizontal stiffeners, and a sole plate. The loading plate and the sole plate are modeled by solid elements, and other structural elements are modeled by shell elements. The corroded defect area is modeled by lack of FE elements. The material properties used are referred to the standard design specifications. The boundary conditions at the support are modeled as those for the line bearing. Since the residual stress due to welding might be released by loss of cross section due to corrosion, it is not considered. The initial deflection is not also considered because this research is a comparative study with parametric analysis. The used stress-strain relationship is assumed to be perfect elasto-plastic type, and the yielding function of von Mises is applied.

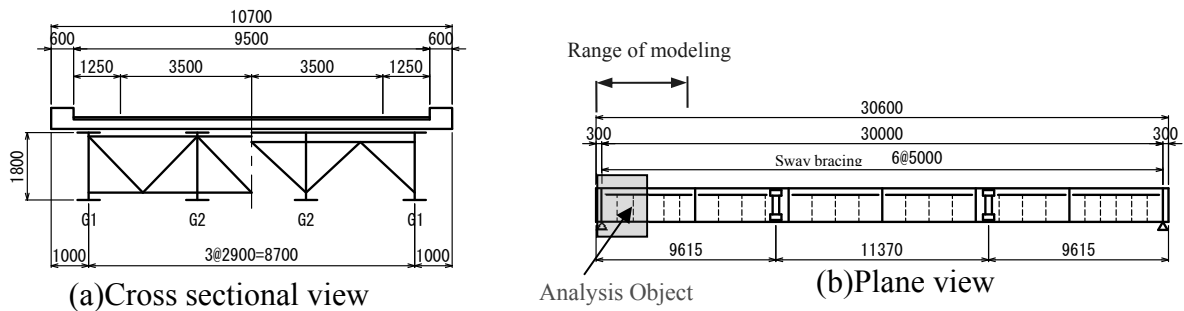


Fig.2 The objective girder end (unit :mm)

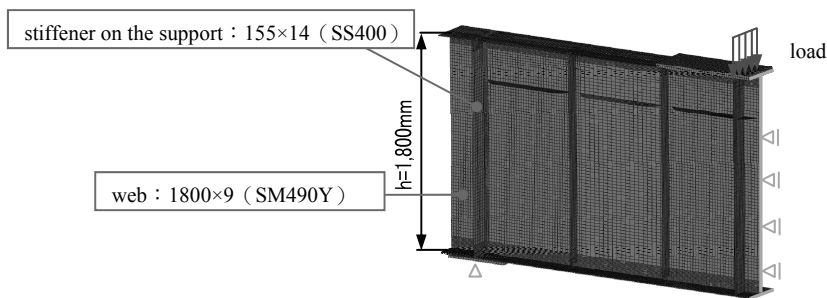


Fig.3 Overview of the model

Table 1 Design conditions

Span	30(m)
Width	9.5(m)
Skew	90°
Live load	B Live load
Snow load	-
Slab thickness	250(mm)
Pavement thickness	80(mm)

Table 2 Geometrical configurations

	Width (mm)	thickness (mm)	Steel grade
Stiffener on the Support	155	14	SS400
Web	-	9	SM490Y
Sole Plate(FIX)※	330	22	SS400

※Axial direction

2.2. PALAMETRIC ANALYSIS

In this study, an intact case and damaged cases in which the cross sectional loss areas are varied are dealt with. Summary of variation of cross sectional area at the support is shown in Fig. 4. As shown in Fig.4, the deficit of the bottom of the web plate, one side or both sides of stiffeners are considered. The height of the deficit cross section is assumed constant, 10mm. In this study, an intact case is called as “Base model”. All analytical cases are tabulated in Table 3.

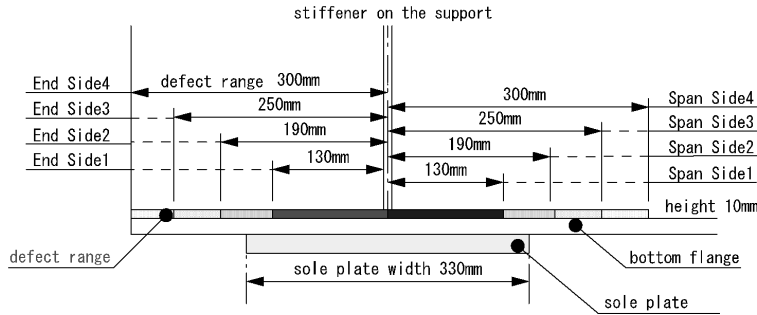


Fig.4 The used deficit parameters in the model

Table 3 Summary of analytical cases

case	Defect width
Base model	none
Web-deficient(Span Side1)	130mm
Web-deficient(Span Side2)	190mm
Web-deficient(Span Side3)	250mm
Web-deficient(Span Side4)	300mm
Web-deficient(End Side1)	130mm
Web-deficient(End Side2)	190mm
Web-deficient(End Side3)	250mm
Web-deficient(End Side4)	300mm
Stiffener-deficient (One side)	155mm
Stiffener-deficient (Both sides)	310mm

3. FEM result and discussion

3.1. Analysis results

Fig. 5 shows the load vs. relative displacement curves obtained.

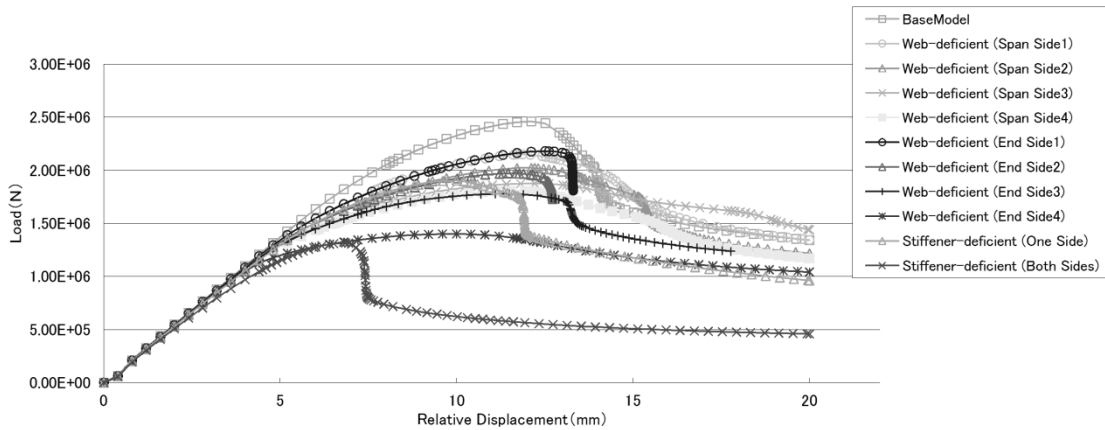


Fig.5 The load vs. relative displacement curves

Table 4 shows the maximum strength of each case obtained from the analysis and the reduction ratio to that of the Base model. For reference, the design strengths of the girder end with various corroded damages have been also evaluated by referring the current design standards, “Specifications for Highway Bridges in Japan”. These are calculated by the following equation.

$$P_d = \sigma_{caw} \cdot \nu \cdot A_{ew} + \sigma_{cas} \cdot \nu \cdot A_{es} \quad (1)$$

P_d : Design strength (N)

σ_{caw} : Allowable axial compressive stress for a web, 210 (N/mm²)

σ_{cas} : Allowable axial compressive stress for a stiffener, 140 (N/mm²)

ν : safety margin (=1.7)

A_{ew} : effective cross sectional area of a web (mm²), A_{es} : effective cross sectional area of a stiffener (mm²)

In the calculation, the safety margin is 1.7, the effective width of the web panel is 24t with exception of a cross sectional lack area.

It is found that the maximum strengths of all cases excepting Web-deficient case (End Side4) and Stiffener-deficient case (Both sides) exceed the design strength of the intact case (Base model). It means that the strength of the girder end with corrosion in which the height is less than 10mm is enough high with comparison of the original design strength.

The design strength considering lack of the cross section of Web-deficient case (End side4) is almost equal to the maximum strength. However, those of other cases are only 63% to 77% of each maximum strength.

Table 4 Analysis results (at the maximum strength)

Height deficit	Content	Deficit position	none	Web-deficient								Stiffener - deficient		
			Base Model	Span Side1	Span Side2	Span Side3	Span Side4	End Side1	End Side2	End Side3	End Side4	One side	Both sides	
			Defect width	0mm	130mm	190mm	250mm	300mm	130mm	190mm	250mm	300mm		
0mm	P_{max} [maximum strength]	kN	2,460	—	—	—	—	—	—	—	—	—	—	—
	$P_{max}/P_{max}(\text{none})$		1.00	—	—	—	—	—	—	—	—	—	—	—
10mm	P_{max} [maximum strength]	kN	—	2,150	2,020	1,880	1,810	2,180	1,970	1,780	1,400	1,900	1,320	
	$P_{max}/P_{max}(\text{none})$		—	0.87	0.82	0.76	0.74	0.89	0.80	0.72	0.57	0.77	0.54	
Reference	P_d [design strength]	kN	1,710	1,365	1,365	1,365	1,365	1,365	1,365	1,365	1,365	1,200	690	
	P_d/P_{max}		0.70	0.63	0.68	0.73	0.75	0.63	0.69	0.77	0.97	0.63	0.52	

3.2. Analysis of the collapse mode

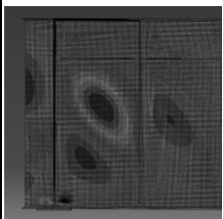
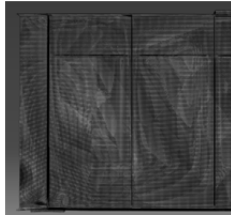
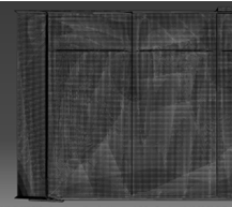
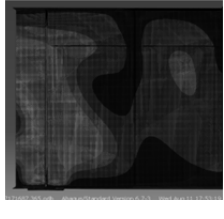
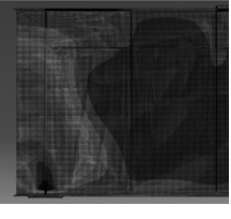
In this section, deformation diagrams, stress distributions and load vs. relative displacement curves are focused in order to analyze the collapse modes in detail considering shear buckling, local buckling, out-of-plane deformation and torsional deformation. In this study, local buckling is defined as the buckling occurred at the bottom of the girder end. The effective width of a web as "column" is 12 times of a web thickness (= 216mm) from the support to both outer sides.

3.2.1. Classification of collapse mode

Fig. 6 shows a flow diagram of the collapse mode. Some examples of the deformation and the stress distribution at the ultimate state are tabulated in Table 5. It is found from observation and the analysis of the analytical results that a collapse mode depends on the location and the amount of deficiency. Classification of the collapse modes are as follows;

sides) (Type 5), it has collapsed by overall buckling of the web panel without local buckling deformation at the bottom of the web panel.

Table 5 Collapse mode list

	Type1	Type2	Type 3	Type 4	Type 5
	Coupled buckling (symmetrical mode)	Coupled buckling (web-asymmetrical mode)	Local buckling	Coupled buckling (stiffener-asymmetrical mode)	Overall buckling
deformation					
case	Base model	Web-deficient • Span Side1,2, 3,4 • End Side1,2,3	Web-deficient • End Side4	Stiffener-deficient One side	Stiffener-deficient Both sides

4. Conclusions

In this study, are focused on the load carrying capacity and the collapse mechanism of the girder end at the support and FE analysis is performed for investigation. Obtained concluding are as follows. :

- 1) Collapse mechanism of the girder end with corrosion damages can be classified into five types focusing on the deformation of the girder end.
- 2) It was found that the out-of-plane deformation of the end side web panel has been caused by loss rigidity of the column on the support.

The future solved issue is to suggest the adequate formulation of strength based on the obtained collapse mechanism.

5. References

- Usukura M, Yamaguchi T, Toyota Y, Mitsugi Y , and Kondo A(2011). Influence of corrosion area of the girder ends of highway bridges to its load carrying capacity. *Journal of Structural Engineering* 57A, pp.724-734.
- Murakoshi J, Tanaka Y, Funaki K (2010) Studies on the anti-corrosion of the steel bridge girder ends , Documents Public Works Research Institute 4142, Japan
- Tamakoshi T, Nakasu K, Ishio M, Takeda T, Suizu N (2006) Resarch on local corrosion of Highway steel bridges, TECHICAL NOTE of National Institute for Land and Infrastructure No.294
- JAPAN ROAD ASSOCIATION(2012) ,SPECIFICATIONS FOR HIGHWAY BRIDGES PART II STEEL BRIDGES

An Analysis on Influencing Factors on Difficulty of Shopping Accessibility by Considering Individual Attributes and Area Characteristics

Noboru ISE* and Yasuo HINO**

(Received October 14, 2013)

Synopsis

Ministry of Economy, Trade and Industry (METI) forecasted that the number of people in food desert (PFD), who have difficulty of shopping accessibility, may be about six million in Japan. However, this forecasting method would not be suitable for forecasting the number of PFD at local level, because of lack of taking consideration into the factors such as individual attributes and area characteristics. Therefore, this paper mainly aims to gain the fundamental knowledge to develop the model for forecasting the number of PFD at local level, from the analysis on influencing factors on difficulty for shopping accessibility by considering individual attributes and area characteristics.

As a result in this study, some major findings related to shopping accessibility came out as follows; 1) some influencing factors on difficulty of shopping accessibility were revealed, 2) shopping accessibility aids such as mobile shopping and delivery service had the complementary role of improving the shopping access problem, 3) actual conditions of needs for shopping accessibility aids were clear, 4) both average WTP (Willingness to Pay) and average usage frequency of each aids for shopping by PFD were revealed. These findings may be useful to develop the forecasting model for not only the number of PFD but also the shopping behavior among some specialized shopping styles.

KEYWORDS: People in food desert, Shopping style, Shopping accessibility aids, Factor analysis

1. Introduction

Ministry of Economy, Trade and Industry (METI) forecasted that the number of people in food desert (hereinafter called “PFD”), who have difficulty of shopping accessibility, is about six million in Japan, because of recent social changes: 1) declining in level of public transport services, 2) declining birth rate and growing proportion of elderly people, 3) progressing the trend of nuclear families and 4) decreasing the number of local commercial facilities and so on. Especially, the food desert problem becomes a serious problem to solve in rural areas. Therefore, METI created “Second edition of Shopping Accessibility Aid Manual” which introduces many practical examples for shopping accessibility aids for PFD in Japan.

* Associate Professor, Department of Civil Engineering, Wakayama National College of Technology

** Professor, Department of Urban Engineering, Osaka City University

However, the number of PFD that forecasted by METI has two problems: 1) it is based on the questionnaire survey data of only people aged 60 and over, and 2) individual attributes and area characteristics are not taken into consideration in this forecasting method. That is, this forecasting method would not be suitable for forecasting the number of PFD at local level. In addition, the number of PFD forecasted based on this forecasting method may not be suitable the effective information to consider a measure for shopping accessibility aids for PFD in any local area.

Such a serious situation has provoked many studies on this topic. Miura et al. (2010) clarified the necessary number of new store to reach a certain level of convenience of shopping, based on geographical approach. Yanagihara et al. (2012) indicated the characteristics of PFD: 1) individual attributes, 2) travel behaviors, 3) use of home delivery services and 4) needs for shopping accessibility aids, by using tabulated analysis. Tanimoto et al. (2012) focused on mental and physical function of elderly person and enabled to forecast the number needs of PFD according to each measure, by developing the multiple choice model. Yoshida et al. (2012) mentioned both substitutability and complementarity of shopping accessibility aids for daily life, based on the relative analysis between transport environment and capability of activities of daily life. Kishino et al. (2011) pointed out some issues about shopping accessibility aids for PFD, based on the relative analysis between the usage of support services for daily life and other factors, such as individual attributes, family structures and capability of going out.

Although a large number of studies have been made on PFD, no studies have ever tried to develop the model for forecasting the number of PFD at local level. Therefore, this paper mainly aims to gain the fundamental knowledge to develop the model for forecasting the number of PFD at local level, from the analysis on influencing factors on difficulty of shopping accessibility by considering individual attributes and area characteristics. In addition, the shopping behavior and the needs of shopping accessibility aids for PFD are analyzed, in order to help to decide the shopping accessibility aids for PFD.

2. Outline of Target Town

Hidakagawa town, as the study field, which is located in the central area of Wakayama prefecture of Japan, and was created by the municipal merger between Kawabe town, Nakatsu village and Miyama village in May 2005, as shown in Figure 1. This town has an area of 331.65 km² (35km from east to west in width, 10km from north to south in width). Population size is very small (population is 10,509 and the number of household is 3,750). The density of population is also very low, but the ratio of elderly people is 10.4% higher than the national average (20.1%). In addition, this town faces some problems such as decreasing of population and increasing of nuclear families.

A railway is located in the southwest of this town, but there are only two stations. In addition to a few stations, train runs once every hour. Bus, community bus and share-ride taxi run in this town, but they run about two to eight times a day. As a result, it is clear that the conditions of public transport in this town is

very poor. Also a lot of local residents pointed out that the condition of public transport is poor and daily shopping is inconvenient. As mentioned above, it is very urgent and important to support the shopping accessibility in food desert in this town.

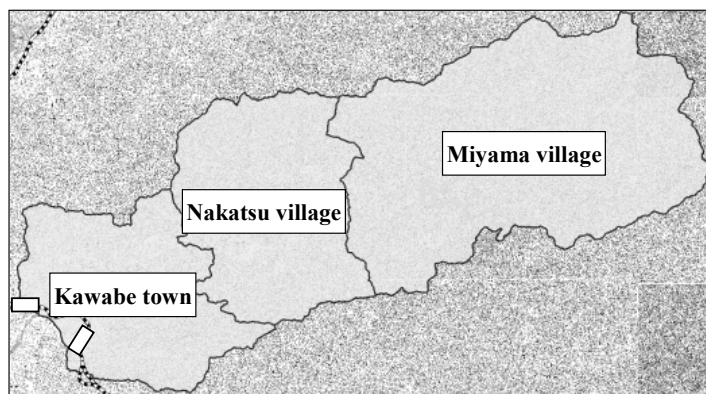


Figure 1. Hidakagawa town as the study field

3. Outline of Questionnaire Survey

The questionnaire survey was conducted from October to November 2012, in order to clarify the influencing factors on difficulty of shopping accessibility. The major items of questionnaire were consisted of individual attributes, conditions of public transport, conditions of shopping accessibility, difficulty of shopping, and shopping style and needs for shopping accessibility aids as shown in Table 1.

The respondents are local residents except students and pupils, who were randomly sampled in Hidakagawa town. As a result, 1749 respondents were obtained from distributed 6000 questionnaire sheets.

Table 1. Major items of questionnaire survey

Items	Details
Individual attributes	<ul style="list-style-type: none"> · Address, · Sex, · Age, · Household composition, · Certification of care need, · Pain-free walking time, · Availability of car and motorbike
Conditions of public transport	<ul style="list-style-type: none"> · Walking time to get to the nearest station · Walking time to get to the nearest stop of bus (including share-ride taxi)
Conditions of shopping accessibility	<ul style="list-style-type: none"> · Type of the nearest shopping store · Distance from home to the nearest shopping store · Conditions of mobile stores and delivery services · Presence of the person who support shopping
Difficulty of shopping accessibility	<ul style="list-style-type: none"> · Difficulty of shopping accessibility
Shopping style	<ul style="list-style-type: none"> · Going out shopping · Mobile store and/or delivery services
Needs of support for shopping	<ul style="list-style-type: none"> · Needs of improvement of each aid for shopping · Intention to use each improved aid for shopping · Willingness to pay for each improved aid for shopping

4. Conditions of Local Public Transport and Current Situation of PFD

4.1. Conditions of local public transport

As for the accessibility to the rail station, all residents of Nakatsu and Miyama village and a half of residents of Kawabe town cannot access to the station within 30 minutes, as shown in Figure 2, because of the location of each residential area (See Figure 1). On the other hand, almost residents may be able to access to the nearest bus stop within 15 minutes, as shown Figure 3. However, from a different angle, ten presents more of residents must be not able to any public transport services.

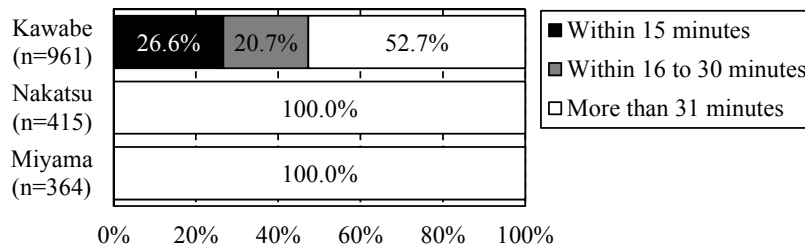


Figure 2. Walking time to get to the nearest station

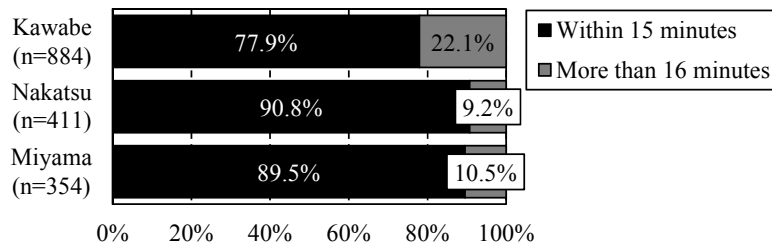


Figure 3. Walking time to get to the nearest bus stop

4.2. Present situation of PFD

Almost residents may not be able to access to any shopping stores, as shown in Figure 4. In addition, it can be seen that other factors except conditions of public transport may have an influence on difficulty of shopping accessibility, as the ration of PFD of Nakatsu village is the highest in Hidakagawa town in this figure. On the other hand, from the age distribution of PFD in Figure 5, it can be said that residents of under 65 years old should be taken into consideration, in order to forecast the number of PFD and consider some shopping accessibility aids for shopping of PFD.

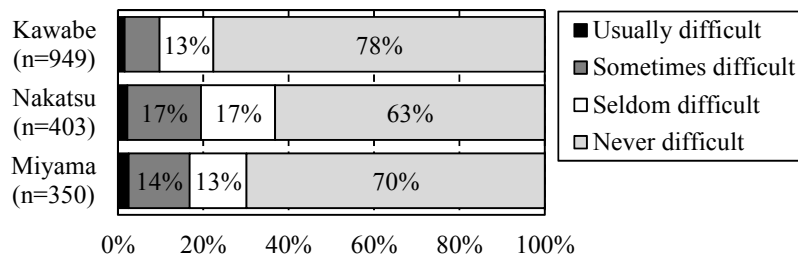


Figure 4. Difficulty of shopping accessibility

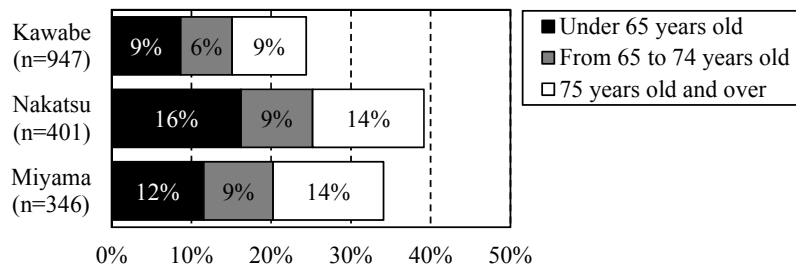


Figure 5. Ratio and age distribution of PFD

5. Analysis on Influencing Factors on Difficulty of shopping accessibility

In order to clarify influencing factors on difficulty of shopping accessibility by using the quantification theory II, respondents who answered “Usually difficult”, “Sometimes difficult” and “Seldom difficult” were defined as “PFD”, respondents who answered “Never difficult” were defined as “Not PFD”.

As a result, some interesting findings came out as follows (See Figure 6). In this analysis, independent variables are tested by the statistical significance based on chi-squared test without multi co-linearity.

1) Individual attributes

Shopping access problems especially depend on 75 years old and over, with-without acknowledgement of support and long-term care, degree of difficulty in walking more than 21 minutes, and impossible users of car and motorbike. Judging from the above, physical depression caused by aging makes it very difficult to go out shopping. And the reason that categorical value of the variable “female” shows positive may depends on the frequency of shopping.

2) Conditions of public transport

As for accessibility to the public transport service, two conditions such as 1) more than 31 minutes to waking to the nearest station and 2) more than 16 minutes to waking to the nearest bus stop must influence to the accessibility of shopping. In addition, it was revealed that bus services must be effective for only residents within 15-minute walk to the stop.

3) Conditions of daily shopping

The factors influenced on shopping access problems was picked out as follows; 1) the inconvenience to the big store as supermarket or shopping center, 2) the 5km and more of access distance to the nearest store, 3) the non-availability of mobile store and delivery services and 4) no support for shopping every time.

As a result, some major findings came out as follows.

- 1) The variety of goods is important to decrease the number of PFD.
- 2) The desirable distance to store may be within 200m.
- 3) It can be considered that the current services of mobile stores and delivery services may contribute to support for shopping of PFD.
- 4) The existence of supporters in each community may also important.

Independent variables			Categorical values			
Individual attributes	Sex	Male				
		Female				
	Age	Under 65				
		65 to74				
		75and over				
	Certification of care need	Not requiring				
		Requiring support				
		Requiring long-term care				
	Pain-free walking time	Within 20 min				
		21 min to 29 min				
		More than 30 min				
	Availability of car and motorbike	Available				
Unavailable						
Conditions of public transport	Walking time to get to the nearest Station	Within 30 min				
		More than 31 min				
	Walking time to get to the nearest stop of bus (including share-ride taxi)	Within 15 min				
		More than 16 min				
Conditions of Shopping for necessities	Type of the nearest grocery store (supermarket or shopping center)	Yes				
		No				
	Distance from home to the nearest grocery store	Within 200m				
		201m to less than 5km				
		More than 5km				
	Conditions of mobile grocery stores and grocery delivery	Existence				
		Nothing				
Presence of the person who support grocery shopping every time	Presence					
	Absence					
Axis	Dependent variable	Center of gravity of axis				
Axis 1	PFD	0.468				
Axis 2	Not-PFD	-0.202				
Correlation ratio	Accurate ratio					
0.31	64%					

Figure 6. Results of influencing factors on difficulty of shopping accessibility

6. Shopping Styles and Satisfaction

6.1. Available shopping style

The users of mobile stores and/or delivery services are 30% or less. On the other hand, almost of PFD have to go out, nevertheless the accessibility of transport services is poor, as shown in Figure 7. From this condition, it can be summarized that support services for shopping such as mobile store and delivery service must be necessary for PFD because of limitation of available shopping style.

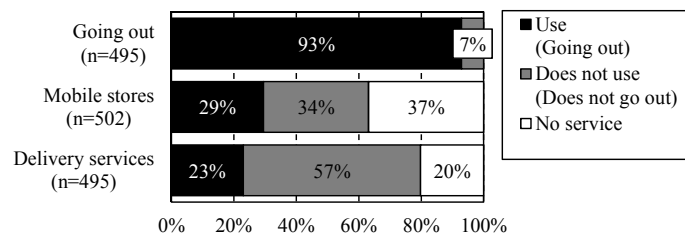


Figure 7. Available shopping style for PFD

In addition, the combinatorial use of each shopping style of PFD is shown in Table 2. From this analysis, it must be clear that 1) about 40% of PFD can choose only “going out”, 2) more than 50 % of PFD choose “going out” and “mobile store” and/or “delivery service”, 3) the ratio of availability of “mobile store” and/or “delivery service” is only 3.5%.

As a result, it is clear that mobile stores and/or delivery services must be insufficient to obtain necessities of life. Therefore, it would be better to say that shopping support by mobile store and delivery services has just the complementary role of shopping by going out.

Table 2. Combinatorial use of each shopping style of PFD

Going out	Mobile grocery store	Grocery delivery	
		Use	Does not use
Go out	Use	11.1%	27.1%
	Does not use	14.1%	40.5%
Does not go out	Use	0.4%	2.3%
	Does not use	0.8%	3.8%

(n=262)

6.2. Shopping satisfaction for each style

Unexpectedly, more than 50% of PFD might be satisfied with each shopping style, as shown in Figure 8. However, it was proved that satisfaction level of shopping style was related to the difficulty of shopping accessibility, based on the chi-squared test. Therefore, it may be obvious that improvement of current shopping aids to more meet the residents’ needs contributes to solve the food desert problem.

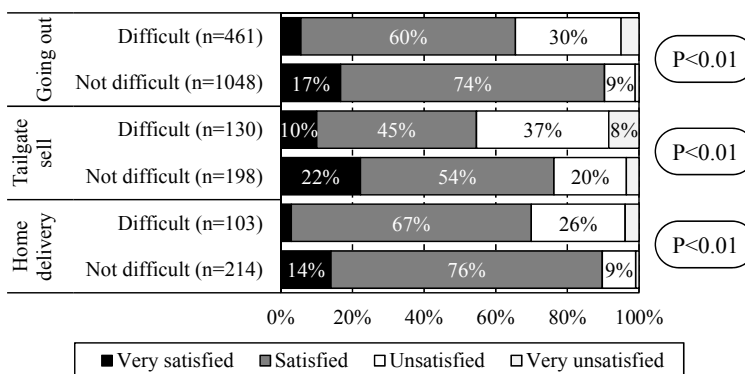


Figure 8. Satisfaction of shopping style for PFD

7. Needs of Shopping Accessibility Aids for PFD

About 80% of PFD desired and 40% and more needed any improvements of shopping accessibility aids including an introduction of new stores, as shown in Figure 9. Then the willingness to pay (WTP) to

realize such improvements was surveyed. As a result, PFD who desired any improvements of shopping accessibility aids have the willingness to pay about 230 JPY for improving the mobile stores and/or delivery services and 266 JPY one way (532 JPY round trip) for introducing the bus or taxi as new aid, as shown in Table 3. These results may show the desire for going out must be strong.

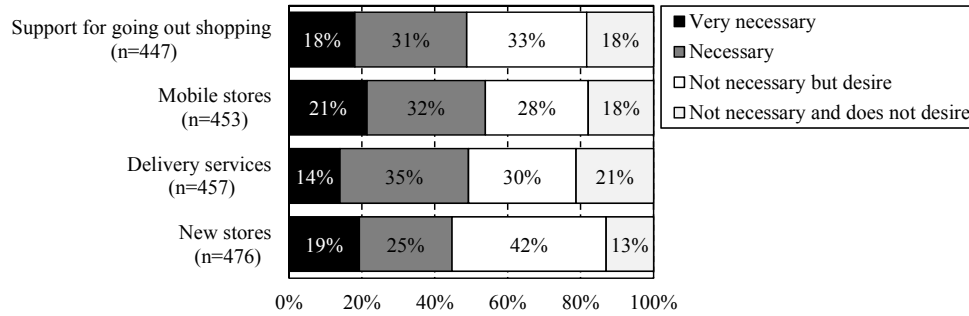


Figure 9. Needs for improvements of shopping accessibility aids

On the other hand, the average usage frequency of support for going out shopping is less than that of use for mobile stores and/or delivery services. It may be guessed that one of the reasons for this result depends on the difficulty for going out shopping. In addition, the average usage frequency of new store is the highest among all support aids, because almost residents expect shortening of the travel distance and the wide variety of goods for the necessities. In that time, the average WTP was 2,754 JPY per month.

Table 3. Willingness to use and to pay for improving the shopping accessibility aids

Support for grocery shopping	Average usage frequency (times/week)	Average willingness to pay (JPY)
Support for going out shopping (n=315)	1.53	266.19 (per one way)
Mobile stores (n=357)	2.20	232.23 (per use)
Delivery services (n=349)	2.02	232.26 (per use)
New stores (n=395)	2.57	2754.82 (per month)

8. Conclusions and toward Next Stage

This study aimed to gain the fundamental knowledge to develop the model for forecasting the number of PFD at local level, from analysis on influencing factors on difficulty of shopping accessibility by considering individual attributes and area characteristics. And some major results came out of this study, as follows.

- 1) Some influencing factors on the difficulty of shopping accessibility were pointed put and each influencing level was revealed.
- 2) Both the setting of bus stop and opening of new store contribute to decrease the number of PFD.
- 3) Bus services are effective to support for shopping accessibility of residents in the area located within

15-minute walk to the bus stop.

- 4) The desirable distance to the store is within 200m, in order to realize to shop the goods for necessities.
- 5) Although almost of all PFD shop the necessities by going out, shopping accessibility aids such as mobile stores and delivery services are necessary and desired for PFD.
- 6) The willingness to use and pay to realize any improvements of shopping accessibility aids including an introduction of new stores were revealed.

These findings may be useful to develop the forecasting model for not only the number of PFD but also the shopping behavior among some specialized shopping styles. Therefore some desired analyses to realize and propose such significant model to improve the shopping accessibility problems for PFD, in the next stage.

Acknowledgements

This study was supported by JSPS KAKENHI Grant-in-Aid for young Scientists (B) of which number is 25820253. We would like to thank to JSPS and cooperators in the questionnaire surveys.

References

- 1) Ministry of Economy, Trade and Industry, *Report of Research Group to consider the future of logistics for supporting the infrastructure for local life* (2010).
- 2) Ministry of Economy, Trade and Industry, *the Manual for Support for Grocery Shopping of People in Food Desert ver.2.0* (2011).
- 3) H. Miura and H. Kotoh, *Distance to Grocery Stores in Depopulating Regions based on Mesh Data: A Case Study in Yamagata Prefecture*, *Journal of the City Planning Institute of Japan*, No.45-3, 643-648 (2010)
- 4) T. Yanagihara and S. Miyake, *A Study on the Support Method for Grocery Shopping of People in Food Desert in Suburban Area*, *Proceedings of Infrastructure Planning* (CD-ROM), Vol.45, 4pages (2012)
- 5) K. Tanimoto and K. Onishi, *A Consideration on the Choice of Support Services of Daily Life according to Physical and Mental Function of Elder People*, *Proceedings of Infrastructure Planning* (CD-ROM), Vol.45, 4pages (2012)
- 6) I. Yoshida, *A Consideration on the Methods to Get the Services of Daily Life –A Case Study in Emergency Temporary Housing in Ofunato City, Iwate Prefecture*, *Proceedings of Infrastructure Planning* (CD-ROM), Vol.45, 4pages (2012)
- 7) K. Kishino, H. Kita, T. Ochi and H. Yotsutsuji, *A Fundamental Analysis on the Methods to Have Opportunities of Daily Activities in Rural Area Study on the Support Method for Grocery Shopping of People in Food Desert in Suburban Area*, *Journal of Traffic Engineering*, Vol.31, 393-398 (2011)

An Empirical Study of Verbal Map Guidelines for Visually-impaired people to Enhance Daily Mobility

Mei TAKAHASHI* and Takashi UCHIDA**

(Received September 30, 2013)

Synopsis

This study was conducted to revise verbal map guidelines for a pedestrian navigation system. The guidelines show rules for describing features in a town to enhance everyday mobility.

This report presents a review of earlier studies and explains the concept of an audio augmented reality (AR) application for visually-impaired people. Then, field experiments are conducted to assess methods to encourage visually-impaired people to use audio guidance through courses and to advance hearing research. Outlines, results, and consideration of the experiments are presented. Finally, verbal map guidelines are revised.

This study assessed a system necessary for a navigation system for visually-impaired people to enhance everyday mobility. The system can be managed continuously by sharing feature information from users with other users according to guidelines.

KEYWORDS: Visually-impaired people, Verbal map, Navigation system, Field experiment

1. Research Background and Objectives

(1) Background

A typical smartphone has a global positioning system (GPS) function and a web access function. Furthermore, augmented reality (AR) applications of smartphones have become commonplace. Such phones can display appropriate information for a location on a screen. However, visually-impaired people cannot see a screen and cannot use AR applications. Therefore, they must ask sighted people to take them to a place to which they have never walked before.

A navigation system must be designed as soon as possible for practical use by visually-impaired people to enhance everyday mobility. Therefore, earlier studies¹⁾²⁾ developed systems using Radio Frequency IDentification (RFID) tags which make up for GPS and a “verbal map” that explains feature information to visually-impaired people using audio guidance. Timing of the explanations of elements and contents on “the verbal map” in a general street were defined in earlier studies¹⁾. In addition, verbal map guidelines were created to show rules for recording feature information.

However, the use of RFID tags has not spread. Therefore, it is necessary to develop a navigation system that is independent of the RFID tag, i.e., which presents no problem even if the position identification precision is low. In addition, elements and contents that should be described on “the verbal map” exist, which are not yet treated in the guidelines.

(2) Research objectives

This study clarifies the “verbal map” in a complicated place that has no verbal map guidelines. A revised edition of the guidelines shall be created by adding results of this study to guidelines of earlier studies.

2. Research approach

The study flow is presented in Figure 1. Previous studies have clarified the usefulness of position identification techniques using RFID and GPS and “the verbal map” in streets and large-scale institutions. Verbal map guidelines for use with general street information have been proposed in earlier studies.

* Student, Master Course of Department of Civil Engineering

** Professor, Department of Civil Engineering

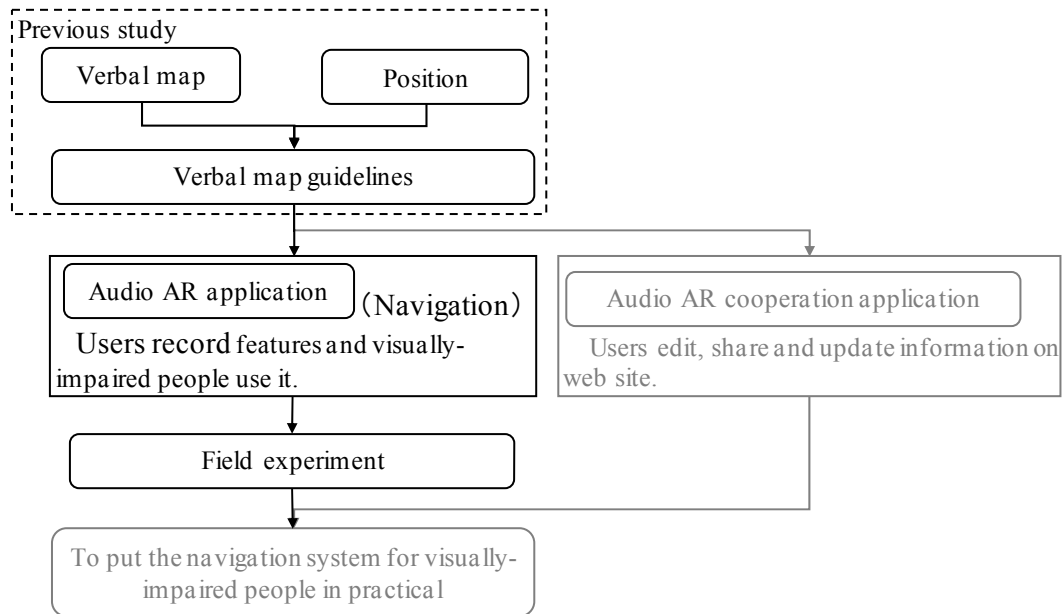


Figure 1 Study flow.

Field experiments are conducted to simulate an audio AR application through a course that includes many elements that were not subjects of the previous studies. In this experiment, subjects that are shot in the previous guidelines are complemented. Then the guidelines are revised.

An audio AR cooperation application can probably be used in the future. The user can expect to share features provided by an audio AR application on a web site. Using this, in a continuous system, users can maintain and update the latest town information. Furthermore, the navigation system can be practical for visually-impaired people to enhance their own everyday mobility.

3. System used for the experiment

(1) Audio navigation

First, it is assumed that a visually-impaired person would like to walk to the first place, for example, a friend's house. When a visually-impaired person walks to a destination from a certain spot, that person needs information about the walking space in addition to directions on how to progress through it. Moreover, the feature information that can be used to discern signs is necessary to determine where the person is or where the person should turn. The message the person can imagine for the whole space is the "verbal map."³⁾

In a navigation system, messages corresponding to the present location specified by GPS are given to a visually-impaired person according to a spot where the person walks. The person hears the message, and checks and judges the related features and signs. Then the person walks by accepting the walk space where the person is presently. Then, after walking, the person arrives at the destination.

This study makes use of an audio AR application as such a navigation system. Furthermore, an audio AR cooperation application can probably be produced for future use with this system.

(2) Audio AR application

The progress of a navigation system for visually-impaired people is of paramount importance. It is ineffective to build the system independently. Furthermore, the widening use of RFID tags used in earlier studies is not good. Therefore, to put a navigation system into practical use for visually-impaired people to enhance daily mobility, a best policy for visually-impaired people is probably to download an audio AR application with a smartphone and use a navigation system.

The navigation system for visually-impaired people to enhance daily mobility comprises 3 systems in a function side, as shown in Figure 2.

- 1) Navigation system
A visually-impaired person hears a message and arrives at the destination from the present location (guidance).
- 2) Feature description data input system
A visually-impaired person inputs and records the feature information as a message.
- 3) Data sharing system
A visually-impaired person updates the town information by sharing the feature information related to a web site.

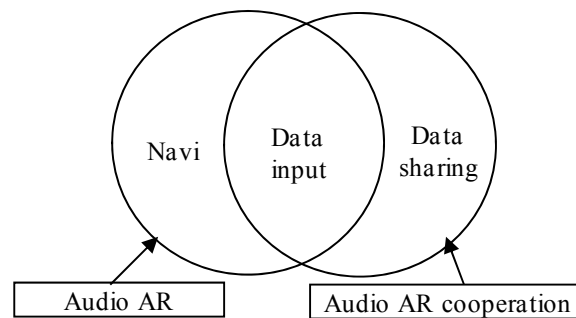


Figure 2 Relation between systems and applications.

A part of an audio AR application is 1) the navigation system and 2) the feature description data input system. An audio AR application can reproduce messages corresponding to the present location in the field performing a town walk. Additionally, it can record audio guidance about features to be recorded as a memory of the person visiting that spot.

A part of an audio AR cooperation application is 2) the feature description data input system and 3) the data sharing system. An audio AR cooperation application can edit an audio guidance inputted as preparations to use an audio AR application. Additionally, it can share and update the guidance on a web site.

4. Experiment outline

In the field experiment, visually-impaired people use audio guidance while walking. Hearing research was conducted with several test subjects.

- 1) Advance preparation
Messages are created through an experimental course according to the guidance. Furthermore, an audio file is recorded on a music player. When the experiment starts, visually-impaired people put on a bone conduction headphone and a microphone for recording experiment conditions. A bone conduction headphone enables a person to walk while hearing surrounding environmental sounds.
- 2) Walking experiment
Looking at the action of visually-impaired people through a course, the music player is operated, passing messages according to a point to a bone conduction headphone by radio. Hearing the messages, visually-impaired people decide the direction of movement according to their own judgment and aim at the destination. A visually-impaired person walks together with a guide helper for safety as needed. However, the user decides the direction of movement. The condition of a walking experiment is recorded with the environmental sound and the utterance by a video camera, as shown in Figure 3.
- 3) Hearing research
After doing the walking experiment, a hearing experiment is conducted in a room. Evaluation of messages is heard, with a mental state through the course and features and signs that visually-impaired people typically use in everyday life.

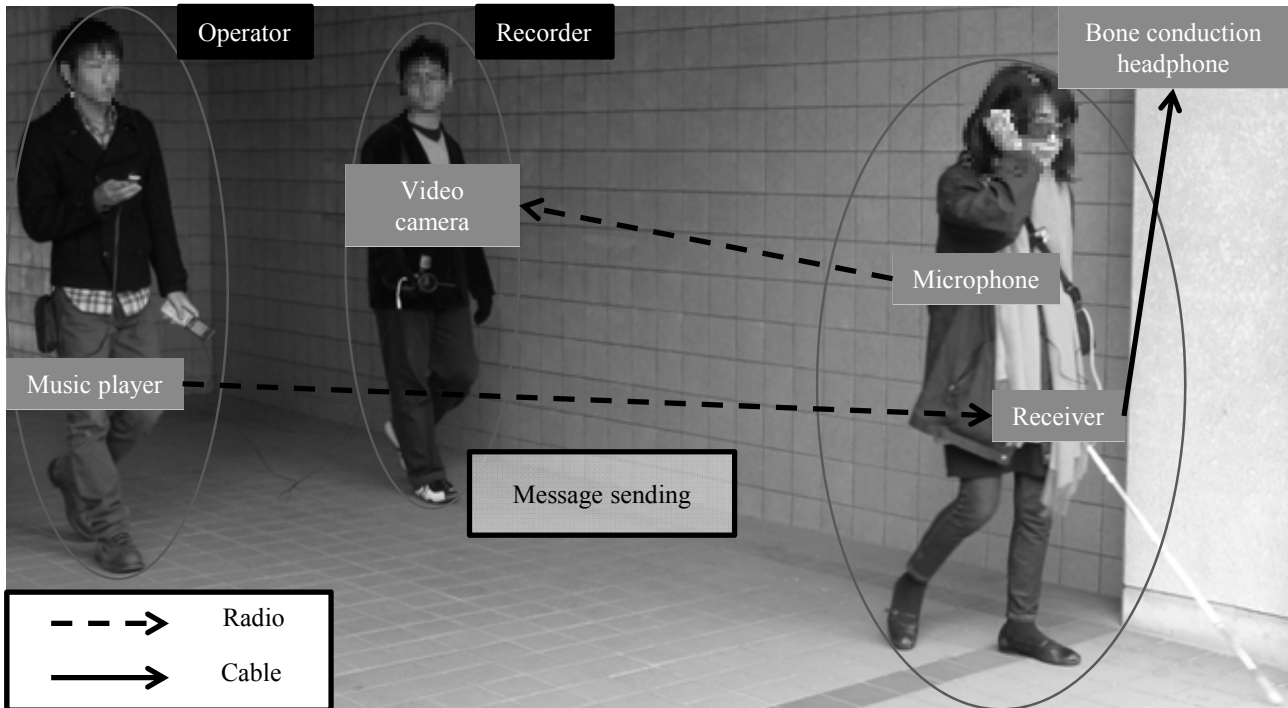


Figure 3 Situation of the walking experiment.

5. Experiment

(1) Experiment challenges

The purpose of the experiment is to complement subjects which are shot in the previous guidelines and to revise the guidelines. The points that are lacking (challenge) in the guidelines are the following 4.

(Challenge 1) Guidance to a pinpoint (vast space → narrow space)

When visually-impaired people are guided from a vast space to a narrow space, such as a narrow feature and a street, they tend to pass a space where they can go ahead. Thereby, they become lost. Necessary feature information is clarified under such a situation.

(Challenge 2) Guidance to the pinpoint (similar features are close to one another)

When similar features are closely arranged in the short section, visually-impaired people cannot choose a suitable feature easily. Therefore, necessary feature information must be clarified in such a space.

(Challenge 3) Special passage

In previous studies, necessary feature information at a passage where visually-impaired people often walk outdoors in everyday life is clear. However, in a special passage where a person might have little walking experience, such as stairs or a roofed passage, necessary feature information is not so clear.

(Challenge 4) Signs

Because visually-impaired people specify the present location, the corners where they should turn and so on, the signs they can determine are clarified.

As the course of the field experiment, we (sighted people) set up a route that includes points that can complement four Challenge points⁴⁾. Specifically, the course extends from the front of the main gate in the whole study common educational building area in the Osaka City University to the B classroom on the fourth floor the whole study common educational building area. We experimented with 28 visually-impaired people (20 completely blind people and 8 weakly sighted people). Characteristics of a point through the course and challenges of the guidelines corresponding to it are presented in Table 1.

There is no corresponding point for Challenge 4. The signs visually-impaired people use in everyday life were known to them after doing the walking experiment.

Table 1 Relations between points and challenges

Point	Characteristic	Challenges			
		1	2	3	4
a	Passage in the garden of the brick pavement with the curb stone on both sides			○*	
b	Piloti			○	
c	Courtyard where 4 types of pavement such as textured paving blocks are spread linearly	○			
d	Grand stairs of the tiling where there is a landing on the way, a handrail in the center, and tiered platforms of the tree on both sides			○	
e	Roofed passage			○	
f	Door of the same kind in the passage in succession		○		

※ Point a is taken as the passage where visually-impaired people often walk outdoors in everyday life.

(2) Results of the experiment

The results of the experiment for every challenge are shown below.

(Challenge 1)

For guidance from a vast space to a narrow space, an open space with a little feature guided by going along with them hand and white canes is chosen, such as a wall, a curb stone and a textured paving block. There is a stone paving like a textured paving block in the open space. The stone paving is explained using information about the pavement. Visually-impaired people can apparently use it effectively as a key by exploring it with a white cane.

(Challenge 2)

In this experiment, a door of the same kind is used in the passage in succession. Consequently, it is the opinion that it is plain for visually-impaired people to have it explained concretely using a number such as “the x-th door from this side” .

(Challenge 3)

Through the course, a piloti, grand stairs, a roofed passage are explained as a special passage with a little walk experience. Therefore, in a special passage to go straight with a little walk experience, if there is no information about a concrete distance how many meters distance must be walked to the terminal, then visually-impaired people become uneasy during walking.

When they pass stairs, they would like to know the width of stairs and the existence of a handrail and a landing because the stair width is easy to imagine and assess. Furthermore, visually-impaired people use handrails in everyday life. However, if there is information about a handrail of stairs that is passed for the first time, then they can walk in comfort. Regarding landing, if they know of the existence and the number of landings, they understand whether they have finished passing the stairs. Therefore, their information is described for a safe and reliable walk. In addition, if there are stairs of special pavement or form, then they should be described.

A visually-impaired person does not understand a term itself like a piloti or a roofed passage. However, they are spaces that are difficult to explain in the form of a “verbal map”. Therefore, it is necessary for visually-impaired people to learn the name and meanings of terms in advance.

(Challenge 4)

The results of the hearing research for signs for visually-impaired people to use in everyday life are shown in Table 2, in which the signs are classified by the degree of an obstacle (completely blind or weakly sighted) and what stimuli they distinguish the sign according to. Consequently, many visually-impaired people use the material of a wall, which is distinguishable by a difference in touch, a convenience store that is distinguishable by the noise of people nearby and an opening-and-closing sound of an automatic door and a restaurant, which is distinguishable by the noise of people and the peculiar smell of food and drink.

Table 2 Signs for visually-impaired people used in everyday life

		Completely blind		Weakly sighted	
Hearing	Sound	Convenience store	4 people	Convenience store	3 people
		Restaurant	4 people		
		Vending machine	2 people		
		Supermarket	2 people		
		Iron plate	1 person		
		Pachinko parlor	1 person		
		Fountain	1 person		
		Manhole	1 person		
Kindergarten and school	1 person				
Smell	Smell	Restaurant	4 people		
Touch	Hand	Wall	6 people	Telegraph pole	1 person
	White cane	Mailbox	3 people	Guardrail	1 person
		Telegraph pole	1 person		
		Iron plate	1 person		
Manhole	1 person				
Sight	Light and darkness [※]			Convenience store	3 people
				Bus stop	1 person

※ This shows features that weakly sighted people said that they can use as a sign by contrast of color and light and darkness.

As the place of a sign, the guidance aside from features at a corner of a way is not necessary. However, visually-impaired people can confirm whether the place shown by the present location and a message are in agreement. Therefore, even if nothing exists at a corner, information about signs is effective.

6. Verbal map guidelines

Results of field experiments, previous studies, and a literature review suggest a revised edition of the verbal map guidelines. The composition of the guidelines is shown in Figure 4. They are the "subject" and the "grammar". The "subject" is a content related to what kind of features should be described as a message. The "grammar" is a rule to describe features according to what kind of vocabulary and order should be used.

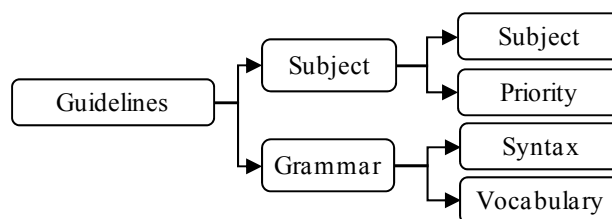


Figure 4 Composition divisions of the verbal map guidelines.

The composition of detailed guidelines can enable classification into subjects, priorities, syntax, and vocabulary:

<a-1> Subject

Feature information necessary for visually-impaired people. Table 3 shows necessary feature and attribute information.

<a-2> Priority

Where there are multiple features that might exist with complicated topography, priority is shown to judge which feature information is most necessary. For example, information about dangerous objects such as a waterway, a ditch, and a step with a possibility of leading to big accidents such as a falling should be

assigned priority. In contrast, priority of the information about pavements and slopes where people can walk in comfort is low.

<b-1> Syntax

The order of feature information is shown to describe the ease of imagining a walk space while visually-impaired people hear a message. For example, they are “A feature is explained from this side to the inside.”, “A feature is explained to a clockwise rotation from the left.” and “When the same kind of feature continues, it is explained as a x-th feature.”

<b-2> Vocabulary

Standardized expressions are used for visually-impaired people to understand them easily. For example, it is difficult for visually-impaired people with congenital blindness to imagine a word using a Chinese reading of a kanji. Therefore, even if it is the same word, for example, a planting, the Japanese reading is used, such as "Uekomi", rather than the Chinese reading such as "Shokusai". The expression "winding" is easy to imagine as a shape for sighted people. However, it should not be used because visually-impaired people cannot imagine such shapes well.

An example of the contents of the verbal map guideline is presented in Table 4, which describes what kind of information should be described for subjects such as landmarks and information about distance and time. According to the guidelines of such contents, a message is created in actual walking space.

Table 3 Features and attribute information

Feature		Attribute information
Passage	Passage	Width, Pavement, Shape, Distance, Name
	Stairs ^{※1}	Width, Pavement, Shape, Handrail, Landing
	Open space	Size, Pavement, Shape, Name
	Crossing	Signal, Traffic lane
Institution		Position, Entrance, Name
Dangerous object		Waterway, Ditch, Step
Textured paving block ^{※2}		Position, Starting and Terminal point, Turning point
Sign		Hearing, Smell Touch, (Sight)

※1 Stairs are walking spaces used for vertical movement, such as stairs, an escalator, a slope, and an elevator.

※2 Dangerous objects are features presenting the danger of falling. When a dangerous object is in a walking space, the kind and position of the dangerous object must be shown.

Table 4 Example of verbal map guidelines

<p>Example 1: Subject <a-1> Landmark</p> <hr/> <p>We describe features without mobility and features that are distinguished by the sense of touch, hearing and smell by stopping as a sign.</p> <ul style="list-style-type: none"> • Sense of touch: a wall with a different feeling, a mailbox, a telegraph pole, and so on • Sense of hearing: a convenience store, a vending machine, a supermarket, a fountain, and so on • Sense of smell: a restaurant (coffee shop, etc.)
<p>Example 2: Subject <a-1> Information about distance and time</p> <hr/> <p>We explain concretely how many meters there are to the next walk space in the walk space with depth. We explain the remaining distance concretely on the way, when there are 100 meters or more of distance.</p>

7. Practical Example

The purpose of a practical example is to create a message through an actual course as a concrete example of application and inspection of the verbal map guidelines created through the field experiment, etc. In this case, experiments were conducted with 2 visually-impaired people (1 completely blind person and 1 weakly sighted person). Contents through the course setting and application of the guidelines are described in this chapter.

The course is a route of the city area covered in a situation in which a visually-impaired person (completely blind person) is passing in everyday life together with a guide helper. Concretely, the course is from the Nankai Nanba Station 3rd floor north wicket to the Osaka visually-impaired person welfare center. The outline through the course is presented in Figure 5. A spot is shown below for which the way of thinking of the guidelines, the application example of the contents of the guidelines and creating a message. In addition, the following geographical numbers are the geographical numbers shown in Figure 5.

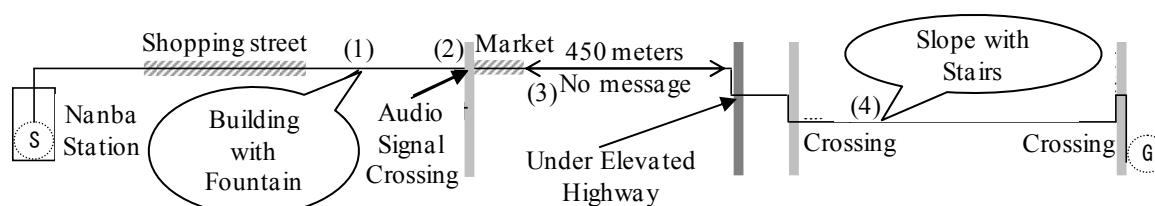


Figure 5 Example of guidelines application (Sketch of the course)

(1) Building with the fountain to hear the sound of water from 2 places

<Way of thinking of the guidelines>

Signs that are necessary for visually-impaired people are explained. A sign used for them is a feature that can identify the place using tactile or audio information. Particularly, it is necessary to describe signs that are distinguishable by the sense of hearing more carefully and in greater detail.

<Contents of the guidelines>

Features without mobility and those which are distinguishable by tactile, olfactory, and audio senses by stopping as a sign are explained. For example, a convenience store, a vending machine, a supermarket, a fountain and so on are distinguishable by hearing, a restaurant (coffee shop, etc.) is distinguishable using the sense of smell, and a wall can be sensed by touch, as are a mailbox, a telegraph pole and so on.

<Creating a message>

“It is in front of the xx building soon. There is a fountain in the building. Please go straight on then.”

(2) The crossing where there is an audio signal of a push button and which crosses a road with many traffic lanes

<Way of thinking of the guidelines>

Features necessary for safe and reliable walking at a crossing are explained.

<Contents of the guidelines>

The existence of a signal is explained (the existence of an audio signal and the position if there is a signal.), in terms of the crossing characteristics (name, kind and number of traffic lanes).

<Creating a message>

“It is a crossing with an audio signal soon. The xx line passes north and south, and the yy market is east. The xx line is a road of 5 traffic lanes of the one-way for north. Please cross a pedestrian crossing, go straight on and go into the yy market.”

(3) Long road on the city outskirts where distance without features must be explained

<Way of thinking of the guidelines>

Features that are necessary for a safe and reliable walking along a single route having no features are explained. When going straight, some unease is felt whether visually-impaired people can walk through the right course or whether the application is operating when long silence continues.

<Contents of the guidelines>

The distance in meters to the next walk space is explained. We explain the remaining distance concretely when there is 100 meters or greater distance.

<Creating a message>

“There is a crossing soon. Please come out of the xx market, go into a thin street with the sidewalk divided into both sides in the white line and go straight on 450 meters”.

※ In fact, for a 450 meters straight passage, no message is passed. Try a long-time long silence daringly.

(4) Slope of stone pavement with stairs on the way

<Way of thinking of the guidelines>

Information necessary to walk on the stairs safely and reliably is explained. Particularly, because the stairs present the danger of leading to big accidents such as a falling, it is necessary to explain information whenever stairs are involved.

<Contents of the guidelines>

The width of stairs, the existence of a landing are explained (the number, and the existence of a landing) and the existence of a handrail. We explain the position of a handrail if it exists. Additionally, information about pavement is explained when the pavement changes in front of and behind stairs.

<Creating a message>

“There is a slope of a stone pavement soon. Stairs are in the middle of the slope. There are 3 landings on the stairs. 3 poles stand on the stairs. The slope continues after that. Please go up the slope and go straight on the narrow street in flat asphalt.”

8. Conclusion

This study provided the following results.

- 1) The verbal map guidelines produced from field experiments which simulate an audio AR application were revised. Results show that creation of the navigation message is enabled in every place throughout the city area.
- 2) A message was created through a course that a visually-impaired person is using in everyday life by application of the revised edition of the verbal map guidelines.

According to these results, the verbal map guidelines for visually-impaired people to enhance daily mobility are created. They are necessary to produce a practical navigation system. Visually-impaired people and people supporting them can create messages in places where they actually walk.

Future studies will evaluate the operability of an audio AR application and the validity of the message composition considering the GPS error, not by simulations such as field experiments, having visually-impaired people use the system with a smartphone.

In the near future, if system users can identify messages created for using the guidelines, other visually-impaired people will be able to walk at the first place and the system will be continuously manageable.

This study was conducted as a part of a Grant in Aid for Scientific Research during Heisei 24-26 year (Base Research B, 24360209) “Practical Use Study of the Town Walk Support Navigation System Fused in Audio AR and RFID for Visually-impaired people”.

References

- 1) Takashi UCHIDA and Yoshiaki YOSHII: A Study of Navigation System for Visually Handicapped to Support Town Walk – Media and Messages for Guidance –, Infrastructure Planning Review, Vol.27, pp.831-839, 2010 (in Japanese)
- 2) Takashi UCHIDA and Tsubasa MOCHIDUKI: Experiments on Sound and Timing of Fundamental Signals of the Pedestrian Navigation System for Visually Disabled People, Papers of Traffic Engineering, Japan Society of Traffic Engineers, No. 27, pp.165-168, 2007 (in Japanese)
- 3) ITS (Intelligent Transport Systems) Social Experiment Investigation – Umeda Terminal District Movement Support Experiment – Report: Osaka City Plan Coordination Bureau, 2002 (in Japanese)
- 4) Kazuyuki NEKI and Takashi UCHIDA: Navigation Messages for a Pedestrian Navigation System for Visually-impaired people to Support Urban Walking – Verbal maps and instructions –, Proceedings of

Annual Meeting, Japan Society of Traffic Engineers, 2pp., 2013 (in Japanese)

Consolidation of Predicted Disaster Information and Expectation of Coincident Disaster

Shouta MORI and Takaaki SHIGEMATSU

(Received October 7, 2013)

Synopsis

The 2011 off the Pacific Coast of Tohoku Earthquake brought serious damage in the wide area in Japan. We must learn most of knowledge and findings from this unexpected giant earthquake disaster. It is said that the return period of the giant earthquake as the 2011 off the Pacific Coast of Tohoku Earthquake is the order of a thousand years. The return period of the expected disaster so far, however, is a few hundred years. As a trial to get rid of an unexpected disaster, information about disaster predictions is collected and the effect of coincidence of some disaster is investigated in this study. The disaster information such as inundation by tsunami, storm surge and flooding, seismic intensity, liquefaction and subsidence is stored as a GIS data and easily used for investigation of coincident disaster.

KEYWORDS: Coincidence of disasters, Prediction of an unexpected disaster, Tsunami inundation, Storm surge and flooding, Seismic intensity, Liquefaction, Subsidence

1. Background and purpose of this study

Many human lives and property in the district along the Sanriku coast were lost by the 2011 off the Pacific Coast of Tohoku Earthquake. The giant earthquake brought not only strong ground motion over a wide area but also a huge tsunami and liquefaction and made the refuge of people difficulty. We did not have the scientific data that such a giant earthquake might have occurred in the Sanriku district. Hence, most of the researcher on earthquakes and tsunamis could not expect an occurrence of the giant earthquake and the provoked tsunami and liquefaction. However, it is not to say that the local governments and residents in the Sanriku district have not prepared measures against tsunami. If anything, there were some advanced cities for the tsunami disaster prevention in the district. A problem is not to have expected that the more severe situations than that brought by the past disasters may occur.

The disaster responses can be classified into hard ones and soft ones. The hard responses are the ones by rigid structures such as breakwaters against tsunami and storm surge barriers and help inhabitants to reach refuges. Because of excess reliability of concrete structures, unfortunately, most inhabitants have acquired a habit of not taking refuge action even if evacuation warning would be issued. On the other hand, the soft responses are the measures to help the rapid refuge action of inhabitants by markers, directional arrows and so on. These days, most local government makes the hazard map which expresses disaster potential on a map and has kept making efforts to let inhabitants know widely. As Tohno¹⁾ pointed out, however, there is hardly such a hazard map as some plural disaster potentials are presented in. From a viewpoint of reviewing prevention from disaster with estimating the severest disaster potential, it is necessary to consider not only a disaster with an extremely less-frequent occurrence but also a coincidence of plural disasters with occurrence frequency which local governments have ever expected.

One of the purposes of this study is to gather the disaster information that has been assumed so far in local governments. The other purpose is to estimate a coincident disaster which may occur in the future based on the knowledge when disasters anticipated in the past would occur concurrently or consecutively in a short duration. In this paper, the disaster information in the Kansai district will be shown by using a geographic information system (GIS).

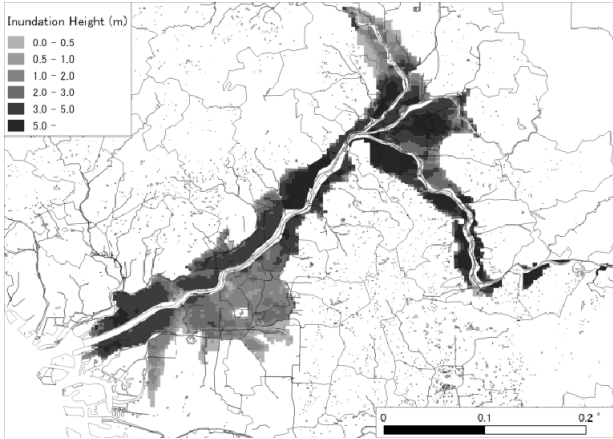
2. Expected disaster

2.1. Inundation by river water

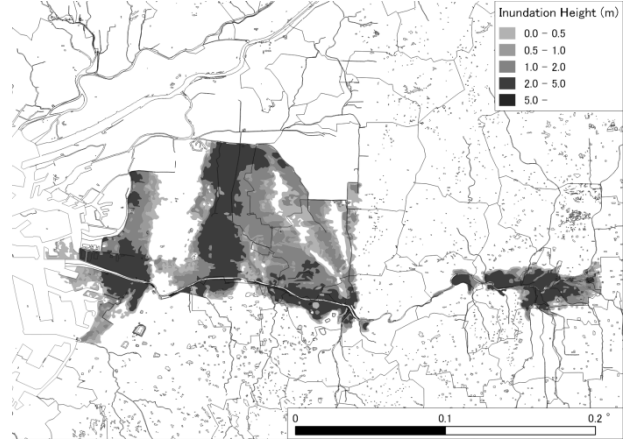
There are 10 class-A rivers which flow into the sea in the Kansai region (strictly speaking, under management by Kinki Regional Development Bureau of the Ministry of Land, Infrastructure, Transport and

* Research Student, Department of Urban Engineering

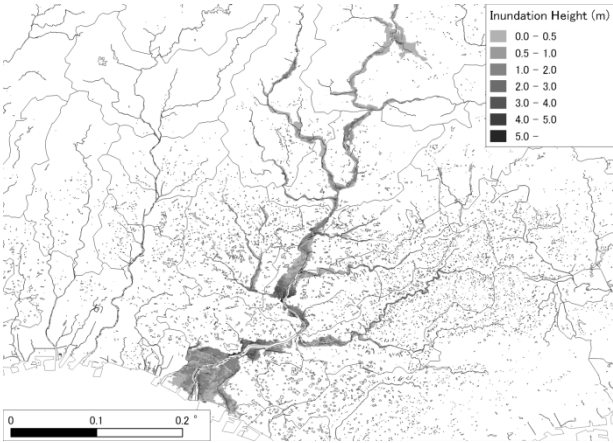
** Professor, Department of Urban Engineering



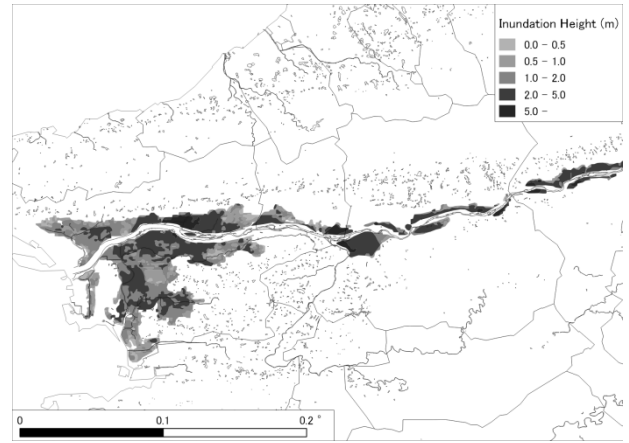
(a) Yodo-gawa river



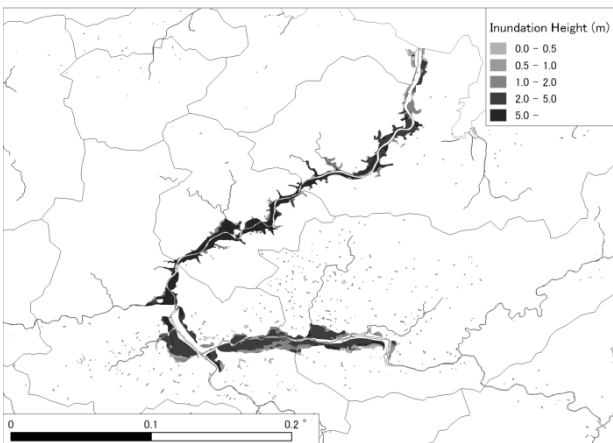
(b) Yamato-gawa river



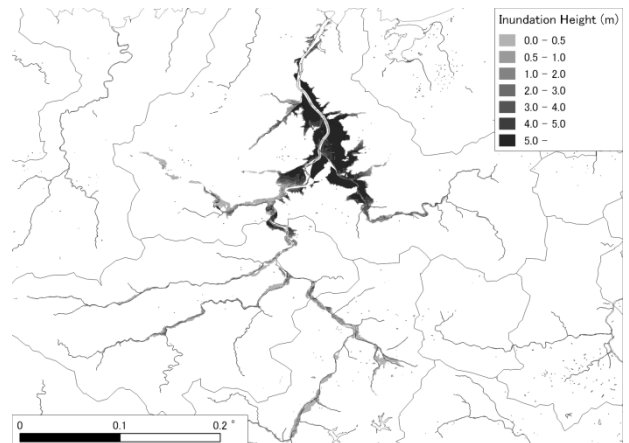
(d) Kako-gawa river



(c) Kino-kawa river



(d) Yura-gawa river



(e) Maruyama-gawa river

Fig. 1 Anticipated inundation area and depth.

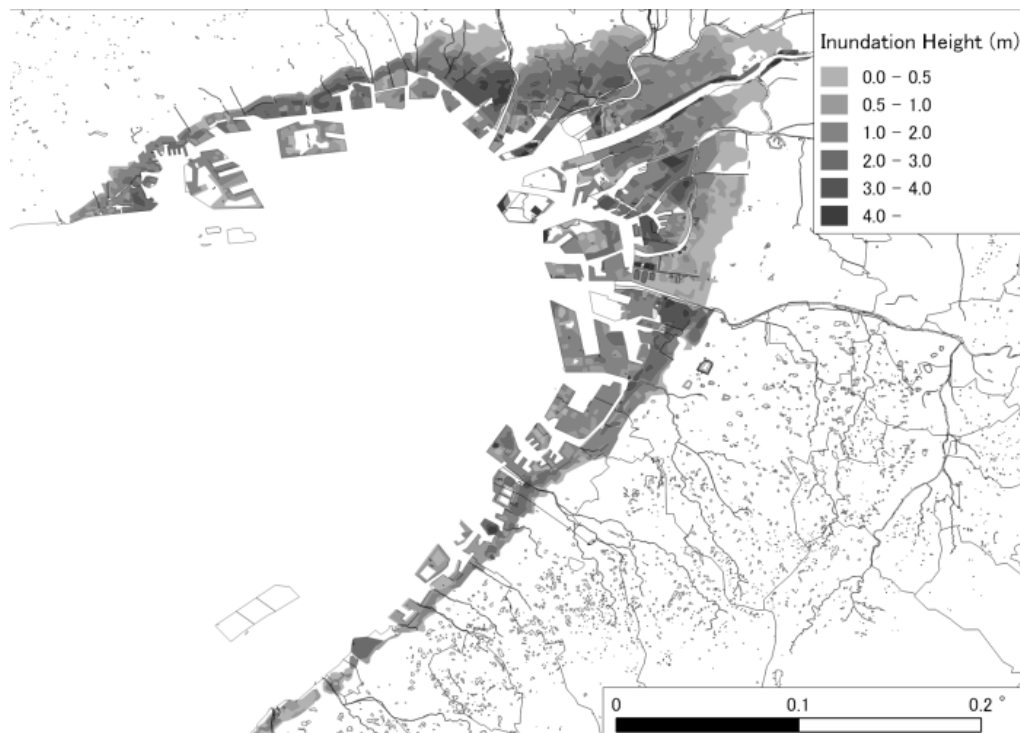


Fig. 2 Anticipated inundation area by storm surge.

Tourism). The data are offered by local governments and the Ministry of Land, Infrastructure, Transport and Tourism as figures. Authors made GIS information from the data as Fig. 1. Populations in each river area are 11,650,000, 2,150,000, 820,000, 689,000, 300,000, and 150,000 respectively. The areas of each river are 8,240, 1,070, 820, 1,750, 1,880, and 1.300 km² respectively. Authors made GIS information from the data which are offered by local governments and the Ministry of Land, Infrastructure, Transport and Tourism as figures. The inundation of Yodo-gawa River is anticipated under the condition of 500 mm two-day precipitation in the upstream region of Hirakata. The inundation of Yamato-gawa River is anticipated under the condition of 268 mm two-day precipitation in the upstream area from Oji or 280 mm two-day precipitation in the upstream area from Kashiwara. The inundation of Kako-gawa River is anticipated under the condition of 288 mm two-day precipitation at Itaba and 271 mm at Kunikane. The anticipation condition of Kino-kawa River is 484 mm two-day precipitation at Hashimoto and 440 mm one at Funato. The condition of Yura-gawa River is 359 mm two-day precipitation in the river basin, which is the same condition of flood on September 1953. The condition of Maruyama-gawa River is 327 mm two-day precipitation in the basin.

2.2. Inundation by storm surge

Fig. 2 shows the anticipated inundation area by the storm surge which is the severest case presented in the guideline of the action plan for crisis management against a storm surge of Osaka bay. The Osaka plain has ever suffered severe damage by storm surges such as Typhoon Muroto, 1934, Typhoon Jane, 1950, Typhoon Nancy, 1961. Osaka Plain was formed by accumulation of a large amount of sand carried by Yodo-gawa and Yamato-gawa River. Much land was formed by some reclamation and landfill. Combining with groundwater pumping due to economic development, zero-meter area, of which elevation is lower than the mean monthly-highest water level T.P. +0.9 m in the typhoon season, spreads widely along the coast line in Amagasaki and Osaka City. In the anticipation of the damage by a storm surge, tide level in consideration of influence of global climate change (T.P. + 1.1 m) and power (900 hPa), a scale, and the decrement of the typhoon are taken into account. Fig. 2 is the anticipated result where the typhoon will cause the water gates

to malfunction and some dikes to be not working.

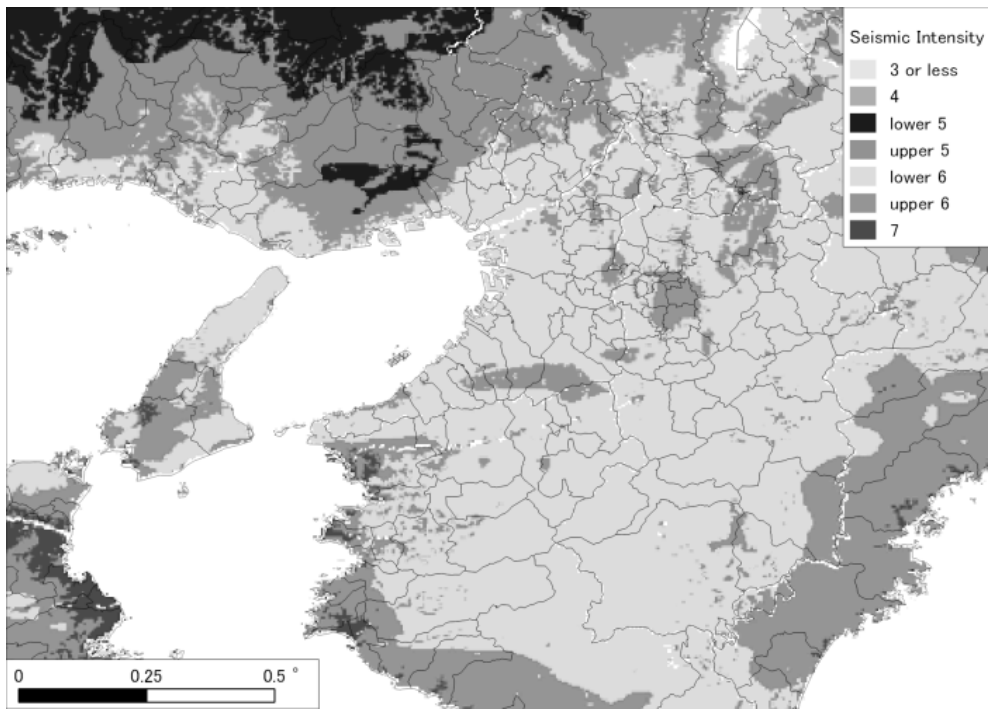


Fig. 3 Seismic intensity map by the Nankai Trough earthquake.

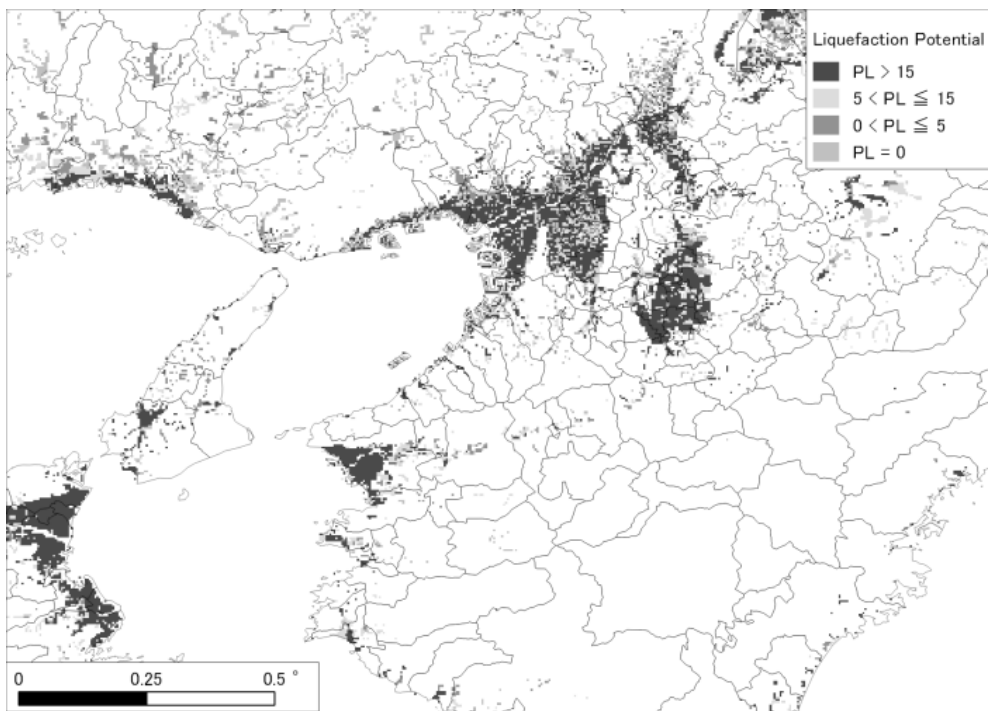


Fig. 4 Liquefaction hazard map by the Nankai Trough earthquake.

2.3. Nankai trough earthquake

After the 2011 off the Pacific coast of Tohoku Earthquake, Cabinet Office, government Japan examined the other giant earthquake which would occur in the Nankai trough with considering every possibility. Fig. 3 shows the expected seismic intensity map in the case where a strong ground motion area will spread into

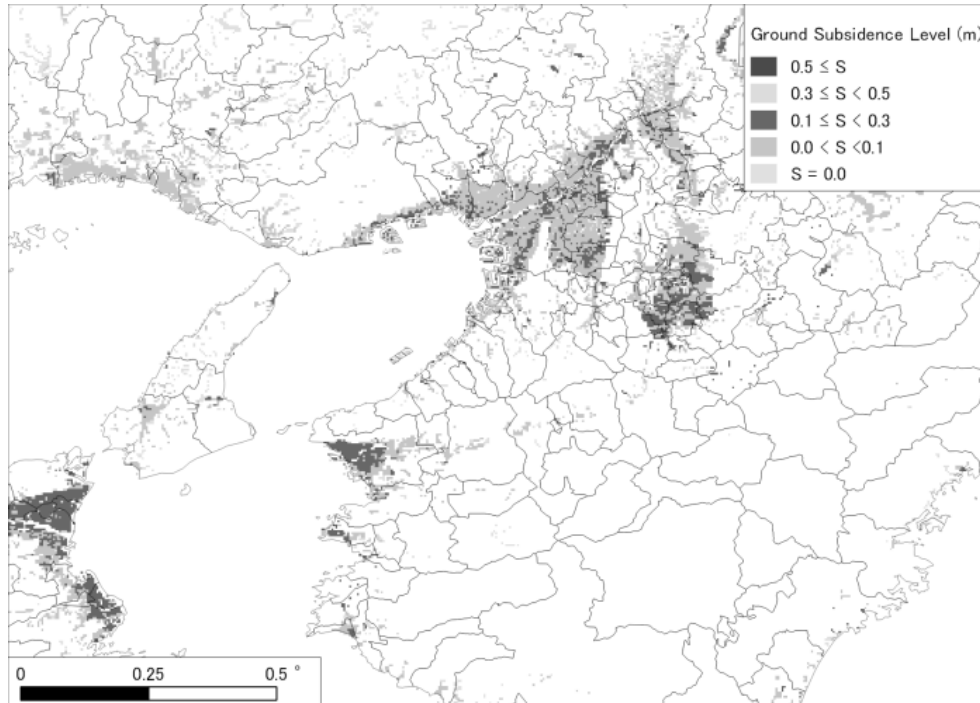


Fig. 5 Subsidence displacement by Nankai Trough earthquake.

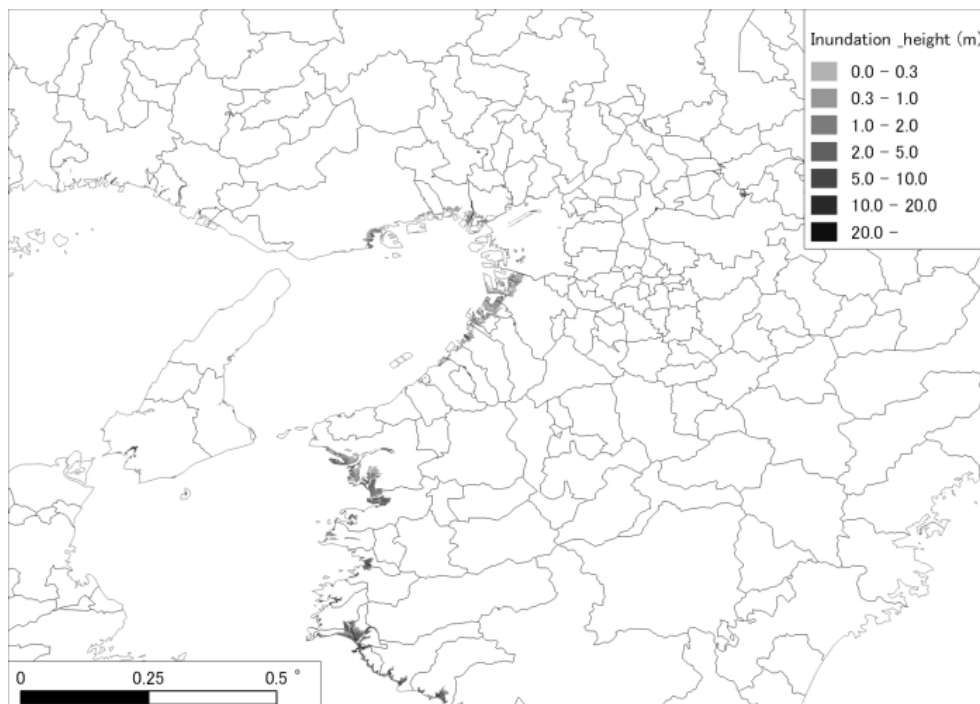


Fig. 6 Tsunami inundation area by Nankai Trough earthquake.

inland of Shikoku region and the Kii Peninsula.

Fig. 4 and Fig. 5 show the liquefaction prediction and subsidence settlement by the earthquake mentioned above. Fig. 6 shows the expected tsunami inundation area caused by Nankai trough earthquake. It should be noticed that the inundation map is made by gathering the maximum inundation depths of estimated results with different sizes and displacements of fault under the condition that sea embankments will be broken instantaneously at tsunami overflowing.

3. Anticipation of coincident damages by some origins

3.1. Anticipation of coincident disasters due to a single origin

It is well known that the giant earthquake sometimes induces liquefaction and tsunami. It was reported that liquefaction due to the 2011 off the Pacific Coast of Tohoku Earthquake made the refuge of inhabitants difficult. Liquefaction depends on not only seismic intensity but also geological condition. Inhabitants are required to get enough knowledge of the tsunami height which might attack and possibility of liquefaction of the inhabited area.

Fig. 7 shows the hazard map which is composed of the liquefaction hazard map shown in Fig. 4 and Tsunami inundation hazard map shown in Fig. 6. It is found from Fig. 7 that the wide area of the alluvial plain with the highly concentrated industry and population has a potential of both risks of liquefaction and tsunami inundation.

Thinking about refuge action after giant earthquake occurring, more detail information will be required. Fig. 8 shows the hazard information about liquefaction and tsunami inundation in Wakayama City located in the Kino-kawa River downstream basin. The color of circles in Fig. 8 represents the liquefaction potential PL, which the larger PL means the higher potential of the liquefaction occurrence. It is found from Fig.8 that the most part of plain in Wakayama City has a very high potential of liquefaction. In addition, tsunami inundation area spread along not only coastal line but also Kino-kawa River. If river bank, sea embankment, coastal levee and so on lost their function to protect the inland from water disaster due to liquefaction, the following tsunami will bring serious damage. Leakage and/or outflow of a hazardous substance including with heavy oil would cause further disaster such as fire disaster and health problem.

3.2. Anticipation of Coincident disaster due to some origins

River banks, sea embankments, coastal levees and so on have been constructed and managed in the past several decades. Consequently, severe damage by a storm surge and flooding has decreased. However, unexpectedly strong rain for a short period has frequently come occur recently. Further, sea level rise and change in the precipitation feature due to typhoon by global climate change are apprehended. It may be said that the flood potential will increase more and more in this sense.

Fig. 9 shows the hazard map which is composed of the inundation areas by Yodo-gawa, Yamato-gawa, and Kino-kawa River and the one by a storm surge. In the figure, the deepest inundation depth among the expected inundation depths is presented. It is found that most area along the coast line and rivers will be damaged if the events occur at the same instant. Severer damage may occur in the wider area if the sea level rises by the progress of the global warming.

Fig. 10 presents the inundation area and depth when storm surge and flood by Yodo-gawa River would occur at the same instant. The storm surge is a phenomenon of the time scale for a few hours. On the other hand, flood is a phenomenon for a few hours of days. The coincidence of these disasters, storm surge and flood, has been hardly predicted because of the extremely low possibility. Although it is said that the return period of the giant earthquake as the 2011 off the Pacific Coast of Tohoku Earthquake may almost a thousand years, the research on the probability of coincidence of plural disaster should be necessary. It is found from Fig. 10 that deeper inundation area spreads not only along coast but also to the inland area in which there is much property and human activity. Some countermeasures are required to protect property and human lives. It is additional notice that the value of the inundation depth in the figure is not accurate because inundation depths by the storm surge and by flood from Yodo-gawa River are only added without considering the physical mechanism.

There are many rivers with bed above the ground in Japan. If river flooding occurred after land subsidence occurring due to earthquake, inundation area would spread wider than that only flood occurs. Fig. 11 shows

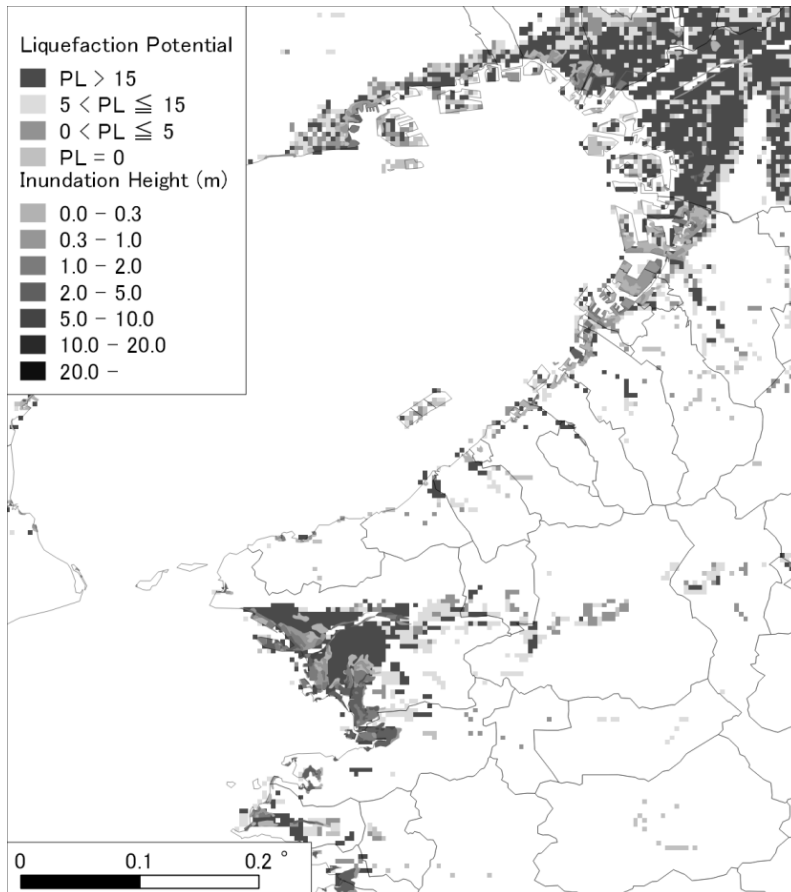


Fig. 7 Tsunami and liquefaction by the Nankai Trough earthquake.

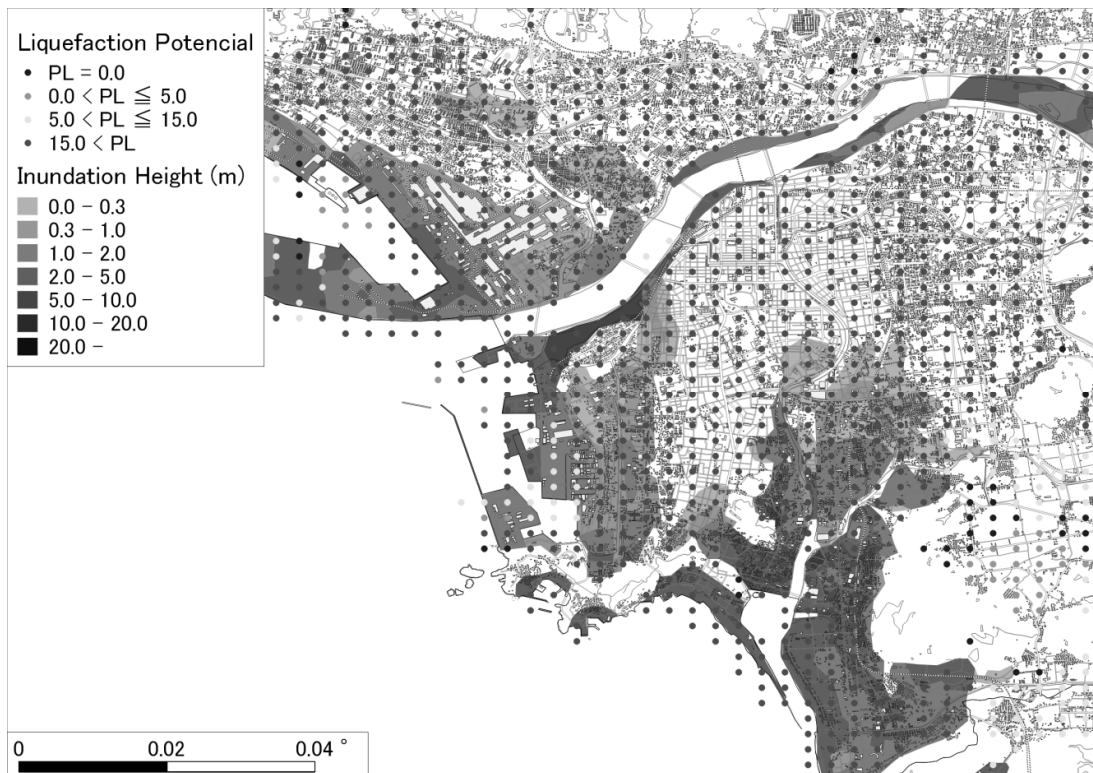


Fig. 8 Coincident disaster of tsunami and liquefaction in Wakayama City.

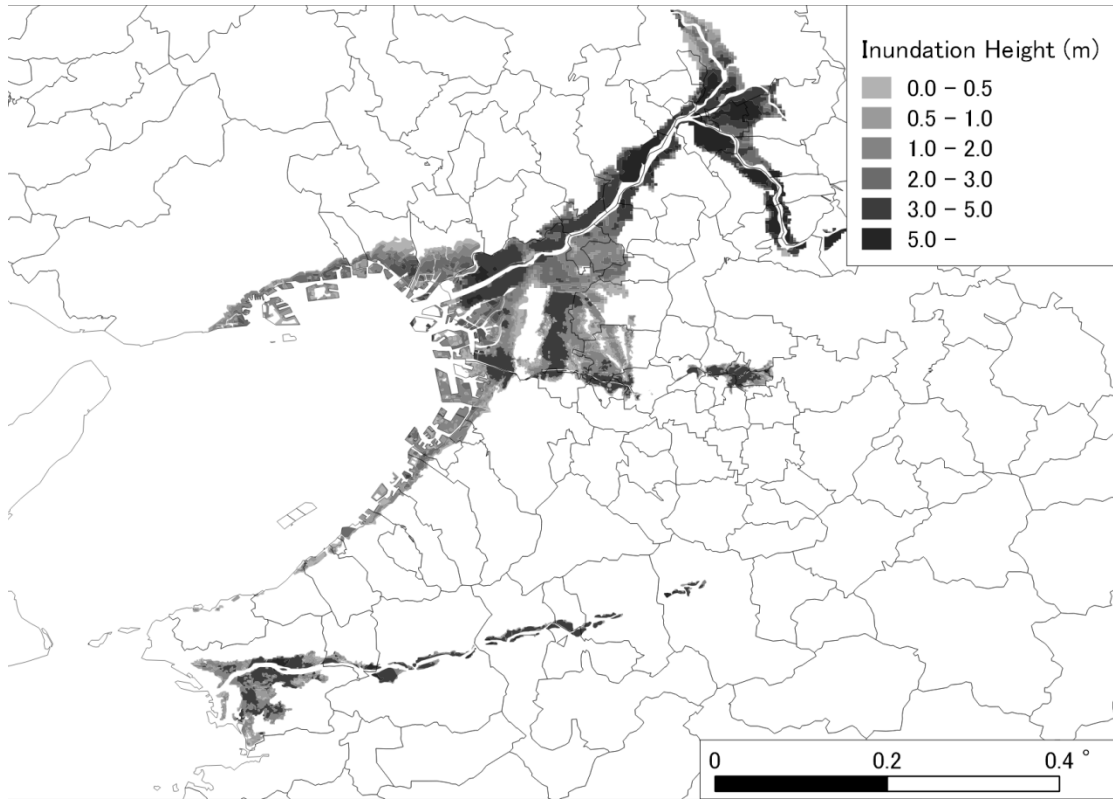


Fig. 9 Coincident disaster of storm surge and river flooding.

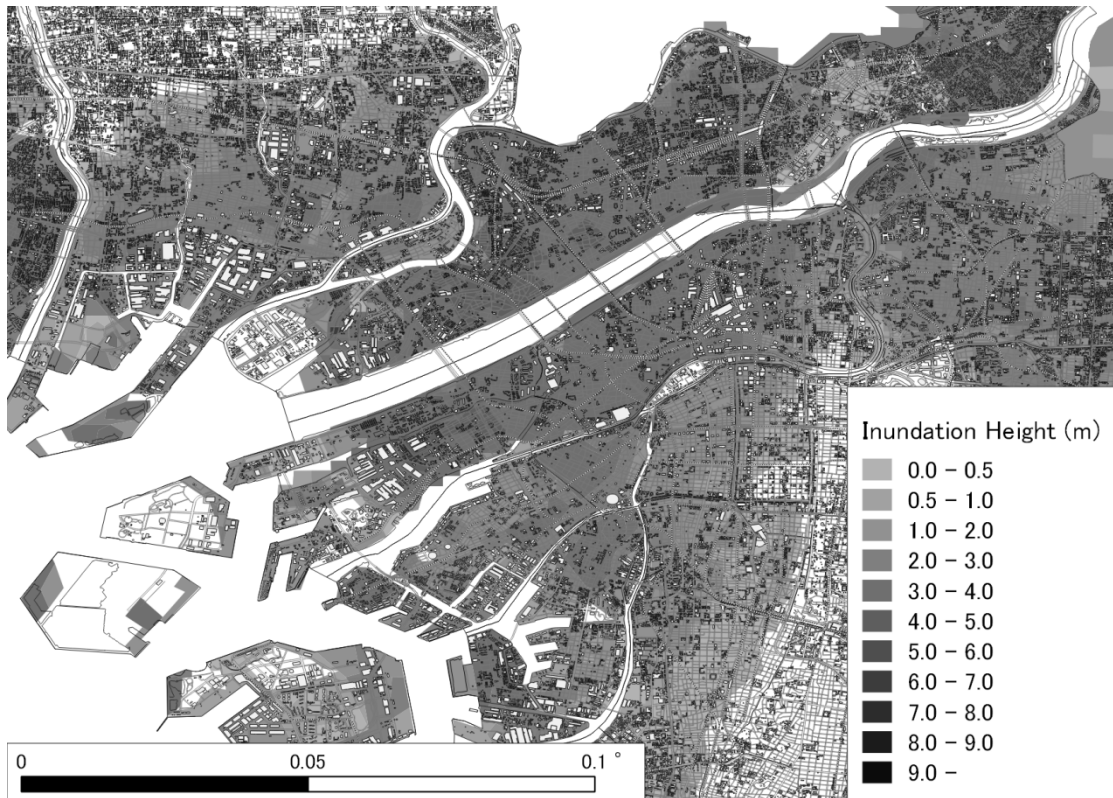


Fig. 10 Coincident disaster of storm surge and a river flooding in the Yodogawa downstream basin.

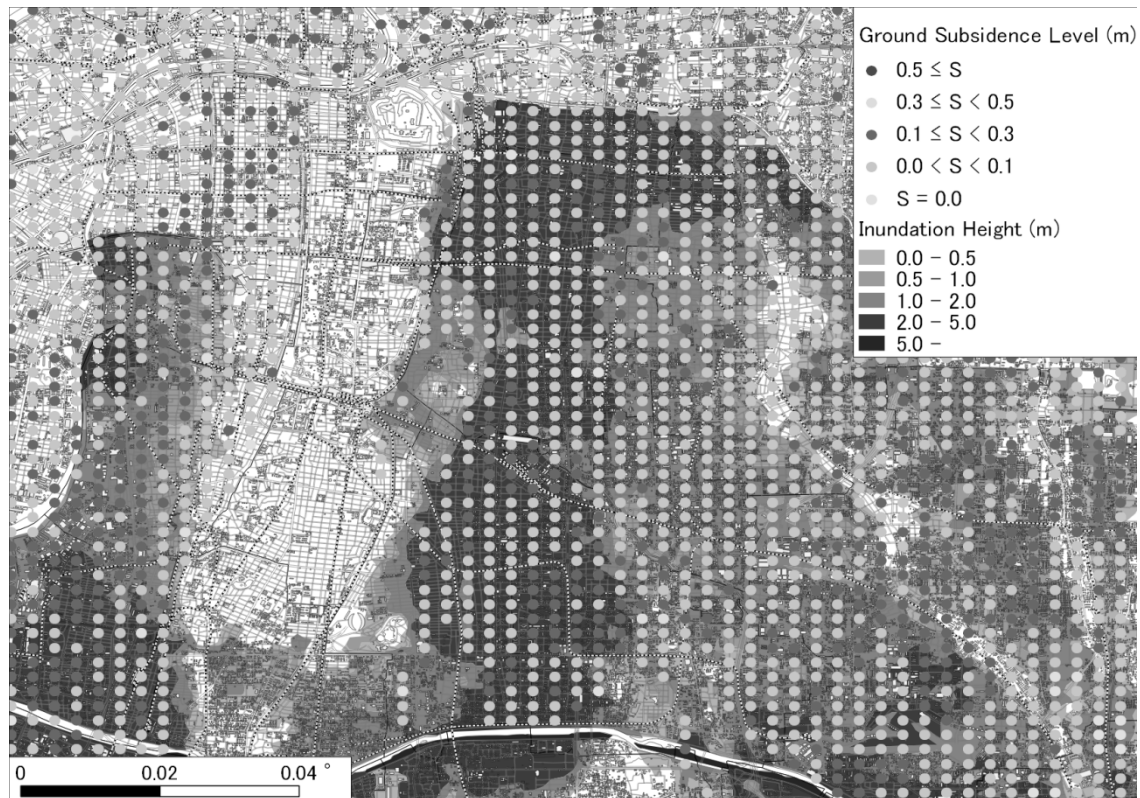


Fig. 11 Coincident disaster of river flooding and subsidence.

the inundation area in the northern part from the Yamato-gawa River, which presents ground subsidence level and inundation depth. Subsidence with 0.3 m is predicted in the area shown in Fig. 11. It is easily inferred that the subsidence makes danger of outbreak of flooding increase and enhances the probability of the rise of propagation velocity and of enlargement of the inundation area.

4. Afterword

In this paper, some disaster information in a part of the Kansai district is presented by using the geographic information system. Some examples of coincident disaster are presented by integrating information about the anticipated disaster. Coincident disaster shown in this paper must be different by the combination of the origins and the time lag between origins. In addition water disaster is anticipated by integrating the values anticipated under the condition which a single origin individually occurs but not considering the physical mechanism. More accurate anticipation with considering change of phenomena over time is necessary to provide rapid and appropriate actions.

5. References

- 1) I. Tohno, "A Study on the Natural Disasters Caused by Multiple Origins - Their Influences and the Comprehensive Hazard Map - ", *The Quaternary Research*, **32(5)**, 339-352. (1992).

Mechanical Engineering

Improving Oil Separation inside CO₂ Rotary Compressor Shell

Tetsuhide YOKOYAMA, Nobuya NISHIMURA, Hideaki MAEYAMA, Keisuke SHINGU, Shinichi TAKAHASHI and Shogo MOROE

Trans. JSRAE, 30(1), pp. 75-86, (2013). (in Japanese)

A CO₂ rotary compressor uses refrigeration oil to lubricate and cool sliding parts and to seal the cylinder. It is difficult to separate the oil in the shell at high pressure from CO₂ gas, whose difference in density from the oil is small. It remains an issue to retain high efficiency with the same shell size as a present hydro fluorocarbon (HFC) compressor. We explored improvements in the oil separation by use of computational fluid dynamics (CFD) analysis and identified two effective measures. One measure is to flatten a lower balance weight of the rotor to prevent the oil mist from moving up through the motor flow paths. Another measure is to set up a rotating disc with a protruding balance weight at the top of the rotor to increase the pressure in the upper space and allow the oil over the stator to return to the lower space by gravity. Experiments with an actual compressor verified that oil separation was improved to the target value.

Method for Measuring Solar Reflectance of Retroreflective Materials Using Emitting-Receiving Optical Fiber

Hiroyuki IYOTA, Hideki SAKAI, Kazuo EMURA, Norio IGAWA, Hideya SHIMADA and Nobuya NISHIMURA

Journal of Heat Island Institute International (Special Issue "the Heat Island 2009 Conference), Vol.7-2, pp.213-217 (2012) (online publishing).

The heat generated by reflected sunlight from buildings to surrounding structures or pedestrians can be reduced by using retroreflective materials as building exteriors. However, it is very difficult to evaluate the solar reflective performance of retroreflective materials because retroreflective light cannot be determined directly using the integrating sphere measurement. To solve this difficulty, we proposed a simple method for retroreflectance measurement that can be used practically. A prototype of a special apparatus was manufactured; this apparatus contains an emitting-receiving optical fiber and spectrometers for both the visible and the infrared bands. The retroreflectances of several types of retroreflective materials are measured using this apparatus. The measured values correlate well with the retroreflectances obtained by an accurate (but tedious) measurement. The characteristics of several types of retroreflective sheets are investigated.

Reduction of Reflected Heat of the Sun by Retroreflective Materials

Hideki SAKAI, Kazuo EMURA, Norio IGAWA and Hiroyuki IYOTA

Journal of Heat Island Institute International (Special Issue "the Heat Island 2009 Conference), Vol.7-2, pp.218-221 (2012) (online publishing).

It is demonstrated that the walls made of retroreflective materials can reduce the reflected heat of the sun in the directions of neighboring roads and buildings. For mitigating the urban heat island effects, the applicable area of retroreflective materials is larger than that of high-reflective paints, because retroreflective materials can be used not only as "cool roofs" but also as "cool walls." Then, the solar retroreflectances of several retroreflective materials, which cannot be measured directly by a spectrophotometer, were measured for the first time. The procedures were as follows: First, the reflectance without retroreflection was measured by using a spectrophotometer with the integrating sphere. Then, the total reflectance was deduced from the amount of temperature rise by solar irradiation. Finally, the retroreflective component was calculated by subtracting the former from the latter. The measured retroreflectances are 20 to 30 percent for the prism-array type, about 20 percent for the capsule-lens type, and about 10 percent for the bead-embedded type.

Steam Condensation-Based Heat Transfer Mechanism Analysis of Cooking Oven

Junko Yamagata, Hiroyuki Iyota and Nobuya Nishimura

Nippon Shokuhin Kagaku Kogaku Kaishi, Vol.59(10), pp491-502 (2012) (in Japanese).

In order to improve the utilization of cooking ovens, we conducted heat transfer mechanism analyses of a convection/steam combined oven by focusing on steam condensation. Spherical wet gauzes were used as the sample material. The heat transfer mechanisms were analyzed by considering the heat balance on the surface of the spherical gauze using the measured mass change of the sample and the temperature changes of the

sample surface and gas flow. In this manner, we could estimate the heat flux in terms of heat transfer and heat flux changes with time. The estimated data were used to draw diagrams that visually depicted the heat transfer mechanisms in terms of the heat flux changes with time. The diagrams provided all possible means to visually understand and compare each heat transfer quantity, incremental moisture content and heat quantity generated because of steam condensation on the sample material, and drying rates under different heating conditions. In addition, the heat transfer mechanism of a steam convection oven was analyzed using this method. We analyzed the effects of each setting condition (e.g., temperature, humidity, and velocity) on the heat flux, moisture content, and temperature of the sample material during heating. From the analysis results, it was possible to understand and compare the heating characteristics between oven types, and to set the proper conditions for achieving optimal oven heating.

Gas Consumed and Kitchen Appliances Used in Training for Food Service Management

Masayo IKEDA, Ayumi KATO, Chiemi TAKEDA, Junko YAMAGATA, Hiroyuki IYOTA, Akemi HOSODA, Chiyoko SEKI and Mitsuru KIMIRA

Journal of Home Economics of Japan, Vol.64(5), pp.233-242(2013.5) (in Japanese).

We examined the kitchen appliances used and gas consumed in training for food service management to enable the design of energy-conservation education programs in training courses for registered dietitians. The average gas consumption per day was $6.32 \pm 0.39 \text{ m}^3$, of which 73% was used by cooking appliances, and 27%, by the dish washer. The gas consumption per minute was most for the tilting kettle ($0.0320 \pm 3.0176 \text{ m}^3/\text{min}$) and least for the combination oven ($0.0131 \pm 1.0049 \text{ m}^3/\text{min}$). The gas consumed per meal was most for the main dish, although differing according to the menu and cooking appliance. The amount of energy consumed at a training institution was influenced by the experience of the cooks, equipment used, food menu, and number of cooks involved in the kitchen. An analysis of the energy consumed in every institution will enable a cost-effective technique for energy conservation to be established, and the fuel, lighting, and water costs to be reduced.

Effect of "Visualization" of Gas Consumption on Student's Awareness About Energy Conservation During Food Service Training

Nanae KURATATE, Hiroyuki IYOTA, Junko YAMAGATA, Tomohiro KAYANO, Masayo IKEDA, Naomi CHISUWA, Mitsuru FUKUI and Yukiko UEDA

Journal of the Japan Institute of Energy, 92(8), pp.695-701(2013.8)

The purpose of this study was to quantitatively assess change in energy conservation awareness after energy education incorporating "visualization" of gas consumption during food service training. An intervention study using a before-and-after design without a control group was conducted with 37 third-year students from the Department of Food and Nutritional Sciences at Osaka City University. The duration of the education intervention was 4 months. During this period, the students attended two lectures and a training session, and a display monitor was installed in the training room to show gas consumption. A scale was developed to objectively assess energy conservation awareness. Changes in awareness were measured by the scale and compared before and after the intervention. Using the scale, of which reliability and validity had been previously determined, the average score was increased in each of the following areas ($p < 0.05$): "motivation for energy saving", "motivation to learn about energy", and "understanding of energy". In conclusion, this study found that the educational intervention changed students' awareness of effective and reduced energy consumption, and indicated the possibility that the educational approach is effective.

Sensory Evaluation of Preference of Baked Food Color

Hideki SAKAI and Hiroyuki IYOTA

Conference Proceedings of International Colour Association (AIC 2013), vol.1, pp.57-60 (July, 2013, Newcastle upon Tyne, UK)(on CD-ROM)

We conducted sensory tests to determine the preference of baked food color of a plain cookie and sliced bread. They are initially white (L^* is about 90), which is the color of wheat flour, and become darker (browning) as baking progresses. A total of 93 Japanese subjects (40 males and 53 females, average 31.8 years old) evaluated the browning colors from raw to overcooked and answered the most preferred color, and the upper (not too raw) and lower (not overcooked) limits as a food to eat. The results were highly individual. There is, however, only one peak in each frequency distribution. Thus, we can determine the range of browning color that most (eg. 75 percent) people can accept. That is between $L^* = 77.5$ and 62.5 for plain cookies and between $L^* = 81.2$ and 63.5 for sliced bread.

Change in Food Color During Cooking with Steam Oven

Hiroyuki IYOTA, Hideki SAKAI and Yusuke MAMIYA

Conference Proceedings of International Colour Association (AIC 2013), vol.3, pp.1241-1244 (July, 2013, Newcastle upon Tyne, UK)(on CD-ROM)

Steam ovens heated with hot air and/or superheated steam are becoming popular for domestic and commercial use. These ovens are known as “superheated steam ovens” or “steam convection ovens.” Food color is one of the most important metrics of an oven-cooking process. However, conventional colorimetric equipment cannot be used for measurement of color during food processing because such processes usually involve high temperatures and wet surfaces. Thus, in the present study, the change in food color during oven heating was measured. A spectrometer and a glass fiber probe were used for continuous measurements during heating under the temperature of 200 °C. Two types of food materials were used as samples: a crumb of sliced bread, and a raw meat pate. In the case of the bread sample, the baking time was shorter under the high humidity (the high dew point temperature) condition. In the case of the raw meat sample, rapidly increasing humidity caused the denaturation of meat protein, and this changed the meat’s color in a short period of time. These results, and the color-measurement techniques used in this study, could contribute to the technological advancement of oven design, and to the optimization of oven operation.

Effects of Popping on Amaranth Seed Nutrients

Taro MURAKAMI, Aiko YUTANI, Hiroyuki IYOTA, Tetsuo YAMANO and Yotaro KONISHI

Proc. of The 6th International Conference of the European Amaranth Association: Neglected and Under-utilized Species Research in 21st Century, pp.51-54, (October 21 - 24, 2012, Nitra, Slovak Republic)

The seeds of amaranth can be popped under suitable heating. The traditional popping method is to heat the seeds manually on a hot plate, although a problem arises because of nutritional value loss through overheating. We developed continuous popping methods based on hot-air heating. This study investigated the effects of heat treatment during seed popping on B-group vitamins and minerals. Results show that the B-group vitamin and mineral contents were not lost when using this method.

Use of Superheated Steam/Moist Air as Heating Media

Hiroyuki IYOTA

Reito, Vol.88 (No.1031), pp.3-7(2013.9) (in Japanese)

Heating using high-temperature steam, which has a temperature above the boiling point of water, is known as superheated steam heating. In this heating method, the humidity (steam mole fraction) of the heating medium contacting the material can vary considerably during the actual heating process, from that of room air to that of superheated steam. In this report, we briefly describe the handling of steam and its generator, and introduced a psychrometric chart to study the condition of humid air and pure superheated steam over a wide range of humidity values. The effects of humidity on the heating process and the use of superheated steam/moist air as heating media are also discussed.

Measurement of Dynamic Surface Tension from a Profile of Horizontal Capillary Jet

Kenji KATOH and Tatsuro WAKIMOTO

Proc. of 23th International Symposium on Transport Phenomena, No. 245 (2012)

A novel method is proposed to measure the dynamic surface tension of surfactant aqueous solutions. The trajectory of a liquid jet ejected horizontally from a circular orifice was theoretically analyzed from a mechanical viewpoint. The ordinary differential equation to govern the jet behavior was obtained from the force balance between inertial force, gravitational force, pressure and surface tension. The jet trajectories calculated from the equation agree well with those measured experimentally for some test liquids. The dynamic surface tension can be determined so as to fit the theoretical trajectory to the measured one for the surfactant solution. Several kinds of surfactant aqueous solutions with different concentration were used to examine the validity of the proposed method. The results of measured dynamic surface tensions agree well with those obtained by the oscillating jet method. The present method has some advantages such as simple measurement or good reproducibility, compared with other methods.

Dynamic Wetting Behavior of Three-Phase Contact Line in Several Experimental Systems

Kenji KATOH, Tatsuro WAKIMOTO, Yasufumi YAMAMOTO (Kansai University) and Takahiro ITO (Nagoya University)

Proc. of 8th International Conference on Multiphase Flow, No. 505, 6pages (2013)

The dynamic wetting behavior is investigated experimentally. First, the movement of liquid column in a capillary tube was observed. Using the measured dynamic contact angles, the solution of modified Lucas-Washburn equation can approximate well the time variance of liquid height in the capillary. Secondly, the dynamic contact angles were measured for two-dimensional meniscus and axi-symmetric droplet, in order to detect the influence of contact line curvature, (i.e., the effect of line tension). The measured dynamic contact angles agree well with each other for droplet with various radii and two-dimensional meniscus. The dynamic wetting behavior is independent on the curvature of three-phase contact line.

Mini -type Wave Power Generation System Using a Slit Type Breakwater

Kenji KATOH, Takaaki SHIGEMATSU, Shin'ya YOSHIOKA and Tatsuro WAKIMOTO
OHM, April, pp. 4-5 (2013) (in Japanese).

A new type of wave power generation system is proposed to be installed in a vertical slit type breakwater. Savonius wheel and bending-plate type generator are examined experimentally to be installed in the breakwater. In the latter system, an elastic rectangular plate connected to a wheel and axle via a string is set in the water. When the wave force bends the plate, the tension of the string rotates the wheel connected to the generator. The experimental results show that the performance of bending plate generator is about 4 times as large as that of Savonius wheel. The output per occupied sea area is much higher than other types of generators treated in literatures. The system proposed in this study does not occupy the sea surface and high energy efficiency is expected because the accelerated flow from the slit of breakwater is applied to the generator.

A Study on Removal of Infinitesimal Particles on a Wall by High Speed Air Flow (2nd Report : Performance Evaluation of Low Flow Rate Nozzles)

Kazuhiko SOEMOTO, Tatsuro WAKIMOTO, Takashi Morimoto and Kenji KATOH
J. of JSEM, Vol. 12, pp. 383-390 (2012)

We investigated the removal mechanism for fine particles from a surface using a high-speed air jet. Generally, it is difficult to remove fine particles of the order of micrometers by the impingement of simple air flow because they strongly adhere to the surface by Van der Waals force and remain immersed in the viscous sublayer of the airflow. To overcome this issue, we developed nozzles with triangular cavities that add strong velocity and pressure fluctuations to a high-speed air flow. Previously, we reported that the fluctuations generated in the cavities improved particle removal. In this study, we designed nozzles with a narrower gap width containing cavities, which provide high performance and require a lesser flow rate for efficiently cleaning large surfaces. Experimental results show that the newly designed nozzle 0.2mm-wide nozzle with triangular cavities exhibits a better particle removal rate than previous nozzles, in spite of the flow rate being approximately half of the previous one. In addition, we estimated adherence and removal forces. The dominant removal force is not drag or lift force, but the pressure gradient induced by the impingement of a strongly turbulent air flow. The predicted relation between particle size and particle removal rate from the estimation agrees with the experimental results.

Removal of Fine Particles on a Wall by High-Frequency Turbulence Added Air Flow

Kazuhiko SOEMOTO, Tatsuro WAKIMOTO and Kenji KATOH
International Journal of Flow Control, Vol. 5, No. 1, pp. 47-58 (2013)

A cleaning technique to remove particles of several micro-meter diameter from a surface under dry environmental conditions is greatly needed in the manufacturing processes of LCDs. However, it is usually difficult to remove the fine particles by simple airflow because the particles adhere to the surface by strong forces. For this reason, a cleaning device equipped with a special nozzle is used in the actual industrial process. The nozzle has triangular cavities to add strong high-frequency fluctuations to the airflow. To clarify the effect of this fluctuation on particle removal quantitatively, we measured the airflow velocity, pressure fluctuation on a surface, and removal ratio for four types of nozzles: two varieties cavity nozzles and two straight nozzles with different lengths. The correlation between the intensity of pressure or velocity fluctuation and removal ratio for the cavity nozzles suggests that the turbulent fluctuation added by the cavity contributes to particle removing.

Numerical Simulations of Spontaneous Capillary Rises with Very Low Capillary Numbers using a Front-Tracking Method Combined with Generalized Navier Boundary Condition

Yasufumi TAMAMOTO(Kansai University), Takahiro ITO(Nagoya University), Tatsuro WAKIMOTO and Kenji KATOH

International Journal of Multiphase Flow, Vol. 51, pp. 22-32 (2013)

We propose a front-tracking method that considers a moving contact line with a generalized Navier boundary condition (GNBC) and with a delta function distribution approximated on the grid scale. A method of evaluating the interfacial balance at the contact line in the form of a body force, which is straightforward with the front-tracking method, cannot give a natural flow field. In contrast, the proposed method using the GNBC, which includes the unbalanced Young's force as stress on the wall, can give a very stable and reasonable flow field. The proposed front-tracking method was applied for the capillary rise of a liquid in a tube, in which the velocity-dependent contact angle dominates the dynamic characteristics. The validity of the proposed method was confirmed by comparing simulation results with experimental measurements and simple theoretical models. The results of the present simulations with adjusted non-dimensional slip parameters agreed very well with experimental measurements. Under the present simulation conditions, the linearity of the GNBC allows the correlation between the dynamic contact angle and the contact line's velocity to follow a simple linear expression that involves the difference of the cosine with the capillary number. The non-dimensional slip parameter, which represents the dynamic nature of the moving contact line, can therefore be easily adjusted to reproduce experimental observations under small-capillary-number conditions.

A Study on Removal of Infinitesimal Particles on a Wall by High Speed Air Flow (Effect of Pressure Gradient)

Kazuhiko SOEMOTO, Tatsuuro WAKIMOTO and Kenji KATOH

Proc. of 4th International Conference on Jets, Wakes and Separated Flows, No. 1157, 6pages (2013)

We investigated the removal mechanism for fine particles from a solid wall using a high-speed impinging air jet. The removable rates of particles with 0.3 to 1.5 μm diameters were measured experimentally by the proposed cleaner system, in order to investigate the removal force of the jet flow. In addition, the adhesion force in the tangential direction was measured from the centrifugal force acting on the particles with 5 to 20 μm diameters set on a rotating disk. In a simple theoretical discussion, the drag and lift of the jet flow are insufficient to overcome the adhesion force. Here we consider the pressure gradient fluctuation induced by the impingement of a strongly turbulent air flow. The theoretical estimation shows that the force of pressure gradient could be equivalent to van der Waals adhesive force. The predicted relation can roughly approximate the experimental particle diameter at which the removal force balances with the adhesive force.

A New Method to Actuate a Droplet on a Plate by Use of Laser Irradiation to Improve Wettability (Estimation of Resultant Force Acting on Droplet)

Tatsuuro WAKIMOTO, Yuzo SATO and Kenji KATOH

J. of JSEM, Vol. 13, pp. 19-26, (2013) (in Japanese)

A new method to actuate a small droplet on a plate is proposed. A laser beam is irradiated on one end of the droplet set on a SAMs (Self-Assembled Monolayers) plate. Since the wettability at the heated side is improved remarkably, the tangential component of surface tension pulls the droplet toward the spot of laser beam. In this report, the resultant force in the tangential direction is estimated experimentally when the droplet starts to slide on the plate. In order to obtain the temperature dependence of contact angles, the axi-symmetric droplet profile is measured while irradiating the laser beam homogeneously over the droplet. The temperature is estimated from the surface tension determined from the comparison between the solution of Laplace equation and experimental droplet profile. Based on the measured temperature dependence of contact angles, the resultant of surface tension acting on the circumference of droplet is calculated at both ends of droplet when the laser beam is irradiated on the one end. The calculated results show that the resultant force is actually positive and rapidly increases when the droplet starts to slide.

Development of Wave Power Generation System Using a Vertical Slit Type Breakwater (Waterwheel and Bending Plate Type Generators)

Tatsuuro WAKIMOTO, Shin'ya YOSHIOKA, Takaaki SHIGEMATSU and Kenji KATOH

J. of JSEM, Vol. 13, No. 1, pp. 60-66 (2013) (in Japanese)

A new type of wave power generation system is proposed to be installed in a vertical slit type breakwater. The merits of the system are listed as follows. (i) no occupation of the sea surface, (ii) maintenance facility, and (iii) high energy efficiency by using accelerated flow from the slit of breakwater. In this study, several kinds of water wheels are examined to be installed in a model wave breaker with 1/12 scale ratio to the actual system. The experimental results show that the drag type water wheel (Savonius wheel) has a higher performance compared with the lift type (Darius wheel), since the latter is not accelerated sufficiently during

relatively short period of the sea wave. Based on the result that the drag type is favorable, a new generator is proposed to perform higher efficiency. An elastic rectangular plate connected to a wheel and axle via a string is set in the water. When the wave drag bends the plate, a tension appears in the string and it rotates the wheel connected to a generator. The performance of bending plate generator is examined under various experimental conditions. The results show that a soft textile with zero elasticity has the highest performance. The output per occupied sea area is expected as $23,500(\text{W}/\text{m}^2)$ in the real system, which is much higher than other types of generators treated in literatures.

Instability of a Planar Liquid Sheet Formed with Surfactant Aqueous Solution

Tatsuro WAKIMOTO, Fujii Ryosuke and Kenji KATOH

Proc. of 12th International Conference on Liquid Atomization and Spray Systems, No. 1277b, 8 pages (2012)

In this study, we clarified the growth characteristics of the instability waves of a planar liquid sheet formed with a surfactant solution. It has been widely reported that a liquid sheet jet oscillates in a sinuous shape because of Kelvin–Helmholtz instability, and that the growth rate of the instability wave depends on surface tension. Therefore, if the liquid is a surfactant solution, the growth characteristics depend on time-dependent surface tension, referred to as dynamic surface tension, which originates from the time delay required for the adsorption of surfactant molecules into a newly formed surface. In this study, wave growth affected by dynamic surface tension was investigated. First, the relation between the growth rate of the wave and the time-invariant surface tension was determined by using ethanol aqueous solutions of different concentrations. Second, the dynamic surface tension of the surfactant solution was measured, and surface tension varying in accordance to the distance from the nozzle was estimated. Third, the spatially varying amplitude of the wave was calculated from the results obtained in the above two steps. Finally, the calculated wave amplitude was compared with the measured amplitude of the surfactant solution. The good agreement obtained between the calculated amplitude and experimental amplitude proved that the growth characteristics for a surfactant solution depend on dynamic surface tension.

A Study on Stabilization Mechanism of Thin Liquid Sheet Formed with Surfactant Solution

Tatsuro WAKIMOTO, Hiroki MORI, Kenji KATOH

Proc. of 8th International Conference on Multiphase Flow, No. 288, 5 pages (2013)

To investigate stabilization mechanism of liquid sheets formed with aqueous surfactant solutions (soap films), slight force was applied to the liquid sheet non-invasively, and time variable sheet thickness was measured optically until the rupture of the liquid sheet. The slight force was created using thermo-capillary effect. When the soap film is heated locally with a laser, spatial temperature distribution induces Marangoni force. The Marangoni force pulls the heated spot outward and causes the rupture. The time variations of sheet thicknesses for the anionic and non-ionic surfactant solutions were quite different. In the case of anionic surfactants, sheet thickness, which was set to be $1.5\mu\text{m}$ initially, decreased into less than 100nm gradually at the central part of the heating spot. The ultrathin part less than 100nm expanded for a while, and then ruptured. The quite small thickness may be sustained by electrostatic force, which is active within about 100nm . On the other hand, sheet thicknesses of non-ionic surfactants maintained initial value until just before the rupture in spite of the addition of the Marangoni force. This stiffness of the liquid sheet suggests the existence of yield stress. It is conceived that the adsorbed layer of the surfactant molecules behaves like Bingham fluid.

Three-Dimensional Deformation and Mergence of Waves Caused by Inflectional Instability in a Radial Liquid Sheet

Tatsuro WAKIMOTO and Kenji KATOH

Proc. of 4th International Conference on Jets, Wakes and Separated Flows, No. 1057, 5 pages (2013)

Three-dimensional deformation and merging of instability waves in a radial liquid sheet was clarified. A radial liquid sheet forms when a radially flowing liquid film on a disk emerges from the disk and destabilizes just outside the disk. Such instability is caused by the inflection point in the flow velocity profile, and is therefore referred to as “inflectional instability.” The instability initially generates two-dimensional waves that grow and deform to cause turbulent transition. The three-dimensional deformation of instability waves is similar to that of vortices formed by inflectional instability in a single-phase free shear flow. This suggests that the deformation of the waves is caused by the enhancement of perturbed vortex filaments. However, the waves scarcely merge, whereas vortices in the free shear flow merge frequently. This implies that merging of instability waves in liquid sheets is prevented by surface tension.

Study on a Power-Assist Control of Two-Wheeled Carry Carts Regarding Handle Angle

Yuta FUKUSHIMA and Atsushi IMADU

Journal of Japan Society for Design Engineering, Vol. 48, No. 3 (2013)

The purpose of this research was to develop a power-assist control method for two-wheeled carry carts. First, we analyzed the motion of two-wheeled carts dragged by a human, where we found that drag force can be decomposed into two forces: “force for dragging” and “force for supporting rotation.” Second, we proposed a power-assist control method that determines the motor torque proportional to the horizontal component of the drag force to assist the “force for dragging.” This component is independent to the cart operator’s height. Experiments demonstrate that the use of the proposed power-assist control method reduces the drag force by 70% from that without the control.

Dynamic Stability Analysis of a Flexible Plate Moving in a Parallel Flow

Katsuhisa FUJITA and Toshiaki IMAI

Transactions of the Japan Society of Mechanical Engineers, Vol.79, No.801, C, pp.1336-1347 (2013) (in Japanese)

The dynamic stability of a flexible plate subjected to a parallel flow is investigated when it moves into a flowing fluid. As the flexible flat plates, the papers in a high speed printing machine, the papers discharged by a paper machine, and the thin plastic film, the fluttering flag and the oscillating doom roof caused by wind are enumerated. The fluid is assumed to be treated as an ideal fluid in a subsonic domain, and the fluid pressure is calculated using the velocity potential theory. The coupled equation of motion of a flexible flat plate which is supported simply at both ends is derived into consideration with the added mass, added damping and added stiffness respectively. Changing the velocities of a plate and a fluid, the specifications of a plate as parameters study, the effects of these parameters on the dynamic stability of a plate are investigated. Moreover, it is found this solution shows a good agreement with the already reported experiments in which the flexible flat plate is a paper.

Dynamic Stability of an Elastic Beam Subjected to Axial Fluid Forces Considered to be Follower Forces

Katsuhisa FUJITA, Akihide GOTOU and Tadao KAWAI

Transactions of the Japan Society of Mechanical Engineers, Vol.79, No.801, C, pp.1348-1358 (2013) (in Japanese)

The stability of nonconservative system of a beam is investigated when an elastic beam is subjected to follower forces. The mathematical formulations for a conservative system and a nonconservative system are established. The displacement of a uniform cantilever is assumed to be obtained by superposing the modal functions which are normal modes in a vacuum. The relationships between forces and frequencies for the undamped system and the damped system of the uniform cantilever subjected to a concentrated force and a uniform force are investigated. When the system is subjected to a conservative force, the divergence phenomenon is confirmed to appear first. On the other hand, when the system is subjected to a nonconservative force such as follower force, the flutter phenomenon is confirmed to appear first. And, by changing the structural damping, the destabilized effect due to the structural damping is confirmed. Moreover, the stability of a simply supported beam and a free-free beam are also studied.

Dynamic Stability Analysis of a Flexible Plate Moving in a Parallel Flow

Katsuhisa FUJITA

Proceedings of the ASME 2013 Pressure Vessels and Piping Division Conference, Paris, France, PVP2013-97132 in CD-ROM (2013)

The dynamic stability of a flexible plate subjected to a parallel flow is investigated when it moves in a flowing fluid. The fluid is assumed to be treated as an ideal fluid in a subsonic domain, and the fluid pressure is calculated using the velocity potential theory. The fluid-structure coupled equation of motion of a flexible flat plate supported simply at the both ends is derived. Changing the velocities of a plate and a fluid, the tension acting on a flexible plate, and the other specifications of a plate, the influences of these parameters on the dynamic stability are clarified. It is made clear that the plate moving in a still fluid becomes unstable at slightly lower velocity than the stationary plate subjected to a parallel flow. Moreover, it is found that the present solution shows a good agreement with the already reported experiments in which the flexible flat plate was a paper.

Movement Control Including Localization for a Wheeled Mobile Robot

Tomoki TAJIRI, Yogo TAKADA, Mitsuhiro TAKADA, Tadao KAWAI

Proceedings of the 16th Asia Pacific Symposium on Intelligent and Evolutionary System, 3-6, CD-ROM (2012)

In this paper, we tried the movement including localization for a wheeled mobile robot when a robot is given a start position and a goal position in outdoor environment. When a robot is used in the outdoor environment, a robot should deal with various obstacles, such as uneven road or obstacles above a head, for safety of the user. To express such as an environment, the map was described with three-dimensional. We used the occupancy grid map as the expression method of a map. About the Localization, the particle filter was used. And we applied the Virtual Force Field method to the movement control of the robot. We were able to confirm that a RoboCar estimated the self-position, avoided obstacles and arrived at a goal position in real and simulation environment.

Path Planning for Autonomous Work for Agricultural Mobile Robots with Wheels

Tomoki TAJIRI, Yogo TAKADA, Tadao KAWAI

Journal of the Japanese Society of Agricultural Machinery, Vol.75, No.3, pp.175-180 (2013) (in Japanese)

In this paper, we attempted generating a moveable path from the start to goal positions with mobile robots with wheels. Because agricultural mobile robots with wheels cannot move onto a step due to mechanical factors, we have devised a path planning method which considers the gradient on the ground. Q-learning is one of the methods which is often used for path planning. Using Q-learning, we made a robot learn the optimum path with the smallest gradient on the ground. We performed an experiment using a real robot in an actual environment with steps and slopes, and investigated the effectiveness of this method. The effectiveness of this method was verified from the experiment results.

Analysis of Flow around Robotic Fish by Three-dimensional Fluid-structure Interaction Simulation and Evaluation of Propulsive Performance

Yogo TAKADA, Toshinori OCHIAI, Noboru FUKUZAKI, Tomoki TAJIRI, Tomoyuki WAKISAKA

Journal of Aero Aqua Bio-mechanisms, Vol.3, No.1, pp.57-64 (2013)

The speed-up of robotic fish is hoped to aim at practical use. It is therefore important to develop methods for making such robots swim faster, and computer simulations are invaluable. In this study, a computational simulation model was developed for three-dimensional fluid-structure interaction analysis. The flow around the caudal fin can be analyzed by treating the fin as an elastic body. Experiments were also carried out and good agreement was found between the experimental results and those of the numerical analysis. Moreover, the effects of the flexibility of caudal fin on the robot's propulsive performance were investigated using computational simulations.

Evaluation of Artificial Caudal Fin for Fish Robot with Two Joints by Using Three-dimensional Fluid-structure Simulation

Yogo TAKADA, Noboru FUKUZAKI, Toshinori OCHIAI, Tomoki TAJIRI, Tomoyuki WAKISAKA

Advances in Mechanical Engineering, Hindawi Publishing Co., Vol.2013, Article ID 310432, 9 pages (2013)

A fish robot with image sensors is useful to research for underwater creatures such as fish and so on. However, the propulsion velocity of a fish robot is very slow compared with live fish. It is necessary to swim at a speed several times faster than the speed of current robots for various usages. Therefore, we are searching for the method of making the robot swim fast. The simulation before making robot is important. We have made the computational simulation program of three-dimensional fluid-structure analysis. The flow around the caudal fin can be examined by analyzing the fin as an elastic body. We compared the results of numerical analysis with the results of PIV measurement. Both were agreed well. Because the performance of a fish robot with two joints is better than that of a fish robot with one joint, we searched for excellent fin for the fish robot with two joints by using CFD. We confirmed that the swimming performance of fish robot becomes very good when the caudal fin is rigid except for the root of fin which is comparatively flexible.

Application to Biomedical Measurement Using a Micro Multipoint LDV (For In-Vivo Evaluation in Early-Stage Blood Flow Velocity Images of Malignant Melanoma)

Yogo TAKADA, Tunenobu TERANISHI, Hiroki ISHIDA, Shunsuke AKIGUCHI, Tsugunobu ANDOH, Tadashi HACHIGA

Transactions of the Japan Society of Mechanical Engineers (Ser.B), Vol.79, No.802, pp.1095-1105 (2013) (in Japanese)

We intend to develop a laser Doppler velocimetry (LDV) system for in-vivo imaging that can measure blood flow velocity, that can generate tomograph of blood vessels with information in the depth direction and that has a high spatial resolution to enable individual microvessels. The present system evolved from a multipoint LDV (MLDV) that we developed for performing simultaneous multipoint measurements of water flow in transparent artificial flow channels. In this paper, we suggest an optical component of advanced MLDV for in-vivo and a method to determine the blood flow velocity from the sampling data. We measured microvessels of an experimental mouse, and succeeded in imaging the blood flow velocity in microvessels as 2 or 3 dimensional images. Finally, we demonstrate that using MLDV of blood vessels is useful for diagnosing malignant melanomas by comparison with visual diagnosis by dermoscopy.

Development of a Bridge Inspection Robot Working in Three-dimensional Environment (Evaluation of Driving Performance of a Moving Mechanism with Permanent Magnets)

Yogo TAKADA, Kousuke KIRIMOTO, Tomoki TAJIRI, Tadao KAWAI

Transactions of the Japan Society of Mechanical Engineers (Ser.C), Vol.79, No.805, pp.3135-3146 (2013) (in Japanese)

As for social infrastructures such as a lot of bridges and tunnels that have been constructed in various places since the high economic growth age of postwar days, deterioration is serious. Taking action to the deterioration of infrastructures is desirable. In this study, we aim to develop the robot that can inspect cracks and corrosion in steel bridge substructures. A four-wheel driving robot for trial purposes has been created with the aid of analysis using software DYMOLA. The robot can climb vertically on a steel wall. Strong permanent magnets are installed on the edge parts in the wheels. This robot does not fall by gravitation when it climbs a steel wall or runs along the ceiling upside down. The running performance of the robot is examined by the experiment.

Monitoring of Post-Cure Process of Resin by Optical Fiber Sensors

Tatsuro KOSAKA, Katsuhiko OSAKA and Yoshihiro SAWADA

J. of the Soc. of Materials Science, Japan, Vol.61, No.7 pp.648-653 (2012) (in Japanese).

In the present paper, residual strains in matrix resin were monitored by embedded FBG sensors during room-temperature cure and post-cure processes by applying various temperature profiles. From the experimental results, it was found that final residual strain became smaller if post-cure process started faster. In order to investigate the strain behavior of resin during all cure processes, a viscoelastic FE analysis of resin in which an FBG sensor was embedded was conducted. The strain behavior calculated by the FE analysis agreed very well with the experimental results quantitatively. The FE analytical results showed that strain behavior of the embedded sensor is governed by thermal strain, cure shrinkage strain and viscoelastic properties of resin. Since cure shrinkage strain and viscoelastic stiffness are functions of degree of cure, it can be said that a relationship between degree of cure and heating profile plays the most significant role in generation of the final residual strain. The present technique is useful to predict residual strain of inserts embedded in resin after molding process.

Detection of Debonding in Adhesively Bonded Al-GFRP Joints with Embedded EFPI Fiber Optic Sensors

Katsuhiko OSAKA, Tatsuro KOSAKA and Yoshihiro SAWADA

J. of the Soc. of Materials Science, Japan, Vol.62, No.3 pp.213-218 (2013) (in Japanese).

In the present study, a monitoring technique has been investigated in which debonding of adhesive composite joints is detected using Extrinsic Fabry-Perot Interferometric (EFPI) optical fiber sensors embedded in the adherend. First, strains at the end of the bonded part in adhesively bonded aluminum-GFRP single lap joints were measured using the monitoring system with an EFPI sensor constructed in our laboratory. The initiation and development of the debonding was also observed by eyes in the experiment. Strain analysis was performed for the joint specimens by FEM. These results showed that the strain monitoring system had the ability to measure the change in strains caused by the initiation and development of the debonding at the bonded part. Secondly, the strain monitoring using two EFPI sensors having the different gage length was performed for the same aluminum-GFRP joint specimens. The tensile loading experiments and strain analysis were performed by almost the same procedure as those using one EFPI sensor. These result showed that two EFPI sensors could measure the high and low mean strain at the bonded area corresponding to their gage lengths and detect the change in strain distributions caused by the occurrence and development of the debonding. Therefore, it was found that this monitoring system had the detection ability of the debonding in the adhesively bonded FRP joints.

Development of New Fiber Optic Strain and Vibration Sensors

Tatsuro KOSAKA, Katsuhiko OSAKA and Yoshihiro SAWADA

Trans. Jpn. Soc. Mech. Eng., Ser. C, Vol.79, No.800 pp.908-917 (2013) (in Japanese).

We have developed fiber optic strain and vibration sensors (FOSVS) suited for health monitoring of structures. A fiber optic gap sensor made of multimode fibers, broad-band light, two photo detectors and FBG filter were used to compose the sensor system. The gap sensor was composed of a cantilever fiber and a reflector fiber. The axial displacement of the sensor was measured from the reflected interference signal. The amplitude of the transmitted signal through the reflector fiber was used to measure the transverse vibration of the cantilever fiber. From the experimental and theoretical results, it appeared that the sensor could measure the axial strain and the transverse acceleration correctly. Furthermore it was proven that the sensor characteristic was predictable by simple elastic beam theory. From these results, it can be concluded that the FOSVS sensor has practical capability of simultaneous measurement of strain and vibration

Damage Behavior in Unidirectional CFRP Laminates with Fiber Discontinuity

Hayato NAKATANI, Kenji NAKAYA, Akira MATSUBA, Yousuke KOUNO and Shinji OGIHARA

Trans. Jpn. Soc. Mech. Eng., Ser. A, Vol. 79, No. 799, pp. 294-303 (2013) (in Japanese)

An investigation into damage onset is presented for unidirectional CFRP laminates which contain fiber discontinuities. Complex carbon fiber composite geometry manufactured using prepregs accompanies fiber discontinuities that result from prepreg cutting. Unidirectional CFRP laminates with 2, 4 and 6-ply discontinuity out of 8 plies are loaded in tension, and show lower fracture stress with more discontinuous plies though fracture strains are almost the same. Non-linear strain behavior just above the discontinuity and

discontinuous strain behavior at 20mm away from the discontinuity are found to correspond to onset of crack in resin rich part at discontinuous fiber tip and interlaminar delamination between continuous and discontinuous plies, respectively. Onset stress of these cracks and delamination decreases with the number of discontinuous plies. A shear-lag analysis model that represents the fiber discontinuity in the laminates is proposed, and it is confirmed that obtained stress distribution agrees with that calculated by finite element analysis. Furthermore, it is identified that the onset stress of the two damage modes can be predicted by the shear-lag analysis in which energy release rate is incorporated.

Locating Point of Impact on an Anisotropic Cylindrical Surface using Acoustic Beamforming Technique

Hayato NAKATANI, Talieh HAJZARGARBASHI, Kaita ITO, Tribikram KUNDU and Nobuo TAKEDA
Key Engineering Materials (in the special issue on Structural Health Monitoring: Research and Applications), Vol. 558, pp. 331-340 (2013)

A beamforming array technique with four sensors is applied to a cylindrical geometry for detecting point of impact. A linear array of acoustic sensors attached to the plate record the waveforms of Lamb waves generated at the impact point with individual time delay. A beamforming technique in conjunction with an optimization scheme that incorporates the direction dependent guided Lamb wave speed in cylindrical plates is developed. The optimization is carried out using the experimentally obtained wave speed as a function of propagation direction. The maximum value in the beamforming plot corresponds to the predicted point of impact. The proposed technique is experimentally verified by comparing the predicted points with the exact points of impact on a cylindrical aluminum plate and a cylindrical composite shell. For randomly chosen points of impact the beamforming technique successfully predicts the location of the acoustic source.

Damage Behavior in Hybrid Thin-Titanium Film Composite Laminates for Bolted Joints

Hayato NAKATANI, Tomoki YAMADA, Yuhei NEKOSHIMA and Shinji OGIHARA
Proc. of the 15th U.S.-Japan Conference on Composites Materials, Arlington, Texas, USA, October 1-3, 2012, Paper No.129 (9 pages) (CD-ROM), (2012)

Fiber-metal laminates that consist of carbon fiber composites and thin titanium films are applied to bolted joint to obtain better bearing strength and reliability. Tensile tests for bolted joints in quasi-isotropic CFRP laminates $[45/0/-45/90]_{2S}$ and the hybrid laminates with five thin titanium films inserted to the CFRP plates are conducted. It has been found that load drop point in load – displacement curve corresponds to damage onset in the plate. As for the CFRP plate the micro-buckling of the carbon fiber in 0° layer (fiber kinking) occurs first and then matrix shear cracking in adjacent layers induced by the kinking follows. The propagation of the matrix shear cracking, on the other hand, is found to be prevented by the titanium films in the hybrid laminates. With the titanium films inserted to form sandwich with inner 0° layer lower damage level is presented compared to the plate with the outer 0° layers are sandwiched by the films since the shear matrix cracking propagates from inside toward surface.

Effect of Constituent Ply Thickness on Mechanical Properties in CFRP Angle-Ply Laminates

Shinji OGIHARA and Hayato NAKATANI
Proc. of the 15th U.S.-Japan Conference on Composites Materials, Arlington, Texas, USA, October 1-3, 2012, Paper No.121 (12 pages) (CD-ROM), (2012)

This paper deals with mechanical property and damage evolution in CFRP symmetric angle-ply laminates with different constituent ply thicknesses. $[(\pm 45)]_S$ angle-ply laminates with the same total laminate thickness but different constituent ply thicknesses which ranges from 0.6mm to 0.05mm are considered. It is found that as the constituent ply thickness decreases, the laminate strength and failure strain increase. The damage evolution behavior is also investigated. An attempt is made to predict the nonlinear stress-strain behavior considering the change in fiber angle.

Mechanical and Thermal Properties of Woven Jute Fabric Reinforced Poly(Butylene Succinate) Laminated Biocomposites

Huu Nam TRAN, Shinji OGIHARA, Hayato NAKATANI, Satoshi KOBAYASHI and Ken GOTO
Proc. of the 8th Asian-Australasian Conference on Composite Materials (ACCM8), Kuala Lumpur, Malaysia, November 6-8, 2012, Paper No. O-NAT-330 (6pages) (CD-ROM), (2012)

In present research, woven jute fabric reinforced poly(butylene succinate) (PBS) laminated biocomposites were developed. These biocomposites were fabricated by compression-molding of sandwiching 4 to 6 jute fabric layers between 5 to 7 layers of PBS sheets. The effect of alkali and combined alkali and silane surface

treatment on the mechanical and thermal properties of jute fabric/PBS biocomposites was investigated. The mechanical properties of surface treated jute fabric/PBS biocomposites were significantly higher than those of untreated ones. Compared with alkali treatment, the combined alkali and silane treatment showed better mechanical properties of jute fabric/PBS biocomposites. The highest mechanical properties of jute fabric/PBS biocomposite with 6 fiber layers were achieved in this study. Fractured surface morphologies of composite specimens exhibited an improvement of interfacial fiber-matrix adhesion in the laminated biocomposites reinforced with surface treated jute fabric. Thermal stability of jute fabric/PBS biocomposites was remarkably to be intermediate between PBS resin and jute fabric. Surface treated jute fabric/PBS biocomposites having good fiber-matrix adhesion resulted in stable composites with better thermal stability than untreated ones.

Effect of Constituent Ply Thickness on Nonlinear Mechanical Response in CFRP Angle-Ply Laminates

Shinji OGIHARA, Hayato NAKATANI and Yasuo KOGO

Proc. of the 8th Asian-Australasian Conference on Composite Materials (ACCM8), Kuala Lumpur, Malaysia, November 6-8, 2012, Paper No. O-MEC-030 (6pages) (CD-ROM), (2012)

The mechanical behavior and damage behavior in CFRP angle-ply laminates with different constituent ply thickness under tensile loading are experimentally evaluated. It has been found that as the constituent ply thickness decreases, the strength and failure strain increases. Difference in damage behavior is also observed. The preliminary results of finite strain viscoplasticity model for laminated composites are shown. It is necessary to implement the damage model into the theory.

Acoustic Emission Measurement Using an FBG Ultrasound-Detection System Incorporating a Fiber Ring Laser

Hiroshi TSUDA, Atsushi TOYAMA, Kenji KUMAKURA, Hayato NAKATANI and Shinji OGIHARA

Progress in Acoustic Emission XVI (Proc. of the 21st International Acoustic Emission Symposium (IAES21)), The Japanese Society for Non-Destructive Inspection, Okinawa, Japan, November 27-30, 2012, pp.127-132, (2012)

A compact FBG ultrasound-detection system incorporating a fiber ring laser is applied to AE measurement of a CFRP and the results are compared with that detected with a piezoelectric sensor. Owing to large background noise level, the FBG sensor system has to set a 20 dB higher threshold level for AE data acquisition than the conventional system with a piezoelectric sensor. However, the FBG sensor has detected the initial AE at the identical time where the piezoelectric sensor detects. Furthermore, both sensors have detected similar AE behavior such as cumulative AE hits and AE amplitude distribution during the test. The AE measurement test has demonstrated that the FBG sensor system could monitor microscopic fracture process of a CFRP comparable with the conventional piezoelectric sensor system.

Damage Behaviour in Quasi-isotropic CFRP Laminates with Small Fibre Orientation Mismatch

Hayato NAKATANI and Shinji OGIHARA

Proc. of the 19th International Conference on Composite Materials (ICCM19), Montréal, Canada, July 28 - August 2, 2013, pp. 3933-3940, (2013)

Mechanical properties and damage behaviour under tensile, out-of-plane indentation and impact are evaluated for the quasi-isotropic (QI) CFRP laminates with small fibre orientation angle mismatch of 15° that consists of thin plies, and these are compared to that of the conventional QI laminates with 45° mismatch. The small mismatch exhibits more isotropy also in tensile strength while the conventional laminates failed much lower stress when they are loaded in inclined direction such as 15° and 22.5°. The laminates with small mismatch have appropriate fibre plies that align at nearly the same direction with any load, then the strength of the carbon fibres effectively work and contribute the strength of the plate. Under out-of-plane indentation loading, it is found that the indenter penetrates the small mismatch laminates in brittle manner with localized damage near the indented point after showing higher maximum load while matrix cracking and delamination occurred in broad area in the conventional QI laminates. Same tendency that localized damage is observed in the small mismatch laminates under drop-weight impact load, however absorbed energy during the impact event are comparable between the small mismatch and conventional QI laminates.

Evaluation of Bearing Damage Behavior in Thin Titanium Films-CFRP Hybrid Laminate

Tomoki YAMADA, Hayato NAKATANI and Shinji OGIHARA

Proc. of the 19th International Conference on Composite Materials (ICCM19), Montréal, Canada, July 28 - August 2, 2013, pp. 5873-5880, (2013)

This paper introduces the fibre-metal laminates using thin titanium films to the composite bolted joints to improve joint strength and bearing damage behavior. Tensile tests for bolted joints in quasi-isotropic CFRP laminates have demonstrated that the out-of-plane fiber kinking in 0° ply occurs and the matrix shear cracking in adjacent layers is induced by the kinking. As for the thin titanium films - CFRP hybrid laminates the matrix shear cracking is prevented from propagating into adjacent layers because of the titanium films. The overall damage level in the hybrid laminates is found to keep low when the titanium films sandwiched the inner 0° layers rather than outer. Stacking sequence which the titanium films sandwiched the inner 0° layers also results in damage onset in higher normalized load compared to the other FML specimens.

Mechanical Behavior of Thin Titanium Films / CFRP Hybrid Laminates containing Transition Region

Yuhei NEKOSHIMA, Daiki MITSUMUNE, Hayato NAKATANI and Shinji OGIHARA

Proc. of the 19th International Conference on Composite Materials (ICCM19), Montréal, Canada, July 28 - August 2, 2013, pp. 5939-5946, (2013)

The effects of four different patterns of the transition region where volume fraction of titanium films gradually changes in the titanium films / CFRP hybrid laminates with various stacking sequence on mechanical behavior are evaluated by tensile tests and 4 point bending tests. Tensile tests have shown that the hybrid laminates in which inner 0° plies are sandwiched by the titanium films and staggered layout of the film edges is adopted in the transition region have the highest tensile strength. With microscope observation it has been found that delamination occurs between the titanium films and 90° plies, however, the delamination can be suppressed by inserting the titanium films adjacent to 0° plies. 4 point bending tests have shown that the highest bending strength is achieved by the transition region pattern that has staggered layout of the film edges. With titanium films inserted near the outermost layer, the hybrid laminates fail in buckling at compression side due to the delamination of the films resulting in lower bending strength.

Modeling of Mechanical Response in CFRP Angle-ply Laminates

Shinji OGIHARA and Hayato NAKATANI

Proc. of the 19th International Conference on Composite Materials (ICCM19), Montréal, Canada, July 28 - August 2, 2013, pp. 7268-7276, (2013)

The mechanical behavior and damage behavior in CFRP angle-ply laminates with different constituent ply thickness under tensile loading are experimentally evaluated. It is found that as the constituent ply thickness decreases, the strength and failure strain increases. The preliminary results of finite strain viscoplasticity model considering the damage effect for laminated composites are shown. A qualitative agreement is obtained.

Difficulties Associated with the Acoustic Source Localization in Anisotropic Plates and its Solution

Hayato NAKATANI, Tribikram KUNDU, Kaita ITO and Nobuo TAKEDA

Proc. of the 9th International Workshop on Structural Health Monitoring 2013: A Roadmap to Intelligent Structures, Stanford University, CA, USA, September 10-12, 2013, pp. 2651-2658 (2013)

Acoustic source localization technique for anisotropic plates proposed by the authors in an earlier publication is applied here to a carbon fiber composite laminate. Difficulties associated with this technique are investigated. It is noted that the accuracy of this technique depends strongly on the accuracy of the measurement of the time delays in recorded signals by three receiving sensors placed in close proximity in the sensor cluster. The sensor cluster is needed to obtain the direction of the acoustic source without knowing the material properties of the plate. It is proposed here that to obtain the accurate time delays not the full time histories but only the beginning part of every time history (the first dip and peak) should be taken for the subsequent steps of signal processing. With these modifications improved predictions are obtained.

Development of Advanced Materials for Spallation Neutron Sources and Radiation Damage Simulation Based on Multi-scale Models

M. KAWAI, H. KURISHITA, H. KOKAWA, S. WATANABE, N. SAKAGUCHI, K. KIKUCHI, S. SAITO, T. YOSHIE, H. IWASE, T. ITO, S. HASHIMOTO, Y. KANEKO, M. FURUKAWA, and S. ISHINO

J.Nucl.Mater., Vol.431 pp. 16-25 (2012).

This report describes the status review of the JSPS Grant Team to develop advanced materials for the spallation neutron sources and modeling of radiation damage. One of the advanced materials is a toughness enhanced, fine-grained tungsten material (W-TiC) having four-times larger fracture toughness than ordinary tungsten and appreciable RT ductility in the recrystallized state. The other is an intergranular crack (IGC)-resistant austenitic stainless steel which was processed by the grain-boundary engineering (GBE). The

experimental results are devoted to corrosion in a lead–bismuth eutectic, arrest of corrosion of weld-decay, radiation damage and creep rupture as well as new technique of GBE using a laser and annealing procedure. New technique seems to be applicable to large or complicated-shaped components. A series of the multi-scale models is built up from nuclear reaction between incident particles and medium nuclei to material property change due to radiation damage. Sample calculation is made on 3 mm thick nickel bombarded by 3 GeV protons.

Cluster Analysis of Acoustic Emissions Measured during Deformation of Duplex Stainless Steels

R. TAKEDA, Y. KANEKO, D.L. MERSON and A. VINOGRADOV

Mater. Trans., Vol. 54 pp.532-539 (2013)

Aiming at better understanding of the deformation mechanisms involved into plastic deformation of duplex stainless steels, acoustic emission (AE) measurements were performed during room temperature tensile deformation of model steels and alloys with different phase structure including single phase α Fe30Cr and γ SUS316L steels and duplex α – γ SUS329J4L, Fe24Cr6Ni alloys. The real time AE investigations were complemented by microscopic investigations of deformed microstructures. The quantitative AE analysis revealed different AE patterns which were correlated with underlying deformation mechanisms and microstructural transformations. The cluster analysis of AE power spectral densities has been proven effective in revealing specific groups of signals (clusters) which appear on different deformation stages in different steel variants, which can be correlated with involved source mechanisms of plastic deformation and microstructural processes including dislocation slip in either fcc or bcc lattice of γ or α phase, respectively, twinning in the SUS 316L steel and γ – α' A martensitic transformation in the Fe24Cr6Ni model alloy.

Cyclic Response of SUS316L Stainless Steel Processed by ECAP

Y. KANEKO, S. HAYASHI and A. VINOGRADOV

Mater. Trans., Vol. 54 pp.1612-1618 (2013)

The cyclic response of the SUS316L stainless steel with the nanostructure induced by profuse twinning during equal channel angular pressing (ECAP) at 423K was investigated with the focus on the shape of the hysteresis loops and their evolution with cycling. The SUS316L steel with the nanostructured twins showed a very high stress amplitude if compared to their conventional counterparts. However, unlike the as-quenched specimens, the ECAPed SUS316L steel revealed considerable cyclic softening at plastic strain amplitudes above 2×10^{-4} . Besides, the ECAPed specimens showed characteristic stress asymmetry behavior during fatigue. At the initial stages of the fatigue tests, a tensile peak stress of the hysteresis loop was higher than a compressive one. Then, the tensile peak stresses gradually decreased with increasing cycles and finally became lower than the compressive peak stress under plastic strain amplitudes higher than 2×10^{-4} . Since no stress asymmetry was detected for the as-quenched sample, the observed stress asymmetry behavior was attributed to the specific asymmetric response of the directionally sheared microstructure created during ECAP.

Modelling of Severe Plastic Deformation: Time-Proven Recipes and New Results

Y. ESTRIN and A. VINOGRADOV

Microstructural Design of Advanced Engineering Materials, (D. Molodov editor), Wiley-VCH Verlag GmbH, Weinheim, Germany, pp. 69-90 (2013)

We discuss microstructure-related constitutive models, which have the capability to describe and predict the mechanical behaviour of metals and alloys at large strains. The modelling frame is provided by a mathematical description of the dislocation density evolution. Depending on the complexity of the model, various features of the microstructure development under large strain deformation are captured. The main target of this paper is severe plastic deformation (SPD) underlying a group of metal processing techniques which lead to extreme grain refinement and substantial gains in strength. Results of numerical simulations of such processes demonstrating the potential of the microstructure-based models as a powerful tool for SPD process design are presented. Some outstanding problems relating to modelling of SPD processes are outlined.

Stages of Fracture Process in a Hydrogen Embrittled High Strength Steel using Acoustic Emission Technique

D. MERSON, M.M. KRISHTAL, D.L. MERSON, A.A. EREMICHEV and A. VINOGRADOV

Deformation and Fracture Vol.9 pp. 41-48 (2012)

Primary sources of acoustic emission (AE) during slow monotonic loading of smooth specimens of hydrogenated steel 70 are revealed and associated with brittle cracking along austenitic grain boundaries or sulphides. The fracture process is composed of five stages including the incubation period (I), stage of increasing rate of damage accumulation (II), overall stable crack growth (III) followed by damage rate reduction (IV) preceding the critical stage corresponding to formation and propagation of a catastrophic crack (V).

Comparative Spectral Analysis of Noiselike Acoustic Signals During Monitoring and Diagnostic of Industrial Facilities

I.A. RASTEGAEV, D.L.MERSON, I.I. RASTEGAEVA, A.V. CHUGUNOV and A.Yu. VINOGRADOV
Control. Diagnostics. Vol.10 pp.80-87 (2012)

A method for signal categorization of continuous noise-like acoustic emission (AE), which is recorded during monitoring and diagnostics of industrial facilities, is described. The method is based on calculation of the power spectral density of short yet statistically representative realizations of the signal followed by a quantitative statistical comparison of normalized spectral densities for each realization. The coefficient of approximation R^2 is used as a similarity criterion, which has been proven effective for AE analysis during mechanical testing of materials. Several examples give evidence that the proposed method can be an effective addition to traditional approaches for AE signal processing for integrity testing of pressure vessels, tribological systems and for control over various mixing rotor devices.

A Real-Time Approach to Acoustic Emission Clustering

E. POMPONI and A. VINOGRADOV,

Mechanical Systems and Signal Processing, Vol.40, pp.791–804 (2013)

A common target of clustering in acoustic emission (AE) non-destructive inspection technique (NDT) is to distinguish between the sources of different origin and to get a deeper insight into the interrelation between the underlying processes such as plastic deformation, crack initiation, corrosion cracking, etc. The major drawback of the most popular conventional schemes such as k -means and fuzzy c -means is that they are iterative in nature, which hinders their real-time applications. Inspired by the sequential k -means procedure, i.e. a non-iterative variant of the classic k -means, we present a novel classification technique designed for real-time applications. The proposed approach is “non-supervised”, i.e., both the number of clusters and their elements are inferred from the data distribution in a multi-dimensional metric space. In its present form the approach is capable to adopt various dissimilarity measures to compare AE power spectral densities. A series of tests on different probing datasets has been performed to prove the efficiency of the proposed approach.

Extreme Grain Refinement by Severe Plastic Deformation: A Wealth of Challenging Science

Y. ESTRIN and A.VINOGRADOV

Acta Materialia Vol.61 pp.782–817 (2013)

This article presents our take on the area of bulk ultrafine grained materials produced by severe plastic deformation (SPD). Over the last decades, research activities in this area have grown enormously and have produced interesting results, which we summarise in this concise review. It is intended as an introduction to this field for the ‘uninitiated’, while at the same time highlighting some polemic issues that may be of interest to those specialising in bulk nanomaterials produced by SPD. A brief overview of the available SPD technologies is given, along with a summary of unusual mechanical, physical and other properties achievable by SPD processing. The challenges this research is facing – some of them generic and some specific to the nanoSPD area - are identified and discussed.

Fabrication of Porous Hydroxyapatite Ceramic Scaffolds with High Flexural Strength Through the Double Slip-Casting Method Using Fine Powders

Yin Zhang, Deshuang Kong, Yoshiyuki Yokogawa, Xia Feng, Yaqiu Tao and Tai Qiu

J.Am.Ceram.Soc., 95 [1], pp.147–152 (2012)

A new technique of twice combining the slip-casting and polymer sponge methods using a slip with different viscosity is introduced in the study to prepare bimodal pore size hydroxyapatite scaffolds, which provides a better control over the microstructures of scaffolds and enhances their mechanical properties. With the technique, we were able to produce scaffolds with mechanical and structural properties that cannot be attained by either the polymer sponge or slip-casting methods alone, or by the polymer sponge and slip-casting once method.

The flexural strength of porous ceramics scaffolds should depend on porous framework. In this study, a new approach combining the twice slip-casting and polymer sponge methods to fabricate porous HAp scaffolds was developed that has the combined advantages of both the methods. A flexural strength of 73.3 MPa for the scaffold with porosity of 52.5% was developed. The resultant bimodal porous HAp ceramics scaffolds should show very high flexural strength. This study shows that the bimodal pore structure of an HAp scaffolds obtained could be potentially suitable for applications as a biomedical bone replacement material.

TEM Observation of Biomolecules on/in Mesoporous SBA-15

Yoshiyuki Yokogawa, Akira Saito, Naoki Ogawa, Atsutomo Nakamura, and Ippei Kishida

Key Engineering Materials, 493-494, pp 728-731 (2012)

The encapsulation and immobilization of biomolecules on/in mesoporous silica materials (MPS) have been studied by using transmission electron microscopy (TEM). The mixture of tetraethyl orthosilicate (TEOS) and the triblock copolymer as a template was stirred, hydrothermally treated to form the mesoporous SBA-15 structure, and heat-treated at 550 °C. SEM observation indicated that long and narrow particles were linked together in the long axis direction to form secondary particles of SBA-15. UV-spectrometry was performed to determine the amount of bovine serum albumin (BSA), cytochrome C, myoglobin or β -lactoglobulin encapsulated on/in SBA-15. The time profiles for adsorption of proteins can be well described by intraparticle diffusion model. The TEM observations of proteins on/in mesoporous SBA-15 revealed that proteins were embedded on/in mesoporous SBA-15 and the protein behaviors given by TEM observations may correspond to the intraparticle diffusion model.

Synthesis and Characterization of Iron Oxide Embedded Hydroxyapatite Bioceramics

Ereath Beeran Ansar, Manmadhan Ajeesh, Yoshiyuki Yokogawa, Wilfried Wunderlich and Harikrishna Varma

J. Amer. Ceram. Soc., 95 [9], pp. 2695–2699 (2012)

A homogeneous dispersion of nano iron oxide (IO) crystallites inside the hydroxyapatite (HA) particles was achieved by a co-precipitation method. This highly stable colloidal dispersion of magnetic nano composite (HAIO) was made without the use of any surfactants. The *in situ* generated dispersion of the composite powders showed submicron HA particles with ~5 nm iron oxide inside. The phase analysis results showed the presence of hydroxyapatite (HA) and iron oxide with no tertiary phase. The enhancement of relative peak intensities with increased percentage of iron oxide phase in X-ray diffraction analysis suggests the formation of iron oxide together with HA without affecting the phase purity of the latter, which is important when the biological behavior of HA is concerned. This also confirms the quantitative nature of the precipitated nanocomposites. The High Resolution Transmission Electron Microscope (HRTEM) of the composite shows elongated crystal flakes or platelike surfaces of HA crystallites having particle sizes in the range 70–100 nm. HRTEM with XRD analysis matches HAIO only with iron oxide particles of Magnetite (Fe₃O₄) and HA phases. The FTIR data confirm that the introduction of iron oxide did not produce any considerable change in the chemical structure of HA.

VSC Adsorptive Properties into Ion Exchanged Zeolite Materials in Gaseous and Aqueous Medium

Y. Yokogawa, M. Sakanishi, N. Morikawa, A. Nakamura, I. Kishida and H.K. Varma

Procedia Engineering, 36, pp.158-172 (2012)

The microporous materials, zeolite, were synthesized and the H₂S adsorption into microporous material was studied. Zeolite has three dimensional framework structure in which SiO₄ and AlO₄ tetrahedrons are bonded, and generally contains alkali metal or alkali-earth metal atoms as univalent or bivalent cations. These electrostatic effect results in the surface potential of zeolite materials, and may influence the adsorptive properties. Two kinds of zeolite materials, LTA (Zeolite A) and MFI (ZSM-5), which have different Si/Al ratios, were synthesized by a wet method. Some starting materials were dissolved in water, and the mixture was heated, filtered, washed, and dried. The Ag-doped zeolite materials were prepared as follows. The sample was put into 2M silver nitrate solution and stirred. The obtained specimen was filtered and washed with water, then dried at 90°C for 24 hrs. The samples, identified by powder X-ray diffraction method, were put into a 5 L glass flask filled with H₂S gas. The initial concentration of H₂S was 30 ppm. When 0.02 g of LTA was applied, the concentration of H₂S fell to 84% for first 2 hours, and was decreased with time. The equilibrium did not seem to reach even for 24 hours. The amount of LTA was increased to be 0.2 g, and then the concentration of H₂S was decreased to be less than 20 % for 24 hrs. In case of Ag-doped LTA, the concentration of H₂S dropped to be 24 % for 2 hrs and to be almost 0 % for 4 hrs. The exchanges of alkali metal or alkali-earth metal atoms to univalent or bivalent metal ions zeolite material remarkably improves

the H₂S reduction. The amount of adsorbed H₂S onto LTA was larger than onto MFI. The difference in the amount of adsorbed H₂S between two types of zeolites can be explained by the surface potential. Polarity of zeolites depends on their Si/Al ratio. XRD patterns of the LTA and H₂S adsorbed LTA specimens seem to be almost identical, and the peaks corresponding to Ag₂S were not observed. So sulfur may be included in zeolite structure. The XRD analysis should be investigated in great detail for further study. H₂S in aqueous medium was also found to adsorb into microporous material, which was confirmed by the headspace gas chromatography with flame photometric detector. The microporous material should be expected to be an adsorbent material, useful for health in mouth.

Synthesis, characterization and in vitro studies of zinc and carbonate co-substituted nanohydroxyapatite for biomedical applications

G. Suresh Kumar, A. Thamizhavel, Y. Yokogawa, S. Narayana Kalkura, and E.K. Girija

Materials Chemistry and Physics, 134 [2–3], pp.1127–1135 (2012)

Ionic substitutions have been proposed as a tool to improve the properties of hydroxyapatite (HA). Zinc and carbonate co-substituted HA have been synthesized by precipitation method and characterized by XRD, FT-IR, XRF, FESEM and TEM. Comparative studies were carried out with HA, zinc substituted HA and carbonate substituted HA. Zinc substituted HA exhibited less dissolution and apatite forming ability but more decomposition into TCP at 1400 °C when compared with carbonate substituted HA. When zinc is co-substituted with carbonate it exerted a control over the apatite forming ability of HA which was found to lie in between the individual substituted samples without compromising the dissolution behavior of CHA. Also, decomposition was reduced to a greater extent. Hence tailoring the properties of HA to the desired extent can be achieved by simultaneous substitution of zinc and carbonate.

Role of material processing on the sinterability and thermal stability of nanocrystalline hydroxyapatite

E.K.Girija, G.Suresh Kumar, A.Thamizhavel, Y.Yokogawa, S.Narayana Kalkura,

Powder Technology 225 (2012) 190-195, Impact factor- 2.080, Elsevier.

Ultrasonic irradiation and freeze drying assisted wet precipitation method is found to offer HA with reduced particle size, low crystallinity and less agglomeration. Sintering of this HA exhibited high crystallinity, enhanced sinterability and thermal stability (Up to 1100°C) than the HA obtained by the conventional route.

The VSC adsorption on hydroxalcite through topochemical reactions

Yoshiyuki Yokogawa, Yutaro Yagi, Hroya Sano, Atsutomo Nakamura, and Ippei Kishida

Key Engineering Materials, 529-530, pp 650-653 (2013)

Volatile sulfur compounds (VSCs) such as hydrogen sulfide (H₂S), methyl mercaptan and dimethyl sulfide produced in mouth. Some oral (Gram-negative) bacteria produce VSCs, which induces permeability of mucous membrane, cause the oral malodor, dental caries, color change of the dental fillings. Thus, material which adsorbs VSCs should be useful to keep health in mouth. Previously, we reported the H₂S adsorptive properties of zeolite and hydroxalcite materials having micro pores. The amount of H₂S adsorbed on the zeolite or hydroxalcite at room temperature was found to be around 300-400 ppm, and and 3 % of H₂S was desorbed when heated at 400 °C. The hydroxalcite, whose composition is Mg_{1-x}Al_x(OH)₂A_x/n·mH₂O, where A is CO₃²⁻, and x is 0.25, was heat-treated at 500 °C, and put into aqueous solution containing H₂S. In this study, the relation between heat-treatment temperature and the sulfide adsorption on hydroxalcite in aqueous solution was investigated. The hydroxalcite materials were hydrothermally synthesized and identified by powder X-ray diffraction method. The change in concentrations of H₂S in aqueous solution was measured using FPD gas chromatography (GC). The concentrations of H₂S was decreased with time for the hydroxalcite heated at 500 °C or 600 °C, and fell to 20 % for 12 hours. But, the concentration was decreased by 40% for 12 hours for the hydroxalcite materials heated at higher temperature. XRD and FT-IR analysis revealed that the sulfides were into or out of the hydroxalcite structure through topochemical reactions.

Time-dependent protein adsorptive behavior on/in mesoporous silica materials

Yoshiyuki Yokogawa, Yuta Yamato, Shinji Ito, Atsutomo Nakamura, and Ippei Kishida

Key Engineering Materials, 529-530, pp 646-649 (2013)

The time – dependent adsorptive behavior of biomolecules on/in mesoporous silica materials (MPS) have been studied by using transmission electron microscopy (TEM). Highly ordered hexagonal mesoporous silica materials (SBA-15) synthesized were immersed in phosphate buffer saline (PBS) solution containing cytochrome C for 2, 48, and 120 hours at 4 °C. After that, MPS materials were rinsed with PBS solution, and then immersed in PBS solution without cytochrome C. The amount of protein adsorbed on/in MPS materials

soaked for 2, 48, and 120 hours was 75 mg/g, 135 mg/g and 178 mg/g, respectively. The time profiles for adsorption of proteins can be well described by intraparticle diffusion model. The holes of MPS materials were observed to be overlapped with stained proteins for first 2 hours immersion. The stained proteins were observed between primary particles and partly inside the mesoporous channels in the MPS material immersed for 48 hours. For MPS immersed for 120 hours, stained proteins were observed in almost all meso-scale channels of MPS. The ratio of desorbed proteins from those embedded on/in MPS materials was 13 % in case of the MPS materials immersed in PBS containing cytochrome C for 2 hours, while 8 % in case of the MPS materials immersed for 48 and 120 hours. Cytochrome C may be strongly embedded on/in MPS materials due to the electrostatic effect.

Dissolution properties of different compositions of biphasic calcium phosphate bimodal porous ceramics following immersion in simulated body fluid solution

Yin Zhang, Jianan Ai, Dinggai Wang, Zhongrong Hong, Wenhui Li, Yoshiyuki Yokogawa
Ceram.Int., Available online 16 February 2013

Biphasic calcium phosphate (BCP) bimodal porous ceramics were prepared from a mixture of fine powders of hydroxyapatite (HAp) and beta-tricalcium phosphate (β -TCP) with varying HAp/ β -TCP ratios. Two types of HAp powders and one type of β -TCP powder were used to produce porous BCP bioceramics with HAp/ β -TCP weight ratios of 20/80, 40/60, and 80/20. Dissolution tests were performed to compare the dissolution properties of BCP-based bioceramics with different structural properties. Porous ceramic samples of approximately 0.5 g were individually soaked in 30 ml of simulated body fluid (SBF) solution at 36.5 °C for 1, 3, 7 and 10 days, respectively. The calcium content of the SBF solution was analyzed by ICP. The porous bodies were filtered, dried, and characterized using SEM, XRD, and FT-IR. The results indicate that the sample structural properties seem to have a greater effect than the storage environment on the dissolution properties.

Layered double hydroxide ceramic materials and its H₂S incorporation through topochemical reactions

Y. Yokogawa, H. Sano, I. Kishida,
J. Ceram. Soc. Jpn., 121(9), pp.788-791(2013).

Oral malodor is produced by microbial putrefaction of food debris, resulting in the formation of volatile sulfur compounds (VSCs), such as hydrogen sulfide (H₂S) and methyl mercaptan, produced in the mouth. VSCs also have a bad influence on the periodontium and cause discoloration of dental alloy. Thus, an adsorbent that highly adsorbs VSCs would be useful for a healthy mouth and may prevent tooth decay. We investigated the possibility of adsorbing H₂S using heat-treated Magnesium aluminum hydrotalcite. We found that H₂S is adsorbed onto heat-treated hydrotalcite materials in an aqueous solution using gas chromatography with a flame photometric detector (FPD/GC), and the sulfide was found between the layers of the hydrotalcite structure by conducting a powder X-ray diffraction (XRD) analysis and using infrared spectroscopy (FT-IR). The amounts of adsorbed sulfide were higher for hydrotalcite heat-treated at 500 and 600°C for 30 min. The hydrotalcite material is expected to be an adsorbent material and useful for maintaining good oral hygiene.

Pulsed laser deposition of hydroxyapatite on nanostructured titanium towards drug eluting implants

P. Rajesh, N. Mohan, Y. Yokogawa, H. K. Varma, *Mater. Sci. Eng. C*, 33(5), pp.2899-904(2013).

(HA) ceramic. The nanostructured surfaces achieved by anodization were capped with HA crystallites by pulsed laser deposition. The implant substrates were studied for their drug carrying capacity using gentamicin as a model. The nano-tubular surface with HA coating had better drug loading capacity of about 800 $\mu\text{g}/\text{cm}^2$ gentamicin while the bare anodized substrate carried less than 660 $\mu\text{g}/\text{cm}^2$. The HA coating alone stored as low as 68 $\mu\text{g}/\text{cm}^2$ and released the drug within the initial burst period itself. The ceramic coated anodized substrates were found to be more efficient in controlled delivery for longer than 160 h with a drug release of 0.5 $\mu\text{g}/\text{cm}^2$ even towards the end. The substrate with nanostructuring alone delivered the whole drug within 140 h. This study proposes the application of laser deposition of HA over nanostructured titanium, which proves to be promising towards controlled drug eluting bioceramic coated metallic prostheses.

Effect of Crosslink Density on Nonlinear Stress-Strain Behavior of Epoxy Glasses Subjected to Large Deformation

Shin'ya YOSHIOKA and Yuichiro YOKOYAMA

J. Soc. Mat Sci, Jpn, Vol.62, pp.22-26 (2013). (in Japanese)

Effects of crosslinked molecular structures in glassy epoxy networks on the nonlinear viscoelastic behavior have been studied in terms of strain-induced structural change. We prepared four epoxy glasses with different crosslink densities from the same epoxy precursor by controlling fractions of chain-extender and crosslinker in curing agents. The epoxy glasses were subjected to uniaxial compression at a temperature 18K below the glass transition temperature of each sample. With increasing crosslink density, initial elastic moduli and yield stresses decreased, whereas flow stresses appearing after the strain softening almost unchanged, except for the most tightly crosslinked sample showing lower flow stresses. Results of density measurement and DSC showed that an increase in the crosslink density made the glassy structures more unstable. These results show that unstable glassy structures due to constraints on segmental mobility introduced by crosslinked molecular structures lessen the initial elastic modulus and the yield stress. On the other hand, the variation of crosslink density had almost no effect on the flow stresses of the glasses. This observation presumably indicates that molecular crosslinks have little effect on the strain-induced structural change. When the crosslink density comes to quite high, however, the crosslinks are likely to start affecting the flow stress, i.e. strain-induced unstable glassy structures.

Applied Physics and Electronics

Detection of a Coherent Longitudinal Optical Phonon in a GaAs Buffer Layer Optically Covered with a GaSb Top Epitaxial Layer Using Terahertz Spectroscopy

H. TAKEUCHI, S. TSURUTA, and M. NAKAYAMA

AIP Conf. Proc., Vol. 1416, pp. 84–87 (2012).

We demonstrate that, in a GaSb/GaAs epitaxial structure, the coherent longitudinal optical (LO) phonon in the GaAs layer optically covered with the GaSb top layer is observed utilizing terahertz spectroscopy. In the terahertz-wave measurement, the Fourier power spectrum of the terahertz waveform exhibits both the GaAs and the GaSb LO phonons; namely, the coherent LO phonon in the optically covered GaAs buffer layer is observed in the terahertz-wave measurement. This fact demonstrates that the instantaneous surface potential modulation originating from the impulsive carrier excitation by the pump pulses reaches the GaAs buffer layer. This surface potential modulation generates the coherent GaAs LO phonon.

DOI:10.1016/1.3671704

Frequency-Tunable Quantum Beats under a Franz–Keldysh Oscillation Condition in a GaAs/Al_xGa_{1-x}As Superlattice

T. HASEGAWA, Y. TAKAGI, and M. NAKAYAMA

Appl. Phys. Express, Vol. 5, 041202 (3 pages) (2012).

We have investigated quantum beats (QBs) related to miniband states under a Franz–Keldysh oscillation condition in a GaAs/Al_{0.1}Ga_{0.9}As superlattice. Franz–Keldysh oscillations, which correspond to electric-field-induced oscillations of optical transition energies in a miniband regime, were clearly detected by electroreflectance spectroscopy. The frequency of the QB changes markedly with an increase in the electric field strength. This frequency change corresponds to the difference between the energy of the $n=1$ heavy-hole exciton and that of the Franz–Keldysh oscillation, depending on the electric field strength. The frequency tunability of this QB is quite different from that of a Bloch oscillation.

DOI: 10.1143/APEX.5.041202

Ultrafast Optical Response Originating from Carrier-Transport Processes in Undoped GaAs/*n*-Type GaAs Epitaxial Structures

T. HASEGAWA, Y. TAKAGI, H. TAKEUCHI, H. YAMADA, M. HATA, and M. NAKAYAMA

Appl. Phys. Lett., Vol. 100, 211902 (4 pages) (2012).

We have investigated ultrafast optical responses of undoped GaAs/*n*-type GaAs (*i*-GaAs/*n*-GaAs) epitaxial structures at room temperature using a reflection-type pump-probe technique. The built-in electric field in the *i*-GaAs layer is controlled by its thickness. It is found that the decay time of a photoexcitation-induced reflectivity change in a sub-picosecond range decreases with an increase in the built-in electric field strength. The observed optical response is related to the transport process of photogenerated carriers from the *i*-GaAs layer to the *n*-GaAs layer. The shortest response time about 60 fs demonstrates that the *i*-GaAs/*n*-GaAs structure is useful for ultrafast optical applications.

DOI: 10.1063/1.4720157

Intense Monochromatic Terahertz Electromagnetic Waves from Coherent GaAs-like Longitudinal Optical Phonons in (11*n*)-oriented GaAs/In_{0.1}Al_{0.9}As Strained Multiple Quantum Wells

H. TAKEUCHI, S. ASAI, S. TSURUTA, and M. NAKAYAMA

Appl. Phys. Lett., Vol. 100, 242107 (4 pages) (2012).

We demonstrate that, in (11*n*)-oriented GaAs/In_{0.1}Al_{0.9}As strained multiple quantum wells, the terahertz electromagnetic wave from the coherent GaAs-like longitudinal optical (LO) phonon is enhanced by a piezoelectric field originating from a tensile strain in the GaAs layer. The presence of the tensile strain is confirmed using Raman scattering spectroscopy. The Fourier power spectrum of the terahertz waveform shows that the intensity of the terahertz band of the coherent GaAs-like LO phonon increases as the index n approaches 1. The amplitude of the GaAs-like LO phonon is proportional to the piezoelectric field in the strained GaAs layer.

DOI: 10.1063/1.4729125

Quantum Beats of Type-I and Type-II Excitons in an $\text{In}_x\text{Ga}_{1-x}\text{As}/\text{GaAs}$ Strained Single Quantum Well

O. KOJIMA, K. MIZOGUCHI, and M. NAKAYAMA

J. Appl. Phys., Vol. 112, 043522 (4 pages) (2012).

We have investigated the quantum beat of the type-I heavy-hole (HH) and the type-II light-hole (LH) excitons in an $\text{In}_{0.15}\text{Ga}_{0.85}\text{As}/\text{GaAs}$ strained single quantum well (SQW) using a reflection-type pump-probe technique. The type-II LH exciton consists of the electron and LH located in the $\text{In}_{0.15}\text{Ga}_{0.85}\text{As}$ and GaAs layers, respectively. The energies of the type-I and the type-II excitons were evaluated with photoreflectance spectroscopy. The exciton states were calculated based on a variational method. The time-domain signals clearly show the oscillatory structure with the period corresponding to the splitting energy of the HH and the LH excitons. From the pump-energy dependence of the Fourier transform spectrum and intensity, it is concluded that the oscillation originates from the quantum beat of the type-I HH and the type-II LH excitons. DOI: 10.1063/1.4748339

Control of Rabi Splitting Energies in CuCl Microcavities with $\text{HfO}_2/\text{SiO}_2$ Distributed Bragg Reflectors

M. NAKAYAMA, K. MIYAZAKI, T. KAWASE, and D. KIM

Physics Procedia, Vol. 29, pp. 6-11 (2012).

The exciton-photon interaction in CuCl microcavities with $\text{HfO}_2/\text{SiO}_2$ distributed Bragg reflectors has been investigated from the viewpoint of the active-layer-thickness dependence of the interaction energy, the so-called vacuum Rabi splitting energy. The active layer thickness was changed from $\lambda/32$ to $\lambda/5$, where λ corresponds to an effective resonant wavelength of the lowest-lying Z_3 exciton. We performed angle-resolved reflectance measurements, and clearly detected three cavity-polariton modes originating from the lower, middle, and upper polariton branches in a strong coupling regime of the Z_3 and $Z_{1,2}$ excitons, and cavity photon. The incidence-angle dependence of the cavity-polariton energies was analyzed with a phenomenological Hamiltonian for the strong coupling. The vacuum Rabi splitting energies are systematically controlled from 22 (37) to 68 (122) meV for the Z_3 ($Z_{1,2}$) exciton with an increase in the active layer thickness. The active-layer-thickness dependence of the Rabi splitting energy is quantitatively explained using a simple model for quantum-well microcavities. DOI: 10.1016/j.phpro.2012.03.68

Time Evolution of Terahertz Electromagnetic Waves from Undoped GaAs/*n*-type GaAs Epitaxial Layer Structures Clarified with Use of a Time-Partitioning Fourier Transform Method

H. TAKEUCHI, S. TSURUTA, H. YAMADA, M. HATA, and M. NAKAYAMA

Physics Procedia, Vol. 29, pp. 30-35 (2012).

We have investigated the time evolution of terahertz electromagnetic waves caused by the surge current of photogenerated carriers, the so-called first burst, in two *i*-GaAs/*n*-GaAs epitaxial layer structures with different *i*-GaAs layer thicknesses of 500 and 1200 nm. The terahertz waveform of the first burst shows a narrowing with a decrease in the thickness of the *i*-GaAs layer. In accordance with the above phenomena, it is observed in the Fourier power spectra that the band of the first burst shows a high frequency shift with a decrease in the *i*-GaAs layer thickness. We elucidate the origin of the high frequency shift, focusing on the time-domain dynamics of the photogenerated carriers: we apply the time-partitioning Fourier transform, which is useful to investigate the time evolution of the frequency. From the time-partitioning Fourier power spectra, we obtain the evidence that the acceleration after the carrier generation dominates the time evolution of the frequency component leading to the high frequency shift. DOI: 10.1016/j.phpro.2012.03.687

Exciton Polaritons in a CuBr Microcavity with $\text{HfO}_2/\text{SiO}_2$ Distributed Bragg Reflectors

M. NAKAYAMA, Y. KANATANI, T. KAWASE, and D. KIM

Phys Rev. B, Vol. 85, 205320 (5 pages) (2012).

We have investigated the characteristics of exciton-photon strong coupling in a CuBr bulk microcavity that consists of a CuBr active layer with an effective thickness of $\lambda/2$ and $\text{HfO}_2/\text{SiO}_2$ distributed Bragg reflectors: λ corresponds to an effective resonant wavelength of the lowest-lying exciton. The CuBr crystal has three excitons labeled Z_f , $Z_{1,2}$ and Z_3 at the Γ point, where the Z_f exciton originates from a triplet state, which is peculiar to CuBr. Angle-resolved reflectance spectra measured at 10 K demonstrate the strong coupling behavior of the Z_f , $Z_{1,2}$ and Z_3 excitons and cavity photon, resulting in the formation of four cavity-polariton branches. Analyzing the cavity-polariton dispersion relations based on a phenomenological Hamiltonian for the strong coupling, we evaluated the vacuum Rabi-splitting energies of the Z_f , $Z_{1,2}$ and Z_3 excitons to be 31, 108, and 84 meV, respectively. These Rabi-splitting energies reflect the magnitudes of the oscillator

strengths of the relevant excitons. Furthermore, we precisely measured angle-resolved photoluminescence (PL) spectra of the lower polariton branch under a weak excitation condition. In the bottleneck region, the population of the cavity polaritons is negligible, and the PL intensity at $k=0$ is the highest. These facts suggest that the relaxation process of the cavity polaritons is not affected by a bottleneck effect.

DOI: 10.1103/PhysRevB.85.205320

Photoluminescence Properties of Self-Assembled Monolayers of CdSe and CdSe/ZnS Quantum Dots

H. YOKOTA, K. OKAZAKI, K. SHIMURA, M. NAKAYAMA, and D. KIM

J. Phys. Chem. C, Vol. 116, pp. 5456-5459 (2012).

The photoluminescence (PL) properties of self-assembled monolayers (SAMs) of CdSe and CdSe/ZnS quantum dots (QDs) were investigated. From measurements of the temperature dependence of PL spectra, it is demonstrated that the thiol group, which is a constituent of the reagent for formation of the SAM, degrades the PL properties during the SAM formation process. With an additional dipping treatment in a Cd(ClO₄)₂ aqueous solution with pH = 10, the band-edge PL intensity is increased remarkably. The improvement of PL properties is attributed to QD surface modification with a Cd(OH)₂ layer. On the other hand, the defect-related PL band is not observed at all, even at 10 K, in the SAMs of CdSe/ZnS core/shell QDs. This fact indicates that the ZnS shell layer prevents degradation of the PL properties during the SAM process.

Active-Layer-Thickness Dependence of Rabi Splitting Energies in ZnO Microcavities

T. KAWASE, D. KIM, and M. NAKAYAMA

Phys. Status Solidi C, Vol.9, pp. 1797–1800 (2012).

We have investigated the active-layer-thickness dependence of Rabi splitting energies in ZnO microcavities. We fabricated ZnO microcavities using rf magnetron sputtering for the HfO₂/SiO₂ distributed Bragg reflector and pulsed-laser deposition for the ZnO active layer. In order to control of the Rabi splitting energies, the active layer thickness was changed from $\lambda/2$ to $3\lambda/2$. In angle-resolved reflectance spectra at 10 K, the cavity polaritons resulting from the strong coupling between A, B, and C excitons peculiar to ZnO and the cavity photon were clearly detected. We estimated the energies of the exciton-photon interaction, the so-called Rabi splitting energies, from the analysis of the cavity polariton dispersions using the phenomenological Hamiltonian for the strong exciton-photon coupling. The Rabi splitting energies markedly increase with an increase in the active layer thickness. The active-layer-thickness dependence of the Rabi splitting energies are explained by a semiquantitative analysis. Consequently, we have succeeded in the control of the Rabi splitting energies in the ZnO microcavities.

DOI 10.1002/pssc.201100583

Characteristics of Cavity Polaritons in a CuBr Microcavity

Y. KANAKANI, T. KAWASE, D. KIM, and M. NAKAYAMA

Eur. Phys. J. B, Vol. 85, 390 (6 pages) (2012).

We report the characteristics of cavity polaritons in a CuBr microcavity consisting of a $\lambda/2$ -thick CuBr active layer and HfO₂/SiO₂ distributed Bragg reflectors: λ corresponds to an effective resonant wavelength of the lowest-lying exciton. The excitonic system of a CuBr crystal has three kinds of excitons labeled Z_f , $Z_{1,2}$, and Z_3 in which the Z_f exciton originates from a triplet state. We have investigated the dispersion relations of the cavity polaritons in the CuBr microcavity with the use of angle-resolved reflectance spectroscopy. The experimental results demonstrate the formation of four cavity-polariton branches due to the strong coupling between the Z_f , $Z_{1,2}$, and Z_3 excitons and cavity photon. The cavity-polariton dispersions were well analyzed with a phenomenological Hamiltonian for the strong coupling. The evaluated Rabi-splitting energies are 28, 95, and 74 meV for the Z_f , $Z_{1,2}$, and Z_3 excitons, respectively. These Rabi splitting energies reflect the magnitudes of the oscillator strengths of the relevant excitons. Furthermore, it was confirmed that the cavity polaritons are fully stable at room temperature. We discuss the temperature dependence of the cavity-polariton energies and detuning, comparing with that of the bare exciton.

DOI: 10.1140/epjb/e2012-30523-2

Control of Rabi-Splitting Energies of Exciton Polaritons in CuI Microcavities

M. NAKAYAMA, M. KAMEDA, T. KAWASE, and D. KIM

Eur. Phys. J. B, Vol. 86, 32 (5 pages) (2013).

We have investigated the active-layer-thickness dependence of exciton-photon interactions in CuI microcavities. The active layer thickness was changed from $\lambda/2$ to 2λ , where λ corresponds to an effective

resonant wavelength of the lowest-lying exciton. In the CuI active layer, thermal strain removes the degeneracy of the heavy-hole (HH) and light-hole (LH) excitons at the Γ point. Angle-resolved reflectance spectra measured at 10 K demonstrate the strong coupling between the HH and LH excitons and cavity photon, resulting in the formation of three cavity-polariton branches: the lower, middle, and upper polariton branches. The energies of the three cavity-polariton modes as a function of incidence angle are reasonably explained using a phenomenological Hamiltonian to describe the exciton-photon strong coupling. It is found that the interaction energies of the cavity-polariton modes, the so-called vacuum Rabi-splitting energies, are systematically controlled from 29 (50) to 48 (84) meV for the LH (HH) exciton by changing the active layer thickness from $\lambda/2$ to 2λ . The active-layer-thickness dependence of the Rabi-splitting energies is semi-quantitatively explained by a simple model.

DOI: 10.1140/epjb/e2012-30503-6

Terahertz Radiation from the Coherent Longitudinal Optical Phonon-Plasmon Coupled Mode in an *i*-GaAs/*n*-GaAs Epitaxial Structure

S. TSURUTA, H. TAKEUCHI, and M. NAKAYAMA

J. Phys. Conf. Ser., Vol.41, 7 012051(2013).

We have investigated the time-domain terahertz radiation from an undoped GaAs/*n*-type GaAs (*i*-GaAs/*n*-GaAs) epitaxial structure using an optical gating method with a femtosecond pulse laser. We have found from the Fourier power spectra of the terahertz waveforms that two terahertz bands, the frequencies of which considerably depend on the pump power, appear in a high density excitation regime in addition to a broad band due to a surge current and a sharp band due to the coherent longitudinal optical (LO) phonon. Based on a model for the LO phonon-plasmon coupled (LOPC) mode, we reasonably explain the pump-power (photogenerated-carrier-density) dependence of the frequencies of the two bands peculiar to the high density excitation. This fact demonstrates that the two terahertz bands are assigned to the lower and upper branches of the LOPC mode. The frequencies of the LOPC modes are determined only by the pump power. Thus, the LOPC modes originate from the *i*-GaAs layer; namely, the plasmon component of the surge current flowing through the *i*-GaAs layer couples with the coherent LO phonon.

DOI:10.1088/1742-6596/417/1/012051

Photogenerated-Carrier-Induced Band Bending Effects on Generation of a Coherent Longitudinal Optical Phonon in a GaAs Buffer Layer Optically Masked by a GaSb Top Epitaxial Layer

H. TAKEUCHI, S. TSURUTA, and M. NAKAYAMA

Phys. Status Solidi C, Vol.9, pp.2610-2613 (2012).

We demonstrate that, in a GaSb/GaAs epitaxial structure, the coherent longitudinal optical (LO) phonon in a GaAs buffer layer optically masked by a GaSb top layer is observed utilizing terahertz spectroscopy. It is confirmed from Raman scattering measurements that only the optical phonons in the GaSb layer is observable. In the terahertz-wave measurement, the Fourier power spectrum of a terahertz waveform exhibits both the coherent GaAs and GaSb LO phonon bands; namely, the coherent LO phonon in the optically masked GaAs buffer layer is observed. This fact demonstrates that the instantaneous surface potential modulation, which originates from the impulsive carrier excitation by a pump beam, reaches the GaAs buffer layer. We perform a time-partitioning Fourier transform analysis in order to investigate the decay dynamics of the coherent GaAs and GaSb LO phonons.

DOI: 10.1002/pssc.201200160

Photon-Field-Shape Effects on Rabi Splitting Energies in CuCl Microcavities

T. KAWASE, K. MIYAZAKI, D. KIM, and M. NAKAYAMA

Eur. Phys. J. B, Vol.86, 69 (6 pages) (2013).

We have investigated the photon-field-shape effects on Rabi splitting energies in CuCl microcavities with HfO₂/SiO₂ distributed Bragg reflectors (DBRs). The CuCl active layer was prepared by vacuum deposition, while HfO₂ and SiO₂ layers were prepared by rf magnetron sputtering. The photon-field shape was tuned to a node-type or an antinode-type by changing the order of the refractive indices in the DBR. In order to control of the Rabi splitting energies, the active-layer thickness was changed from $\lambda/12$ to $9\lambda/20$. In angle-resolved reflectance spectra at 10 K, three cavity polaritons resulting from the strong coupling between the Z_3 and $Z_{1,2}$ excitons and cavity photon were clearly detected. We estimated the energies of the exciton-photon interaction, the so-called vacuum Rabi splitting energies, from the analysis of the cavity polariton dispersions

using a phenomenological Hamiltonian for the strong exciton-photon coupling. The active-layer-thickness dependence of the Rabi splitting energies are explained by a semiquantitative analysis taking account of the overlap between the exciton and photon-field wave functions. We have demonstrated that the photon-field shape drastically affects the active-layer-thickness dependence of the Rabi splitting energies.

DOI: 10.1140/epjb/e2012-30505-4

Photoluminescence Dynamics of Excitons at the Mini-Brillouin-Zone Edge in a GaAs/AlAs Superlattice

M. Nakayama, T. Yamashita, and T. Hasegawa

J. Cryst. Growth, Vol. 378, pp. 61-64 (2013).

We have investigated the photoluminescence (PL) dynamics of excitons at the mini-Brillouin-zone edge ($k_z=\pi/D$), the so-called π point, a GaAs/AlAs superlattice (SL): D is a SL period. Under the resonant excitation condition of the first quantized ($n=1$) heavy-hole (HH) exciton at the Γ point ($k_z=0$), it was found that the PL band of the $n=1$ HH exciton at the π point is observed from time-resolved PL spectra. The temporal profile of the PL of the π -point exciton exhibits a considerable delay time, ~ 40 ps, to that of the Γ -point exciton and a very short decay time, ~ 12 ps. Note that the PL of the π -point exciton has been never observed under off-resonant excitation of the Γ -point exciton. The delay time is attributed to the transit time from the Γ point to the π point in the mini-Brillouin zone. The very short decay time results from that the π point is a metastable state in the miniband dispersion. The mechanism of the transit process of the excitons is discussed from aspects of excitation-power dependence and scattering by folded longitudinal acoustic phonons peculiar to the SL.

DOI: 10.1016/j.jcrysgro.2012.12.166

Temperature Dependence of Cavity-Polariton Energies in ZnO and CuCl Microcavities

T. KAWASE, K. MIYAZAKI, D. KIM, and M. NAKAYAMA

J. Appl. Phys., Vol. 112, 093512 (7 pages) (2012).

We have investigated the temperature dependence of the cavity-polariton energies in ZnO and CuCl microcavities with $\text{HfO}_2/\text{SiO}_2$ distributed Bragg reflectors. From angle-resolved reflectance spectra at 10 K, we experimentally confirmed the cavity-polariton dispersions. The experimental dispersions were analyzed with a phenomenological Hamiltonian for the exciton-photon strong coupling. Furthermore, the temperature dependence of the angle-resolved reflectance spectra was measured. We analyzed the experiment results of the temperature dependence of the energies of the cavity polaritons on the basis of the phenomenological Hamiltonian, taking account of Varshni's law to treat the temperature dependence of the band-gap energy in a bulk crystal. Note that the temperature dependence of the exciton energies in a CuCl bulk crystal is extraordinary, which is in reverse to that in a ZnO bulk crystal. We have revealed that the temperature dependence of the energies of the cavity polaritons, which deviates from that of the exciton in the bulk crystal, considerably depends on the relative fractions of the exciton and cavity-photon components in the cavity polaritons.

DOI: 10.1063/1.4764327

Circular Polariscopic Analysis of a ZnO Wafer for Highly Sensitive and Speedy Evaluation of Residual Strains: Its Relation with X-ray Diffraction Pattern and Topography

H. TAKEUCHI

Phys. Status Solidi C, Vol.9, pp.1817-1820 (2012).

We have explored the effectiveness of applying the circular polariscopic measurement to the mapping of the strains in a ZnO wafer. Initially, monochromatic x-ray topography, which is regarded as a fundamental evaluation technique for wafers, is applied. The measured monochromatic x-ray topograph shows that the image contrast is remarkably inhomogeneous; namely, the dark patterns exist in various regions. In order to clarify the origin of the above-mentioned dark patterns, we apply the circular polariscopic measurement, which is sensitive to strains through the photoelastic effect. The brightness of the circular polariscopic wafer map reveals that the dark pattern in the monochromatic x-ray topograph results from the strain. Thus, we conclude that the circular polariscopic analysis has the ability to compliment the information obtained by the monochromatic x-ray topographic measurement. The presence of the relatively large strains is confirmed from the fact that the forbidden reflection lines are observed in the θ - 2θ x-ray diffraction pattern.

DOI: 10.1002/pssc.201100514

First-Sharp Diffraction Peaks in Amorphous GeTe and Ge₂Sb₂Te₅ Films Prepared by Vacuum-Thermal Deposition

T. NAKAOKA, H. SATOH, S. HONJO, and H. TAKEUCHI

AIP Advances, Vol.2, 042189 (6 pages) (2012).

We report on a presence of intermediate-range order in amorphous GeTe and Ge₂Sb₂Te₅ phase change films prepared by simple vacuum-thermal deposition. We find that thermally deposited GeTe and Ge₂Sb₂Te₅ films show significant first sharp diffraction peaks (FSDPs) in the X-ray diffraction pattern, although the intensities in GeTe and Ge₂Sb₂Te₅ fabricated by sputtering technique have previously been reported to be very small due to their characteristic structures. This is in contrast to the case of strong network forming glasses like As-S(Se) and Ge-S(Se), in which FSDPs are clearly observed both in evaporated and sputtered films. The observed fabrication-dependent intermediate-range structures in the amorphous Ge-Sb-Te system help in exploring the physics of the metastable forms of amorphous semiconductors and the phase change mechanism.

DOI: 10.1063/1.4773329

Enhancement Effects on Excitonic Photoluminescence Intensity Originating from Misaligned Crystal Blocks and Polycrystalline Grains in a ZnO Wafer

H. TAKEUCHI

Eur. Phys. J. B, Vol.86, 50 (5 pages) (2013).

We have systematically investigated a relation between excitonic photoluminescence intensity and crystal quality in a (0001)-oriented ZnO wafer. We visualize the crystal quality of a whole wafer using a circular polariscopic measurement and a reflection-type x-ray topograph measurement. The reflection-type x-ray topograph exhibits regions of grain-like patterns that result from internal strains. The circular polariscopic map shows that the internal strains induce local stresses. The θ - 2θ x-ray diffraction pattern indicates the presence of misaligned crystal blocks and polycrystalline grains. We have measured photoluminescence spectra and found that the presence of misaligned crystal blocks and polycrystalline grains leads to enhancement of the excitonic photoluminescence intensity. The present phenomenon is attributed to the suppression of exciton diffusion caused by the grain and domain boundaries that connect with the grain-like patterns in the x-ray topograph.

DOI: 10.1140/epjb/e2012-30502-7

Optical Properties of Plasmonic Crystal at Terahertz Frequencies and the Advanced Application

S. NASHIMA and Y. OGAWA

IEEJ Transactions on Electronics, Information and Systems, Vol.133, No.3, pp. 484-489 (2013) (in Japanese).

We introduce the recent topics concerning the 1D- and 2D- plasmonic crystals, i.e., a wire grid polarizer and a metal mesh device at terahertz frequencies. We show the remarkable increase in polarization characteristics on a freestanding double-layered wire grid polarizer. We also show the performance of metal mesh devices for biosensing application.

Terahertz radiation characteristics on BNA crystal by terahertz time domain spectroscopy

S. NASHIMA, K. SHIBATA, M. HOSODA, T. YOKOE, K. INOUE, H. HASHIMOTO, K. MIYAMOTO, T. NOTAKE, H. MINAMIDE, and H. ITO

International Symposium on Frontiers in THz Technology (FTT 2012), Nov. 2012, Nara, Japan.

Three-dimensional deformation and merging of instability waves in a radial liquid sheet was clarified. A radial liquid sheet forms when a radially flowing liquid film on a disk emerges from the disk and destabilizes just outside the disk. Such instability is caused by the inflection point in the flow velocity profile, and is therefore referred to as “inflectional instability.” The instability initially generates two-dimensional waves that grow and deform to cause turbulent transition. The three-dimensional deformation of instability waves is similar to that of vortices formed by inflectional instability in a single-phase free shear flow. This suggests that the deformation of the waves is caused by the enhancement of perturbed vortex filaments. However, the waves scarcely merge, whereas vortices in the free shear flow merge frequently. This implies that merging of instability waves in liquid sheets is prevented by surface tension.

Terahertz absorption spectroscopy of protein-containing reverse micellar solution

H. MURAKAMI, Y. TOYOTA, T. NISHI, and S. NASHIMA

Chem. Phys. Lett., Vol.519-520, (2012), pp. 105-109.

Terahertz time-domain spectroscopy has been carried out for AOT/isooctane reverse micellar solution with myoglobin at the water-to-surfactant molar ratios (w_0) of 0.2 and 4.4. The amplitude of the absorption spectrum increases with increasing the protein concentration at $w_0 = 0.2$, whereas it decreases at $w_0 = 4.4$. The molar extinction coefficients of the protein-filled reverse micelle, and the constituents, i.e., myoglobin, water, and AOT, have been derived by use of the structural parameters of the micellar solution. The experimental results are interpreted in terms of hydration onto the protein and surfactant in the reverse micelle.

Growth of Ultrathin and Highly Efficient Organic Nonlinear Optical Crystal 4'-Dimethylamino-N-methyl-4-Stilbazolium p-Chlorobenzenesulfonate for Enhanced Terahertz Efficiency at Higher Frequencies

S. BRAHADEESWARAN, Y. TAKAHASHI, M. YOSHIMURA, M. TANI, S. OKADA, S. NASHIMA, Y. MORI, M. HANGYO, H. ITO, and T. SASAKI

Cryst. Growth Des. Vol.13, (2013), pp. 415-421.

Growth of an ultrathin (thickness as low as 23 μm) organic nonlinear optical crystal of 4'-dimethylamino-n-methyl-4-stilbazolium p-chlorobenzenesulfonate (DASC) has been achieved by the slope nucleation method for generating THz waves with relatively higher efficiencies especially at higher frequencies. The propensity of lower solubility of this material in methanol solvent as compared to 4'-dimethylamino-n-methyl-4-stilbazolium tosylate (DAST) was favorably exploited to obtain these thin crystals. The DASC crystals thus obtained were studied for the generation of THz waves, and their efficiency was compared with DAST and zinc telluride (ZnTe) single crystals. The enhancement THz efficiency observed in thinner DASC could be attributed to better velocity matching and weaker absorption as compared to thicker crystals of the same material.

Time-Domain Measurements of Terahertz Waves Generated from Picosecond Optical Parametric Oscillator

Y. TADOKORO, Y. TAKIDA, H. KUMAGAI, and S. NASHIMA

The Review of Laser Engineering, Vol.41, No. 2, (2013), pp. 125-128 (In Japanese).

This paper describes the first demonstration of the time-domain measurements of terahertz (THz)-wave pulses generated from a picosecond optical parametric oscillator (ps-OPO). Unlike pyroelectric detectors, photoconductive antennas allow us to observe the time-discrete THz-wave pulses that depend on arrayed Si-prism Couplers. By replacing them with a larger single type, the phase distortion of THz-wave pulses was compensated and a single THz-wave pulse with the peak frequency of ~ 0.2 THz was obtained.

Tunable Picosecond Terahertz-Wave Parametric Oscillators Based on Noncollinear Pump-Enhanced Idler-Resonant Cavity

Y. TAKIDA, T. OHIRA, Y. TADOKORO, H. KUMAGAI, and S. NASHIMA

IEEE J. Sel. Top. Quantum Electron. Vol.19, Issue 1, (2013) pp. 8500307(9pages).

We have succeeded in developing tunable picosecond terahertz (THz)-wave parametric oscillators (ps-TPOs) by employing a noncollinear pump-enhanced idler-resonant cavity. As a parametric gain medium, we use two different shapes of unpoled, 5 mol% MgO-doped lithium niobate ($\text{MgO}:\text{LiNbO}_3$) crystal: (1) a rectangle for Si-prism output-coupler technique; and (2) a trapezoid for surface-emitted configuration. Unlike conventional nanosecond TPOs (ns-TPOs), these ps-TPOs are synchronously pumped by a mode-locked 1.5-ps Ti:sapphire laser operating at 780 nm. To overcome the high pump threshold due to the strong absorption by $\text{MgO}:\text{LiNbO}_3$ in the THz region, we employ a pump-enhanced cavity which is carefully designed for the noncollinear double resonance of both pump and idler waves. By slightly translating the position of one of the ps-TPO cavity mirrors, we experimentally find that the THz-wave frequency is continuously tunable from 1.0 to 3.2 THz with the average output power of several nanowatts. In all the above tuning range, especially above 2 THz, the THz-wave output of the surface-emitting ps-TPO using the trapezoidal $\text{MgO}:\text{LiNbO}_3$ crystal is enhanced several times more than that of the Si-prism-coupled ps-TPO using the rectangular $\text{MgO}:\text{LiNbO}_3$ crystal due to the suppression of the absorption loss in $\text{MgO}:\text{LiNbO}_3$.

Study on the mechanism of field adsorption of helium and neon above a single tungsten atom with a pulse counting analysis of field ions

A. KOBAYASHI, K. TETSUMOTO and H. KUMAGAI

Journal of The Surface Science Society of Japan Vol. 34, pp. 409-414 (2013).

For investigating the interaction of He and Ne in the field adsorption and ionization process above a single tungsten atom, field ion signals have been directly measured as a function of time using a micro-probe hole field ion microscope combined with a pulse counting analysis. Observed ion signals clearly show the transitions between a field adsorbed He state and a field adsorbed Ne state, and enable the determination of average adsorption time of He and Ne. Simple probabilistic model of adsorption and exchange of atoms at field adsorption site taking account of gas densities close to the surface well reproduced the observed behavior of average adsorption times. The results indicate the pronounced increase of Ne gas density near the sample surface. Particularly in the case of an initial mixed ratio of less than 0.5% of Ne for He, the increment reaches more than a hundred times.

Time-Domain Measurements of Terahertz Waves Generated from Picosecond Optical Parametric Oscillator

Y. TADOKORO, Y. TAKIDA, H. KUMAGAI, S. NASHIMA and A. KOBAYASHI

The Review of Laser Engineering Vol. 41, pp. 125-128 (2013).

This paper describes the first demonstration of the time-domain measurements of terahertz (THz) wave pulses generated from a picosecond optical parametric oscillator (ps OPO). Unlike pyroelectric detectors, photoconductive antennas allow us to observe the time discrete THz-wave pulses that depend on arrayed Si-prism couplers. By replacing them with a larger single type phase distortion of THz-wave pulses was compensated and a single THz-wave pulse with the peak frequency of ~ 0.2 THz was obtained.

Comparative study on THz time-domain spectroscopy using 780-nm 1.3-ps laser pulses with different detections of LT-GaAs photoconductive antenna and ZnTe electro-optic sampling

Y. TADOKORO, Y. TAKIDA, H. KUMAGAI, S. NASHIMA, and A. KOBAYASHI

Proceeding of SPIE Vol. 8604, 86040D: pp. 1-6 (2013).

We have demonstrated the comparison of terahertz (THz) time-domain spectroscopy (THz-TDS): a low-temperature grown GaAs photoconductive antenna (PCA) and ZnTe electro-optic (EO) sampling with 780-nm 1.3-ps laser pulses. As a result, the different detection limits up to approximately 0.8, 1.0, and 1.3 THz are obtained with a bow-tie, dipole antenna, and ZnTe crystal, respectively. In the PCA sampling, the frequency at main peak of the spectrum measured with the dipole antenna is higher than the one with the bow-tie antenna. The dynamic range of the power spectrum measured with the bow-tie antenna is higher than any other detection methods. In addition, we compare the PCA sampling with femtosecond laser pulses to the one with picosecond laser pulses in terms of the response of the PCAs.

Tunable picosecond THz-wave generation based on trapezoidal MgO:LiNbO₃ crystal in novel pentagram-shaped pump-enhancement cavity

Y. TAKIDA, Y. TADOKORO, H. KUMAGAI, S. NASHIMA, and A. KOBAYASHI

Proceeding of SPIE Vol. 8604, 86041F: pp. 1-6 (2013).

It is well known that lithium niobate (LiNbO₃) has excellent characteristics for efficient tunable/broadband THz-wave generation. Over the last few years, we have investigated novel THz-wave sources based on MgO-doped LiNbO₃ (MgO:LiNbO₃), and have succeeded in developing a tunable picosecond THz-wave source by using a novel pentagram-shaped pump-enhancement cavity. One of the limiting factors in efficient THz-wave generation is the strong absorption by MgO:LiNbO₃ in THz-wave region. To overcome this problem, we employ a surface-emitted configuration which consists of a trapezoidal MgO:LiNbO₃ crystal and a pump-enhancement cavity folded in the shape of a pentagram. The pentagram-shaped cavity is designed for the noncollinear dual resonance of both pump and one of the down-converted waves. As a result, 1.5-ps pump pulses from a mode-locked Ti:sapphire laser operating at 780 nm allow tunable THz-wave generation via parametric down-conversion resulting from stimulated phonon-polariton scattering in the MgO:LiNbO₃ crystal. By slightly translating the position of one of the cavity mirrors, we experimentally find that the THz-wave frequency is tunable in the range from 0.1 to 3.5 THz with the average output power of dozens of nanowatts. The maximum THz-wave average power is up to 40 nW around 2 THz at the pump power of 800 mW, which is several times higher than the THz-wave output generated by using rectangular MgO:LiNbO₃ crystals for Si-prism-coupled configuration under the same pump condition.

Monte Carlo Study of Spin-Peierls Transition in Quasi-One-Dimensional Heisenberg Model with Finite-Frequency Phonons

Y. MATSUMOTO and A. TERAJ

J. Phys.: Conf. Ser. 400, 032102 (4 pages) (2012).

A quasi-one-dimensional spin-1/2 Heisenberg antiferromagnet coupled with optical phonons is numerically studied by the quantum Monte Carlo method. We have implemented the stochastic series expansion method for the spin part of the Hamiltonian and the path-integral quantization method for the phonon part. Keeping the spin-phonon coupling strength unchanged, we have calculated the spin-Peierls transition temperature as a function of the frequency of optical phonons. It is found that the transition temperature decreases as the phonon frequency increases. Above a critical frequency, the spin-Peierls transition does not occur all the way down to zero temperature due to quantum fluctuations. We have determined the universality class of the spin-Peierls transition by the phenomenological finite-size scaling analysis. The transitions at low frequencies belong to the universality class of the two-dimensional Ising model while that at a high frequency is found to be characterized by the tricritical exponents of the two-dimensional spin-1 Blume-Capel model.

Dynamics of Fractionally Charged Phase Soliton in One-Dimensional Quarter-Filled Electron-Lattice Systems

K. HIROKAWA, A. TERAJ, and Y. ONO

J. Phys. Soc. Jpn. Vol. 82, 104708 (7 pages) (2013).

The dynamical properties of a phase soliton with a fractional charge $\pm e/2$ in the bond-charge-density-wave (BCDW) background of one-dimensional quarter-filled electron-lattice systems are studied by numerical and semi-phenomenological methods using the Su-Schrieffer-Heeger (SSH) model. A special focus is on the time evolutions of the velocity and energy of the charged soliton subject to an electric field. Several interesting properties are obtained: the saturation of the soliton velocity, the divergence of the soliton energy and the propagation of condensed acoustic phonons. The saturation velocity, which is independent of the applied field strength, is less than the phason velocity. These properties are different from those of the sine-Gordon model which was believed to describe the commensurate BCDW systems. The velocity-energy relation is also different from that of the sine-Gordon soliton but is described by the same form as that of the acoustic polaron in the SSH model. These results suggest that it is necessary to take into account the interactions between the electrons and the acoustic phonons in order to really understand the dynamics of the fractionally charged soliton in the electron-lattice system.

Geometrical pumping in quantum transport: Quantum master equation approach

T. YUGE, T. SAGAWA, A. SUGITA and H. HAYAKAWA

Phys. Rev. B Vol. 86, 235308 [10 pages] (2012).

For an open quantum system, we investigate the pumped current induced by a slow modulation of control parameters on the basis of the quantum master equation and full counting statistics. We find that the average and the cumulant generating function of the pumped quantity are characterized by the geometrical Berry-phase-like quantities in the parameter space, which is associated with the generator of the master equation. From our formulation, we can discuss the geometrical pumping under the control of the chemical potentials and temperatures of reservoirs. We demonstrate the formulation by spinless electrons in coupled quantum dots. We show that the geometrical pumping is prohibited for the case of noninteracting electrons if we modulate only temperatures and chemical potentials of reservoirs, while the geometrical pumping occurs in the presence of an interaction between electrons.

Geometrical Excess Entropy Production in Nonequilibrium Quantum Systems

T. YUGE, T. SAGAWA, A. SUGITA and H. HAYAKAWA

J. Stat. Phys. Vol. 153, pp. 412-441 (2013).

For open systems described by the quantum Markovian master equation, we study a possible extension of the Clausius equality to quasistatic operations between nonequilibrium steady states (NESSs). We investigate the excess heat divided by temperature (i.e., excess entropy production) which is transferred into the system during the operations. We derive a geometrical expression for the excess entropy production, which is analogous to the Berry phase in unitary evolution. Our result implies that in general one cannot define a scalar potential whose difference coincides with the excess entropy production in a thermodynamic process, and that a vector potential plays a crucial role in the thermodynamics for NESSs. In the weakly nonequilibrium regime, we show that the geometrical expression reduces to the extended Clausius equality derived by Saito and Tasaki (*J. Stat. Phys.* 145:1275, 2011). As an example, we investigate a spinless electron system in quantum dots. We find that one can define a scalar potential when the parameters of only one of the reservoirs are modified in a non-interacting system, but this is no longer the case for an interacting system.

Floating volumetric image formation using a dihedral corner reflector array device

D. MIYAZAKI, N. HIRANO, Y. MAEDA, S. YAMAMOTO, T. MUKAI, and S. MAEKAWA (NICT)
Appl. Opt. Vol.52, A281-A289 (2013).

A volumetric display system using an optical imaging device consisting of numerous dihedral corner reflectors placed perpendicular to the surface of a metal plate is proposed. Image formation by the dihedral corner reflector array (DCRA) is free from distortion and focal length. In the proposed volumetric display system, a two-dimensional real image is moved by a mirror scanner to scan a three-dimensional (3D) space. Cross-sectional images of a 3D object are displayed in accordance with the position of the image plane. A volumetric image is observed as a stack of the cross-sectional images. The use of the DCRA brings compact system configuration and volumetric real image generation with very low distortion. An experimental volumetric display system including a DCRA, a galvanometer mirror, and a digital micro-mirror device was constructed to verify the proposed method. A volumetric image consisting of $1024 \times 768 \times 400$ voxels was formed by the experimental system.

Volumetric display using a rotating prism sheet as an optical image scanner

Yuki MAEDA, Daisuke MIYAZAKI, and Takaaki MUKAI
Appl. Opt., Vol. 52, pp. A182-A187 (2013).

We developed a volumetric display that uses a rotating prism sheet as an optical scanner. A cross-sectional image of a three-dimensional (3D) object was moved laterally by the rotating prism sheet. A stack of the cross-sectional images constructed a 3D volume image that satisfies all requirements of stereoscopic vision. Since the mechanical load of the proposed scanning method was small, it is easy to enlarge the effective area of the scanner and its scanning area. We used a concave mirror to collimate rays emitted from each point to reduce the aberration caused at the prism sheet. A displayed 3D image had a size of $7 \text{ cm} \times 5 \text{ cm} \times 7 \text{ cm}$ and a resolution of $1024 \times 768 \times 200$ voxels.

Volumetric display based on optical scanning of an inclined image plane by an image rotator and imaging by a dihedral corner reflector array

Yuki MAEDA, Daisuke MIYAZAKI, Takaaki MUKAI and Satoshi. MAEKAWA (NICT)
Proc. Soc. Photo-Opt. Instrum. Eng., Vol.8648, 86481O (2013).

We propose to use a rotational optical scanning method for a volumetric three-dimensional (3D) display based on optical scanning of an inclined image plane. The image plane was moved by an image rotator and formed by a dihedral corner reflector array, which is a distortion free imaging element forming a real image at a plane-symmetrical position. A stack of the moved and formed image planes of a two-dimensional (2D) display created displayable space of a 3D image, which satisfies all the criteria of stereoscopic vision and can be seen by the naked eyes. The image rotator used in this study was constructed of prism sheets and planar mirrors. The image plane was moved rotationally by rotating the proposed image rotator on an axis parallel to the mirror plane. Enlargement of the displayable space is achieved by just extending the distance between the 2D display and the mirror, so that the proposed scanning method is effective to display a large 3D image for our volumetric display system. We made a prototype display and observed a moved image plane to measure the displayable space of the 3D image. The size of the displayable space was $1200 \text{ [cm}^3\text{]}$ that is approximately six times as large as our previous display using a translational optical scanning method.

Large viewing region auto-stereoscopic display using a slanted cylindrical lens array

Tetsuro OKUYAMA (Panasonic), Toshikazu OHTSUKI (Panasonic), Akio NISHIMURA (Panasonic), Hiroyuki YOSHIDA (Panasonic), Takahiro TOYOTA, Kenta OKODA, and Daisuke MIYAZAKI
Proceedings of 3DSA2013, P5-2 (2013).

New auto-stereoscopic display method, which has a large viewing region, is proposed. It forms exit pupils at the positions of viewer's eyes by tracking them and shows parallax images individually. This paper demonstrates the principle of it with a prototype display system.

Multi-Color See-Through Retinal Projection Head-Mounted Display

Yutaka ITO, Katsushi TAKAICHI, and Hideya TAKAHASHI

ICIC Express Letters, Vol.7, 6, pp.1755-1760 (2013).

We have previously proposed a multi-color see-through retinal projection head-mounted display (HMD). It consists of an image projection system and a holographic optical element (HOE). To implement the color HOE, we proposed the superimposing method of convergent points of each primary color. In this method, it is important to exactly superimpose the reconstructed convergent points to avoid causing color shift of retinal projection images. To overcome this problem, we proposed the extended Maxwellian view by using the extended convergent points. On the other hand, in a retinal projection see-through HMD, the extremely long focal depth is the most important feature. However, the focal depth of the prototype HMD did not discussed previously. Therefore, in this paper, we confirmed the feature of the extremely long focal depth of the extended Maxwellian view. Additionally, we estimated the size of the extended viewing zone of the extended Maxwellian view. This paper describes the principle of the extended Maxwellian view and also describes the experimental results.

Tele-Auscultation Support System with Mixed Reality Navigation

Kenta HORI(Gunma Prefectural College of Health Sciences), Yusuke UCHIDA(Kyoto University), Tsukasa KAN, Maya MINAMI(Kyoto University Hospital), Chisako NAITO(Kyoto University Hospital), Tomohiro KURODA(Kyoto University Hospital), Hideya TAKAHASHI, Masahiko ANDO(Nagoya University Hospital), Takashi KAWAMURA(Kyoto University), Naoto KUME(Kyoto University Hospital), Kazuya OKAMOTO(Kyoto University Hospital), and Tadamasu TAKEMURA(University of Hyogo), and Hiroyuki YOSHIHARA(Kyoto University Hospital)

Proc. 35th Annual International Conference of the IEEE EMBS, pp.4646-4649, (2013).

The aim of this research is to develop an information support system for tele-auscultation. In auscultation, a doctor requires to understand condition of applying a stethoscope, in addition to auscultatory sounds. The proposed system includes intuitive navigation system of stethoscope operation, in addition to conventional audio streaming system of auscultatory sounds and conventional video conferencing system for telecommunication. Mixed reality technology is applied for intuitive navigation of the stethoscope. Information, such as position, contact condition and breath, is overlaid on a view of the patient's chest. The contact condition of the stethoscope is measured by e-textile contact sensors. The breath is measured by a band type breath sensor. In a simulated tele-auscultation experiment, the stethoscope with the contact sensors and the breath sensor were evaluated. The results show that the presentation of the contact condition was not understandable enough for navigating the stethoscope handling. The time series of the breath phases was usable for the remote doctor to understand the breath condition of the patient.

Wide-Viewing Angle Three-Dimensional Display Using Curved HOE Lens Array

Yoshiaki OSHIMA, Hideya TAKAHASHI, and Kenji YAMADA (Osaka University)

Proc.SPIE-IS&T Electronic Imaging, Vol.8648, pp. 86481N-1-86481N-9 (2013).

We propose an omnidirectional three-dimensional (3D) display system. This is a tool for communication around a 3D image between a small number of people. This 3D display consists of multiple basic 3D display units. Each basic 3D display unit consists of a projector and a curved HOE lens array sheets. The projector is located on the center of the curvature of the curved HOE lens array, and it projects light rays on the curved HOE lens array with ascending vertical angle 45-degree. Projected light rays are reflected and reconstruct the 3D image over the center of the curvature by the curved HOE lens array. In this method, even though the viewing angle of each HOE lens does not increase, the viewing angle of the 3D image by the curved HOE lens array can be increased. To verify the effectiveness of the proposed method, we constructed the prototype basic 3D unit. The viewing angle of a 3D image was 44-degree. Therefore, the viewing angle was increased by the proposed method com-

pared to 17-degree by the conventional flat HOE lens array. This paper describes the principle of proposed 3D display system, and also describes the experimental results.

Evaluation of a Compound Eye Type Tactile Endoscope

Kayo YOSHIMOTO(Osaka University), Kenji YAMADA(Osaka University), Nagisa SASAKI(Osaka University), Maki TAKEDA(Osaka University), Sachiko SHIMIZU(Osaka University), Toshiaki Nagakura(Osaka Electro-Communication University), Hideya TAKAHASHI, and Yuko OHNO(Osaka University)
Proc.SPIE-BIOS2013 Endoscopic Microscopy VIII, Vol.8575, pp. 85750Z-1-85750Z -6 (2013).

Minimally invasive surgical techniques for endoscope become widely used, for example, laparoscopic operation, NOTES (Natural Orifice Transluminal Endoscopic Surgery), robotic surgery and so on. There are so many demand and needs for endoscopic diagnosis. Especially, palpation is most important diagnosis on any surgery. However, conventional endoscopic system has no tactile sensibility. There are many studies about tactile sensor for medical application. These sensors can measure object at a point. It is necessary to sense in areas for palpation. To overcome this problem, we propose compound eye type tactile endoscope. The proposed system consists of TOMBO (Thin Observation Module by Bound Optics) and clear silicon rubber. Our proposed system can estimate hardness of target object by measuring deformation of a projected pattern on the silicon rubber. The purpose of this study is to evaluate the proposed system. At first, we introduce approximated models of the silicone and the object. We formulate the stiffness of object, the deformation of silicone, and the whole object. We investigate the accuracy of measured silicone's lower surface for deformation of silicone by prototype system. Finally, we evaluate the calculated stiffness of the soft object.

Multi-Color See-Through Retinal Projection Head-Mounted Display

Katsushi TAKAICHI and Hideya TAKAHASHI

ICIC Express Letters, Vol.6, 5, pp.1291-1296 (2012).

We developed a multi-color see-through retinal projection head-mounted display (HMD). Its notable features are the extremely deep focal length and the high contrast image by using the principle of the Maxwellian view. It consists of an image projection optics system and a holographic optical element (HOE). The HOE is used as a combiner that superimposes the virtual image on the real scene to realize a function of the see-through. The HOE also works as a condenser lens to achieve the Maxwellian view. See-through HMDs provide an effective capability for Mixed Reality tools such as a personal mobile information display. In this application, since the capability to display color images is important, the HOE can be reconstructed by some primary colors. This paper describes the principle of the proposed multi-color see-through retinal projection HMD and also describes the experimental results.

Wide-Viewing Angle Three-Dimensional Display Based on the Ray Reconstruction Method Using Multiple Micro-Projectors

Hideya TAKAHASHI, Kenta HIROOKA, and Kenji YAMADA (Osaka University)

Proc.SPIE-IS&T Electronic Imaging, Vol.8288, pp. 828824-828824-6 (2012).

We propose an omnidirectional three-dimensional (3D) display system. This is a tool for communication around a 3D image among a small number of people. This 3D display system consists of multiple basic 3D display units. The basic unit consists of a micro-projector, a lenticular lens array sheet, and a cylindrical lens. In this basic unit, since a screen is not used, the light rays from a micro-projector pass through a lenticular lens array sheet and observed directly. Thus, the spatial density distribution of projected light rays is partial. To average the spatial density of projected light rays, we use a cylindrical lens. To increase the viewing angle, we aligned multiple basic units in a circle, and displayed 3D images at the center of the circle. To verify the effectiveness of the proposed 3D display, we constructed the prototype system. This prototype consists of 8 basic units. They are aligned 18-degree apart in a circle and the radius is 95 mm. The maximum size of displayed 3D images is 35 mm x 40 mm x 35 mm. The viewing angle of a 3D image is 124-degree. This paper describes the principle of proposed 3D display system, and also describes the experimental results.

Matching between Ellipsoid Model and 3D Points Using Gaussian Function for Measurement of Angle of Human Joint

Shigeyoshi NAKAJIMA and Mitsuhiko IKEBUCHI

ICIC (Innovative Computing, Information and Control) Express Letters, Vol.7, No.6, pp.1833-1838(2013)

We propose a new contactless method to measure an angle of a human joint. An ordinary medical staff makes an angle scale (i.e. goniometer) to contact skin of a patient in a conventional method. But results of such contacting method include error over 5 degree. We employed an infra-red depth sensor, Gaussian evaluation function and an optimization algorithm. We show errors less than the conventional method and good grouping of measurement results of the proposed method.

Applied Chemistry

Performance of the “SiO”-Carbon Composite-Negative Electrodes for High-Capacity Lithium-Ion Batteries; Prototype 14500 Batteries

J. Power Sources, **225**, 221-225 (2013).

Masayuki YAMADA, Kazutaka UCHITOMI, Atsushi UEDA, Kazunobu MATSUMOTO, Tsutomu OHZUKU
Prototype 14500 batteries (14 mm dia. and 50 mm hgt.; AA size) consisted of the “SiO”-carbon composite-negative and $\text{LiCo}_{1/3}\text{Ni}_{1/3}\text{Mn}_{1/3}\text{O}_2/\text{LiCoO}_2$ (7/3 by weight)-positive electrodes were designed, fabricated and examined in voltage ranging from 2.5 to 4.2 V at -20, -10, 0, and +23 °C. The batteries were stored and delivered 1 Ah at 200 mA and 0.96 Ah at 2 A, and the capacity remained after 300 cycles at 23 °C was 0.7 Ah. Abuse tests, such as overcharging to 12 V, nail penetration, and heating of fully charged batteries in an oven at 150 °C, were also carried out and shown that the batteries showed neither smoke nor fire for all the tests examined. The battery performance was compared to that of conventional batteries with graphite-negative electrodes in the same size and the characteristic features of the lithium-ion batteries with the SiO-carbon composite-negative electrodes were discussed from the experimental results.

Capacity Fading of Lithium-Ion Cells Having $\text{Li}[\text{Li}_{1/3}\text{Ti}_{5/3}]\text{O}_4$ (LTO)-Negative Electrodes for the First- and Second-Generation 12 V Lead-Free Batteries

J. Electrochem. Soc., **159**, A1710-A1715 (2012).

Lina WANG, Kensuke NAKURA, Mitsuyasu IMAZAKI, Narumi KAKIZAKI, Kingo ARIYOSHI and Tsutomu OHZUKU

Lithium-ion cells consisting of $\text{Li}[\text{Li}_{1/3}\text{Ti}_{5/3}]\text{O}_4$ (LTO) and $\text{Li}[\text{Li}_{0.1}\text{Al}_{0.1}\text{Mn}_{1.8}]\text{O}_4$ (LAMO) or $\text{Li}[\text{Ni}_{1/2}\text{Mn}_{3/2}]\text{O}_4$ (LiNiMO) were examined at currents higher than 1 mA cm^{-2} at room temperature. Capacity fading was observed for both LTO/LAMO and LTO/LiNiMO cells during the continuous charge and discharge at 1, 2, and 4 mA cm^{-2} when a microporous membrane usually used so far was applied. In order to understand the capacity fading, Li/LAMO and Li/LTO cells together with zero-volt lithium-ion cells consisting of LTO or LAMO were fabricated and examined. Among these cells, the rechargeable capacity of a zero-volt lithium-ion cell of LTO with a microporous membrane faded cycle by cycle, while the other cells did not show such obvious capacity fading. From these results, a possible source of capacity fading was discussed in terms of a mass transport problem due to the “zero-strain” insertion electrode combined with a microporous membrane. A solution of the problem is also given in such a way that a non-woven cloth is substituted for the microporous membrane as a separator in LTO/LAMO and LTO/LiNiMO cells for the first- and second-generation 12 V lead-free batteries, respectively.

Reaction Mechanism of “SiO”-Carbon Composite-Negative Electrode for High-Capacity Lithium-Ion Batteries

Masayuki YAMADA, Akira INABA, Atsushi UEDA, Kazunobu MATSUMOTO, Tomio IWASAKI and Tsutomu OHZUKU

J. Electrochem. Soc., **159**, A1630-A1635 (2012).

The reaction mechanism of a “SiO”-carbon composite-negative electrode for high-capacity lithium-ion batteries is examined by Si K-edge X-ray absorption near edge structure (XANES), ^7Li and ^{29}Si nuclear magnetic resonance (NMR), and scanning transmission electron microscopy (STEM) with Si L-edge electron energy loss spectroscopy (EELS) and energy dispersive X-ray spectroscopy (EDX). According to the analytical results, “SiO” consisting of nano-size Si particles dispersed in amorphous SiO_2 is converted to lithium-silicon alloys and lithium silicon oxides during the first charge in lithium-ion batteries, and the nano-size silicon particles surrounded by lithium silicon oxides are rechargeable for subsequent cycles. Molecular dynamics (MD) simulation of “SiO” is also carried out and shown that silicon particles grow during the first cycle and are surrounded by a good lithium-ion conductor of lithium silicon oxides. From these results, the reaction mechanism of “SiO” is discussed in terms of high-capacity negative electrodes for lithium-ion batteries.

Removal of Ion implanted poly vinyl phenol using Wet ozone

Yousuke GOTO, Yukihiro ANGATA, Masashi YAMAMOTO, Toshio SEKI, Jiro MATSUO and Hideo HORIBE
J. Photopolym Sci. Technol., **26**(4), 467–472 (2013).

We have investigated the removal of poly vinyl phenol (PVP) into which was B, P and As ions implanted with a dose of $5 \times 10^{13} \sim 5 \times 10^{15}$ atoms/cm² at 70keV, using wet ozone. Also, we investigated the thickness of altered layer of ion-implanted PVP using Secondary Ion Mass Spectrometry (SIMS). We investigated the chemical reactivity of wet ozone and ion-implanted PVP by FT-IR. The removability of ion-implanted PVP using wet ozone decreased with increasing dose because the degrees of alteration of benzene ring and O-H group increase with increasing dose. From the results of SIMS, the thickness of altered layer of B-ion-implanted PVP was 387nm, that of P-ion-implanted PVP was 232nm, and that of As-ion-implanted PVP was 142nm. However, the degree of alteration should increase in order of B, P and As because any samples were implanted at same acceleration energy (70keV). FT-IR indicated that benzene ring content percentage was almost same at removed and not removed. On the other hand, in O-H group, there is a clear difference at removed and not removed, O-H group content percentage decreased drastically at implanted PVP with a dose of 5×10^{14} atoms/cm² over. Therefore, the removability of ion-implanted PVP using wet ozone depends on O-H group content than that of benzene ring.

Relationship between Interfacial Hydrophobicity and Hydroxylation Activity of Fungal Cells Located on an Organic-Aqueous Interface

S. Oda, N. Sakamoto, H. Horibe, A. Kono, and S. Ohashi,
J. Bioscience and Bioengineering, **115** (5), 544-546 (2013).

In a liquid–liquid interface bioreactor, fungal cells locate in a hydrophilic polyacrylonitrile microsphere layer on an aqueous–organic interface. In this article, effects of hydrophobicity of the interface on *n*-decane hydroxylation activity of *Monilliera* sp. NAP 00702 was examined. (–)-4-Decanol production was significantly enhanced to 132% by addition of polytetrafluoroethylene.

Development of Ni Particle Dispersed Poly(methylmethacrylate) Composites Exhibiting Conductor/Insulator Transition by the Positive Temperature Coefficient Effect of Electrical Resistivity

A. Kono, K. Shimizu, H. Nakano, Y. Goto, S. Takahashi, T. Ougizawa, H. Horibe, and M. Yamamoto
Polymer J., **45**(7), 690-694 (2013).

This paper discusses the positive-temperature-coefficient effects of resistivity in Ni particle-dispersed poly(vinylidene fluoride) (PVDF) composites based on experiment results from SEM, DSC, and pressure-volume-temperature (PVT) measurements. The melting points of composites with Ni content of 10, 20, 30, 40, and 50vol.% were equal to that of pure PVDF. The PTC effects in composites with Ni content of 40 and 50vol.% occurred at temperatures near the melting point of the PVDF matrix, whereas those in composites with Ni content of 20 and 30vol.% occurred at temperatures below the melting point of the PVDF matrix. We found that the PTC effect occurs even without melting of the matrix polymer. Moreover, we determined that a slight increase in specific volume at temperatures below the melting point of the matrix polymer acts fully as a driving force for forming a gap between fillers. This suggestion was backed up by theoretical analyses using percolation theory and a thermal-fluctuation-induced tunneling model.

Estimation of the Activation Energy of Resist Removal Using Wet Ozone

Yousuke GOTO, Tomohiro FUNASAKA, Masashi YAMAMOTO, Kunihiro KOIKE, Hideo HORIBE
KOBUNSHI RONBUNSHU, **70**(6), 295–299 (2013)

Using environmentally friendly wet ozone instead of conventional chemicals, we removed positive-tone novolak resists. In the wet ozone process, resists are decomposed and removed through ozonolysis of the resists and the hydrolysis of the ozonolysis products. It was revealed that the temperature difference (= “wet ozone temperature” – “substrate temperature”), to control water requirements for the hydrolysis strongly influences the resist removal rate. The activation energy of the removal reaction of this process was estimated to be 28.0 kJ/mol. The activation energy is 10~20 kJ/mol lower than that of the commonly-used ashing process, therefore the resist can be removed at a higher rate and at a lower temperature.

Effect of Heat-Treatment Temperature after Polymer Melt and Blending Ratio on the Crystalline Structure of PVDF in a PVDF/PMMA Blend

H. Horibe, Y. Hosokawa, H. Oshiro, Y. Sasaki, S. Takahashi, A. Kono, T. Danno, and T. Nishiyama

Polymer J., (26 June 2013) doi:10.1038/pj.2013.53

We analyzed control of the crystalline structure of poly(vinylidene fluoride) (PVDF) in a PVDF/poly(methylmethacrylate) (PMMA) blend by varying the polymer blend ratio (PVDF/PMMA=60/40, 70/30 and 80/20 wt%) and the heat-treatment temperature (160–210 °C) just after the polymer melt. We obtained PVDF (form I) limitedly by heat treatment at 185 and 190 °C after blending PVDF/PMMA 70/30 wt%. The samples produced under other conditions indicated PVDF (form II). Results of differential scanning calorimetry (DSC), polarized light micrography and light transmittance indicated that samples of PVDF/PMMA 70/30 wt% heat-treated at 185 and 190 °C exhibited high compatibility between PVDF and PMMA, respectively. In contrast, PVDF (form II) samples obtained in other conditions indicated lower compatibility. We assumed that PVDF crystalline structure became the structure of the PVDF (form I) according to decrease of the crystallization rate by the highest compatibility between PVDF and PMMA. Pure PVDF crystallized very fast, so PVDF (form I) cannot be developed from pure PVDF by simply controlling the heat-treatment temperature.

Correlation between Different Crystal Structures and Physical Properties of PVDF Films Fabricated by Solvent Casting from a Single Solvent

Yasutaka SASAKI, Hironori OSHIRO, Seiji TAKAHASHI, Akihiko KONO, Takashi Nishiyama, Koji AIZAWA, and Hideo HORIBE

KOBUNSHI RONBUNSHU, in press

Poly(vinylidene fluoride) (PVDF) has three crystal structures: form I, II, and III. The relationship between the PVDF crystal structures and physical properties had not been investigated. We have previously reported that three PVDF crystal structures were made from a single solvent. In this study we evaluated the thermal, optical, and electrical properties of all three PVDF crystal structures which can be made by solvent casting using a single solvent. Light transmittance (wavelength: 800 nm, 33 μm film thickness) was 93 % (form II), 95 % (form III), and 97 % (form I). Melting point was 165 °C (form I), 174 °C (form II), and 173 °C (form III). The relative permittivity was 13 (form I), 6 (form II), and 11 (form III). From these results, we confirmed that the physical properties of PVDF depended on the difference in the crystal structure.

Quantification of the solvent evaporation rate during the production of three PVDF crystalline structure types by solvent casting

Hideo Horibe, Yasutaka Sasaki, Hironori Oshiro, Yukari Hosokawa, Akihiko Kono, Seiji Takahashi and Takashi Nishiyama

Polymer J., in print.

In this study, we quantified the solvent evaporation rate in the production of three poly(vinylidene fluoride) (PVDF) crystalline structures using the solvent casting method, the first known report on such quantification. The evaporation conditions of drying temperature and pressure for the solvent species during solvent casting were varied. The results indicated that the crystalline structures of forms I, II and III of PVDF were obtained when the solvent evaporation rates were < 0.0001 , > 0.2 and between 0.03 and $0.00058 \text{ g min}^{-1}$, respectively. From the above quantitative analysis, it was established that the crystalline structure of PVDF from solvent casting is predominantly determined by the solvent evaporation rate.

Quantitative Analysis of Positive Temperature Coefficient Characteristics of Conductive Composites

Hajime NAKANO, Katsuya SHIMIZU, Yuto KOSHIMORI, Yoji NOMURA, Seiji TAKAHASHI, Akihiko KONO, Toshiaki OUGIZAWA, and Hideo HORIBE

KOBUNSHI RONBUNSHU, in press

Conductive polymer composites filled with carbon or metal particles exhibit a positive-temperature-coefficient (PTC) of resistivity. In our previous studies, we speculated that only the volume expansion of polymers upon heating cause the PTC effect and we conducted quantitative analyses focusing on the decrease of the apparent

filler content of the composites during volume expansion of polymers. Later, we found that PTC effect occurs when the conductive path is cut off due to crystal melting and volume expansion of the base polymer along with rising temperature. In this study, we analyzed the PTC effect of polyvinylidene fluoride (PVDF)/Ni composite quantitatively and found that the apparent Ni content (C_{Ni(T)}) decreases along with rising temperature. When C_{Ni(T)} becomes about 98% of the Ni content at room temperature (C_{Ni-R.T.}), the resistivity is 10 times of that at room temperature. When C_{Ni(T)} becomes about 96% of C_{Ni-R.T.}, the resistivity exceeds 1083 · cm and the composites serve as insulators. In conclusion, we proved that, the Ni content is not constant when the PTC effect occurs.

Electrical property of Ni composite based on HDPE and PMMA having different M_w

Katsuya SHIMIZU, Hajime NAKANO, Akihiko KONO, Seiji TAKAHASHI, and Hideo HORIBE
KOBUNSHI RONBUNSHU, in press

This paper discusses the relationships between electrical properties of Ni particle dispersed high-density polyethylene (HDPE) and Poly (methyl methacrylate) (PMMA) composites and Ni content and weight-average molecular weight (M_w) of base polymer. Moreover, we considered about the difference of conductive actions to M_w by HDPE/Ni and PMMA/Ni. In HDPE/Ni and PMMA/Ni, the ρ_L decreased by increasing Ni content. It is because many electric conductive paths are formed because Ni content increases. When Ni content is equal, in HDPE/Ni composites, resistivity at room temperature (ρ_L) was decreased, and revelation of the PTC effect became high temperature so that M_w is small. In PMMA/Ni composites, ρ_L decreases and it was hard coming to revealed of the PTC effect so that M_w is large. This was a tendency that contrary to HDPE/Ni. By SEM images, in HDPE/Ni, Ni particles distributes unevenly, in PMMA/Ni, it was distributing uniformly to the whole. Therefore, we considered that in HDPE/Ni, change of the degree of crystallinity by the difference in M_w influences in conductivity strongly, in PMMA/Ni without crystalline part, the increase in the viscosity by M_w having become large has influenced.

Organotellurium-Mediated Living Radical Polymerization (TERP) of Acrylates Using Ditelluride Compounds and Binary Azo Initiators for the Synthesis of High-Performance Adhesive Block Copolymers for On-Demand Dismantlable Adhesion

Tadashi INUI, Keisuke YAMANISHI, Eriko SATO, and Akikazu MATSUMOTO
Macromolecules, **46**(20), 8111-8120 (2013)

We report the organotellurium-mediated living radical polymerization (TERP) using diphenylditelluride (DT-Ph) and di-*n*-butylditelluride (DT-Bu) in the presence of a binary azo initiator system consisting of 2,2'-azobis(isobutyronitrile) (AIBN) and 2,2'-azobis(4-methoxy-2,4-dimethylvaleronitrile) (AMVN) with different decomposition rates for the facile synthesis of high-molecular-weight block copolymers containing a polar side group. The block copolymers containing the poly(*tert*-butyl acrylate) (PtBA) sequence as the reactive segment and the random copolymer sequences of *n*-butyl acrylate (nBA) or 2-ethylhexyl acrylate (2EHA) with 2-hydroxyethyl acrylate (HEA) as the adhesive segment were synthesized. The concurrent use of the binary initiators was revealed to effectively increase both the polymerization reactivity and the molecular weight of the polymers along with a narrow molecular weight distribution. The produced block copolymers exhibited high performance for the dismantlable adhesion responsible for the dual external stimuli consisting of photoirradiation and postbaking in the presence of a photoacid generator.

Reversible Thickness Control of Polymer Thin Films Containing Photoreactive Coumarin Derivative Units

Eriko SATO, Sayoko NAGAI, and Akikazu MATSUMOTO
Progress in Organic Coatings, **76**(12), 1747-1751 (2013)

The reversible control of the thickness of polymer thin films was investigated using (meth)acrylic polymers containing photoreactive coumarin derivative units in the side chain. Coumarin derivative units underwent dimerization and the reverse-dimerization by photoirradiation and were used as a reversible cross-linking point. The homopolymer of 7-methacryloyloxy-4-methylcoumarin ($T_g = 194^\circ\text{C}$) did not cause changes in film

thickness after photoreactions. The homopolymer of 7-(2-acryloyloxyethoxy)-4-methylcoumarin (AEMC) ($T_g = 89^\circ\text{C}$) decreased 19% of film thickness by photodimerization and 73% of the decreased thickness was recovered after the reverse-dimerization and the subsequent thermal annealing at 130°C . The reverse-dimerization of the copolymer of AEMC and *n*-butyl acrylate (AEMC content = 19 mol%, $T_g = 11^\circ\text{C}$) resulted in 53% of recovery from the decreased film thickness without annealing. The mobility of polymer main-chain was revealed to be essential factor to change film thickness by photoreactions. Photodimerization of coumarin derivative units in low glass transition temperature (T_g) tended to proceed faster than in high T_g polymers and resulted in larger decrease in film thickness.

Precise Synthesis of Acrylic Block Copolymers and Application to On-Demand Dismantlable Adhesion Systems in Response to Photoirradiation and Postbaking

Keisuke YAMANISHI, Eriko SATO, and Akikazu MATSUMOTO

Journal of Photopolymer Science and Technology, **26**(2), 239-244 (2013)

High-molecular-weight and functional acrylic block copolymers containing both the reactive and polar repeating units were synthesized using organotellurium-mediated living radical polymerization (TERP) technique. The block copolymers consisted of poly(*tert*-butyl acrylate) as the reactive segment and the random copolymer sequence containing *n*-butyl, 2-ethylhexyl, and 2-hydroxyethyl acrylate repeating units as the adhesive segment. The block copolymers exhibited high performance for the dismantlable adhesion responsible to dual external stimuli consisting of photoirradiation and the postbaking in the presence of a photo acid generator.

Facile Synthesis of Well-Defined High Molecular Weight Acrylic Polymers by Living Radical Polymerization Using Binary Radical Initiators (Hot Topics)

Eriko SATO

Kobunshi (High Polymers, Japan), **62**(9), 53 (2013)

Design and Performance Enhancement of Dismantlable Adhesion Materials Using Degradation and Side-Chain Reactions of Polymers

Eriko SATO

The 148th Regular Meeting of Polymers-in Concrete Commission, Invited Lecture, Tokyo, November 14, 2012 (in Japanese)

“Reversible Transformation of Wettability Using Cure Shrinkage” and “Introduction of the Society for Young Scientists in Kansai Branch of the Adhesion Society of Japan”

Eriko SATO

The 11th Forum for Young Scientists in Industry-Government-Academia, Chubu Branch of the Adhesion Society of Japan, Invited Lecture, Nagoya, December 7, 2012 (in Japanese)

Design of Dismantlable Adhesion Materials Using Reactive Polymers

Eriko SATO

The 1st Meeting of Interface Chemistry Association, Invited Lecture, Osaka, June 6, 2013 (in Japanese)

Design of Dismantlable Adhesive Materials Using Photoacid Generators-Compatibility of Dismantlability and Stability-

Eriko SATO

The 132nd Lecture Meeting of Japanese Research Association for Surface Finishing by UV, EB, Laser, and Ion Beams, Invited Lecture, Osaka, June 12, 2013 (in Japanese)

There has been considerable interest in adhesives providing both strong bonding during use and easy debonding on demand, so-called dismantlable adhesion technique. We are currently investigating polyacrylates-based dismantlable pressure-sensitive adhesives in combination with a photoacid generator (PAG). Polyacrylates such as poly(*t*-butyl acrylate) undergo acid-catalyzed side-chain degradation and are converted to polyacrylic acid

involving an increase in glass transition temperature (T_g) and isobutene evolution. The increased T_g and gas evolution effectively reduce peel strength. High molecular weight acrylic block copolymers containing PAG showed good peel strength and thermal stability before UV irradiation, and resulted in quick and effective dismantling after UV irradiation and a subsequent heating.

Design of Transformable Polymer Materials Using Reactive Polymers

Eriko SATO

NAIST Colloquium of Future Development 2013 –Networks on Molecules and Human Resources Making Tomorrow, Invited Lecture, Nara, August 9, 2013 (in Japanese)

X-ray Spectrometry

Kouichi TSUJI, Kazuhiko NAKANO, Yoshio TAKAHASHI, Kouichi HAYASHI, and Chul-Un RO

Anal. Chem., Vol. 84, pp. 636-668 (2012).

In this review, we focus on the most significant and essential progress in X-ray spectrometry (XRS) published during the period from January 2010 to August 2011 covering developments and improvements in X-ray optics, X-ray detectors, new quantification models in X-ray spectra and data evaluation, micro-X-ray fluorescence (micro-XRF) including 3D X-ray fluorescence (3D-XRF), elemental imaging techniques, electron probe microanalysis (EPMA), total reflection X-ray fluorescence (TXRF), particle-induced X-ray emission (PIXE) analysis, and X-ray absorption spectrometry (XAS). Herein, we focus on X-ray spectrometry, and thus X-ray radiography used for only investigating inside structure images and X-ray diffraction (XRD) is not covered. However, we will introduce articles including combinations of these X-ray imaging techniques and other spectroscopic techniques. In addition, different applications in each subfield of XRS, including sample preparation, standard materials, energy-dispersive XRF (ED-XRF) and wavelength-dispersive XRF (WD-XRF), are described. We attempt to look over the current trends in this analytical field with a critically citing of selected papers to support the research activity of the community of X-ray scientists.

Sample Preparation of Seawater for Total Reflection X-ray Fluorescence Analysis

Tatsushi YOSHIOKA, Yukiko IMANISHI, Kouichi TSUJI, Hideki TAKABE, Kouji AKIOKA, Takashi DOI, and Masahiro ARAI

Advances in X-Ray Chemical Analysis, Japan, Vol.43, pp. 211-221 (2012).

Total Reflection X-ray Fluorescence (TXRF) is effective technique for analysis of the sample placed on flat substrate. When TXRF is applied for solution samples, it is important to prepare a thin residue to reduce self-absorption of X-rays and scattered X-rays. The dried residue of solution sample like seawater tends to form relatively large crystal, therefore it is usually difficult to make a flat and thin residue. Thus, we studied sample preparation of seawater for TXRF analysis. In this paper, the influence of substrate-temperature and surfactant in drying process is discussed. We proposed to add surfactant, which is useful for reducing interfacial tension, on the droplet of seawater. As a result, by using surfactant and being substrate-temperature of 70 degree in drying process, a thin film-type residue was obtained. RSD of TXRF intensities for dried residues was less than 5%. We found that the optimum condition of seawater for TXRF analysis was a substrate-temperature of 70 degree with surfactant in drying process.

Development of Compact X-ray Analytical Microscope

Shintaro KOMATANI, Tomoki AOYAMA, Sumito OHZAWA, and Kouichi TSUJI

Advances in X-Ray Chemical Analysis, Japan, Vol.43, pp. 241-247 (2012).

In the case of conventional X-ray analytical microscopes, the focused primary X-rays were used for the micro analysis. However, by focusing the X-rays and making the analysis area smaller, the intensity of the X-rays decreases, requiring a powerful X-ray tube. As a result, it turned into a large XRF instrument. At this point, we chose not to focus the primary X-rays, but to focus our attention only on the detection of the fluorescence X-rays excited from the sample. Moreover, attempting to improve the size and weight of the system as a whole, we realized a portable system. In this technique, we were able to use X-ray tubes of small size and low electronic

power without limitations of the spot size. Using this technique, we developed a portable system using a battery. We used a polycapillary half lens for collecting X-ray fluorescence from a small area, leading to a special resolution of 140 μm for the additional advantage, we can apply this portable micro-XRF instrument for on-site analysis in environmental science, industrial process, etc.

Development of 2D Dispersive Device for XRF Imaging Spectrometer

Takashi OHMORI, Masatoshi HATAYAMA, Hisataka TAKENAKA, and Kouichi TSUJI

Advances in X-ray Analysis, Vol. 55, pp. 228-233 (2012).

Micro-XRF analysis provides us with elemental maps, which are very useful for understanding the samples under test. Usually, scanning-type elemental mapping is performed. That means, a sample stage is scanned to a fixed X-ray micro beam. XRF analysis is performed at the scanned points, leading to 2D elemental mapping. One of the drawbacks of this technique is the long acquisition time depending on the area being mapped and the lateral resolution required. Thus, projection-type elemental mapping has been studied. We have studied the projection type XRF imaging by using a straight polycapillary optic combined with an X-ray CCD camera. To obtain the elemental map, we applied a wavelength dispersive spectrometer (WDS). In this paper, we report a newly developed 2D dispersive device. The construction and analytical performance of this X-ray optic will be explained.

Micro-X-ray Fluorescence Analysis of Sr in Fish Otolith of Ayu *Plecoglossus altivelis*

Takashi NAKAZAWA, Kazuhiko NAKANO, Hiromitsu ONCHI, Mayu NAMITA, Susumu YAMOCHI, and Kouichi TSUJI

BUNSEKI KAGAKU, Vol. 61, pp. 637-642 (2012).

We have applied a polycapillary X-ray focusing optic to a micro X-ray fluorescence analysis (micro-XRF) instrument. The spatial resolution of the developed instrument was about 10 micrometers. We used the micro-XRF instrument to determine the migratory environmental history of a fish (ayu : *Plecoglossus altivelis*) from the Sr intensity profile in a otolith (ear stone). The obtained 2D elemental map showed a high concentration of Sr distributed in the center of the otolith, indicating that this ayu stayed in the sea during the corresponding period. In order to investigate the migratory environmental history of the ayu, we compared captured fishes with cultivated fishes based on the Sr intensity profile. The results suggest that captured fishes include four cultivated fishes. We could easily estimate the migratory environmental history of fishes by using this method and measured nondestructively in air.

Development of X-ray 2D Dispersive Device for WD-XRF Imaging Spectrometer

Takashi OHMORI, Masatoshi HATAYAMA, Tadayuki OHCHI, Hisashi ITO, Hisataka TAKENAKA and Kouichi TSUJI

Powder Diffraction, Vol. 27, pp. 71-74 (2012).

Micro-X-ray fluorescence (XRF) analysis provides us with elemental maps that are very useful for understanding the samples under test. Usually, scanning-type elemental mapping is performed. That means a sample stage is scanned to a fixed X-ray microbeam. XRF analysis is performed at the scanned points, leading to 2D elemental mapping. One of the drawbacks of this technique is the long acquisition time depending on the area being mapped and the lateral resolution required. Thus, projection-type elemental mapping has been studied. We have studied the projection type XRF imaging by using a straight polycapillary optic combined with an X-ray CCD camera. To obtain the elemental map, we applied a wavelength dispersive spectrometer (WDS). In this paper, we report a newly developed 2D dispersive device. The construction and analytical performance of this X-ray optic will be explained.

Liquid / Liquid Near Interface Analysis by Micro-XRF Using Needle-Type Collimators

Yoshihiko NISHIDA and Kouichi TSUJI

Memoirs of the Faculty of Engineering Osaka City University, Vol. 53, pp. 27-30 (2012).

We have developed a method of micro XRF using injection needle-type collimators. Two injection needle-type

collimators were attached to an x-ray tube and the detector. The beam size of the primary x-rays was evaluated to be 740 μm , depending on the inner diameter of the first collimator for excitation. These injection needle-type collimators were inserted into solution samples. The end of each collimator was covered with an x-ray transparent plastic sheet. The x-ray fluorescence was detected by an energy-dispersive detector through the second collimator. The positions of the two injection needle-type collimators were fixed, while the glass container for sample solution was moved in x-y-z directions. Therefore, it was possible to perform in-situ XRF depth analysis and 3D-XRF analysis in the solution. This technique was applied to liquid-liquid near surface analysis. The distributions of Cu in HCl solution and Fe in MIBK solution were successfully obtained near the liquid-liquid interface.

Enhancement of Hydrothermal Oxidation of Chlorobenzene by the Fenton-type Reaction Using Cu(II)-grafted Tungsten Trioxide Catalyst

Noritsugu KOMETANI and Yasuaki SUMIYOSHI

Chemistry Letters, Vol.42, No.8, pp.804–806 (2013).

The catalytic and photocatalytic hydrothermal oxidation of chlorobenzene has been examined at reaction temperature ranging from 25 to 400°C and at a fixed pressure of 30 MPa using Cu(II)-grafted tungsten trioxide (Cu/WO₃) as a catalyst and hydrogen peroxide as an oxidizing reagent. The decomposition efficiency of chlorobenzene is dramatically promoted with the aid of Cu/WO₃ and approximately 100% decomposition efficiency has been achieved in the dark at reaction temperature of 200°C. It is proposed that the formation of hydroxyl radicals from hydrogen peroxide via Fenton-type reaction catalyzed by Cu ions is subjected to the substantial acceleration under subcritical conditions of water around 200–300°C, resulting in the enhancement of decomposition efficiency. The irradiation of catalysts with near-UV~visible light also facilitates the decomposition of chlorobenzene because of the photocatalytic action.

Molecular Rotational Relaxation in Room-Temperature Ionic Liquids at High Pressures

Noritsugu KOMETANI and Atsuko TAI

33rd International Conference on Solution Chemistry (33ICSC), Kyoto, Japan, July7-12, 2013, Preprint p.59.

Plasmonic Enhancement of a Photocycloreversion Reaction of a Diarylethene Derivative Using Individually Dispersed Silver Nanoparticles

Hiroyasu NISHI, Tsuyoshi ASAH, and Seiya KOBATAKE

Chem. Phys. Chem., Vol. 13(16), pp. 3316–3621 (2012).

The fabrication of silver nanoparticles covered with polymers with a well-defined core-shell structure and the quantitative evaluation of the plasmonic enhancement effect on a photochemical reaction in the vicinity of these silver nanoparticles individually dispersed in a medium are described. The photocycloreversion reaction of a diarylethene polymer in the vicinity of silver nanoparticles was enhanced by 2-6 times relative to the reaction without the nanoparticles. The promotion of the photocycloreversion reaction is due to enhancement of the electromagnetic field near the surface of the silver core.

Thermo- and Photoresponsive Reversible Changes in Localized Surface Plasmon Resonance of Gold Nanoparticles Covered by Poly(*N*-isopropylacrylamide) with Photochromic Diarylethene End Group

Shotaro IMAO, Hiroyasu NISHI, and Seiya KOBATAKE

J. Photochem. Photobiol. A: Chem., Vol. 252, pp. 37–45 (2013).

Thermoresponsive poly(*N*-isopropylacrylamide) (poly(NIPAm)) with a diarylethene (DE) chromophore at the end group (DE-poly(NIPAm)) was synthesized by reversible addition-fragmentation chain transfer polymerization. The resulting polymer has a lower critical solution temperature at 33 °C and exhibits photochromism in water upon photoirradiation. Gold nanoparticles covered with DE-poly(NIPAm) were prepared by malate reduction, followed by the addition of DE-poly(NIPAm) with SH at the ω -end group. The localized surface plasmon resonance band of the gold nanoparticles exhibits a bathochromic shift with heating and photoirradiation. This is ascribed to changes in the refractive index by the shrunken dehydrated state and the

photochromic reaction of the DE chromophore with heating and photoirradiation, respectively.

Systematic Study on the Thermal Cycloreversion Reactivity of Diarylethenes with Alkoxy and Alkyl Groups at the Reactive Carbons

Hiroaki SHOJI, Daichi KITAGAWA, and Seiya KOBATAKE

Res. Chem. Intermed., Vol. 39(1), pp. 279–289 (2013).

The relationship between the thermal cycloreversion reactivity of diarylethenes and the bulkiness of the substituents at the reactive carbons was systematically investigated. Two photochromic diarylethenes, 1,2-bis(2-isobutoxy-5-phenyl-3-thienyl)perfluorocyclopentene and 1,2-bis(2-neopentoxy-5-phenyl-3-thienyl)perfluorocyclopentene, were newly synthesized and their optical properties and thermal cycloreversion reactivity were examined, because there is insufficient data for diarylethenes with alkoxy groups at the reactive carbons. The steric substituent constant was employed to correlate the relationship between the thermal cycloreversion reactivity of diarylethenes with alkyl and alkoxy groups at the reactive carbons and the bulkiness of the substituent. A good correlation was obtained for the substituent constant using CH₂ instead of oxygen in the alkoxy groups. The results indicate that this is a very useful strategy for the design of novel diarylethenes with desired thermal cycloreversion reactivity.

Thermal Bleaching Reactions of Photochromic Diarylethenes with Thiophene-*S,S*-dioxide for a Light-starting Irreversible Thermosensor

Hiroaki SHOJI and Seiya KOBATAKE

Chem. Commun., Vol. 49(23), 2362–2364 (2013).

Thiophene-*S,S*-dioxidized diarylethenes introducing bulky substituents at the reactive positions were newly synthesized. The diarylethenes showed reversible photochromism, whereas the photocycloreversion reaction was suppressed by thiophene-oxidation. The diarylethene closed-ring isomers having secondary alkyl groups at the reactive positions were found to undergo thermal bleaching reactions which produce at least three types of byproducts. Such materials could find application as light-starting irreversible thermosensors.

Photoinduced Twisting of a Photochromic Diarylethene Crystal

Daichi KITAGAWA, Hiroyasu NISHI, and Seiya KOBATAKE

Angew. Chem. Int. Ed., Vol. 52(35), pp. 9320–9322 (2013). [Published as VIP]

The colorless needle-like crystal of the diarylethene, which were newly synthesized, rapidly twisted accompanying the color change to blue upon irradiation with ultraviolet (UV) light. The twisting of the crystal relaxed back to the original shape in a few seconds with visible light irradiation. The photoreversible twisting of the crystal could be repeated over 30 cycles by alternating irradiation with UV and visible light. The photoinduced crystal twisting takes place in both left-handed helix and right-handed helix. The direction of the twisting depends on the face irradiated with UV light. Furthermore, the direction of contraction in the unit cell was determined using the contracted crystal which underwent the photocyclization reaction in the whole crystal by irradiation from both sides on the crystal surfaces. From these results, the twisting of the crystal requires both the gradient of the photocyclization conversion in the thickness direction and the contraction of the crystal in the diagonal direction. Such a photoinduced crystal twisting provides a new type of photomechanical actuators.

Thermodynamic Phase Transition Through Crystal-to-Crystal Process of Photochromic 1,2-Bis(5-phenyl-2-propyl-3-thienyl)perfluorocyclopentene

Daichi KITAGAWA and Seiya KOBATAKE

Chem. –Asian J., in press [DOI: 10.1002/asia.201301020].

A photochromic diarylethene, 1,2-bis(5-phenyl-2-propyl-3-thienyl)perfluorocyclopentene (**1a**), was found to have two polymorphic crystal forms, α - and β -crystals. From X-ray crystallographic analysis, the space groups of α - and β -crystals are $P2_1/c$ and $C2/c$, respectively. The difference between two crystal forms is ascribed to orientation of two of four molecules in the unit cell. The thermodynamic phase transition from α - to β -forms occurred via a crystal-to-crystal process, as confirmed by differential scanning calorimetry measurement, optical

microscopic observation in reflection mode and under crossed nicols, and powder X-ray diffraction profile. The movement of the molecules in the crystal was evaluated by the change of face indices before and after the phase transition.

Crystal Thickness Dependence of Photoinduced Crystal Bending of 1,2-Bis(2-methyl-5-(4-(1-naphthoyloxymethyl)phenyl)-3-thienyl)perfluorocyclopentene

Daichi KITAGAWA and Seiya KOBATAKE

J. Phys. Chem. C, in press [DOI: 10.1021/jp4083079].

The photoinduced crystal bending of a photochromic diarylethene derivative, 1,2-bis(2-methyl-5-(4-(1-naphthoyloxymethyl)phenyl)-3-thienyl)perfluorocyclopentene (**1a**), has been particularly investigated. The rod-like crystal of **1a** shows reversible photoinduced bending upon alternating irradiation with ultraviolet (UV) and visible light. The photoinduced crystal bending can be repeated over 80 cycles. The rod-like crystal of **1a** shows different bending behavior depending on the faces irradiated with UV light. This is ascribed to the molecular orientation viewed from the faces. Furthermore, we found that the bending speed depends on the crystal thickness and the curvature change against the crystal thickness is well fitted to Timoshenko's bimetal model. These findings provide a new useful strategy to design for the photomechanical actuators.

Rapidly Photoresponsive Molecular Machinery of Photochromic Diarylethene Crystals

Seiya KOBATAKE

26th International Conference on Photochemistry (ICP 2013), Invited Lecture, Leuven, Belgium, July 21–26, 2013; Abstract, p. 45 (2013).

Photoinduced Crystal Shape Change of Diarylethene Derivatives Having Naphthyl Groups

Daichi KITAGAWA and Seiya KOBATAKE

26th International Conference on Photochemistry (ICP 2013), Poster Presentation, Leuven, Belgium, July 21–26, 2013; Abstract, p. 317 (2013).

Crystal Thickness Dependence of Photoinduced Crystal Bending of a Photochromic Diarylethene derivative

Daichi KITAGAWA and Seiya KOBATAKE

7th International Symposium on Photochromism (ISOP 2013), Poster Presentation, Berlin, Germany, September 23–26, 2013; Abstract, p. 130 (2013).

Light-starting Irreversible Thermosensors of Photochromic Diarylethenes: Thermal Reactivities by Introducing Substituents

Seiya KOBATAKE, Hiroaki SHOJI, and Daichi KITAGAWA

7th International Symposium on Photochromism (ISOP 2013), Short Oral & Poster Presentation, Berlin, Germany, September 23–26, 2013; Abstract, p. 132 (2013).

Chiral Silicon Lewis Acids Having Pentacoordinate Stereogenic Silicon Center : ²⁹Si NMR Studies and Application to Asymmetric Diels-Alder Reaction

Yuhsuke SAKAGUCHI, Yuhki IWANE, Tohru SEKIKAWA, Tatsuya MINAMI, and Yasuo HATANAKA

Chemical Communications, Vol. 49, pp. 11173–11175 (2013).

The ²⁹Si NMR studies of chiral pentacoordinate silyl triflimides having stereogenic center at silicon have revealed that a chiral silicon center is highly configurationally unstable. Such a configurational instability has an enormously beneficial effect on the diastereo- and enantioselectivity of the catalytic asymmetric Diels-Alder reaction.

Synthesis of Silaoxazolinium Salts Bearing Weakly Coordinating Anions: Structures and Catalytic Activities in the Aldol Reaction

Anugu Chandra Sheker REDDY, Zhang CHEN, Tohru HATANAKA, Tatsuya MINAMI, and Yasuo HATANAKA

Organometallics, Vol. 32, pp. 3575–3582 (2013).

The synthesis and the structures of silaoxazolinium salts **2**, and their application to the catalytic Mukaiyama aldol reaction are described. The reaction of *N*-amidomethyl(dimethyl)chlorosilane **1a** or *N*-amidomethyl[bis(trimethylsilyl)]chlorosilane **1b** with metal salts of weakly coordinating anions such as Cs[TFPB] (TFPB: B[3,5-(CF₃)₂C₆H₃]₄⁻) and Na[CB₁₁H₁₂] (CB₁₁H₁₂⁻: carba-*closo*-dodecaborate) gave the corresponding five-membered ring silaoxazolinium salts **2** in high yields (93-97%, Scheme 1). The structures of a series of silaoxazolinium salts **2** were determined by X-ray crystal analysis as well as ²⁹Si NMR spectra. It was proved that the silicon atoms of silaoxazolinium salts **2a** and **2b** are nearly completely free from the coordination of anions, and the geometries of the silicon centers are distorted tetrahedral. The ²⁹Si chemical shifts of salts **2** appeared in a range of +31 to +49 ppm, revealing the appreciable silylium cation character of the silicon. Silaoxazolinium salt of TFPB anion **2a** exhibited effective catalytic activity for the Mukaiyama aldol reaction of low reactive unactivated-ketones such as cyclohexanone and acetophenone, giving the corresponding aldol products in high yields. The catalytic activity is highly dependent on the nature of the counter anions and the substituents on the silicon. DFT calculation of silaoxazolinium cation has disclosed that positive charges of silaoxazolinium cations are mainly located at the silicon atoms, while the nitrogen atoms and oxygen atoms are negatively charged.

Catalytic Enantioselective Direct Vinylogous Michael Addition of 3H-2-Furanones to Nitroolefins

Tohru SEKIKAWA and Yasuo HATANAKA

Chemical Communications, in press.

A direct vinylogous Michael reaction of 5-substituted 3H-2-furanones with nitroolefins has been developed with the help of a new quinine-derived bifunctional catalyst, allowing the synthesis of densely functionalized γ -lactones with contiguous quaternary and tertiary stereocenters in excellent yield with perfect diastereoselectivity (>20 : 1 dr) and high enantioselectivity (up to 99 : 1 er). The present reaction highly effective in terms of low loading of catalyst (0.01 mol %) as well as very wide substrate scop.

Bioengineering

Crystal Structure Analysis of the Translation Factor RF3 (Release Factor 3)

Kiyohito KIHIRA, Yoshihiro SHIMIZU, Yasuhito SHOMURA, Naoki SHIBATA, Masaya KITAMURA, Atsushi NAKAGAWA, Takuya UEDA, Kozo OCHI, and Yoshiki HIGUCHI

FEBS Lett., Vol. 586, pp. 3705–3709 (2012).

The bacterial translational GTPases release factor RF3 promotes translation termination by recycling RF1 or RF2. Here, we present the crystal structures of RF3 complexed with GDP and guanosine 3',5'-(bis)diphosphate (ppGpp) at resolutions of 1.8 and 3.0 Å, respectively. ppGpp is involved in the so-called “stringent response” of bacteria. ppGpp binds at the same site as GDP, suggesting that GDP and ppGpp are two alternative physiologically relevant ligands of RF3. We also found that ppGpp decelerates the recycling of RF1 by RF3. These lines of evidence suggest that RF3 functions both as a cellular metabolic sensor and as a regulator.

Development of an Affinity-Matured Humanized Anti-Epidermal Growth Factor Receptor Antibody for Cancer Immunotherapy

Takeshi NAKANISHI, Takamitsu MARU, Kazuhiro TAHARA, Hideaki SANADA, Mitsuo UMETSU, Ryutaro ASANO, and Izumi KUMAGAI

Protein Eng. Des. Sel., Vol. 26, pp. 113–122 (2013).

We showed previously that humanization of 528, a murine anti-epidermal growth factor receptor (EGFR) antibody, causes reduced affinity for its target. Here, to improve the affinity of the humanized antibody for use in cancer immunotherapy, we constructed phage display libraries focused on the complementarity-determining regions (CDRs) of the antibody and carried out affinity selection. Two-step selections using libraries constructed in a stepwise manner enabled a 32-fold affinity enhancement of humanized 528 (h528). Thermodynamic analysis of the interactions between the variable domain fragment of h528 (h528Fv) mutants and the soluble extracellular domain of EGFR indicated that the h528Fv mutants obtained from the first selection showed a large increase in negative enthalpy change due to binding, resulting in affinity enhancement. Furthermore, mutants from the second selection showed a decrease in entropy loss, which led to further affinity maturation. These results suggest that a single mutation in the heavy chain variable domain (i.e. Tyr⁵² to Trp) enthalpically contributed for overcoming the energetic barrier to the antigen-antibody interaction, which was a major hurdle for the *in vitro* affinity maturation of h528. We reported previously that the humanized bispecific diabody hEx3 Db, which targets EGFR and CD3, shows strong anti-tumor activity. hEx3 Db mutants, in which the variable domains of h528 were replaced with those of the affinity-enhanced mutants, were prepared and characterized. In a growth inhibition assay of tumor cells, the hEx3 Db mutants showed stronger anti-tumor activity than that of hEx3 Db, suggesting that affinity enhancement of h528Fv enhances the anti-tumor activity of the bispecific diabody.

A Key Factor for Ultrafast Rates of Photoinduced Electron Transfer among Five Flavin Mononucleotide Binding Proteins: Effect of Negative, Positive, and Neutral Charges at Residue 13 on the Rate

Seiji TANIGUCHI, Haik CHOSROWJAN, Fumio TANAKA, Takeshi NAKANISHI, Shuta SATO, Yoshihiro HARUYAMA, and Masaya KITAMURA

Bull. Chem. Soc. Jpn., Vol. 86, pp. 339–350 (2013).

Crystal structures of E13K [Glu13 with negative charge in wild type (WT) was replaced by Lys with positive charge] and E13R (Glu13 was replaced by Arg with positive charge) of flavin mononucleotide-binding protein (FMN-bp) from *Desulfovibrio vulgaris* (Miyazaki F) were determined by X-ray diffraction method. Ultrafast fluorescence dynamics of FMN in these proteins were measured by fluorescence up-conversion. The average lifetimes of E13K and E13R were 0.198 and 0.186 ps, which are compared to the reported lifetimes of WT, E13T (Glu13 was replaced by Thr with neutral charge) and E13Q (Glu13 was replaced by Gln with neutral charge) FMN-bp, 0.220, 0.872, and 1.10 ps, respectively. These ultrashort lifetimes are ascribed to photoinduced electron transfer (ET) from Trp32, Tyr35, and Trp106 to the excited isoalloxazine. The observed lifetimes of the five FMN-bp isoforms were simultaneously analyzed with both Marcus and Hush, and Kakitani and Mataga ET theories, in order to characterize the ET mechanisms. It was concluded that the electrostatic (ES) energy between

the photoproducts and ionic charges inside the proteins is a key factor for the ET rate in the flavoproteins.

Domain Order of a Bispecific Diabody Dramatically Enhances Its Antitumor Activity Beyond Structural Format Conversion: The Case of the hEx3 Diabody

Ryutaro ASANO, Takashi KUMAGAI, Keisuke NAGAI, Shintaro TAKI, Ippei SHIMOMURA, Kyoko ARAI, Hiromi OGATA, Mai OKADA, Fumitaka HAYASAKA, Hideaki SANADA, Takeshi NAKANISHI, Teemu KARVONEN, Hiroki HAYASHI, Yu KATAYOSE, Michiaki UNNO, Toshio KUDO, Mitsuo UMETSU, and Izumi KUMAGAI

Protein Eng. Des. Sel., Vol. 26, pp. 359–367 (2013).

The domains of bispecific diabodies (BsDBs) can be ordered in four different ways; however, the influence of domain order on the cytotoxicity of BsDBs that retarget immune cells against tumor cells had not been addressed. We previously reported the marked antitumor effects of a humanized BsDB that targets epidermal growth factor receptor and CD3 (hEx3-Db). Here, we rearranged the domains of hEx3-Db to examine the influence of domain order on the function of BsDBs. We successfully prepared homogenous dimers of hEx3-Db in all four domain configurations. Interestingly, all three rearranged hEx3s inhibited cancer growth more effectively than did the original hEx3-Db, in which both components were in variable heavy domain (VH)-variable light domain (VL) order (redesignated as hEx3-HL), and the highest effects were observed with hEx3-LH (hEx3-Db with both components in VL-VH order). In addition, hEx3-LH had comparable *in vitro* growth inhibitory effects to those of the tandem single-chain variable fragment (scFv) format of hEx3-Db (hEx3-tandem scFv (taFv)), which we previously showed to have greater cytotoxicity than does hEx3-HL. Flow cytometry suggested that the enhanced cytotoxicity of hEx3-LH is attributable to structural superiority for cross-linking, similar to that of hEx3-taFv. Furthermore, hEx3-LH inhibited cancer growth in mice more effectively than did hEx3-taFv; this difference may be due to differences in antibody stability. Our results show that merely rearranging the domain order of BsDBs can enhance their effects beyond those with structural format conversion.

Mechanism of Photoinduced Electron Transfer from Tyrosine to the Excited Flavin in the Flavodoxin from *Helicobacter pylori*. A Comparative Study with the Flavodoxin and Flavin Mononucleotide Binding Protein from *Desulfovibrio vulgaris* (Miyazaki F)

Kiattisak LUGSANANGARM, Somsak PIANWANIT, Arthit NUEANGAUDOM, Sirirat KOKPOL, Fumio TANAKA, Nadtanet NUNTHABOOT, Kumiko OGINO, Rikako TAKAGI, Takeshi NAKANISHI, Masaya KITAMURA, Seiji TANIGUCHI, and Haik CHOSROWJAN

J. Photochem. Photobiol. A: Chem., Vol. 268, pp. 58–66 (2013).

Photoinduced electron transfer in the *Helicobacter pylori* flavodoxin (HPFD) was investigated using both experimental and theoretical techniques. Recombinant (r)HPFD was prepared by expression in *Escherichia coli* and the ultrafast fluorescence dynamics of the purified rHPFD was measured by means of fluorescence up-conversion. The fluorescence was found to decay with a lifetime of 173 fs (amplitude, 0.963) and 2.08 ps (0.037). These data were used in the Kakitani and Mataga theory to calculate the electron transfer (ET) rate inside the native HPFD. Molecular dynamics simulations of HPFD were performed over a 50 ns period to enable an inclusion of the protein dynamics effect on the ET process. The ET rate from Tyr91 to an excited isoalloxazine (Iso*) ranged from 6 to 23 ps⁻¹, depending on the analysis method used, while the ET rates from Trp63 and Tyr120 to Iso* were negligibly slow. The logarithmic ET rate and net electrostatic (ES) energy between the photo-products and ionic groups inside HPFD both displayed a parabolic relationship with the total free energy gap, indicating that the net ES energy is one of the most influential factors upon the ultrafast ET rate. Although the logarithmic ET rate should theoretically be decreased with increasing center-to-center distances according to Dutton's law, this relationship was not observed in this system. One possible reason for this was elucidated by comparing our results with those from the flavin mononucleotide binding protein.

Repeated Cooling Crystallization for Production of Microcrystals with a Narrow Size Distribution

Z. XING, K. IGARASHI, A. MORIOKA and H. OOSHIMA

Journal of Chemical Engineering of Japan, Vol. 45(10), pp. 800–804 (2012)

The batch cooling crystallization of an organic compound, *p-acetanisidide*, was carried out using methanol as a solvent and no seed crystal. The crystallization needed an induction period of 10–200 min before nucleation, and the size distribution of the product crystals was broad with sizes ranging from 10 to 270 μm determined as the diameter of a circle with equal projection area. In order to control the nucleation process and obtain microcrystals with a narrow size distribution, the dissolution of crystals obtained by cooling crystallization, followed by recrystallization was adopted. Thus, the crystals once obtained by cooling crystallization were completely dissolved by heating the slurry to a temperature 17°C that was higher than the saturation temperature by 1.5°C. After the solution was maintained at that temperature for a given time, it was cooled again. In the case of repeated crystallization, the induction period observed in the first crystallization disappeared, and small crystals with a mean diameter of 40 μm and a narrow size distribution were obtained. However, the effect of the complete dissolution of crystals on the production of microcrystals with a narrow size distribution disappeared when the solution was incubated at 17°C over 90 min. These results were explained on the basis of the history of the solution structure.

Structure of supersaturated solution and crystal nucleation induced by diffusion

H. OOSHIMA, K. IGARASHI, H. IWASA, R. YAMAMOTO

Journal of Crystal Growth, Vol. 373, pp.2-6 (2013)

The effect of a seed crystal on nucleation of L-alanine from a quiescent supersaturated solution was investigated. When a seed crystal was not used, nucleation did not occur at least for 5 h. When a seed crystal was introduced into the supersaturated solution with careful attention to avoid convection of the solution, fine crystals appeared at the place far from the seed crystal. At that time, there was no convection at the place that fine crystals appeared. Namely, there was no possibility that those fine crystals came from the surface of seed crystal. We supposed that nucleation was induced by directional diffusion of solute molecules caused by growth of the seed crystal. In order to prove this hypothesis, we designed an experiment using an apparatus composed of two compartments divided by a dialysis membrane that L-alanine molecules could freely permeate. Two supersaturated solutions having a supersaturation ratio of 1.2 and a smaller ratio were placed in the two compartments in the absence of seed crystals. This apparatus allowed the directional diffusion of solute molecules between two solutions. Nucleation occurred within 30 min. The frequency of nucleation among 7-times repeated experiments was in proportion to the difference of supersaturation ratio between the two solutions. This result poses a new mechanism of the secondary nucleation that the directional diffusion caused by growth of existing crystals induces nucleation.

Oiling-out in Crystallization and Avoidance

Hiroshi OOSHIMA

Series of Separation Technology 28 "Easy-to-Understand Anti-Solvent Crystallization", Ed. by Noriaki Kubota, The Society of Separation Process Engineers, Japan, pp. 77-84 (2013) (in Japanese)

The behavior of oiling out in crystallization and its avoidance method were explained.

Crystal Polymorphism

Hiroshi OOSHIMA

How to Scale up and Avoid Troubles for Drugs and its Intermediates Production (Popular Edition), Ed. by Mitsunori Hashimoto, CMC Publishing Co. Ltd., pp. 103-113 (2013) (in Japanese)

The control method of crystallization of polymorphs was explained.

Tumor growth suppression by gadolinium-neutron capture therapy using gadolinium-entrapped liposome as gadolinium delivery agent

Novriana DEWI, Hironobu YANAGIE, Haito ZHU, Kazuyuki DEMACHI, Atsuko SHINOHARA, Kazuhito YOKOYAMA, Masaki SEKINE, Yuriko SAKURAI, Yasuyuki MORISHITA, Naoko IYOMOTO, Takeshi NAGASAKI, Yukichi HORIGUCHI, Yukio NAGASAKI, Jun NAKAJIMA, Minoru ONO, Kazuhiro KAKIMI and Hiroyuki TAKAHASHI

Biomed. Pharmacother., Vol. 67(6), pp. 451-457 (2013).

Neutron capture therapy (NCT) is a promising non-invasive cancer therapy approach and some recent NCT research has focused on using compounds containing gadolinium as an alternative to currently used boron-10 considering several advantages that gadolinium offers compared to those of boron. In this study, we evaluated gadolinium-entrapped liposome compound as neutron capture therapy agent by in vivo experiment on colon-26 tumor-bearing mice. Gadolinium compound were injected intravenously via tail vein and allowed to accumulate into tumor site. Tumor samples were taken for quantitative analysis by ICP-MS at 2, 12, and 24 h after gadolinium compound injection. Highest gadolinium concentration was observed at about 2 h after gadolinium compound injection with an average of 40.3 $\mu\text{g/g}$ of wet tumor tissue. We performed neutron irradiation at JRR-4 reactor facility of Japan Atomic Energy Research Institute in Tokaimura with average neutron fluence of 2×10^{12} n/cm². The experimental results showed that the tumor growth suppression of gadolinium-injected irradiated group was revealed until about four times higher compared to the control group, and no significant weight loss were observed after treatment suggesting low systemic toxicity of this compound. The gadolinium-entrapped liposome will become one of the candidates for Gd delivery system on NCT.

S-Allyl cysteine improves nonalcoholic fatty liver disease in type 2 diabetes Otsuka Long-Evans Tokushima Fatty rats via regulation of hepatic lipogenesis and glucose metabolism

Shigekazu TAKEMURA, Yukiko MINAMIYAMA, Shintaro KODAI, Hiroji SHINKAWA, Takuma TSUKIOKA, Shigeru OKADA, Hideki AZUMA and Shoji KUDO

J. Clin. Biochem. Nutr., Vol. 53(2), pp. 94-101 (2012).

It is important to prevent and improve diabetes mellitus and its complications in a safe and low-cost manner. S-Allyl cysteine, an aged garlic extract with antioxidant activity, was investigated to determine whether S-allyl cysteine can improve type 2 diabetes in Otsuka Long-Evans Tokushima Fatty rats with nonalcoholic fatty liver disease. Male Otsuka Long-Evans Tokushima Fatty rats and age-matched Long-Evans Tokushima Otsuka rats were used and were divided into two groups at 29 weeks of age. S-Allyl cysteine (0.45% diet) was administered to rats for 13 weeks. Rats were killed at 43 weeks of age, and detailed analyses were performed. S-Allyl cysteine improved hemoglobinA1c, blood glucose, triglyceride, and low-density lipoprotein cholesterol levels. Furthermore, S-allyl cysteine normalized plasma insulin levels. S-Allyl cysteine activated the mRNA and protein expression of both peroxisome proliferator-activated receptor α and γ , as well as inhibiting pyruvate dehydrogenase kinase 4 in Otsuka Long-Evans Tokushima Fatty rat liver. Sterol regulatory element-binding protein 1c and forkhead box O1 proteins were normalized by S-allyl cysteine in Otsuka Long-Evans Tokushima Fatty rat liver. In conclusions, these findings support the hypothesis that S-allyl cysteine has diabetic and nonalcoholic fatty liver disease therapeutic potential as a potent regulating agent against lipogenesis and glucose metabolism.

Evaluation of importance of nuclear import in artificial viral gene delivery using programmable cellular image tracer

Takeshi NAGASAKI, Takeshi KAWAZU, Kazumi HAKAMADA, Yusuke ODA, Jun MIYAKE and Kazuo MARUYAMA

The First International Symposium on Biofunctional Chemistry, Tokyo, Japan, November 28-30, 2012; Abstract pp. 126-127 (2012).

Estimation of boron-containing rare earth oxides as drugs for boron neutron capture therapy

Hiroko YUKAWA, Riku KAWASAKI, Masashi SAKURAMOTO, Kiyofumi KATAGIRI, Koji TOMITA, Shin-ichiro MASUNAGA, Koji ONO, Yoshinori SAKURAI, Mitsunori KIRIHATA, Hideki AZUMA and Takeshi NAGASAKI

The 40th Annual Meeting & Exposition of the Controlled Release Society, Honolulu, HI, USA, July 21-24, 2013; Preprints.

Kojic acid-appended carborane/hydroxypropyl- β -cyclodextrin complex: melanoma-selective drug for

boron neutron capture therapy

Riku KAWASAKI, Koji ONO, Shin-ichiro MASUNAGA, Yoshinori SAKURAI, Mitsunori KIRIHATA and Takeshi NAGASAKI

The 5th Asian Arden Conference, Nagoya, Japan, August 5-6, 2013; Abstract, pp. 95 (2013).

Origin of double targeting concept is molecular machinery: photoresponsive gene carrier and boron carrier for BNCT

Takeshi NAGASAKI

New Trends of Nano- or Bio-materials Design in Supramolecular 2013, Fukuoka, Japan, September 20-21, 2013; Abstract, pp. 43 (2013).

Development of microbial biofuel cell - Electric energy which was produced through the life -

Azuma M

Manufacturing & Technology, Vol. 65 (4), in press (2013) (in Japanese)

Functional activity of RLIM/Rnf12 is regulated by phosphorylation-dependent nucleo-cytoplasmic shuttling.

Jiao B, Taniguchi-Ishigaki N, Gungör C, Peters MA, Chen YW, Riethdorf S, Drung A, Ahronian LG, Shin J, Pagnis R, Pantel K, Tachibana T, Lewis BC, Johnsen SA, Bach I.

Mol. Biol. Cell, 24, 3085-3096. (2013)

The X-linked gene Rnf12 encodes the ubiquitin ligase really interesting new gene (RING) finger LIM domain-interacting protein (RLIM)/RING finger protein 12 (Rnf12), which serves as a major sex-specific epigenetic regulator of female mouse nurturing tissues. Early during embryogenesis, RLIM/Rnf12 expressed from the maternal allele is crucial for the development of extraembryonic trophoblast cells. In contrast, in mammary glands of pregnant and lactating adult females RLIM/Rnf12 expressed from the paternal allele functions as a critical survival factor for milk-producing alveolar cells. Although RLIM/Rnf12 is detected mostly in the nucleus, little is known about how and in which cellular compartment(s) RLIM/Rnf12 mediates its biological functions. Here we demonstrate that RLIM/Rnf12 protein shuttles between nucleus and cytoplasm and this is regulated by phosphorylation of serine S214 located within its nuclear localization sequence. We show that shuttling is important for RLIM to exert its biological functions, as alveolar cell survival activity is inhibited in cells expressing shuttling-deficient nuclear or cytoplasmic RLIM/Rnf12. Thus regulated nucleocytoplasmic shuttling of RLIM/Rnf12 coordinates cellular compartments during mammary alveolar cell survival.

Substrate specificity of Pasteurella multocida toxin for α subunits of heterotrimeric G proteins.

Orth JH, Fester I, Siebert P, Weise M, Lanner U, Kamitani S, Tachibana T, Wilson BA, Schlosser A, Horiguchi Y, Aktories K.

FASEB J. 27, 832-842. (2013)

Pasteurella multocida is the causative agent of a number of epizootic and zoonotic diseases. Its major virulence factor associated with atrophic rhinitis in animals and dermonecrosis in bite wounds is *P. multocida* toxin (PMT). PMT stimulates signal transduction pathways downstream of heterotrimeric G proteins, leading to effects such as mitogenicity, blockade of apoptosis, or inhibition of osteoblast differentiation. On the basis of $G\alpha(i2)$, it was demonstrated that the toxin deamidates an essential glutamine residue of the $G\alpha(i2)$ subunit, leading to constitutive activation of the G protein. Here, we studied the specificity of PMT for its G-protein targets by mass spectrometric analyses and by utilizing a monoclonal antibody, which recognizes specifically G proteins deamidated by PMT. The studies revealed deamidation of 3 of 4 families of heterotrimeric G proteins ($G\alpha(q/11)$, $G\alpha(i1,2,3)$, and $G\alpha(12/13)$ of mouse or human origin) by PMT but not by a catalytic inactive toxin mutant. With the use of G-protein fragments and chimeras of responsive or unresponsive G proteins, the structural basis for the discrimination of heterotrimeric G proteins was studied. Our results elucidate substrate specificity of PMT on the molecular level and provide evidence for the underlying

structural reasons of substrate discrimination.

Production of a Monoclonal Antibody Specific for Pou5f1/Oct4.

Arakawa T, Yoshimi T, Azuma M, Tachibana T.

Monoclonal Antibodies in Immunodiagnosis and Immunotherapy, 32, 229-231. (2013)

Pou5f1/Oct4, a member of the POU transcription factor family, is exclusively expressed in embryonic stem cells, which are involved in self-renewal and maintaining pluripotency. In the present study, we report on the establishment of a monoclonal antibody that is specific for Oct4 using the rat medial iliac lymph node method. In an immunoblotting analysis, our antibody detected endogenous Oct4. In addition, immunocytochemical staining using the antibody revealed the nuclear localization of Oct4. This monoclonal antibody has the potential for use in the further analysis of Oct4 function in stem cells.

A panel of specific monoclonal antibodies directed against various phosphorylated histone H3.

Yoshimi T, Ohkawa Y, Azuma M, Tachibana T.

Monoclonal Antibodies in Immunodiagnosis and Immunotherapy, 32, 119-124. (2013)

Modification of histone plays a critical role in the epigenetic regulation of gene expression. However, unlike the widely studied roles of histone methylation or acetylation of histone H3, relatively little is known about the molecular mechanisms involved in translating histone phosphorylation into a specific outcome. The present study reports on the development of antibodies (MAbs) directed against phosphorylated histone H3 (S10, T11, S28, S31, and T32), produced by the hybridization of mouse myeloma cells with lymph node cells from an immunized rat or mouse. The MAbs produced specifically recognize different sites of phosphorylation on histone H3. All of these MAbs are suitable for immunoblotting and immunofluorescence analysis. We believe that these antibodies should significantly facilitate our efforts to investigate epigenetic regulation.

Contribution of Leydig and Sertoli cells to testosterone production in mouse fetal testes.

Shima Y, Miyabayashi K, Haraguchi S, Arakawa T, Otake H, Baba T, Matsuzaki S, Shishido Y, Akiyama H, Tachibana T, Tsutsui K, Morohashi K.

Mol Endocrinol. 27, 63-73. (2013)

Testosterone is a final product of androgenic hormone biosynthesis, and Leydig cells are known to be the primary source of androgens. In the mammalian testis, two distinct populations of Leydig cells, the fetal and the adult Leydig cells, develop sequentially, and these two cell types differ both morphologically and functionally. It is well known that the adult Leydig cells maintain male reproductive function by producing testosterone. However, it has been controversial whether fetal Leydig cells can produce testosterone, and the synthetic pathway of testosterone in the fetal testis is not fully understood. In the present study, we generated transgenic mice in which enhanced green fluorescence protein was expressed under the control of a fetal Leydig cell-specific enhancer of the Ad4BP/SF-1 (Nr5a1) gene. The transgene construct was prepared by mutating the LIM homeodomain transcription factor (LHX9)-binding sequence in the promoter, which abolished promoter activity in the undifferentiated testicular cells. These transgenic mice were used to collect highly pure fetal Leydig cells. Gene expression and steroidogenic enzyme activities in the fetal Leydig cells as well as in the fetal Sertoli cells and adult Leydig cells were analyzed. Our results revealed that the fetal Leydig cells synthesize only androstenedione because they lack expression of Hsd17b3, and fetal Sertoli cells convert androstenedione to testosterone, whereas adult Leydig cells synthesize testosterone by themselves. The current study demonstrated that both Leydig and Sertoli cells are required for testosterone synthesis in the mouse fetal testis.

A co-localization model of paired ChIP-seq data using a large ENCODE data set enables comparison of multiple samples.

Maehara K, Odawara J, Harada A, Yoshimi T, Nagao K, Obuse C, Akashi K, Tachibana T, Sakata T, Ohkawa Y.

Nucleic Acids Res. 41, 54-62. (2013)

Deep sequencing approaches, such as chromatin immunoprecipitation by sequencing (ChIP-seq), have been successful in detecting transcription factor-binding sites and histone modification in the whole genome. An

approach for comparing two different ChIP-seq data would be beneficial for predicting unknown functions of a factor. We propose a model to represent co-localization of two different ChIP-seq data. We showed that a meaningful overlapping signal and a meaningless background signal can be separated by this model. We applied this model to compare ChIP-seq data of RNA polymerase II C-terminal domain (CTD) serine 2 phosphorylation with a large amount of peak-called data, including ChIP-seq and other deep sequencing data in the Encyclopedia of DNA Elements (ENCODE) project, and then extracted factors that were related to RNA polymerase II CTD serine 2 in HeLa cells. We further analyzed RNA polymerase II CTD serine 7 phosphorylation, of which their function is still unclear in HeLa cells. Our results were characterized by the similarity of localization for transcription factor/histone modification in the ENCODE data set, and this suggests that our model is appropriate for understanding ChIP-seq data for factors where their function is unknown.

Architecture and Building Engineering

Effect of Quasi-static Seismic Loads on Plane Lattice Frames with Columns

Kenta TOKUDA and Yoshiya TANIGUCHI

Proceedings of the International Association for Shell and Spatial Structures (IASS) Symposium 2013, „BEYOND THE LIMITS OF MAN”23-27 September, Wroclaw University of Technology, Poland, No.1251 (2013)

The relation between dynamic collapse behavior and static load carrying capacities has been studied for lattice structures of several types. The studies had been carried out with vertical loads, to present an estimation method for dynamic collapse levels without any time-history analysis. This paper highlights the effect of quasi-static seismic loads in vertical and horizontal directions on the load carrying capacities for lattice frames with columns, in order to determine which type is appropriate for the choice of quasi-static loads in using the estimation method.

Deployable Polyhedron Unit with Stretchable Membrane

Junichi KATO, Susumu YOSHINAKA and Yoshiya TANIGUCHI

Proceedings of the International Association for Shell and Spatial Structures (IASS) Symposium 2013, „BEYOND THE LIMITS OF MAN”23-27 September, Wroclaw University of Technology, Poland, No.1197 (2013)

This paper presents a novel structure unit consisting of at least 3 fundamental components, named membrane panel comprising 1 rectangle frame constructed of 4 rods, 4 universal joints and 1 stretchable membrane. This unit is stabilized by membrane, tension so the unit is elastically deformable, foldable and deployable. Moreover, several variations of the unit can fill the space. Thus, those units can construct various complex modules by jointing each unit. The paper shows some cases of space-filling and complex structures.

Proposal of Design Formulas of Tuned Mass Dampers with Initial Displacement to Control Impulse Response Focusing on Vibration Modes

Susumu YOSHINAKA and Yoshiya TANIGUCHI

Journal of Structural and Construction Engineering (Transactions of AIJ), AIJ, No. 688, pp. 1071-1079 (2013) (in Japanese)

In this study, we aim to propose tuned mass dampers with initial displacement that are possible to control impulsive seismic responses effectively for architectural structures. In advance of the study on control of seismic responses, we aim to propose design formulas to control the structural responses subjected to impulse forces. In our previous study, we have proposed the design formulas using the optimal tuning and damping ratios for harmonic ground vibration. But to improve control effect on overall time history responses is difficult, because these formulas are based on the principle of the beating phenomenon. Then, in this paper, we focus on the vibration property when the damping ratio of the tuned mass damper is larger than that of our previous study and propose new design formulas with high control effect on impulse forces. Moreover, we propose design formulas considering the damping of the structure.

Proposal of Design Formulas of Tuned Mass Dampers with Initial Displacement to Control Impulse Response

Susumu YOSHINAKA and Yoshiya TANIGUCHI

Proceedings of the 13th World Conference on Seismic Isolation, Energy Dissipation and Active Vibration Control of Structures, Sendai, September 24-27, Paper No.865245, (2013)

We study a new vibration control method applying TMDs (Tuned Mass Dampers) to spatial structures and propose the spatially distributed MTMDs (Multiple TMDs) method. We select the TMD as a vibration control device because it has been widely applied to large-span light-weight structures. Moreover, the TMD is considered to be superior especially in application to complex-shaped large-span roof structures because it can be installed without any device reaction force. However, it is recognized that the performance of conventional TMDs in controlling impulsive seismic responses is limited, because there is a time interval before they become fully effective. Thus, to control transient responses more effectively, we propose TMDs with initial displacements, that is to say, whose spring is stretched until the appropriate release timing.

In advance of the study on control of seismic responses, we propose design formulas for controlling structural responses under impulse loading. In our previous study, we proposed design formulas using optimal tuning and damping ratios for harmonic ground vibration, and confirmed improved control performance on the initial

response by both analytical and experimental studies. However, improvement of control performance over the entire time history is limited, because those formulas are based on the principle of the beat phenomenon. Therefore, in this paper, we focus on the relationship between the TMD damping ratio and the modal damping ratio for the condition in which the TMD damping ratio is larger than that in our previous study and propose new design formulas for high control performance over the entire time history under impulse loading.

Faults and Claims about Thermal Environments in Relation to Building Equipment and Energy Conservation Measures in Smaller Office Buildings

Noriko UMEMIYA and Ryota MATSUI

Proceedings of the 7th Windsor Conference 2012: The Changing Context of Comfort in an Unpredictable World, pp. 1-10 (2012)

Building equipment, energy-saving systems, and claims of inappropriate indoor thermal environments were analyzed in relation to the floor area using responses to a questionnaire survey of service managers of 157 buildings. Results show the following. 1) In smaller buildings (<5000 m²), set temperatures are higher in summer and lower in winter, effects of ‘uncomfortable radiation from windows’ are greater, energy-saving systems decrease indoor thermal comfort, but claims of ‘hot’ and ‘cold’ are fewer. 2) Claims of ‘hot’ and ‘cold’ are unrelated to the setting temperature and whether the air-conditioning control system is central or local. Finally, 3) the adoption rates of ‘COOL-BIZ’ or ‘WARM-BIZ’ are higher than those of temperature mitigation of air conditioning.

Estimation of CIE STANDARD SKIES Based on Sunshine Duration and Cloud Cover

Tomoko IWATA and Noriko UMEMIYA

Proceedings of 2012 CJK Lighting Conference, pp. 369-372 (2012)

Frequencies of sky types from a set of 15 standard skies (CIE Standard General Sky) were estimated based on sunshine duration and cloud cover. Sunshine duration and cloud cover data obtained hourly and at three-hour intervals are available from websites of meteorological observatories. Sunshine duration 0.0 and cloud cover 10 are typical of sky types 1 and 3, sunshine duration 1.0 and cloud cover 0 are typical of sky type 12, sky type numbers reflect graduated differences between them. The frequency distribution of the sky type at a site can characterize the daylight climate. Such data might be useful as bases for effective use of daylight in particular regions.

Estimating Occurrence of CIE Standard Skies from Sunshine Duration and Cloud Cover

Tomoko IWATA and Noriko UMEMIYA

Proceedings of LUX PACIFICA 2013, pp. 32-37 (2013)

Measurement of Pressure and Velocity Distribution Around Cross-ventilated Building and Accuracy Study of CFD Analysis

Tomohiro KOBAYASHI, Hisashi KOTANI (Osaka University), Toshio YAMANAKA (Osaka University), Kazunobu SAGARA (Osaka University) and Yoshihisa MOMOI (Osaka University)

Proceedings of the 12th International Conference on Air Distribution in Rooms (ROOMVENT 2011), Trondheim, Norway, In Digital Media, (2011)

The final goal of this work is to establish an improved prediction method of wind-induced ventilation rate when large openings are provided with a room in series, where conventional prediction method based on the so-called Orifice equation cannot work well. This is because the conventional method cannot consider that the dynamic pressure could remain after passing through an opening, and the improved prediction method should be established based on actual phenomenon inside the stream tube. Since this needs the analyses using CFD prediction, this paper presents the accuracy of CFD, especially flow around the building, by comparing them with experimental results. Studied model has a rectangular configuration and it is assumed to include nine one-room residences where openings of the central room are opened. In analysing energy loss inside the flow path, both static pressure and velocity are important, and these quantities are measured by using five-hole pitot tube and PIV system in a wind tunnel. For the measurement using five-hole pitot tube, three calibration curves regarding wind angle, velocity magnitude, static pressure are first created. Based on these calibration curves, static pressure and velocity are simultaneously measured around the model. Meanwhile, velocity distribution was also measured by 2-D PIV because each experimental method has both strength and weakness. Those experimental results are to be compared with CFD results using Standard k- ϵ Model, Reynolds Stress Model, and Large Eddy Simulation to study accuracy of the calculation. At the same time, the scope of each experimental technique is also studied. It is

finally shown that Large Eddy Simulation has sufficient accuracy to predict pressure and velocity distribution around the building model.

Evaluation of Ventilation Performance of Monitor Roof in Residential Area Based on Simplified Estimation and CFD Analysis

Tomohiro KOBAYASHI, Tomoyuki CHIKAMOTO (Ritsumeikan University) and Keishi OSADA (Ritsumeikan University)

Building and Environment, Vol. 63, pp. 20-30 (2013)

Wind-induced natural ventilation is beneficial to assure thermal comfort and to reduce cooling load in the hot and humid summertime. In the urban environment, where buildings are grouped closely, it is often difficult to obtain a large enough wind pressure difference to drive the natural ventilation. As architectural feature, this work focuses on “monitor roof” which has the potential to promote wind- induced natural ventilation, and aims to evaluate its ventilation performance. This paper analyses a two-story residential building model equipped with a monitor roof which is built in a long building row, assuming a densely populated residential area. Since the monitor roof shows complicated flow resistance, the conventional method to predict flow rate cannot be easily applied. Based on the correlation between internal pressure and flow rate, and wind pressure coefficients obtained from previous work, a simplified estimation method of flow rate is first applied in this paper. In addition, more detailed flow characteristics inside the room are analysed by Computational Fluid Dynamics using a Reynolds- Averaged Navier-Stokes model, and a certain level of accuracy is verified by comparison with wind tunnel measurement. By comparing flow rate between numerical simulation and measurement, the validity of the simplified estimation method is also verified. To analyse substantial ventilation performance including the effect of turbulence, numerical simulation using Large Eddy Simulation is also performed and particle tracking technique is applied. Based on those results, Purging Flow Rate is evaluated, and it is finally shown that the monitor roof can work well to promote natural ventilation.

On Buckling Load and Strength of Single Layer Two-way Grid Cylindrical Shell Roof with Tension Members in Out-of-plane

Z. ZHANG and M. FUJIMOTO

Journal of Structural Engineering, Vol. 59B, pp. 519-527 (2013) (in Japanese)

This study treats the effect of tension member installation on the buckling load and strength of single layer two-way grid cylindrical shell roof by the numerical methods. The tension members are installed to stiffen the rigidity of the two-way grid shell roof. The tension member placement pattern, the load distribution patterns and the initial imperfections are considered as numerical calculation parameters. It is confirmed that the tension members in out-of-plane and diagonals caused the increase in the buckling and strength of two-way grid shell in the numerical analysis.

Experimental Study on Buckling Behavior of Single Layer Two-way Grid Cylindrical Shell Roof Composed of Small Round Timber with Tension Members in Out-of-plane

Z. ZHANG, M. FUJIMOTO, A. TAKINO(Nara Women’s University) and K. IMAI

Journal of Structural and Construction Engineering (Transactions of AIJ), Vol. 78 No. 686, pp. 781-789 (2013) (in Japanese)

This paper treats the experiment of single layer two-way grid cylindrical shell roof composed of round timber with tension members. The short diagonal tension members and the long tension members are used to stiffen the rigidity of two-way grid cylindrical shell roof. The tension member placement, the introducing initial axial force to tension members and the load patterns are considered to investigate the buckling behavior of the single layer two-way grid cylindrical shell roof. The effects of tension member placement and tension member initial axial force on the load-deformation behavior and the buckling behavior are examined to use the experimental and numerical results.

Civil Engineering

Experimental Study on Mechanical Behavior of the Composite Steel Girder with High Strength Bolted Frictional Joints Subjected to Bending

Takashi YAMAGUCHI, Masatsugu NAGAI (Nagaoka University of Technology), Takeshi MIYASHITA (Nagaoka University of Technology), Yoshihiko TODA, Natsuki YOSHIOKA (Komaihaltec Inc.) and Toru MATSUOKA (Nagaoka University of Technology)

Journal of JSCE, Ser.A1 (SE/EE), Vol.68, No.1, JSCE, pp.16-27 (2012) (in Japanese)

Generally speaking, it is possible to make the cross section small and to reduce 20% of the weight of the steel girder by adoption of Euro code/AASHTO-LRFD to the composite girder subjected to positive bending moment. Therefore, the new design method for connections which can deal with the ultimate state after major slip is needed from the viewpoint of further rationalization of the composite steel girder bridge design. Therefore, at Nagaoka University of Technology, the basic experiment has been carried out by authors in order to investigate the behavior of such a connection after major slip. In this study, the evaluation method of ultimate bending strength of the composite girder with high strength bolted friction joints are proposed and desirable design concept of the friction type joints for composite girder bridges are also summarized.

Study on Load Carrying Capacity of a Small Power Transmission Tower Made of Angle Steel Members

Masahide MATSUMURA, Akira HATANAKA (Hitachi Zosen Corp.) and Takashi YAMAGUCHI

Journal of Structural Engineering, Vol.58A, JSCE, pp.50-61 (2012) (in Japanese)

Equal angle steel members are widely used and generally bolted to other members. Then, the axial compression load eccentrically subjected to the member greatly influences on the ultimate strength and post-buckling behavior of the member. Also member buckling will influence on the ultimate strength of trussed structures, which are assemblage of the angle members. In this paper, transmission line tower consisting of equal angle steels bolted is focused on and the ultimate strength of it and the modeling method of the component members for non-linear analysis are discussed by focusing on decrease of the load carrying capacity due to the eccentric loading to the members. Through comparisons between analytical and experimental results of angle members, a plane trussed structure and an actual transmission tower, an adequate modeling method of the member is verified. Also investigated is Sensitivity Index of the member which represents the decrease ratio of the ultimate strength due to the absence of member.

Tensile and Shear Break Tests of M12 High Strength Bolts with Slit around Their Shanks

Masahide MATSUMURA and Kazuyuki ISHIHARA (Hitachi Zosen Corp.)

Journal of Structural Engineering, Vol.58A, JSCE, pp.83-91 (2012) (in Japanese)

In reducing and in preventing the damage to bridge structures, knocking-off members or devices are adoptable. Then, it is important to understand their brittle fractures and to obtain their controlled and stable breaking loads. In this paper, high strength bolts inserted a slit around their shanks are dealt with among the knocking-off members and their breaking characteristics are investigated through tensile and shear break tests. It is concluded that the height and depth of the slit is not sensitive to the shear breaking load of the slitted bolts and the breaking load is approximately figured out by using the cross sectional area of the slitted part and tensile strength of the bolt material.

Experimental Study on Bending Behavior of Riveted Steel I Shaped Girder Corroded at Rivet Heads

Tsuguho HORI, Kunitaro HASHIMOTO (Kyoto University), Takashi YAMAGUCHI, Kunitomo SUGIURA (Kyoto University) and Yukiko MITSUGI (Ishikawa National College of Technology)

Journal of Structural Engineering, Vol.58A, JSCE, pp.701-709 (2012) (in Japanese)

In this paper, in order to study on bending behaviors of a riveted steel girder with corrosion damage at heads of some rivets, bending loading tests are carried out. The steel girders used as specimens were cut out from the bridge that had been used for 55 years. Considering the results of the bending experiment, it is found that the initial rigidity of the specimen with the rivet heads corroded is decreased a little. But the effect of corrosion damage at rivet heads of riveted steel I shaped girder for ultimate load is nothing.

Friction Test for High Strength Bolted Joints between the Surface of the Inorganic Zinc Rich Paint and the Different Surfaces

Yoshio TAMBA (Hanshin Expressway Technology Center), Satoshi KIMURA, Hiroki SUGIYAMA (Hanshin Expressway Co., Ltd.) and Takashi YAMAGUCHI

Journal of Structural Engineering, Vol.58A, JSCE, pp.803-813 (2012) (in Japanese)

On the site of the maintenance and strengthening work for steel bridges, the high strength bolted friction type joints are often applied. But, the surface preparation of the existing steel member may not be able to be processed adrasive blast-cleaning depending on site conditions. Therefore, the slip tests were carried out using splice plates processed the inorganic zinc rich paint on surfaces and connected plates varied surface preparation and the kind of painting specification on surfaces. As a result of the slip test, it was found that the slip coefficient of 0.4 or more can be ensured by the surface preparation with the power tool.

Analytical Study on Vibration Control of Illumination Poles on Bridges by Using Wire Ropes

Takeshi KITAHARA (Kanto Gakuin University), Shinya SATOH (Kanto Gakuin University), Tomohiko ISHIBASHI (Nasu Denki-Tekko Co., Ltd.) and Takashi YAMAGUCHI

The Journal of Technological Researches, The College of Engineering, Vol. 55, No.2, Kanto Gakuin University, pp.77-83 (2012) (in Japanese)

Recently, it becomes a large problem that bridge vibration induced by vehicles causes damages to not only the bridge but also pole type steel structures, such as lighting poles, marker poles on the elevated bridge. Since such damage tends to cause more severe damage, the vibration problem should be solved. As a number of such poles are large enough, it is important to improve damping performance of the steel pole with cheap cost. Then the authors suggested a vibration controlling technique for a steel pole by using wire ropes. The effect was verified in analysis and it turned out the effect originated in the nonlinear characteristics of wire ropes.

Fundamental Study of Vibration Transfer between Bridge and Passing Vehicles

Yoshinobu OSHIMA (Kyoto University), Yoshikazu KOBAYASHI (Nichizou Tech, Co., Ltd.), Takashi YAMAGUCHI and Kunitomo SUGIURA (Kyoto University)

Journal of JSCE, Ser.A1 (SE/EE), Vol.68, No.2, JSCE, pp.384-397 (2012) (in Japanese)

In this study, the heavy vehicle with excitation system that can control its axle forces passed over a bridge associated with a cargo and a passenger's vehicle to evaluate the vibration transfer between the bridge and vehicles. As a result, it was found that when the bridge vibrates on some level at a frequency close to cargo's eigenfrequency, dominant frequencies corresponding to those found in the bridge vibration can be also found in the cargo vibration. As for the passenger's vehicle, its vibration behavior was complicated due to high sensitivity of road roughness and it was difficult to find the frequencies corresponding to the bridge vibration in the vibration of passenger's vehicle.

Study on a Seismic Force Reduction Method of the Bridge Pier Foundation Using Energy Absorption Connector Devices

Kentaro TANAKA (Setsunan University), Takeshi KITAHARA (Kanto Gakuin University), Masahide MATSUMURA and Hiroshi ZUI (Setsunan University)

Journal of JSCE, Ser.A1 (SE/EE), Vol.68, No.4, JSCE, pp.704-712 (2012) (in Japanese)

In this paper, the energy absorption performance of steel bellows as one of energy absorption connector devices is examined through non-linear time-history analysis of a viaduct supported on lead lubber bearings, a three continuous span girder bridge considering piers and pier foundations. The effectiveness of the steel bellows on seismic force reduction is verified by focusing on the differences in the energy absorption capacity of the bellows and combination use of them. It is concluded that the steel bellows set between the girders can reduce the seismic inertia force delivered to the substructures of the viaduct effectively both against the level 1 Earthquakes and the level 2 Earthquakes defined in the Specification for Highway Bridges in Japan.

Fundamental Study on Rigid Connection Detail of Steel-Concrete Composite Rigid Frame Bridge Using Bearing Plate

Kazuaki TANI (Takada Kiko Co., Ltd.), Takao YAMADA (Takada Kiko Co., Ltd.), Dai SAGOU (Takada

Kiko Co., Ltd.), Takashi YAMAGUCHI and Yuhei KAWAMOTO

Proceedings of the Sixth International Conference on Bridge Maintenance, Safety and Management, full paper in CDROM, 8-12 July, Stresa, Italy (2012)

Recently, the number of steel-concrete composite rigid frame bridges is increasing for short and medium span length in Japan. To make this type of bridge more rational, it is important to ensure a good performance of the rigid connection, which can transfer the load from the steel girder to the abutment. Therefore, a new type of the connection detail with a bearing plate has been proposed by the authors. In this study, effectiveness and applicability of the newly proposed rigid connection detail was examined by elasto-plastic finite displacement analysis. Mechanical behavior of the connection detail up to the ultimate limit state is investigated based on them. It is found that the load can be securely transferred from the steel girder to the abutment through the bearing plate. It is concluded that the proposed connection detail can be one of the practical and effective rigid connection detail considering easiness of construction.

Investigation of Structural Health of Timber Piles Supporting Aged Bridge

Tadashi NISHIKAWA (Osaka Municipal Government), Yasutomo KOMATSU (Osaka Municipal Government), Shinsuke YUMOTO (Osaka Municipal Government), Takashi YAMAGUCHI, Tomohiro MINO (CTI Engineering Co., Ltd.), Takashi MATSUMOTO (CTI Engineering Co., Ltd.)

Proceedings of the Sixth International Conference on Bridge Maintenance, Safety and Management, full paper in CDROM, 8-12 July, Stresa, Italy (2012)

In case of deciding whether a bridge should be replaced or enhanced its service life, it is important to evaluate the seismic resistance performance of the foundation because of huge amount of expense for its retrofitting. However, verification and modeling method of timber piles subjected to the earthquake are not specified in current Japanese Specifications for Highway Bridges [Japan Road Association, 2004], seismic resistance of the timber pile foundation is not clear as well as that of intact state. Osaka city has about 100 bridges supported by timber pile foundation, it is severely necessary to clarify the seismic resistance performance of it. This paper presents the experimental and analytical investigation conducted by authors, in order to evaluate the structural health of an aged timber pile and its seismic resistance performance under the strong earthquake.

Seismic Response Analysis of a Bearing Structure Consisting of a Low Frictional Sliding Bearing and a Knock-Off Device

Masahide MATSUMURA, Yasuyuki NAKANISHI (NEWJEC Inc.), Takahiro KANATA and Takashi YAMAGUCHI

Proceedings of the 15th Symposium on Performance-based Seismic Design Method for Bridges, JSCE, pp.385-388 (2012) (in Japanese)

In this study, a new type of bearing structure for bridge; combination use of a low frictional sliding bearing and a knock-off device, is presented. In the bearing structure, the knock-off device is designed and installed to the sliding bearing as triggers in order to change dynamic vibration mode from fixed condition to unfixed one during seismic attack to enhance seismic safety of bridge structures. Fundamental effects and dynamic response of the bearing structure is investigated through seismic response analysis of a viaduct with 5 spans of continuous girder bridge.

Dynamic Response of Isolated Viaduct considering Knocking-off Effects of Displacement Restrainers

Masahide MATSUMURA and Masahiko YOSHIDA (Kawakin Core-Tech Co., Ltd.)

Proceedings of the International Conference on Bridge Maintenance, Safety and Management, IABMAS 2012, pp.3480-3485 (2012)

Displacement restrainers, which are usually set besides isolation rubber bearings to restraint transverse displacement of superstructure for damage protection of expansion joints during earthquake, can be utilized as a trigger device to differ vibration modes before/after their breaks. Then, the authors have been developing displacement restrainers with knocking-off function, called as CSB, to mitigate damage of bridge pier and/or its foundation against a strong earthquake. That is, after the CSBs break, a system vibration is expected to shift into isolated one when the breaking load controlled with high accuracy. In this study, the breaking characteristics of the CSBs are experimentally investigated through static breaking tests and the installation effects of the CSBs besides the rubber bearings are also verified through shaking table tests. Moreover the

installation effects of the CSBs in a viaduct are revealed through dynamic response analysis.

Research and Design Trends on High Strength Bolted Connections for Steel Bridge Structures in Japan
Takashi YAMAGUCHI, Toshikazu TAKAI and Xue PENG

Joint Seminar on “Advanced technologies of steel and composite bridge engineering”, JSCE-EIT, 29 August, Thailand (2012)

In Japan, high strength bolted joints, such as friction type joints, tensile type joints, bearing type joints are generally used for joining primary bridge structural members. In particular, the researches on the joints with super high strength bolts, joints with thick plates and many bolts in a line and so on have been conducted actively considering current design trend in Japan which prefers to use thicker steel plates. In this paper, introduced are research and design trends on high strength bolted connections for steel bridge structures in Japan. Furthermore, future of bolted connections for bridge structural members is also discussed paying attention to their qualification assurance.

Strength and Behavior of Anchoring Devices of CFRP Rods for Steel Girder Strengthening

Katusyoshi NOZAKA (Ritsumeikan University), Akira TSUKIYAMA (Ritsumeikan University), Masahide MATSUMURA, Nobuhito OCHI (Akashi National College of Technology), Toshiyuki ISHIKAWA (Kyoto University) and Nobuhiro HISABE (Mitsubishi Plastics Inc.)

Proceedings of the International Conference on Bridge Maintenance, Safety and Management, IABMAS 2012, pp.1243-1250 (2012)

For the strengthening methods of steel girders by bonding CFRP plates, continuous strengthening is not an easy task at the location of splice plates. For this case, placing CFRP rods over the splice plates can be a possible solution, and CFRP rods need to be anchored to the ends of CFRP plates at each side of the splice plates. The adhesion, between adhesive and steel girders and between adhesive and CFRP rods, becomes a key issue in this anchoring device. In this study, several shapes for anchoring device were tested to investigate the behavior and bond strength. Force transfer mechanism in this device was discussed and the effective shape was proposed.

Fundamental Study on Load Carrying Capacities of Steel Bridge Piers under Dozens of Cyclic Loading

Takeshi KITAHARA (Kanto Gakuin University), Kentaro TANAKA (Setsunan University), Takashi YAMAGUCHI, Yusuke KISHI (Kanto Gakuin University) and Tsuyoshi HAMANO (Kanto Gakuin University)

Journal of JSCE, Ser.A1 (SE/EE), Vol.68, No.4, JSCE, pp.499-508 (2012) (in Japanese)

Recently, long-period and long-duration time seismic waves caused by huge ocean-trench earthquakes have been observed in Japan, and a few dozen to several hundred times of cyclic shaking were occurred after principal motion in these waves. However, seismic performances of structures subjected to long- duration time motions are not clear. Therefore, this paper discusses the load bearing capacities of steel bridge piers during dozens of cyclic loading. Cyclic load carrying tests and a pseudo-dynamic test were carried out in order to investigate the cyclic load bearing capacity of steel bridge piers. More-over, complex nonlinear analyses were conducted to simulate the experimental tests. Consequently, it is found that the load bearing capacity after maximum load is decreased about 10% due to cyclic loading over 10 times. Furthermore, numerical analyses have shown a part of the reason for deterioration of load bearing capacity after maximum load.

A Design Method on Temperature Girder Deformations and Estimation Method of Seismic Maximum Displacement of Steel Bellows as Energy Absorbing Seismic Control Devices

Hiroshi ZUI (Setsunan University), Kentaro TANAKA (Setsunan University), Masahide MATSUMURA, Masahiko YOSHIDA (Kawakin Core-Tech Co., Ltd.) and Hitoshi SAGO (Takada Kiko Co., Ltd.)

Steel Construction Engineering, Vol.19, No.75, JSSC, pp.41-53 (2012) (in Japanese)

This paper proposes a design method of steel bellows as seismic control devices for girder bridges on temperature girder deformations. Steel bellows are connected between girders and abutments in order to reduce the damage of superstructures and substructures. Local plastic strains of bellows are permitted due to temperature expansion and contraction of girders considering fatigue strength. This paper also proposes an

estimation method of seismic maximum displacement of steel bellows using nonlinear response spectrum. The size of bellows can be designed based on the proposed methods and the maximum displacements are estimated using nonlinear response spectrum. The estimated values are compared with calculated values by FEM and the estimated values agree fairly well with those of the non-linear time history analyses.

Fundamental Study on Arrangement of Bolted Patch Plate for Repairing Fatigue Crack

Chao PAN, Takashi YAMAGUCHI, Yukiko MITSUGI (Ishikawa National College of Technology), Kunitaro HASHIMOTO (Kyoto University), Kunitomo SUGIURA (Kyoto University), and Akihisa KONDO (Sogo Engineering Inc.)

18th Congress of IABSE, 6pages in CDROM, 19-21 September, Seoul, Korea (2012)

In Japan, the bolted patch plate method is often used for repairing the steel member with a fatigue crack on the bridge. However, it is not clear that how to arrange bolted patch plate position for repairing fatigue crack rationally and effectively. In this paper, study aims to investigate the influence of bolted patch plate arrangement for fatigue strength even though the bolted patch plate were slipped by a severe earthquake.

Finite Element Analysis on the Mechanical Behavior of High Strength Bolted Friction Type Joint with Filler Plate

Xue PENG, Toshikazu TAKAI, Honghe SUN and Takashi YAMAGUCHI

18th Congress of IABSE, 6pages in CDROM, 19-21 September, Seoul, Korea (2012)

Resent year, from the viewpoint of rational fabrication of the steel bridges, there are some applications using extremely thick plates which thickness is more than 75mm for primary members of bridge structures. However, to cut down on costs, some steel plates of bridge structures still use thin plates. So that, in case of joining such thick plates and thin plates by using high strength bolted friction type joints, it becomes serious problem for joining such thick plate and thin plate by using the filler plate. And, it is lack of enough technical information of influence about thickness of filler plate. Under the background, the tensile experiment about filler plates with extremely thick plates is carried out in 2010. Based on these experimental results, the reduction rate of slip coefficient becomes high as the thickness of the filler plate increase. For complementing experiment results, and solving slipping mechanical of filler plates in detail, the finite element analysis (FEA) has been carried out.

In this study, the FEA model is 1/4 of experimental specimens. About models, the thickness of the connected plates are 50mm-38mm, 60mm-38mm, 75mm-38mm and the thickness of the filler plates are 12mm, 22mm, 37mm. Focusing on FEA results, the relationship between slip coefficient and thickness of plate has been discussed. Also, the mechanical behavior including slip load relationship, slip coefficient, relative displacement, and reduction rate of bolt axial force of such joint was studied. It is understood that slip coefficient becomes low as the thickness of plate increase since bending moment between the connected plate and splice plate had occurred.

Applications of Steel Bellows with Different Steel Material for Seismic Safety of a Viaduct

Shinya HIRAHARA, Masahide MATSUMURA, Hiroshi ZUI (Setsunan University), Kentaro TANAKA (Setsunan University) and Takashi YAMAGUCHI

Proceedings of the 9th German-Japanese bridge symposium, 6pages in CDROM, Kyoto, Japan (2012)

Bridge isolation using high damping rubber bearings, which makes vibration period of the bridge long, is very effective to enhance the seismic safety of a viaduct. The authors have been investigated adaptabilities of steel bellows as girder connectors and have been reported that the steel bellows are effective for damage mitigation of the bridge due to stable energy absorbing capacities of the bellows. In this study, the influence of stress-strain relationship of the steel bellows on vibration control effect of elevated bridge is investigated by FEM analysis. 5 span continuous girder bridge supported by 6 bridge piers is used in the analysis and the steel bellows made of 3 types steel materials are installed at the both ends of the girder ends. The steel bellows is modeled by spring elements, of which the load-displacement relationship and an equivalent damping coefficient were decided by referring to cyclic and dynamic loading tests results in the axial direction of the steel bellows. It is concluded that all the steel bellows can provide stable vibration controlling effects.

Loading Test and Monitoring of the Newly Constructed Portal Rigid-frame Bridge in Osaka

Yuhei KAWAMOTO, Takashi YAMAGUCHI, Masahide MATSUMURA, Akihiko YOSHIKAWA (Katayama Stratech Corp.) and Nobuhito OKUBO (Katayama Stratech Corp.)

Proceedings of the 9th German-Japanese bridge symposium, 9pages in CDROM, Kyoto, Japan (2012)

Recently, the number of steel-concrete composite rigid frame bridges for short and medium span length is increasing in Japan. Structural features of this type of the bridge are rigid connections between steel girders and RC abutments without expansion joints. Application of this type of the bridge can expect enhancement of the service life, reduction of the life cycle cost and improvement of earthquake resistance due to no bearings and expansions. However, structural performance of the rigidly connected part and vibration characteristic of the bridge are not clear, so a conservative design method has been done frequently. Moreover the performance after aged deterioration is not clear too. Carried out in this study are the actual bridge instrumentations to clarify structural performance of the rigidly connected part and vibration characteristic of the bridge. In addition, initial data of the bridge is measured before in-service and the aged change for the next 2 years also will be investigated.

Experimental Study on Slip Behavior of High Strength Bolted Joints for Underwater Steel Structure

Honghe SUN, Takashi YAMAGUCHI, Kyoichi NAKAYASU (Hitachi Zosen Corp.), Toshiaki MORII (Hitachi Zosen Corp.) and Masahide MATSUMURA

Proceedings of the 9th German-Japanese bridge symposium, 7pages in CDROM, Kyoto, Japan (2012)

In recent years, the growing needs for the refurbishment of the superannuated hydraulic steel gates become a problem to be solved. Most of field joints of them are welded on site in spite of some difficulties in welding such as thermal strain concentrations, work space limitations and so on. On the other hand, high strength bolted frictional type joints are hardly applied to their refurbishment because of the following unclear points; a slip coefficient with water ingress, decrease of bolt axial force by corrosion, delayed fracture of the high strength bolt and so on. If the high strength bolted frictional type joints can be applied to them, it widely contributes to improve the workability, reliability and economic efficiency. In this study, slip behavior of the high strength bolted frictional joints subjected to tensile load is investigated by focusing on water pressure, bolt axial force and the difference of plates' thickness. Based on the experimental results, the slip coefficient is revealed in the case of water ingress into the frictional surface.

Study on Mechanical Property of Higher Yield Strength Steel Plates for Bridges

Takahiro TARUI (Osaka University), Kiyoshi ONO (Osaka University), Masahide MATSUMURA and Jumpei YOSHIYAMA

Proceedings of the 9th German-Japanese bridge symposium, 6pages in CDROM, Kyoto, Japan (2012)

Higher yield strength steel plates for bridges, SBHS has been standardized by Japanese Industrial Standards (JIS). In order to use SBHS for bridges generally, it is important to grasp the mechanical property of SBHS. However, there is not enough information on the mechanical property of SBHS500 and SBHS700. In this study, tensile tests of SBHS500 and SBHS700 were conducted to gain the information on the mechanical property and the stress-strain relationship. The test specimens were cut along rolling direction and perpendicularly to rolling direction. Based on the test results, the information on the mechanical property and stress-strain relationships of SBHS500 and SBHS700 were gained and the feature of them was investigated.

Analytical Study on Strengthening Effects of U-shaped Attached Plates onto Steel Deck Plates with U-ribs

Satoshi KIMURA, Takashi YAMAGUCHI, Yoshio TAMBA (Hanshin Expressway Management Technology Center), Hiroki SUGIYAMA (Hanshin Expressway Co., Ltd.) and Masahide MATSUMURA

Proceedings of the 9th German-Japanese bridge symposium, 6pages in CDROM, Kyoto, Japan (2012)

Prevention of fatigue cracks at orthotropic steel deck consisting steel box girders of viaducts in urban area is one of major concerns to be solved urgently. Then, a strengthening method by filling mortar into the existing U-shaped ribs and adding inverted U-shaped attached plates between the existing ones by high strength one-side bolts and adhesives is proposed. This strengthening method does not require the traffic restriction. In this study, FEM analysis is carried out in order to clarify the strengthening effects of the method by focusing on the bolt pitch connecting both the U-shaped attached plates. Also adhesion effects of the adhesive applied the contact surfaces between the deck plates and the additional U-shaped attached plates are investigated. It can be concluded that adhesion is necessary to obtain sound strengthening effect by the

strengthening method. In addition, the differences of the bolt pitch do not provide significant changes on the minimum principal stress.

Seismic Retrofit for a Network Arch Bridge with Slit-type Knock-off Bearings

Koichi SUGIOKA (Hanshin Expressway R&D Co., Ltd.), Nobuhiro MASHIMA (Hanshin Expressway Co., Ltd.), Hiroaki MATSUSHITA (Hitachi Zosen Corp.), Takehiko HIMENO (Kawakin Core-Tech Co., Ltd.) and Masahide MATSUMURA

Proceedings of the 15th World Conference on Earthquake Engineering, 10pages, Lisbon, Portugal (2012)

Seismic retrofit of an existing network arch bridge against large-scale (Level 2) earthquake ground motions was performed by modifying existing fixed steel bearings into slit-type knock-off bearings. Three-dimensional non-linear dynamic response analyses were carried out considering site-specific ground motions. It was confirmed that shear panel dampers as passive energy-dissipation were needed on both fixed-side and movable-side pier tops to avoid the potentially difficult retrofit work for the undersea pier anchors and foundations. The authors proposed slit-type knock-off bearings with the knock-off function as triggers against the Level 2 earthquake ground motions to provide isolation effect. Performance tests of the slit-type knock-off bearings were conducted to verify the required performance for the seismic retrofit design.

Characteristic of Tensile Strength and Charpy Absorbed Energy of Welded Joints for Steel Bridge Structures

Kuniaki MINAMI (Japan Railway Construction, Transport and Technology Agency) and Takashi YAMAGUCHI

Journal of JSCE, Ser.A1 (SE/EE), Vol.68, No.3, JSCE, pp.623-634 (2012) (in Japanese)

Many kinds of steel are widely used in steel bridge structures. This report summarized the welding procedure tests carried out in 2003-2010. In these welding tests, four kinds of steel were employed to fabricate welded joint specimens, which were SM490Y, SMA490W, SM570Q and SMA570W. In this report, the results of tensile strength and Charpy absorbed energy were shown. Tensile strength exceeded to the nominal base metal strength for all tensile coupon specimens. Charpy absorbed energy of HAZ (heat affect zone) also exceeded to 200J on an average in many type of steel. However, there were a few cases that an average of Charpy absorbed energy of Depo (weld metal) is beyond 100J, regardless of welding wire and welding method. It has been shown that the mechanical properties, such as tensile strength and Charpy absorbed energy, of welding materials does not exceed to that of steel material.

Experimental Study on Cyclic Loading Behavior of Rivet Jointed Panel Point Damaged by Corrosion

Takamasa FUJIMOTO (Kyoto University), Kunitaro HASHIMOTO (Kyoto University), Kunitomo SUGIURA (Kyoto University) and Takashi YAMAGUCHI

Proceedings of Constructional Steel, Vol.20, JSSC, pp.349-356 (2012) (in Japanese)

In this study, cyclic loading experiment is carried out in order to clarify the mechanical behavior and the relationship between corrosion of rivet head and residual strength of rivet jointed panel point. In the experiment, non-damaged and damaged rivet jointed panel point specimens are subjected to cyclic load, which cut from the demolished steel bridge members. From the result, it is found that the residual strength of damaged rivet jointed panel point showed almost consistent result with the non-damaged specimen. On the other hand, it is found that energy absorption performance decreases because the rivet is slipping out.

Basic Study on the Performance after the Slip for Bolted Joint for Friction Type

Mami NISHIKAWA (Ishikawa National College of Technology), Yukiko MITSUGI (Ishikawa National College of Technology), Takashi MATSUNAMI (Ishikawa National College of Technology) and Takashi YAMAGUCHI

Proceedings of Constructional Steel, Vol.20, JSSC, pp.371-376 (2012) (in Japanese)

Bolted joint for friction type is designed supposing that slip is not occurred. However, after bolted joint for friction type is slipped, the joint resists through shear and bearing mechanism. In order to study the performance of the bolted joint for friction type after the joint slipped, we carried out the examination on the bolted joint. It is concluded that the capacity of joint after it slipped can be below the slip load. The capacity of the joint after slip is influenced by the distance of end. Therefore, it is necessary that the distance of end is

designed on the viewpoint break of the end to expected the capacity of the joint after slip.

Experimental Study on the Behavior of Anchoring Devices for Strengthening of Steel Girders with CFRP Rods

Katsuyoshi NOZAKA (Ritsumeikan University), Akira TSUKIYAMA (Fuji Engineering Co., Ltd.), Masahide MATSUMURA, Nobuhito OCHI (Akashi National College of Technology), Toshiyuki ISHIKAWA (Kyoto University) and Nobuhiro HISABE (Mitsubishi Plastics Inc.)

Proceedings of Constructional Steel, Vol.20, JSSC, pp.647-654 (2012) (in Japanese)

Repair and strengthening technique using CFRP strips of high elasticity to steel bridge members provide an easy adoptability and an effective strengthening effect. When considering application of the technique to a lower flange plate of steel I-shaped girder, pointed out are difficulties in installation of the CFRP strips at the connection parts due to projection of the splice plates. Then a new strengthening technique using CFRP rods to the projecting part is devised to prevent debonding and to ensure stress reduction at the edges of the strips. Then in this study, a strengthening effect using an anchor part made of CFRP cover filled with epoxy resin and CFRP rods connecting the anchor parts is experimentally checked through pull-out tests.

Extraction and Interpretation of Geological and Geotechnical Characteristics: In the Case of Kansai Geo-database

Geotechnical Engineering Magazine, JGS, Vol.61, No. 6, pp.20-23, 2013 (in Japanese)

Naoko KITADA(Geo-Research Institute), Keiji TAKEMURA(Kyoto Univ.), Muneki MITAMURA(Faculty of Science), and Akihiko OSHIMA

In the Kansai area, there are many sedimentary basins that are surrounded by active faults and many sediment layers deposit in the basin. These consist of sand and clay deposit, and clay sediments are classified into marine clay and non-marine clay. The Kansai Geo-informatics Network has developed a geotechnical database. This borehole database consists of dense distributed data over 60 thousands. Several geological investigated borehole data area available in the Kansai area. We are attempting to do geological interpretation for these dense distributed geotechnical borehole data. The classified faces using sedimentary environment and tephra chronology will help to explain the difference in soil properties in this area.

Liquefaction Countermeasure by Groundwater Lowering in Osaka Plain

Geotechnical Engineering Magazine, JGS, Vol.61, No. 6, pp.36-37 (2013) (in Japanese)

Akihiko OSHIMA

Lecture: Foundation Design of Residential Land

Geotechnical Engineering Magazine, JGS, Vol.61, No. 9, pp.40-47 (2013) (in Japanese)

Akihiko OSHIMA

Recent Trends in Ground Improvement Technologies III : Ground Disaster and Ground Improvement Technologies on Earthquake

Journal of the Society of Materials Science Japan, Vol.62, No. 5, pp.342-349 (2013) (in Japanese)

Akihiko OSHIMA, Shigeyoshi HIRATA(Daiwa House Industry), Shigehiro MURAKAMI(Fudo Tetra Corporation) and Hajime IMANISHI(Tohoku Institute of Technology)

A simplified technique for slope stability assessment based on insitu S-Wave velocity measurement

M. U. QURESHI (Univ. of Wah), S. YAMADA and I. TOWHATA (Univ. of Tokyo)

Earthquake-Induced Landslides, Springer, pp. 869-979 (2012)

Natural disasters such as earthquakes or heavy rainfalls thwart the potential stability of weathered slopes which has significant effects on the safety of infrastructure in the vicinity. In the case of developing countries, this situation is inevitable and necessitates to develop a quick and economical technique for overall progress in safety. In dealing with the slope instability problems for such regions, at first it is important to identify the potentially unstable slopes and then decide the mitigation strategies. In this regard, in-situ shear strength of weathered geo-material exposed on slopes should be carefully delineated which is a time consuming procedure. Therefore, a relation of in-situ shear strength of weathered geo-material to the geophysically measured S-wave velocity is employed in the present study. Field experiments were conducted to evaluate the shear-wave velocity, depth and in-situ shear strength of surface weathered layer which included seismic refraction, portable dynamic cone penetration and field direct shear tests. Field studies were conducted in

Japan (Yokosuka, Nagano, Izu and Kobe), and Pakistan (Muzaffarabad and Taxila). The investigated sites were recently disturbed by strong earthquakes or heavy rainfalls. By using the depth and in-situ shear strength of surface weathered layer stability analysis (infinite slope) was carried out and correlated to S-wave velocity, which suggested that the safety factor of a weathered slope reduces to half during the rainfall event. Moreover a safety assessment matrix (SAM) is presented which by inputting the slope angle and the S-wave velocity of the weathered geo-material on slope surface categorizes the safety in to, a) stable, b) Potentially stable and, c) Unstable. The authors envision using SAM for the direct evaluation of potential instability by a continuous monitoring of S-wave velocity and slope angle. Therefore, it is recommended that, monitoring of S-wave velocity of surface weathered layer for risk assessment is a quick and economical technique other than time consuming, local and expansive intrusive methods.

Laboratory Shear Tests on Effect of Soil Improvement by Fibers

M. THU (Univ. of Tokyo), I. TOWHATA (Univ. of Tokyo) and S. YAMADA

Proc. of Int. Conf. Ground Improvement & Ground Control, Wollongong, Oct. 30- Nov. 2, pp. 843-848 (2012)

Fiber-reinforced soil is a promising technique for increasing the shear strength and stability of soils. The technique is used today in a various application such as retaining structures, stabilization of various types of embankments and footings. Reinforcement effect may vary greatly with the use of either steel, polymeric fabrics or natural fibers. In this study, all of laboratory tests were conducted by means of a torsion shear machine using 50 kPa of mean effective principal stress and various orientations of fiber arrangement in the specimen. In order to explore the stress-strain and dilation behavior of fiber-reinforced soil, a series of consolidated drained monotonic torsion shear tests were carried out under dry condition. All of test programs were conducted on dry Toyoura sand with "Polyester Sewing Thread" of vertical position (0°), inclined position (both for $+45^\circ$ and -45°), and randomly distributed long, medium and short length. Throughout the testing program, the relative density of 60~63% or 80~83% were employed. The results show that (1) the greater fiber content increases the peak strength, (2) the longer fibers can give greater strength than shorter fibers, (3) $+45^\circ$ orientation of fibers (tensile deformation of fibers) gives the highest strength among all of tests, and (4) -45° orientation of fibers (fibers undergoing compression) tends to weaken the sand.

Experimental study on mitigation of liquefaction-induced lateral displacement using deep mixing

R. RASOULI (Univ. of Tokyo), N. TAKAHASHI (Sumitomo Mitsui Construction CO., LTD), A. DERAKHSHANI (Univ. of Tokyo), S. YAMADA, Y. TAKAOKA (Sumitomo Mitsui CO., LTD) and I. TOWHATA (Univ. of Tokyo)

Proc. of 7th Int. Conf. Case Histories in Geotechnical Engineering, Chicago, Apr. 29- May. 4, Paper No. 3.24a (2013)

After 1990s' earthquakes in Japan, lateral flow of liquefiable slopes a serious concern of engineers. Especially Kobe earthquake (1995) in which high subsidence of river levee as a result of liquefied sand lateral flow was observed, because a turning point in geotechnical engineering approach in dealing with this phenomena. From that time many different kinds of mitigation measures for preventing or at least controlling the extent of lateral flow have been proposed. Improving soil by deep mixing columns is one of the common methods of soil improvement that can also be used for controlling the consequences of liquefied sand flow. For analyzing the factors affecting the efficiency of this method, several shaking table tests have been done. This article is showing the effects of studied factors including columns pattern, the length and improvement ratio. Moreover the magnitude of flow inside and outside of improved area are scrutinized. Finally, based on experimental observations, behavior of liquefied sand in existence of deep mixed soil is modeled numerically.

Undrained cyclic resistance of liquefiable sand undergoing long duration of earthquake motion

T. SASAKI (Univ. of Tokyo), S. YAMADA and I. TOWHATA (Univ. of Tokyo)

Proc. of 5th Int. Geotechnical Symposium, Incheon, May. 22-24, pp.301-309 (2013)

The 2011 Great Ear Japan Earthquake (Mw=9.0) caused severe liquefaction in the reclaimed subsoil in the Tokyo Bay area. As the long duration of earthquake may have influenced the severity of liquefaction, its effect on the safety against liquefaction need to be evaluated. In the present study, undrained cyclic shear tests as well as the cumulative damage analysis were carried out to incorporate duration effects into the C_w parameter which is set equal to 1.0 against an earthquake of magnitude 8.0. the result suggests that C_w will be less than 1.0 for an earthquake of magnitude 9.0 and the safety against liquefaction will decrease relative

to that for an earthquake of magnitude 8.0.

One- g shaking-table experiments on buried pipelines crossing a strike-slip fault

W.W. SIM (Imperial College), I. TOWHATA (Univ. of Tokyo) and S. YAMADA

Gotechnique, Vol. 62, No. 12, pp.1067-1079 (2012)

Buried pipelines provide essential services to the urban population, and as a result of their geographical dispersion they remain particularly vulnerable to damage caused by natural disasters. Among many damage mechanisms, the present study addresses those induced by seismic fault action and its related ground distortion. A better understanding of the factors influencing the forces acting on buried pipelines due to imposed ground displacements will enable more appropriate design of pipelines in the future and contribute towards reducing damage incurred by the buried pipes. To this end, 1g shaking table experiments were performed on buried instrumented model pipelines installed in Toyoura sand and monitored in terms of strain whilst subjected to four different levels of dynamic excitation and right-lateral strike-slip faulting. The experiments indicate that simultaneous shaking and faulting, which is a more realistic condition than tests performed without shaking, reduce measured pipe strains. Tests also indicated there is a linear decrease in the maximum strains experienced by the buried pipe as the sine of the pipe-fault crossing angle decreases and that there is a non-linear relationship between the relative density and the strains experienced by the buried pipe.

The Comprehensive Evaluation of BRT System Based on Introduced Examples in Major Cities of China

BanBan LI and Yasuo HINO

Proceedings of the Eastern Asia Society for Transportation Studies, Vol. 19, 12 p. (CD-ROM) (2013)

In recent year, in the major cities of China, in order to improve the problems caused by motorization, the countermeasure to develop Bus Rapid Transit system as the central of public transit has been implementing. This paper aims to propose the evaluation method, based on the internal and external effects and their relationship obtained by analyzing the actual data of four major cities. As a result, some typical individual factors were selected and both internal and external effects were evaluated based on their factors. In addition, an idea of the comprehensive effects by integrating internal and external effects was proposed.

Effect of Information Provision toward Sustainable Bus Transport

Noboru ISE, Yasuo HINO and Takeshi HIROSE

Proceedings of the Eastern Asia Society for Transportation Studies, Vol. 19, 15 p. (CD-ROM) (2013)

Recently, it has an increased need for introduction of public involved approach into local public transport planning, in order to fully grasp and reflect opinions of local residents and build consensus. However, it seems that there are some issues such as information provision, components of approach, division of roles in the public involved process to realize local public transport. Therefore, this study focused on the effectiveness of information provision in a public involved process from both aspects of awareness and behavior. As a result, it was revealed that the provision of appropriate information related to the future condition of individuals and local area, and actual condition and the importance of public involvement promotes not only understanding for necessity of bus transport, awareness of collaboration and intention to use bus, but also bus use behavior.

Study on Major Issues of Road Safety Education based on Safety Consciousness of Bicycles for School Students

Yusuke KOTAKE, Yasuo HINO and Nagahiro YOSHIDA

Japan Society of Civil Engineers, Infrastructure Planning Review, No.29, pp. 1185-192 (2012) (in Japanese)

Recently, the number of accidents involved school students by riding bicycle has been increasing. One of the reasons may be the lack of understanding rules of traffic including bicycle and consciousness of road safety. Then, this study focused on not only the consciousness of road safety of school students and parents especially in case of using bicycle, but also the actual condition and major issues of road safety education in school and home. In this study, the important issues concerned with road safety mentioned above were revealed by analyzing the data of large scale questionnaire research including 6,000 and more respondents and selected 29 schools in Hyogo prefecture. As a result, a lack of road safety education in junior high school and high school and understanding and interest of road safety came out of these analyses. Furthermore, based on the additional feedback survey, what is important is continuous instruction and training for teachers about

road safety. In addition, it must be important to investigate the cooperation among school students and parents, teacher, police officer and researcher, in order to the effective education system for road safety.

Integrated Evaluation Methods for Introducing BRT System based on Case Studies in Major Chinese Cities

Ban Ban LI and Yasuo HINO

Japan Society of Traffic Engineers, Papers on Traffic Engineering, No. 33, pp. 551-557 (2013) (in Japanese)
In China, BRT (Bus Rapid Transit system) as the central of public transit has been implementing, in order to improve the problems caused by motorization and urbanization. However, it has not been enough to evaluate effects for introducing BRT systems. This paper approaches three aims, such as, 1) review of some conditions at introducing the first BRT system of 4 case study cities, 2) analyses of relationship between internal effects and external effects and 3) proposal of integrated evaluation methods for both effects of internal and external. As a result, some typical individual factors were selected and both internal and external effects were evaluated based on their factors. In addition, an idea and the suitable model to evaluate the comprehensive effects by integrating internal and external effects was proposed. This modelling must be necessary and important to introduce the appropriate BRT system from viewpoint of not only fairness taxation but also social cost including environmental pollution.

Evaluation of External Effects on Introducing BRT System in Major Cities of China

Ban Ban LI and Yasuo HINO

Japan Society of Civil Engineers, Proceedings of Infrastructure Planning, No. 45, 4 p. (CD-ROM) (2012) (in Japanese)

In recent year, in the major cities of China, in order to improve the problems caused by motorization, BRT (Bus Rapid Transit System) has been introducing. In the former study, we analyzed the inner effects of BRT system as the first step to investigate the evaluation method for BRT system. This paper aims to reveal the external effects obtained by introducing BRT, as the second step to propose the evaluation method of BRT. As a result, it was clear that the introduction of BRT system should influence not only the improvement of environmental pollution but also the increase of population of both residents and employees, and the price of land and so on. In addition, these influences were depended on the characteristics of city and the policy of development in the future.

Review on Road Safety Facilities of Arterial Road in the Gobi Desert of Uighur

Kelem ZULPIKAL and Yasuo HINO

Japan Society of Civil Engineers, Proceedings of Infrastructure Planning, No.45, 4 p. (CD-ROM) (2012) (in Japanese)

The road safety facilities must be important to not only provide the safety driving but also reduce both traffic accidents and potential risk of accidents. However, in the desert region, the influences of desert weather to road safety have become important issues. This study aims to review the actual condition of road safety facilities of arterial road in Gobi desert and reveal the problems concerned to these facilities, based on the onsite survey and questionnaire survey for drivers. As a result, some important findings came out as follows. The insufficiency of road safety facilities not only give rise to occur the traffic accidents, but also make difficult to support some persons involved accident. In order to improve such situation, the development of data base should be essential and the analyses of the relation between major facilities and accidental occurrences based on data base must be necessary.

A Study on Investigation of Environmental Improvement Measures based on Road Space Evaluation by Analyzing Questionnaire Survey for Pedestrians

Tatuya OGIHARA, Yasuo HINO, Takashi UCHIDA and Nagahiro YOSHIDA

Japan Society of Civil Engineers, Proceedings of Infrastructure Planning, No. 45, 4 p. (CD-ROM) (2012) (in Japanese)

Recently, environmental factors have been the essential requirement to draw up the comprehensive plan in many cities. However, the evaluation of urban environment must be not easy in comparison with the natural environment, because the evaluation may be depend on by personal properties. The aims of this study consist of three parts, as follows. First of them is to find some key elements such as “prosperity”, “fondness” and “landscape” related to “environment”. Secondly, the relationship among them will be analyzed. Finally, the environmental improvement measures must be evaluated by these relationships of four elements based on

analyses of questionnaire data for pedestrians. As a result, it was revealed that nevertheless environmental evaluation was different by road types, four elements have interrelationship. In addition, some environmental improvement measures were evaluated quantitatively, including the indirect effects of other elements. These findings may be helpful to introduce the suitable measures for environmental improvement of road space.

Information Provision of Public Structure to Resolve Information Gaps between Citizen and Public Administration

Hirokazu MATSUMOTO and Takashi UCHIDA

Sociotechnology Research Network, SOCIOTECHNICA, Vol. 9, pp. 109-119 (2012) (in Japanese)

With advent of an information society and citizen society, information held in public administration should be used broadly. This study proposes “Public Structure Traceability System” to fill in information gaps between public administration and citizen. And we have worked toward the implementation.

In this paper, we analyze present situation about administrative information and clarify the problem. Then an information system demanded by the results and process that we determine the information on the system is showed. And two experiments show citizens’ information needs and prove the benefit of the system.

An Analysis of Town Navigation System Practices and Preliminary Modeling of Sightseeing Spot Choices Seeking for User Oriented Recommendation System

Yuki OKUHATA and Takashi UCHIDA

Journal of Japan Society of Civil Engineers, Ser. D3, Vol. 68, No. 5, pp. I_641-I_648 (2012) (in Japanese)

As the falling birthrate and the aging population, increasing suburban shopping malls, urban area is on a cavitation phenomenon. In order to solve the problem, a lot of countermeasures like digging up concealed spots by local residents, transmitting information about sightseeing, are worked on positively for local revitalization. In all of the countermeasures, “Pedestrian ITS (Intelligent Transport System)” is in a center of attention to deliver information for sightseeing. Recently, wide variety town navigation systems are adopted in each place. However, most of them aren’t done well for themselves because their operations are stopped soon after management is started. External factor bring down the problems and contents doesn’t attend to user’s needs are causes of that difficulties. In this study, we clear up the causes of that and modeling of sightseeing spot choices required for user recommendation system.

A Study on the Urban River Waterfront Development: A Case of Medium and Small Size Rivers in the Built-up Area

Yasumasa FUKUSHIMA and Takashi UCHIDA

Japan Society of Civil Engineers, Proceedings of Infrastructure Planning, No. 46, 9 p. (CD-ROM) (2012) (in Japanese)

Recent urban river development has been implemented in the actions of the waterfront development concerning not only flood control and water use but also environment and utilization. Waterfront development involves several parties such as an operating body, residents along the river embankment, planners, and the relevant organizations and bodies, but in some cases immature consensus building blocks the completion of the projects.

This study takes a case of the waterfront development in the newly built-up area along medium and small size rivers; bases the evidences obtained through the process from the planning and the implementation till the subsequent secular changes; and makes analyses especially focusing on the relationship among these concerned parties. Then we also propose the way it could be such as the viewpoints desired in planning, the management in administration, post-improvement monitoring and hearing, and the feed-back, as for the concrete measures targeting the smooth completion of an enterprise and consensus buildings in the urban river waterfront development.

Study on the Public Awareness of the Community Bus from the Perspective of Public Support and Maintenance

Yusuke KURASHIMA and Takashi UCHIDA

Japan Society of Civil Engineers, Proceedings of Infrastructure Planning, No. 46, 7 p. (CD-ROM) (2012) (in Japanese)

A large amount of public support is supplied to public transport every year. For maintenance, It is important to turn to acquisition of an understanding by grasping and utilizing the consciousness to the enterprise of the citizen who has subscribed funds.

In this study, we tried grasp of public awareness used as the basic intelligence towards acquisition of understanding by analyzing by multivariate analysis about "the resident questionnaire about public transport (community bus *etc.*) of Izumi city" for the citizen of Izumi city in Osaka. We clarified public awareness as "the actual condition of the intention about public support." and "the actual condition of the knowledge and an information deficit for declaration of intention." paying attention to intention undisplayed replies. We also described the importance of analyzing intention undisplayed replies such as "it is not which, either", "it not understanding", and a "blank."

An Analysis of Bicycle Path Choice Behavior by Knowledge and Infrastructure

Takuya OKADA and Nagahiro YOSHIDA

Japan Society of Civil Engineers, Proceedings of Infrastructure Planning, No. 46, 6 p. (CD-ROM) (2012) (in Japanese)

It is well known that promoting bicycle would bring some health benefits as well as environmental effects. In addition, it is also important to note that bicycle would offer equal opportunity even for those who don't have cars. On the other hand, as most of people in Japan still believe that bicycle should be used on pavement rather than on-road path because of its safety concerns and historical issues. In order to extract with potential benefits from the nature of cycling, some intervention of soft or hard countermeasures are required. To clarify and control these psychological or physical effects on their behavior properly, it is important to understand the relationship between cyclist knowledge and infrastructure effects on their path choice behavior. So in this study, we prepared some composite photographs controlled by the combination of different traffic and road condition with different bicycle paths like bicycle lane, shared marking, and shared-use-path. An online survey using the photographs was conducted for four different knowledge-controlled groups to distinguish their knowledge from their preference of path conditions. We also analyzed the effect on different road user, road segment, road width and scale of junction.

A Comparative Experiment on Health Benefit of Bicycle Path Conditions Using Indirect Energy Consumption Estimation Method

Japan Society of Civil Engineers, Infrastructure Planning Review, No. 29, pp. 991-1003 (2012) (in Japanese)
Soichiro NOTAKE, Nagahiro YOSHIDA, Yasuo HINO, Takashi UCHIDA and Yutaka KIMURA

Recently, several researches showed that riding bicycle has some health benefits in many countries. Riding bicycle in Japan also attracts people who have concerns about their health and environment while bicycle trip statistics showed that the average trip distance was much shorter than other countries. Under these conditions, some bicycle transport planners focuses on the engineering property of bicycle network to realize health benefit effectively, but there is few researches describing the health effects on existent bicycle path conditions. Therefore we conducted the preliminary experiment that 8 students ride on 3 courses representing urban road conditions with approx. 5km length including different types of bicycle path and traffic condition. During the experiment, heart rate was monitored as dependent variable. Before the experiment, expiratory gas analysis was conducted in laboratory which gives an indirect estimation of energy consumption using the relationship between the load strength of physical activity and energy consumption. This study analyses the relationship between energy consumption rate and bicycle path conditions such as degree of gradient, interval of signals, and accumulation of physical tiredness using indirect energy consumption estimation method. It also investigated the effect of psychological pressures on heart rate caused by road or traffic conditions.

Accident Risk Analysis of Bicycle at Non-Signalized Junctions along Trunk Roads

Yoshihito TAKENAKA and Nagahiro YOSHIDA

Japan Society of Civil Engineers, Proceedings of Infrastructure Planning, No. 47, 4 p. (CD-ROM) (2013) (in Japanese)

Recently bicycle transport is considered to have some environmental and health benefits. On the other hand, the number of bicycle-related accidents still remains high. Some statistical research showed that bicycle-related collisions are mainly occurred at non-signalized junction. One of the main causes of this type of accidents are considered that bicyclists and drivers can't recognize each other properly at non-signalized junctions. Therefore this study focuses on bicycle-related accidents at non-signalized junctions along trunk road. An accident risk analysis was conducted to understand potential factors related with recognition like geometric junction layout, regulations and safety facilities.

An Experimental Study on Characteristics of Cyclist's Eye Movement and Behavior on Bicycle Facilities

Takanori OKAWA and Nagahiro YOSHIDA

Japan Society of Civil Engineers, Proceedings of Infrastructure Planning, No. 47, 4 p. (2013) (in Japanese)
Bicycle lanes with legal control have been introduced on carriageway as a Japanese governmental pilot project since 2008. However the facility design standard for cyclists on roadways is not determined yet while many standards remain the same as for cars/drivers. There are few researches on cyclists' specific eye movement and behavior with road conditions. The amount of visual information for cyclists on road should be minimized to avoid confusion, but required to be an informative road space for bicyclists even without driving license. Therefore, some empirical experiments have been conducted to understand differences of cyclist's eye movement and behavior on various types of facilities.

A Study on Effect of Urban Heat Release into an Enclosed Sea on Water Temperature Using the Regional Ocean Modeling System with Two-Way Nesting Method

Takaaki SHIGEMATSU, Masatoshi MAEKAWA, Masaki NAKAO and Susumu YAMOCHI

Journal of Japan Society of Civil Engineers, Ser. B2 (Coastal Engineering), Vol. 68, No. 2, pp. I_1149-I_1150 (2012) (in Japanese)

Numerical simulation was carried out to evaluate effect of urban heat release into an enclosed sea on the water temperature. To improve the condition of releasing the heated effluent, the resolution near release point was made release but tidal range, tidal elevation, and wind condition. Moreover, it is found that sea surface temperature in Osaka Bay strongly depends on wind stress.

A Study on Reproducibility of Thermal Stratification Using the Regional Ocean Modeling System

Masatoshi MAEKAWA, Takaaki SHIGEMATSU, Toru ENDO and Ryuichiro KIZU

Journal of Japan Society of Civil Engineers, Ser. B2 (Coastal Engineering), Vol. 68, No. 2, pp. I_941-I_945 (2012) (in Japanese)

Numerical simulation and field investigation were carried out to examine reproducibility of thermal stratification using Regional Ocean Modeling System. Water temperature distribution was measured in enclosed water area with weather information. As a result of numerical simulation, it is found that fluctuation of thermal stratification such as destruction caused by fierce wind and development caused by solar radiation can be reproducible. Furthermore, according to calculation results of kinematic viscosity coefficient, it was indicated destruction of thermal stratification was strongly influenced by wind stress.

A Study on Outflow Condition from a Dredged Trench of Turbid Water Induced by Backfill using a Vertical Pipe

Tatsunori HIRANO, Takaaki SHIGEMATSU, Tsuyoshi KANAZAWA

Journal of Japan Society of Civil Engineers, Ser. B2 (Coastal Engineering), Vol. 68, No. 2, pp. I_751-I_755 (2012) (in Japanese)

In order to predict turbidity flow induced by backfill using a vertical pipe, a numerical model has been developed. As a result of analysis on outflow condition from a dredged trench of the turbid water by the developed model, turbid water spreads out of a dredged trench when its thickness in front of the wall is more than 80 percent of height of the wall. Further, water including sulfide and oxygen-poor water in a dredged trench outflow anytime turbidity mass outflows from a dredged trench. In addition, it is figured out that impact to surrounding sea areas by the backfill can be controlled by the sediment dumping time interval.

A Study on Process of Heat Transfer at Sea Surface Layer Based on Measurement data

Masatoshi MAEKAWA, Takaaki SHIGEMATSU, Toru ENDO

Journal of Civil Engineers, Ser. B3 (Ocean Engineering), Vol. 68, No. 228, pp. I_929-I_934 (in Japanese)

Water temperature distribution in enclosed water area, especially from water surface to 0.5m under water surface, was measured with weather information, wind, and solar radiation. Seasonal change of vertical thermal distribution including violent weather effect is presented. Based on the measurement data, latent heat flux and sensible heat flux are estimated. Moreover thermal diffusivity in the water surface layer with 0.5m depth is evaluated. Finally, thermal flux between water surface and atmosphere is discussed with considering thermal supply from deeper water to water surface.

A Study on Effect of Discharge of Thermal Water on Structure of Water Temperature in an Enclosed

Bay

Takaaki Shigematsu and Masatoshi Maekawa, *Proceedings of the Twenty-third (2013) International Offshore and Polar Engineering*, pp.1314-1320, Anchorage, Alaska, USA, June 30-July 5 (2013)

Numerical simulation is carried out to evaluate effect of urban heat release into an enclosed sea on the water temperature. To improve the condition of releasing the thermal effluent, the resolution near release point was made higher using two-way nesting method. As a result, it is found that the effect was not influenced by only conditions of release but tidal range, tidal elevation, and wind condition. Moreover, it is found that sea surface temperature in Osaka Bay strongly depends on wind stress.

Environmental Urban Engineering

Dynamics of Refractory Organic Nitrogen in Osaka Bay and the Yodo and Yamato River

Masaki NAKAJIMA, Hiroshi MATSUMOTO and Susumu YAMOCHI

Journal of Japan Society of Civil Engineering, Ser. B2 (Coastal Engineering), Vol. 68, pp. 1036-1040 (2012) (in Japanese)

Field surveys and indoor experiments were conducted in 2011 to clarify the dynamics of refractory nitrogen along the Osaka Bay and at the lower areas of the Yodo and Yamato rivers. In the process of dispersion of brackish waters from the inner areas to the mouth of Osaka Bay, most of the dissolved organic nitrogen (DON) changed to a refractory form. A small amount of nitrogen was available for primary producers in offshore areas of Osaka Bay since the percentage of non- or less-biodegradable DON to total nitrogen was high. These results demonstrate that emphasis should be placed on the establishment of environmental quality standards for water based on the nitrogen available for coastal organisms, along with the regulation of water quality by total nitrogen.

Distributions of *Ulva ohnoi* and Currents at the Artificial Tidal Flat of Hannan Second District in Osaka Bay

Daiki SAKAI, Toru ENDO, Takaaki SHIGEMATSU and Susumu YAMOCHI

Journal of Japan Society of Civil Engineering, Ser. B2 (Coastal Engineering), Vol. 68, pp. 1186-1190 (2012) (in Japanese)

Field surveys were carried out to clarify the effect of geographical features and currents on the distribution of green-tide forming seaweed, *Ulva ohnoi* at the artificial tidal flat of Hannan Second District in 2011-2012. Thalli of *Ulva* accumulated on the northern part of the flat due to the tidal current on the flood tide. In contrast, they did not move from the north to the south of the flat because of the slow current on the ebb tide. Wind-driven currents also acted as a factor for the accumulation of *Ulva* on the flat. The water route was thought to play an important role on the accumulation or dispersion of *Ulva* at the artificial tidal flat of Hannan Second District.

A Fundamental Study on Evaluation of Water Mixing in Density-Stratified Fluids by using an Image Analysis

Toru ENDO and Tetsuya KOJO

Journal of Japan Society of Civil Engineering, Ser. B2 (Coastal Engineering), Vol. 68, pp. 1491-1495 (2012) (in Japanese)

It is important to evaluate the water mixing effect before applying water exchange technologies for resolving the pycnocline which causes some environmental problems. In this study, a new image analysis method was developed to estimate the spatial distribution of salinity for evaluating the water mixing effects in density stratified fluid. The effectiveness of developed image analysis was validated by comparing the estimated salinity with the measured salinity by salinometer. Furthermore, the water mixing effect for the case of supplying the surface water to the bottom in density stratified fluid was discussed by using the developed image analysis.

Water Quality in Osaka Bay Based on Simultaneous Water Quality Survey

Satoshi SASAKURA, Kazufumi KAWASAKI, Kenji OKUYAMA, Yasuhiko SAKAI and Susumu YAMOCHI

Journal of Japan Society of Water Environment, Vol. 35, pp. 211-216 (2012) (in Japanese)

A Simultaneous Water Quality Survey in Osaka Bay has been conducted in cooperation with private sectors, universities and governments every summer since 2004. The survey is characterized by almost the same sampling date and sampling depth and by widespread sampling from the shore to the bay mouth. In this report, we describe an overview of the survey and investigate the relationship between climate conditions and the distributions of bottom dissolved oxygen (DO) and surface chemical oxygen demand (COD) as well as the distributions of nitrogen and phosphorus from the shore to the bay mouth. Bottom DO and surface COD, which are indexes of water quality targets in the Action Plan to Revive Osaka Bay, do not reach their target values in the inner bay. These distributions vary according to climate conditions. Dissolved inorganic nitrogen (DIN) and dissolved inorganic phosphorus (DIP) concentrations at the upper layer, which are $0.34 \text{ mg}\cdot\text{L}^{-1}$ and $0.032 \text{ mg}\cdot\text{L}^{-1}$ in the inner bay, decrease to $0.03 \text{ mg}\cdot\text{L}^{-1}$ and $0.008 \text{ mg}\cdot\text{L}^{-1}$ in the bay mouth,

respectively.

Effects of Desiccation and Salinity on the Outbreak of a Green Tide of *Ulva pertusa* in a Created Salt Marsh along the Coast of Osaka Bay, Japan

Susumu Yamochi

Estuarine, Coastal and Shelf Science, Vol. 116, pp. 21-28 (2013)

Field surveys and laboratory experiments were conducted to examine the effect of desiccation and salinity on the outbreak of a green tide of *Ulva pertusa* at Osaka Nanko bird sanctuary. Reduction of biomass of *Ulva* spp. was observed at stations where the exposure rate to air was from 30 to 40%. In addition, the exposure rate of 30 to 40% to air showed no negative impacts on the biomass of benthic microalgae, infauna and non-motile epibenthos. Laboratory experiments revealed that photosynthetic activity of *Ulva pertusa* decreased when exposed to air for 4 to 7 hours at 25-35 °C. Salinity decreases from 30 to 25 or 20 accompanied with exposure to air drastically reduced the rate of photosynthesis of this species. These results suggest the possibility of controlling a green tide of *Ulva pertusa* without serious physico-ecological damage to benthic microalgae, infauna and non-motile epibenthos by a combination of exposure to air with low salinity. Distributions of Dissolved Oxygen and Carbon Dioxide in Eastern Osaka Bay and their Effects on the Survival of Adult Southern Rough Shrimp, *Trachysalambria curvirostris*

Fractionation Analysis of Phosphorus in Anaerobic Digestion Process for Sewage Sludge and Garbage

Masafumi OHTA, Munehiro TAKAHASHI and Yoshinori KANJO

Proceedings of the 3rd Forum on Studies of the Environmental & Public Health Issues in the Asian Mega-cities, pp. 82-85 (2012)

Phosphorus is one of the essential elements as a fertilizer to cultivated area. But lack of phosphorus resources becomes serious problem, because mineral phosphate is located eccentrically in the world, and the export control of mineral phosphate in the producing countries becomes tight. Since we have no mineral phosphate in Japan, the stable securing of phosphate resources is important task. In this study, we focused on the distribution of each chemical form of phosphorus in sewage sludge and garbage, and the changes in the phosphorus fractionations through an anaerobic digestion process. As a result of study, it has been observed that; 1) the thickened sewage sludge and seed sludge contained high ratio of SRP and DRP. Compared with these two sludges, the ratio of SRP in the garbage was as low as 6%, 2) 91% of total phosphorus in digested sludge was inorganic forms such as phosphate ion or metal phosphates, 3) two-thirds of total phosphorus in the digested sludge were the metal phosphates such as calcium, manganese, aluminium and ferric phosphate. Judging from these results, we concluded that main form of phosphorus in the digested sludge was metal phosphates.

Phosphate Material Balance and Improvement of Phosphate Removal Efficiency in Centralized Sewage Sludge Treatment Plant

Satoshi NAKAO, Yasuichi SAGAWA, Yuko FUJIOKA, Yoshinori KANJO

Journal of Japan Sewage Works Association, Vo. 49, No. 599, pp. 123-130 (2012) (in Japanese)

In a sewage treatment process, phosphate is a removal target for preventing from eutrophication. Recently, the recovery of phosphate has been widely noticed. From these points of view, we have been performed that the injections of polyferric sulphate solution to the thickener for reducing the load of phosphate in the recycle flow at Eastern Hyogo Regional Sewage Sludge Treatment Plant. This method can reduce the load of phosphate in the recycle flow easily, and can also improve the phosphate removal efficiency in the whole treatment process. In this paper, we demonstrated the improvement of phosphate removal efficiency with polyferric sulphate solution to the thickener by the table and field experiments, and showed the results of long term operation in the whole treatment process. Furthermore, we confirmed that the cost involving this method could be compensated by reducing the cost of the expensive coagulants in the dewatering process and recycle flow. Finally, we concluded the effectiveness of phosphate removal method with polyferric sulphate solution.

Modified Sediment Test Method for Analysis of Total Cyanide Content by means of Cascade Sample Bulking

Mitsuo MOURI and Yoshinori KANJO

Journal of Japan Society of Civil Engineers, Sr. G (Environmental Research), Vol. 68, No. 4, pp. 224-233 (2012) (in Japanese)

Soils at Manufactured Gas Plant (MGP) sites are often contaminated by cyanide (CN). Besides free-CN, contaminated soils at MGP sites contain less or little toxic Metal-CN complexes (mostly iron-CN complexes) as a large part of total CN. The total CN is an important index used for the evaluation of soil remediation process such as soil washing. The total CN content is measured by the sediment test method. After having experiences of soil washing for several MGP sites, it has been noticed that the mass balance was not maintained when the total CN content was measured by the sediment test method.

In order to eliminate the observed inadequacy of the sediment test method, an experimental study was conducted to modify the method. Each soil sample from three MGP sites was divided into six parts to make a series of cascade bulk samples. Each cascade bulk sample was mixed with clean sand in such a way that the prepared sample had increased its dry weight by 1, 2, 5, 10, 20 and 50 times the divided soil sample. Then the relationship between the rate of bulking and the test value of total CN content was investigated. The same test is repeated for a standard sample comprising ferric ferrocyanide ($\text{Fe}_4[\text{Fe}(\text{CN})_6]_3$) and clean sand. As a result of study, it has been observed that; 1) a bulking factor of 10 is enough to get near true of total CN content for highly contaminated soils, 2) the test with standard samples of varying total CN content showed a maximum CN recovery rate of 805, and 3) no bulking of sample is necessary for soil with less than 50mg/kg of CN. It is concluded that the modified sediment test method is effective and necessary for the quantitative evaluation of cleanup of soils contaminated with CN.

Recovery of indium from end-of-life liquid-crystal display panels using aminopolycarboxylate chelants with the aid of mechanochemical treatment

Hiroshi HASEGAWA, I. M. M. RAHMAN, Yuji EGAWA, Hikaru SAWAI, Zunnat A. BEGUM, Teruya MAKI, Satoshi MIZUTANI

Microchem. J., 106, pp. 289-294 (2013)

The metal indium termed as 'rare' in recent days due to its increasing demand in the formulations of electronic and energy-related gadgets and scarce supply resources. Hence, the attempts to recover indium from the secondary resources, such as recycling of the indium abundant waste materials, received increasing research focus. The major indium consumption happens in the form of indium tin oxide (ITO) that used for the fabrication of liquid crystal displays (LCD). The end-of-life LCD screens, termed as ITO-glass hereafter, are an emerging contributor to the global e-waste load and can be an impending secondary source of indium. The present work introduces a new technique for the treatment of waste ITO-glass using aminopolycarboxylate chelants (APCs) in combination with mechanochemical treatment process. APCs are capable of forming stable complexes with the indium deposited on the ITO-glass, whereas the rate of recovery was not substantial. The mechanochemical treatment induces the destruction of crystalline structure with which the ITO fragments are attached and facilitate the increased indium dissolution with the chelants. The increase was more prominent followed by a decrease in the cumulative processing time from 24 to 6 h when the vitrified ITO-glass was simultaneously crushed and washed with the chelants. The extraction of indium was better at the acidic pH condition, and it was further intensified when the operating temperature was raised to ≥ 120 °C.

A silica gel-bound macrocycle system for the selective separation of toxic cadmium from metal-affluent aqueous matrix

Hiroshi HASEGAWA, Ismail M. M. RAHMAN, Zinnat A. BEGUM, Yoshihiro UMEHARA, Teruya MAKI, Yoshiaki FURUSHO, Satoshi MIZUTANI

Cent. Eur. J. Chem., 11, pp. 341-347 (2013)

Selective separation of cadmium (II) on a macrocycle immobilized solid phase extraction (SPE) system namely AnaLig Cd-01, and commonly known as molecular recognition technology (MRT) gel, have been examined. The MRT-SPE able to retain the cadmium from the metal-affluent aqueous matrix at the pH range of 2 to 8, and the captured species can be recovered via elution with 1 and 6 M HNO_3 . Besides the effects of solution pH and eluent concentration, the impacts of sample loading flow rates and coexisting matrix ions were also investigated and optimized. The Cd (II) retention capacity of the MRT-SPE was 0.26 mmol/g, and it can be reused for more than 100 loading and elution cycles. The Cd (II) recovery attained from the metal-spiked natural waters was satisfactory (95.3–98.1%). However, the Cd (II) retention ability of the

MRT-SPE was significantly decreased when excess of chelant remain in the aqueous waste matrix.

Chelant-induced reclamation of indium from the spent liquid crystal display panels with the aid of microwave irradiation

Hiroshi HASEGAWA, Ismail M. M. RAHMAN, Yuji EGAWA, Hikaru SAWAI, Zinnat A. BEGUM, Teruya MAKI, Satoshi MIZUTANI

J. Hazard. Mater., 254-255, pp. 10-17 (2013)

Indium is a rare metal that is mostly consumed as indium tin oxide (ITO) in the fabrication process of liquid crystal display (LCD) panels. The spent LCD panels, termed as LCD-waste hereafter, is an increasing contributor of electronic waste burden worldwide and can be an impending secondary source of indium. The present work reports a new technique for the reclamation of indium from the unground LCD-waste using aminopolycarboxylate chelants (APCs) as the solvent in a hyperbaric environment and at a high-temperature. Microwave irradiation was used to create the desired system conditions, and a substantial abstraction of indium ($\geq 80\%$) from the LCD-waste with the APCs (EDTA or NTA) was attained in the acidic pH region (up to pH 5) at the temperature of ≥ 120 °C and the pressure of ~ 50 bar. The unique point of the reported process is the almost quantitative recovery of indium from the LCD-waste that ensured via the combination of the reaction facilitatory effect of microwave exposure and the metal extraction capability of APCs. A method for the selective isolation of indium from the extractant solution and recycle of the chelant in solution is also described.

Selective recovery of indium from the etching waste solution of the flat-panel display fabrication process

Hiroshi HASEGAWA, Ismail M. M. RAHMAN, Yoshihiro UMEHARA, Hikaru SAWAI, Teruya MAKI, Yoshiaki FURUSHO, Satoshi MIZUTANI

Microchem. J., 110, pp. 133-139 (2013)

The waste byproducts from the indium-consuming fabrication processes are considered as the viable resource for indium due to the unique preference to the element in designing optoelectronic devices. The present work introduces a new technique for the selective recovery of indium from the etching waste, which produced during the patterning of indium tin oxide (ITO) layer on the flat-panel displays. The process includes the application of a solid phase extraction (SPE) assembly, known as molecular recognition technology (MRT) gel, consisting of a metal-selective ligand immobilized to silica gel or polymer substrates. The samples were the real solution of etching waste from the liquid-crystal display fabrication process, and the simulated waste solution prepared using the commercially available etching solution composition containing ethanedioic acid. The retention and the corresponding indium recovery rate (%) were the key characteristics for the appraisal of MRT-SPE types: AnaLig TE 02 (TE 02), AnaLig TE 03, AnaLig TE 07, AnaLig TE 13 and AnaLig PM 02. The other conclusive factors were the influence of ion intensity in solution and the interfering effects from tin, the co-content element in the ITO-formulation. The TE 02 MRT-SPE came across all the requisite aspects for the selective recovery of indium from the etching effluent. The indium retention or recovery with TE 02 MRT-SPE from the real etching waste solution was in the range of 97 to 99% with the relative standard deviation of $< 4.4\%$. The separation of the ITO co-element tin from the waste mixture was successively selective, and thereby minimizes the possibility of interference. A three-step elution with 0.3 mol/L HNO₃, 6 mol/L HCl and 1 mol/L HCl/ 10 mmol/L EDTA was required to accomplish the sequential selectivity in the process. The indium retention capacity of the TE 02 MRT-SPE was 0.147 mmol/g.

Comparison study of environmental standards of soil in East Asian region in relation to utilization of recycling materials

Hirofumi SAKANAKURA, Satoshi MIZUTANI, Rieko KUBOTA

Proc. of International Conference on Environmental and Hazardous Substance Management towards a Green Economy, 21-23 May, Bangkok, Thailand (2013)

In order to enhance the recycling of by-products and solid wastes such as ferrous slag, coal combustion ash, municipal solid waste incineration ash and C&D waste ensuring the environmental safety, there has been a discussion to standardize the environmental quality standards and its testing methods in the East Asian region, such as Japan, Korea and Taiwan and China. The difference and characteristics of current soil

environmental standards and its test methods in the region is discussed. It suggests the necessity of legally binding guidelines for utilization of recycling materials and their environmental quality and its testing methods based on the understanding of different background for soil environmental standards including the climate and geographic differences within the region.